Novel nanoparticle synthesis in self-organizing water-based systems

Dissertation

Zur Erlangung des Doktorgrades der Naturwissenschaften (Dr. rer. nat.)
an der Naturwissenschaftlichen Fakultät IV
– Chemie und Pharmazie –
der Universität Regensburg



vorgelegt von
Bastian Rödig
aus Ingolstadt

August 2026

This thesis is based on the experimental work done between December 2022 and December 2025 under the supervision of Prof. Dr. Werner Kunz at the Institute of Physical and Theoretical Chemistry, Faculty of Chemistry and Pharmacy, University of Regensburg, Germany.

Dissertation Submission: 03.08.2026
Dissertation Defense: 20.10.2026

Supervisor Prof. Dr. Werner Kunz

Examination committee

Chair	Prof. Dr. Oliver Tepner
1st Examiner	Prof. Dr. Werner Kunz
2nd Examiner	Prof. Dr. Rainer Müller
3rd Examiner	Prof. Dr. Arno Pfitzner

Acknowledgements

The achievements made during this PhD thesis would not have been possible without the valuable aid and support of numerous people:

First of all, I want to thank my supervisor, **Prof. Dr. Werner Kunz**, for the opportunity to carry out this interesting thesis at his institute. His mentoring offered advice whenever required and the freedom to find my own path into research.

I want to thank also **Prof. Dr. Rainer Müller** for being the second referee and for his help with BET measurements. Furthermore, thanks to **Prof. Dr. Arno Pfitzner** for being the third referee and giving me the opportunity to measure XRD at his chair. Lastly, thanks to **Prof. Dr. Oliver Tepner** for completing the examination board.

I sincerely thank **Prof. Dr. Lorenz Kienle** and **Dr. Ulrich Schürmann** from the Chair of Synthesis and Real Structure, Faculty of Engineering, Kiel University for granting access to their facilities and the measurements and discussions of HRTEM micrographs. I want to extend my gratitude toward **Prof. Dr. Reinhard Rachel** from the Department of Microbiology, Faculty of Biology and Preclinical Medicine, University of Regensburg, for granting access to a TEM device and fruitful discussions. Also, I want to thank **Dr. Matthias Kellermeier** for infrequent but fruitful conversations and helpful input.

I am thankful for the experimental help provided by the CTA trainees **Anna Mändl**, **Anna Selmeier**, **Arne Hornberg**, **Julian Dolina**, and **Olga Gebert** during their work at our chair. I further want to thank the students **Anita Fuchs**, **Daniel Nagin**, **Elias Wild**, **Lukas Vala**, **Verena Graf**, and **Verena Schlüter** for their practical contributions to this work.

I also thank the **European Synchrotron Radiation Facility** (**ESRF**) for providing beam time and for the opportunity to conduct research at this internationally renowned institution.

A big thanks goes to the members of our institute: the secretaries: **Bianca Heiligtag**, **Rosemarie Röhrl**, and **Steffi Meinel**, the permanent staff: **Dr. Eva Müller**, **Dr. Johnny Hioe**, **Dr. Peter Krageorgiev**, **Prof. Dr. Rainer Müller**, and **Dr. Thomas Herl**, and the CTAs: **Daria Nieder**, **Franziska Wolf**, **Hellmuth Schönsteiner**, and **Theresa Edenharter** for their support whenever needed and for the pleasant working climate during the time I spent at the institute.

I sincerely thank my (former) colleagues for the supportive and wonderful atmosphere in our group: **Adrien**, **Ann-Christin**, **Clara**, **Eliott**, **Eva**, **Lea**, **Lena**, **Jenny**, **Jonas**, **Moritz**, **Nadja**, **Patrick**, **Selina**, and **Vanessa**. Especially I want to thank my lab partner and dear friend **Dr. Patrick Denk** and my former office colleagues **Dr. Jonas Blahnik**, **Jennifer Schuster**, **Dr. Lea Rohr**, and **Lena Schmauser** for scientific and non-scientific discussions, exceptional

team spirit, and the supportive moments we shared. The time we spent together has helped us all grow and become better scientists.

Last but not least, my deepest gratitude goes towards my family, my parents **Anja** and **Wolfgang**, my sister **Ramona**, and my girlfriend **Lea** for their never-ending love and support. None of this would have been possible without you.

Thank you all very much!

Abstract

Nanoparticle synthesis has evolved into a highly diverse discipline, characterized by increasingly sophisticated precursor designs, reactor engineering, and templating strategies to achieve precise control over particle properties. Although this diversity has significantly advanced the field, it has also diverted attention from the fundamental physicochemical principles governing nanoparticle formation. This thesis adopts an alternative approach: instead of increasing synthetic complexity, it seeks to mechanistically elucidate nanoparticle formation in simple, water-based systems under mild conditions, and to exploit this understanding to control and, where feasible, optimize particle properties for targeted applications.

Three (and a half) structurally distinct systems were investigated: surfactant-free ternary mixtures for Stöber-type silica synthesis; spontaneous, one-pot coprecipitation of transition metal carbonates and sulfides within silica matrices, including the effects of ligand-controlled precipitation phenomena on this coprecipitation process; and polyacrylic acid/transition-metal coacervates as templates for nanoparticle formation. In all systems, particle formation was determined to depend more on the kinetics governing the availability, interaction, and assembly of the relevant building blocks than on the complexity of the synthesis route. Interfacial diffusion across microemulsion boundaries, pH-coupled silica condensation, precursor complex stability, ligand-mediated surface passivation, and confinement-induced changes in chemical potential were each identified as tunable, rate-limiting steps. Based on these insights, highly monodisperse nanoscale silica particles, silica-encapsulated transition-metal carbonate and sulfide nanodots, precursor- and ligand-tuned CdS/ZnS quantum dots, and coacervate-templated ultra-small carbonate, sulfide, and oxide nanoparticles were synthesized using only water as the solvent under near-ambient conditions.

Building on this mechanistic understanding, application-oriented optimization was conducted for selected synthesized materials. Notably, iron oxide/silica core–shell particles produced via the coprecipitation route were developed into heterogeneous Fenton-like catalysts that operate at circumneutral pH, achieving activity comparable to or surpassing that of more complex multistep systems. Additional application-specific optimization was performed for the remaining materials and is discussed in conjunction with the relevant mechanistic findings. Collectively, these results demonstrate that a kinetically informed understanding of nanoparticle formation offers a robust and transferable framework for the rational, application-driven design of functional nanomaterials using simple, sustainable, and scalable water-based synthesis methods.

Zusammenfassung

Die Synthese von Nanopartikeln hat sich zu einem äußerst vielfältigen Forschungsgebiet entwickelt, das durch immer ausgefeiltere Vorläuferkonzepte, Reaktortechnik und Templatierungsstrategien gekennzeichnet ist, um eine präzise Steuerung der Partikeleigenschaften zu erreichen. Diese Vielfalt hat zwar das Fachgebiet erheblich vorangebracht, jedoch auch die Aufmerksamkeit von den grundlegenden physikalisch-chemischen Prinzipien abgelenkt, die der Bildung von Nanopartikeln zugrunde liegen. Diese Dissertation verfolgt einen alternativen Ansatz: Anstatt die Komplexität der Synthese zu erhöhen, zielt sie darauf ab, die Nanopartikelbildung in einfachen, wasserbasierten Systemen unter milden Bedingungen mechanistisch aufzuklären und dieses Verständnis zu nutzen, um die Partikeleigenschaften für gezielte Anwendungen zu steuern und, soweit möglich, zu optimieren.

Insgesamt wurden drei(einhalb) strukturell unterschiedliche Systeme untersucht: tensidfreie ternäre Gemische für die Synthese Stöber-artige Siliciumdioxidpartikel; die spontane Kopräzipitation von Übergangsmetallcarbonaten und -sulfiden eingebettet in Siliciumdioxid-Matrizen, einschließlich der Auswirkungen ligandengesteuerter Fällungsphänomene auf diesen Kopräzipitationsprozess; sowie Polyacrylsäure/Übergangsmetall-Koazervate als Template für die Nanopartikelbildung. In allen Systemen zeigte sich, dass die Partikelbildung stärker von der Kinetik abhängt, die die Verfügbarkeit, Wechselwirkung und Anordnung der relevanten Bausteine bestimmt, als von der Komplexität des Synthesewegs. Grenzphasendiffusion über Mikroemulsionsgrenzen hinweg, pH-gesteuerte Siliciumdioxid-Kondensation, Stabilität der Vorläuferkomplexe, Liganden-gestützte Oberflächenpassivierung und Änderungen des chemischen Potenzials wurden jeweils als einstellbare, geschwindigkeitsbestimmende Schritte identifiziert. Auf der Grundlage dieser Erkenntnisse wurden monodisperse nanoskalige Siliciumdioxidpartikel und mit Siliciumdioxid eingekapselte Übergangsmetallcarbonat- beziehungsweise -sulfid-Nanomaterialien hergestellt. Ebenso konnten durch Vorläufer und Liganden abgestimmte CdS/ZnS-Quantenpunkte sowie durch Koazervate als Templat ultrakleine Carbonat-, Sulfid- und Oxid-Nanopartikel unter Verwendung von ausschließlich Wasser als Lösungsmittel bei nahezu Umgebungsbedingungen synthetisiert werden.

Aufbauend auf diesem mechanistischen Verständnis wurde eine anwendungsorientierte Optimierung für ausgewählte synthetisierte Materialien entwickelt. Insbesondere wurden Eisenoxid/Siliciumdioxid-Kern-Schale-Partikel, die im Kopräzipitationsverfahren hergestellt wurden, zu heterogenen Fenton-ähnlichen Katalysatoren weiterentwickelt, die bei einem nahezu neutralen pH-Wert arbeiten und dabei eine Aktivität erreichen, die mit den komplexeren

mehrstufigen Systemen vergleichbar ist oder diese sogar übertrifft. Für die übrigen Materialien wurde eine zusätzliche anwendungsspezifische Optimierung durchgeführt, die im Zusammenhang mit den entsprechenden mechanistischen Erkenntnissen erörtert wird. Insgesamt zeigen diese Ergebnisse, dass ein kinetisch fundiertes Verständnis der Nanopartikelbildung einen robusten und übertragbaren Rahmen für das rationale, anwendungsorientierte Design funktioneller Nanomaterialien unter Verwendung einfacher, nachhaltiger und skalierbarer Syntheseverfahren auf Wasserbasis bietet.

List of Abbreviations

ACC	amorphous calcium carbonate
AI	artificial intelligence
AOP	advanced oxidation process
BET	Brunauer-Emett-Teller
cf.	confere
CNT	classical nucleation theory
CV	cyclic voltammetry
DE	defect-related emission
DLS	Dynamic Light Scattering
DLVO	Derjaguin-Landau-Verwey-Overbeek
EDX	Energie dispersive X-ray Analysis
Eqn.	equation
EtOH	ethanol
FWHM	full width at half max
(HR)TEM	(high resolution) transmission Electron Microscopy
MWCO	molecular weight cutoff
NP	nanoparticle
NTA	Nanoparticle Tracking Analysis
PAA	polyacrylic acid
PDI	polydispersity index
PL	Photoluminescence
QD	quantum dot
ref	reference
rH	hydrodynamic radius
ROS	reactive oxygen species
S(W)AXS	small- (and wide-)angle x-ray scattering
SAED	selected area diffraction
SEM	Scanning Electron Microscopy
SFME	surfactant-free microemulsion
SHMP	sodium hexametaphosphate
TEOS	tetraethyl orthosilicate

UV	ultraviolett
VIS	visib le light
XRD	X-ray diffraction nalysis

Table of Contents

Acknowledgements ..... **III**

Abstract ..... **V**

Zusammenfassung ..... **VI**

List of Abbreviations ..... **VIII**

Table of Contents ..... **X**

Chapter I. General Background **1**

1.1 Introduction 1

1.2 Fundamentals 3

1.2.1 Classical Nucleation Theory (CNT) 3

1.2.2 Colloidal Stability of Nanoparticles 5

1.2.3 LaMer Model of Nucleation and Growth 9

1.2.4 Strategies to Control Nanoparticle Syntheses 10

1.2.5 Special Properties of Nanoparticles Deviating from Bulk Materials 11

1.3 References 14

Chapter II. Surfactant-free Microemulsion as Template for Stöber Silica Nanoparticles Synthesis **23**

2.1 Abstract 23

2.2 Introduction 25

2.2.1 Chemistry of Silica 25

2.2.2 Parameter Dependence of the Stöber Synthesis 27

2.2.3 Models for Particle Formation 29

2.2.4 Surfactant-free Microemulsion (SFME) 31

2.2.5 H_2O / EtOH / TEOS a Ternary Mixture and a SFME? 33

2.3 Experimental 35

2.3.1 Materials 35

2.3.2 Apparatus 35

2.3.3 Methods 35

2.4 Results and Discussion 39

2.4.1 Ternary Phase Diagrams and Structuring of Different Mixtures 39

2.4.2 Kinetics of Stöber Nanoparticle Formation in the Different Mixtures (Refutation of Mechanisms Proposed in Literature) 44

2.4.3 Proposed Mechanism of Nanoparticle Formation in the Regular SFME Systems 48

2.5 Conclusion 51

2.6 References 52

2.7 Supporting Information 61
Chapter III. Nanodots of Transition Metal Sulfides, Carbonates and Oxides Obtained by Spontaneous Co-Precipitation with Silica 69
3.1 Abstract 69
3.2 Introduction 71
3.3 Experimental 74
3.3.1 Materials 74
3.3.2 Apparatus 74
3.3.3 Methods 77
3.4 Results 81
3.4.1 Coprecipitation of Various Transition Metal Sulfides and Carbonates and their Transition into Oxides 81
3.4.2 Influence on the Formed Particles by Synthesis Parameter Variation and Addition of Small Molecules 89
3.5 Discussion 101
3.6 Conclusion 105
3.7 References 106
3.8 Supporting Information 115
Chapter IV. Heterogeneous Fenton Reaction at Neutral pH Values Catalyzed by One-Pot Synthesized Iron Oxide/Silica Core Shell Nanoparticles 137
4.1 Abstract 137
4.2 Introduction 139
4.2.1 The Fenton Reaction 139
4.2.2 Reaction Kinetics of Heterogeneous Fenton Reactions 140
4.2.3 Mechanism of Hydrogen Peroxide Activation on Silica-supported Iron Oxides 142
4.2.4 Silica-supported Iron Oxides Derived from a One-Pot Coprecipitation Reaction 143
4.3 Experimental 145
4.3.1 Materials 145
4.3.2 Apparatus 145
4.3.3 Methods 147
4.4 Results and Discussion 149
4.4.1 Structural Overview 149
4.4.2 Catalytic Difference in Sulfide and Carbonate Derived Materials 150
4.4.3 Effective Utilization of Oxidative Species by the Nanomaterial? 152
4.4.4 Tuning Silica Shell Formation and Accessibility 155
4.5 Conclusion 162
4.6 References 164
4.7 Supporting Information 170

Chapter V. Influence of Complex Precursors on the Coprecipitation of Transition Metal Sulfides and Silica 179
5.1 Abstract 179
5.2 Introduction 181
5.2.1 Nanoparticles Formation Utilizing Complexation 181
5.2.2 Complexes Used for Nanoparticle Formation 183
5.3 Experimental 186
5.3.1 Materials 186
5.3.2 Apparatus 186
5.3.3 Methods 187
5.4 Results and Discussion 190
5.4.1 Cation and Ligand Screening in the Coupled Coprecipitation Process 190
5.4.2 Variation of Synthesis Parameters – Mixed Ligand Complexes -Enabling Coprecipitation for Particles Derived from $CdCys_2$? 199
5.4.3 Tuning of the Bandgap – From CdS to $Zn_xCd_{1-x}S$ 208
5.5 Conclusion 212
5.6 References 214
5.7 Supporting Information 225
Chapter VI. Nanoparticle Formation Utilizing Simple Polyacrylic Acid-Cation Coacervates as Template 241
6.1 Abstract 241
6.2 Introduction 243
6.2.1 Simple and Complex Coacervation 243
6.2.2 Mechanisms of Coacervate Formation of PAA and Divalent Cations 244
6.2.3 Coacervates as Template for Nanoparticle Formation 245
6.3 Experimental 246
6.3.1 Materials 246
6.3.2 Apparatus 246
6.3.3 Methods 246
6.4 Results and Discussion 249
6.4.1 Coacervate Formation 249
6.4.2 Coacervate Characterization 250
6.4.3 Mineralization of the Coacervates 253
6.5 Conclusion 259
6.6 References 261
6.7 Supporting Information 266

General Conclusion and Outlook 273

Appendix **277**

List of Figures *277*

List of Tables *294*

Scientific Contributions *296*

Eidesstattliche Erklärung *297*

Chapter I. General Background

1.1 Introduction

Nanoparticles (NPs) have become a major focus of research over the past decades due to their unique physicochemical properties, which differ significantly from those of their bulk counterparts. Their high surface-to-volume ratio, tunable size, and versatile surface chemistry enable applications across a broad range of scientific disciplines, including catalysis [1], electronics [2], energy storage [3], (bio-)sensors [4], functional coatings [5,6], and many more [7]. In particular, nanomaterials have attracted considerable attention in biomedical research because they offer promising opportunities for targeted drug delivery [8], bioimaging [9,10], diagnostics [10], and therapeutic applications [10,11].

Nanoparticles are generally defined as particles possessing at least one dimension in the range of 1-100 nm. Whereas NPs are common in biology and nature, industrial production with specified properties is a current field of research [12]. Objects of comparable dimensions include DNA molecules and viruses, as illustrated in **Figure I-1**.

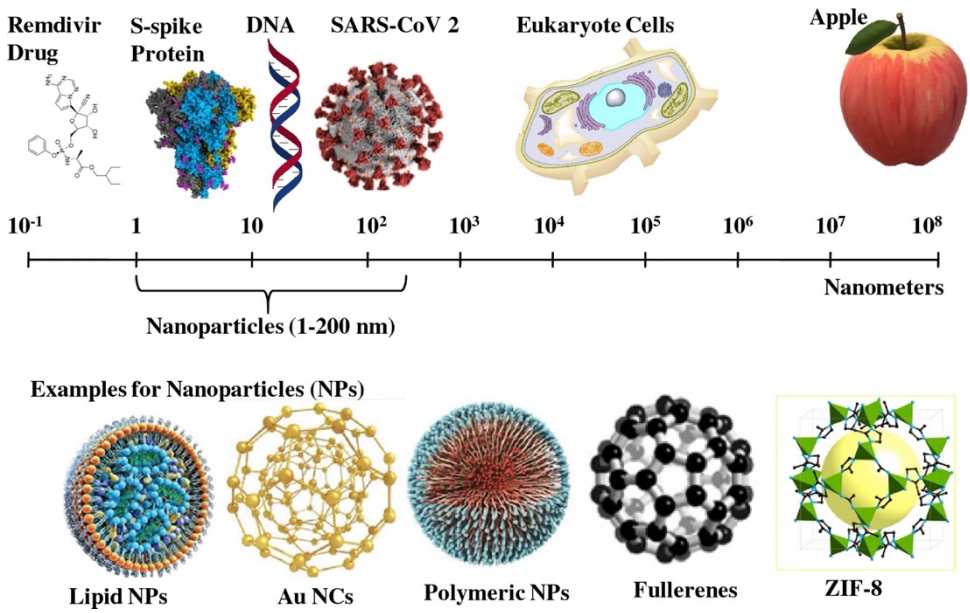


Figure I-1. Scale of NPs with some examples for size comparison. Reprinted with permission from ref [12].

Two different approaches are pursued to produce NPs industrially. The top-down method produces NPs from bulk materials, and the bottom-up approach forms NPs directly from atoms or molecules [13].

In this study, various bottom-up strategies were used to produce a diverse range of particles. Some of these particles were also tested in application-specific areas.

The influence of structuring solvents on one of the most investigated/researched nanoparticle synthesis methods, the Stöber synthesis [14], was investigated in **Chapter II**. In particular, the highly dynamic system of surfactant-free microemulsions [15,16] were examined for their potential templating properties [17,18].

A self-organizing system that enables the formation of core-shell nanoparticles was examined in **Chapter III**. As with known silica biomorphs [19,20], the overlap of precipitation pH zones is exploited to achieve coprecipitation [21,22]. The use of such structures as catalysts was investigated in **Chapter IV**. In particular, iron oxides were used as heterogeneous Fenton catalysts [23,24]. In **Chapter V,** ways of gaining a deeper understanding of and better control over the coprecipitation reaction were examined. To this purpose, complexes were used as precursors to utilize their potential kinetic inhibitory effect on precipitation [25–27].

In **Chapter VI**, the extent to which polyelectrolyte solutions [27] – or, more precisely, specific phase states in polymer solutions [28] – can be utilized as templates for particle synthesis [29], was studied. To this purpose, the liquid-liquid phase separation, simple coacervation, of divalent cations and anionic polyelectrolytes was triggered and mineralized.

The fundamentals of particle formation in solution are explained below.

1.2 Fundamentals

1.2.1 Classical Nucleation Theory (CNT)

Nucleation is a thermodynamic model describing the appearance of a new phase (nucleus) in the metastable primary phase. The thermodynamic driving force for nucleation is the reduction of the Gibbs free energy of the system [30,31].

Typically, a distinction is made between homogeneous and heterogeneous nucleation. In classical nucleation theory (CNT), both are treated within the framework of the macroscopic Gibbs capillary approximation, where the nucleus is assumed to possess bulk properties and a defined surface tension [30]. Homogeneous nucleation occurs spontaneously and randomly, triggered by a supercritical state, such as supersaturation [32].

The Gibbs free energy of a seed can then be described as the sum of a negative and a positive contribution. The negative contribution accounts for the energetically favorable binding of a monomer to a cluster, reducing the Gibbs free energy of the volume. The positive contribution captures the energetic cost of this binding, resulting from the increase in Gibbs surface energy. In the simplest case of a spherical nucleus, the Gibbs free energy (ΔG) can be written as [30,31]:

$$\Delta G = -\frac{4}{3}\pi r^3 |\Delta G_v| + 4\pi r^2 \gamma \tag{I-1}$$

with the radius r, the change in Gibbs free energy per unit volume $|\Delta G_v|$, and the surface energy per unit area γ. For the precipitation of solids from solutions, ΔG_v depends on the supersaturation S, the molar volume v of the solid, and the temperature T [33]:

$$\Delta G_v = -\frac{k_B T \cdot ln(S)}{v} \tag{I-2}$$

Due to the positive and negative contributions, a maximum at the critical radius (r_c) with the energy barrier (activation energy, ΔG_c) is created. (cf. **Figure I-2a**)

Clusters smaller than r_c are more susceptible to dissolution, while for larger clusters growth is favored. The critical radius can be written, by solving $d\Delta G/dr = 0$, as:

$$r_c = \frac{2\gamma}{|\Delta G_v|} \tag{I-3}$$

The nucleation rate $J(T, \Delta G_c)$ can be written using the Arrhenius equation [34]:

$$J(T, \Delta G_c) = A \cdot \exp\left(-\frac{\Delta G_c}{k_B T}\right) \tag{I-4}$$

Heterogeneous nucleation refers to the formation of nuclei at preferential sites such as the existing surface of particles in solution. These preferential sites, e.g., phase boundaries, reduce the effective surface energy, thus lowering the activation energy and making nucleation more probable. In nanoparticle synthesis, both types of nucleation usually occur simultaneously [32,35].

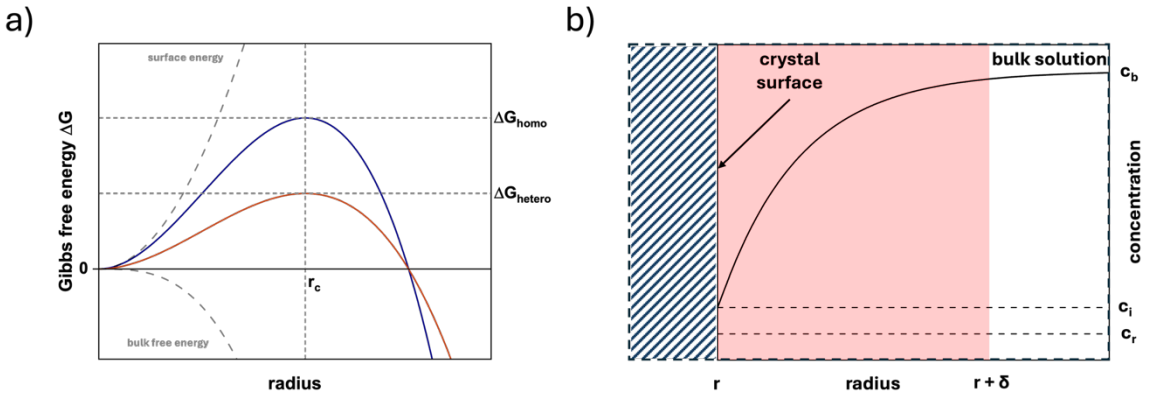


Figure I-2. (a) Change in Gibbs free energy ΔG for nucleation as a function of radius (r) for homogeneous nucleation (blue line) and heterogeneous nucleation (red line) according to CNT. The curves show a maximum free energy (ΔG) at the critical radius r_c. (b) Schematic representation of the diffusion layer on the surface of forming nuclei. The plot represents the concentration as a function of distance from the surface. After a distance of r + δ the concentration of the bulk phase is reached [36].

Although CNT successfully describes nucleation in many systems, it relies on several simplifying assumptions, e.g., a crystalline nucleus formed from monomeric species, bulk-like properties of very small nuclei, and a sharp interface between the nucleus and the surrounding phase. Experimental observations in a variety of systems have revealed deviations from these assumptions, motivating the development of non-classical nucleation models [37–42]. These models do not replace CNT but rather extend it by accounting for intermediate states and alternative pathways.

One of the most prominent extensions is the two-step nucleation model. In this model, solute species first form metastable, dense liquid-like or amorphous clusters. Crystallization

subsequently occurs within these precursor structures, reducing the nucleation barrier compared to direct crystal formation from dissolved monomers [37,42,43].

Further, stable prenucleation clusters have been reported in several systems. These clusters may exist even below the classical nucleation threshold and can serve as precursors for subsequent particle formation [39,42].

In addition to nucleation-related mechanisms, particle growth may proceed through oriented attachment, where individual nanocrystals align along common crystallographic orientations and fuse into larger crystalline structures. Such growth pathways differ fundamentally from the monomer-by-monomer growth assumed in classical models [38].

One final weakness of the CNT is that it describes only nucleation, with particle growth treated as a subsequent process. Generally, particle growth depends on surface reactions and monomer diffusion to the surface [44–46]. (cf. **Figure I-2b**) In a system where diffusional growth would only be dependent on the monomer flux, smaller particles will grow faster in the presence of larger particles, resulting in a narrowing of the size distribution [47]. However, in a real system, aggregation, coalescence, and dissolution must also be considered [44–46].

Nevertheless, CNT remains a valuable framework for describing and rationalizing nanoparticle formation across many systems and provides the conceptual basis for most of the synthesis strategies discussed in this work.

1.2.2 Colloidal Stability of Nanoparticles

Particles at the nanoscale typically tend to agglomerate or undergo coalescent processes. Thus, one of the main aspects in colloid science is the stabilization of NPs in the dispersing medium [48,49]. Colloidal stability involves kinetic and thermodynamic considerations. The kinetic behavior depends on the interaction potential. When two particles approach each other, the interaction has two components, static forces and the dynamic effect derived from hydrodynamic interaction [50].

The DLVO (Derjaguin-Landau-Verwey-Overbeek) theory combines two types of static interactions: the electrostatic repulsion (also called double-layer repulsion) and the van der Waals attraction [51,52]. If particles are of the same type, the Van der Waals interaction is always attractive, whereas the electrostatic interaction is repulsive. In the absence of a repulsive energy barrier (maximum between the first and second minima), particles come close together and become energetically trapped in the primary minimum, leading to aggregation. If the particles settle energetically into the secondary minimum, the resulting process is called

flocculation. (cf. **Figure I-3a**) Most colloids are thermodynamically unstable and are only hindered from falling into the primary minimum if the barrier exceeds the thermal energy $k_B T$. The total interaction potential $V(r)$ can be described as [50]:

$$V(r) = V_A(r) + V_R(r) \tag{I-5}$$

with the distance between the particles r, the potential for repulsive forces $V_R(r)$, and the potential for attractive forces $V_A(r)$. These potentials can be specified for the interaction between two spherical colloids [50].

$$V_A(r) = -\frac{H}{6r} \cdot \frac{R_1 R_2}{(R_1 + R_2)} \tag{I-6}$$

$$V_R(r) = \frac{64\pi k_B T R c_0^* \gamma^2}{\kappa^2} e^{-\kappa r} \tag{I-7}$$

with the Hamaker constant of the suspension medium H, the radii of particles R_1 and R_2, the Boltzmann constant k_B, the temperature T, the gas constant R, the bulk electrolyte concentration c_0^*, the Debye screening length κ^{-1}, and the reduced surface potential γ.

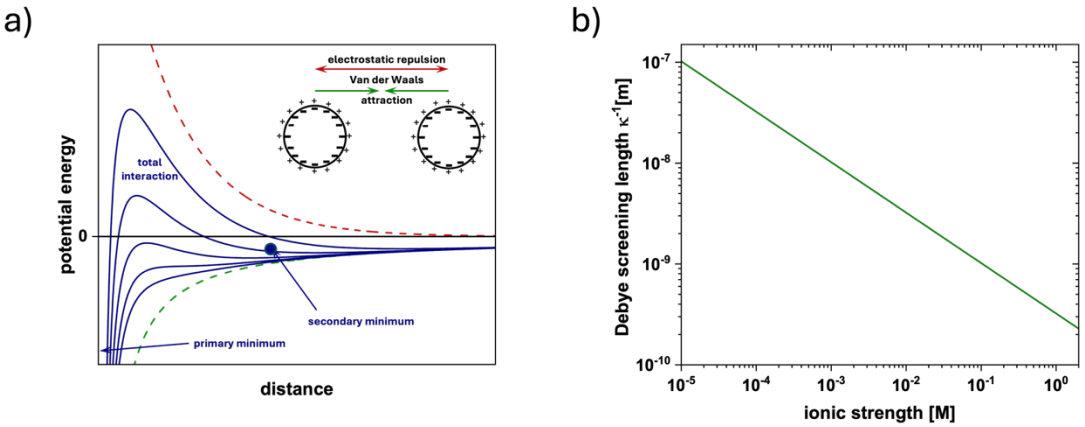


Figure I-3. (a) Schematic DLVO plot of potential energy against the distance of two particles, showing the attractive van der Waals forces (green), the repulsive double layer forces (red), and the resulting total interaction at differing ionic strengths (blue). (b) Dependence of the Debye screening length κ^{-1} on the ionic strength I.

The decrease of the total interaction potential wall with increasing Debye screening length is shown in **Figure I-3a**. The Debye screening length and the ionic strength can be described as [50]:

$$\frac{1}{\kappa} = \sqrt{\frac{\epsilon_0 \epsilon_r k_B T}{2 N_A e^2 I_c}} \tag{I-8}$$

$$I_c = \frac{1}{2} \sum_{i=1}^{n} c_i z_i^2 \tag{I-9}$$

with the elementary charge e, the relative static permittivity ϵ_r, the vacuum permittivity ϵ_0, the Avogadro constant N_A, the concentration c_i of component i, and the number of charges z_i on component i. The Debye screening length κ^{-1}, describing the characteristic decay length of the electrostatic potential in electrolyte solutions, can be written as a function of the total ion concentration. (cf. **Eqn I-8**, **Figure I-3b**) The total ion concentration is expressed as the ionic strength I_c. (cf. **Eqn I-9**) Increasing electrolyte concentrations will promote aggregation as more counterions gather at the particle surface and lead to higher electrostatic screening [50]. The first layer of oppositely charged ions strongly bound to the nanoparticle surface is called the Stern layer. (cf. **Figure I-4)** Around this, a more diffuse layer consisting of loosely associated ions forms.

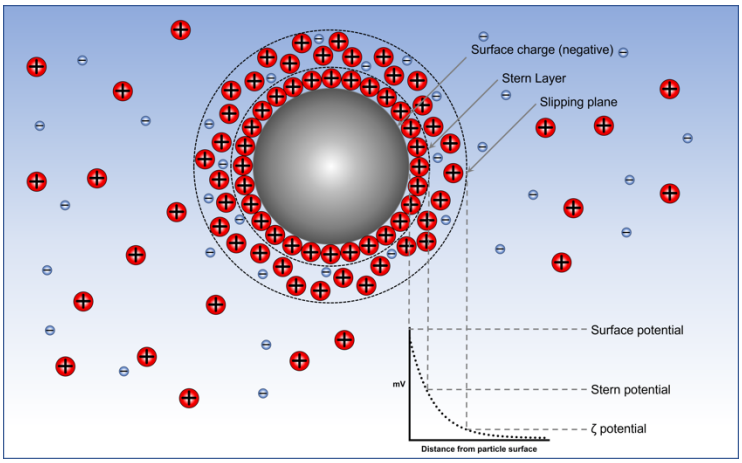


Figure I-4. Schematic representation of the ion association around charged particles in electrolyte solution. Visualization of the moving particle with its corona and differentiation between surface charge and zeta potential.

When the particle is moving in the solution, it is possible to distinguish between ions that move alongside it and those that stay behind. The potential at the boundary between these ions, also called the slipping plane, is the zeta potential, which is related to the surface charge of the particle [53,54].Particles with measured zeta potentials between -10 mV and 10 mV are considered insufficiently charged for electrostatic stabilization. When the zeta potential exceeds 30 mV or -30 mV, the particles are referred to as strongly anionic or cationic, respectively [53–55].

The dependencies of the total interaction potential shown bear fundamental features necessary for understanding particle growth processes [32].

Steric stabilization can be provided by the adsorption of large molecules onto the particle surface, such as polymers or surfactants. Such particles with sterically demanding surface modifications cannot come infinitely close together. (cf. **Figure I-5)**

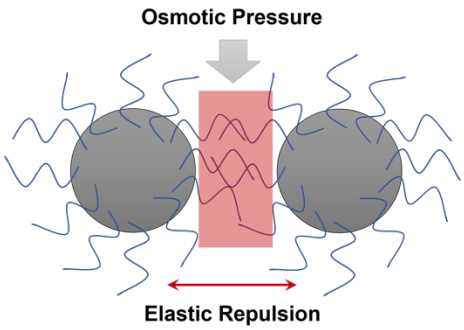


Figure I-5. Osmotic pressure and elastic repulsive forces caused by polymer coatings.

As the density of the adsorbed molecules in the interparticle distance decreases, the entropy decreases. The resulting increase in Gibbs free energy is thermodynamically unfavorable, driving the particles apart. Additionally, elastic repulsion derived from the entanglement of the polymer chains, which strive to be more linear, arises. Because of the excluded solute volume (cf. **Figure I-5** red square), an osmotic pressure arises to redissolve the polymer chains. This leads to a flow of solute molecules between the particles, resulting in a repulsive force driving the particles apart [56].

1.2.3 LaMer Model of Nucleation and Growth

The first transfer of CNT to a model, combined with subsequent growth, was reported by LaMer, introducing the concept of burst nucleation [57]. The basic idea is a temporal separation of nucleation and growth.

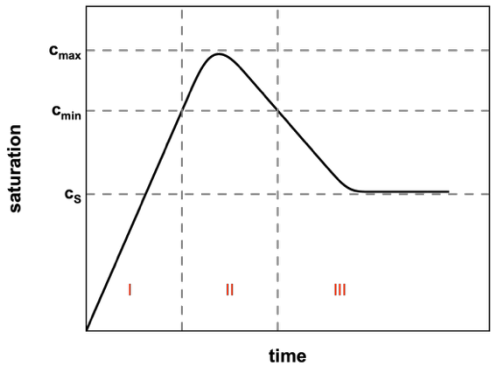


Figure I-6. The principle of NP nucleation due to LaMer's mechanism based on CNT. The curve describes the monomer concentration as function of time.

The mechanism (cf. **Figure I-6)** can be described in three distinct stages:

(I) The monomer concentration increases, until a critical supersaturation level (c_S) is reached. Homogeneous nucleation becomes thermodynamically feasible but remains effectively negligible [57].

(II) Continued supersaturation leads to a higher concentration level (c_{min}), where the nucleation energy barrier can be overcome, triggering rapid self-nucleation in the form of burst nucleation.

(III) The resulting rapid monomer consumption results in decreased supersaturation below the self-nucleation threshold, thereby terminating the nucleation stage. Subsequent particle growth proceeds through the diffusion of additional monomers from the solution to the particle surfaces and can be regarded as a process of heterogeneous nucleation and growth.

The LaMer model can neither predict nor adequately describe the evolution of nanoparticle (NP) size distributions. While the model captures the nucleation phase and the subsequent growth of stable nuclei, it provides only a limited and largely qualitative description of the underlying growth mechanisms and their properties [32,57].

Therefore, theoretical models to accurately predict the growth and the final size distributions have been developed. Typical growth processes include diffusion-limited growth [47], aggregation [58], and Ostwald ripening [59].

The aggregation model reduces the three-step LaMer model to a two-step model. After a first burst of nucleation, no monomer addition to the surfaces occurs. Instead, existing nuclei aggregate and fuse during the growth period [58].

Ostwald ripening is a growth mechanism based on the size-dependent solubility of nanoparticles (NPs) described by the Gibbs-Thomson relation. Smaller particles have a higher chemical potential due to their greater curvature than larger particles. Due to their higher solubility and surface energy, they dissolve preferentially in the solution, thereby providing material for the growth of larger particles [59–61].

Alternative models characterize the particle growth using rate equations and develop kinetic models. In all cases, the precise control of nucleation, growth, and the termination of the growth phase is crucial for the formation of particles at the nanoscale instead of infinitely grown particles [62,63].

1.2.4 Strategies to Control Nanoparticle Syntheses

The controlled synthesis of nanoparticles represents a key challenge in modern materials science. Different strategies to manipulate particle formation in desired ways include control over nucleation, growth, and aggregation, spatial confinement, and termination of growth [32,33,35,41,64,65]. In addition to particle size, these mechanisms are frequently used to tailor particle morphology by selectively promoting or suppressing growth along specific crystallographic directions [64,66].

Nucleation control is based on the targeted regulation of the nucleation rate, for example via temperature, supersaturation, or the conversion (availability) of precursors. This method primarily controls the number of nuclei at the start of the reaction. According to LaMer, simultaneous growth of the particles is expected afterward, without additional nucleation, resulting in uniform particles [57].

In contrast, control over the growth phase can be achieved in different ways. Generally, both the diffusion of monomers to the surface and the surface reaction rate can be tailored. The supply of monomers or ions to the particle surface can be limited, by for example low precursor concentrations, increased solvent viscosity, or ligand-controlled transport inhibition. The surface reaction rates can be tailored by surface ligands, solvent interactions, and modifications

of the particle-solution interface [67,68]. This slows down growth and allows the particle size to be adjusted more precisely [69]. Selective adsorption of ligands on specific crystal facets may additionally direct anisotropic growth and thereby influence particle morphology/shape [64,66].

In addition to nucleation and growth, the suppression of particle aggregation is crucial for obtaining monodisperse nanoparticles. High colloidal stability is typically achieved by one of the two approaches. First, enhancing the electrostatic repulsion using appropriate pH values and/or reduce the ionic strength in solution. Second, introducing sterically demanding surface ligands promotes repulsion.

One powerful strategy to limit the growth of particles is to predetermine the final particle size using spatial confinement. To this purpose, nanoscale cavities formed by structured materials such as micelles [70,71], microemulsions [72–74], porous matrices [75,76], or polymer networks [77–79] are used as templates. The resulting particle size is often closely related to the dimensions of the cavities [17].

Further strategies rely on nanoparticles reaching a defined final size because influx of reactants is either interrupted or completely exhausted. This can be achieved either by quenching the reaction, e.g., chemically stopping further growth, or by targeted precursor depletion. Additionally, intrinsically self-limiting growth modes exist in which growth automatically ceases due to increasing surface passivation, the loss of reactive growth sites, or thermodynamic stabilization of the particle surface [80–82].

Another strategy is the so-called seed-mediated growth. By inducing pre-formed seeds, the nucleation and the growth phase can be temporally completely separated. In this way, highly monodisperse particles can be produced [64].

1.2.5 Special Properties of Nanoparticles Deviating from Bulk Materials

Compared to bulk material, NPs comprise a limited number of atoms, of which a significant fraction is on the particle surface. Atoms on the surface are energetically unfavorable, which results in properties of NPs differing from those of bulk material [83]. The surface-to-volume ratio of spherical NPs is given by:

$$x = \frac{4\pi r^2 l}{\frac{4}{3}\pi r^3} = \frac{3l}{r} \tag{I-10}$$

In this equation, r is the particle radius, and l is the estimated surface thickness of the outermost atom layer [84]. This equation is shown graphically with an estimated surface layer thickness of 0.5 nm in **Figure I-7a**. For NPs smaller than 100 nm, the influence of the surface layer on the properties cannot be neglected. Even smaller particles can also show so-called quantum confinement. (c.f. **Figure I-7b**)

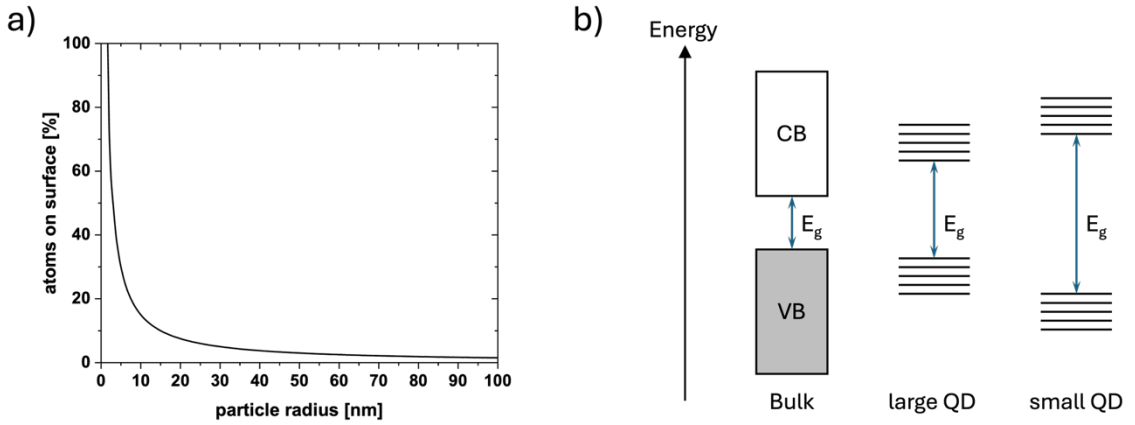


Figure I-7. (a) Surface-to-volume ratio for small particles with an estimated surface layer thickness of 0.5 nm. (b) Quantum confinement model for particles smaller than the materials Bohr exciton radius.

In the bulk material, the energy states are divided into a valence band (VB) and a conduction band (CB). These bands can be considered continuous and are separated for semiconductors with a band gap E_g ranging from a few to several electron volts. If there is no band gap, the material is a conductor, and if the band gap exceeds 4 eV, the material typically is an isolator [83]. If a photon gets absorbed, an electron from the valence band is elevated into the conduction band, leaving an electron-hole behind. The electron in the conduction band and the electron-hole in the valence band interact electrostatically to form an electron-hole pair, also called an exciton. Because of their attraction, they remain at an optimal distance, the so-called Bohr exciton radius. If the particle becomes smaller and quantum confinement sets in, the exciton cannot maintain the desired distance. Because of the confinement in all three dimensions, the energy states become discrete, and the band gap E_g rises [85–87]. The term quantum dot (QD) refers to a semiconductor NP exhibiting quantum confinement. Ultimately, the optical properties of QDs are tunable by their size.

The fluorescence of QDs is also a consequence of quantum confinement. Photons with energy greater than the band gap E_g can be absorbed, creating an exciton. After the relaxation of the electron and the electron-hole in the lowest possible energy state for their respective band, they can recombine and emit a photon with a shifted wavelength. The energy of the re-emitted photon is lower, leading to a redshift in color, also called the Stokes shift [85,86].

In addition to the changes in the electronic band structure caused by quantum confinement, defect states can also make a significant contribution to the optical properties. The overall intensity I at a specific wavelength λ is then given by the sum of the intensities of the individual contributions [88–90]:

$$I(\lambda) = I_{BE}(\lambda) + I_{Trap}(\lambda) \tag{I-11}$$

with the intensity of the bandedge emission I_{BE}, and the intensity of the defect-related emissions I_{Trap}. Defects are deviations from the ideal crystal structure, such as vacancies or interstitial atoms, that arise as a result of the synthesis process. Such defects create localized energy levels within the bandgap that can act as recombination centers for charge carriers. The resulting defect-related emission (DE) typically occurs at lower energies than band-edge emission. Due to the high surface-to-volume ratio of nanomaterials (cf. **Figure I-7a**), surface-related defects can become particularly important and may even dominate the photoluminescence (PL) behavior [87,91,92].

1.3 References

[1] Astruc D. Introduction: Nanoparticles in Catalysis. Chem Rev 2020;120:461–3. https://doi.org/10.1021/acs.chemrev.8b00696.

[2] Payal, Pandey P. Role of Nanotechnology in Electronics: A Review of Recent Developments and Patents. Recent Pat Nanotechnol 2021;16:45–66. https://doi.org/10.2174/1872210515666210120114504.

[3] Pomerantseva E, Bonaccorso F, Feng X, Cui Y, Gogotsi Y. Energy storage: The future enabled by nanomaterials. Science (1979) 2019;366. https://doi.org/10.1126/science.aan8285.

[4] Sabela M, Balme S, Bechelany M, Janot JM, Bisetty K. A Review of Gold and Silver Nanoparticle-Based Colorimetric Sensing Assays. Adv Eng Mater 2017;19:1–24. https://doi.org/10.1002/adem.201700270.

[5] Jiang C cong, Cao Y ke, Xiao G yong, Zhu R fu, Lu Y peng. A review on the application of inorganic nanoparticles in chemical surface coatings on metallic substrates. RSC Adv 2017;7:7531–9. https://doi.org/10.1039/c6ra25841g.

[6] Kumar S, Ye F, Dobretsov S, Dutta J. Nanocoating Is a New Way for Biofouling Prevention. Frontiers in Nanotechnology 2021;3:1–16. https://doi.org/10.3389/fnano.2021.771098.

[7] Khondakar KR, Kaushik AK. Nanotechnology in Cancer Management. Elsevier; 2021. https://doi.org/10.1016/C2018-0-02630-4.

[8] Tang F, Li L, Chen D. Mesoporous silica nanoparticles: Synthesis, biocompatibility and drug delivery. Advanced Materials 2012;24:1504–34. https://doi.org/10.1002/adma.201104763.

[9] Hong L, Cheung TL, Rao N, Ouyang Q, Wang Y, Zeng S, et al. Millifluidic synthesis of cadmium sulfide nanoparticles and their application in bioimaging. RSC Adv 2017;7:36819–32. https://doi.org/10.1039/c7ra05401g.

[10] Bogart LK, Pourroy G, Murphy CJ, Puntes V, Pellegrino T, Rosenblum D, et al. Nanoparticles for Imaging, Sensing, and Therapeutic Intervention. ACS Nano 2014;8:3107–22. https://doi.org/10.1021/nn500962q.

[11] Aggarwal P, Hall JB, McLeland CB, Dobrovolskaia MA, McNeil SE. Nanoparticle interaction with plasma proteins as it relates to particle biodistribution, biocompatibility and therapeutic efficacy. Adv Drug Deliv Rev 2009;61:428–37. https://doi.org/10.1016/j.addr.2009.03.009.

[12] Abdelhamid HN, Badr G. Nanobiotechnology as a platform for the diagnosis of COVID-19: a review. Nanotechnology for Environmental Engineering 2021;6:1–26. https://doi.org/10.1007/s41204-021-00109-0.

[13] Khan I, Saeed K, Khan I. Nanoparticles: Properties, applications and toxicities. Arabian Journal of Chemistry 2019;12:908–31. https://doi.org/10.1016/j.arabjc.2017.05.011.

[14] Stöber W, Fink A, Bohn E. Controlled growth of monodisperse silica spheres in the micron size range. J Colloid Interface Sci 1968;26:62–9. https://doi.org/10.1016/0021-9797(68)90272-5.

[15] Klossek ML, Touraud D, Zemb T, Kunz W. Structure and Solubility in Surfactant-Free Microemulsions. ChemPhysChem 2012;13:4116–9. https://doi.org/10.1002/cphc.201200667.

[16] Prevost S, Lopian T, Pleines M, Diat O, Zemb T. Small-angle scattering and morphologies of ultra-flexible microemulsions. J Appl Crystallogr 2016;49:2063–72. https://doi.org/10.1107/S1600576716016150.

[17] Pileni M-P. The role of soft colloidal templates in controlling the size and shape of inorganic nanocrystals. Nat Mater 2003;2:145–50. https://doi.org/10.1038/nmat817.

[18] Blahnik J, Schuster J, Müller R, Müller E, Kunz W. Surfactant-free microemulsions (SFMEs) as a template for porous polymer synthesis. J Colloid Interface Sci 2024;655:371–82. https://doi.org/10.1016/j.jcis.2023.10.162.

[19] Opel J, Wimmer FP, Kellermeier M, Cölfen H. Functionalisation of silica-carbonate biomorphs. Nanoscale Horiz 2016;1:144–9. https://doi.org/10.1039/c5nh00094g.

[20] Kellermeier M, Cölfen H, García-Ruiz JM. Silica biomorphs: Complex biomimetic hybrid materials from “sand and chalk.” Eur J Inorg Chem 2012:5123–44. https://doi.org/10.1002/ejic.201201029.

[21] Funkner D, Frank T, Kohlmann N, Zahnweh D, Rieder J, Kienle L, et al. Functional nanoparticles from chemically coupled precipitation processes. Mater Today Chem 2023;29:101438. https://doi.org/10.1016/j.mtchem.2023.101438.

[22] Rödig B, Funkner D, Frank T, Schürmann U, Rieder J, Kienle L, et al. Nanodots of Transition Metal Sulfides, Carbonates, and Oxides Obtained Through Spontaneous Co-Precipitation with Silica. Nanomaterials 2024;14:1–15. https://doi.org/10.3390/nano14242054.

[23] Pham AL-T, Lee C, Doyle FM, Sedlak DL. A Silica-Supported Iron Oxide Catalyst Capable of Activating Hydrogen Peroxide at Neutral pH Values. Environ Sci Technol 2009;43:8930–5. https://doi.org/10.1021/es902296k.

[24] Coelho J V., Guedes MS, Prado RG, Tronto J, Ardisson JD, Pereira MC, et al. Effect of iron precursor on the fenton-like activity of Fe2O3/mesoporous silica catalysts prepared under mild conditions. Appl Catal B 2014;144:792–9. https://doi.org/10.1016/j.apcatb.2013.08.022.

[25] Helz GR, Horzempa LM. EDTA as a kinetic inhibitor of copper(II) sulfide precipitation. Water Res 1983;17:167–72. https://doi.org/10.1016/0043-1354(83)90097-0.

[26] Bae W, Abdullah R, Mehra RK. Cysteine-mediated synthesis of CdS bionanocrystallites. Chemosphere 1998;37:363–85. https://doi.org/10.1016/S0045-6535(98)00051-4.

[27] Yi C, Yang Y, Liu B, He J, Nie Z. Polymer-guided assembly of inorganic nanoparticles. Chem Soc Rev 2020;49:465–508. https://doi.org/10.1039/c9cs00725c.

[28] Chollakup R, Smitthipong W, Eisenbach CD, Tirrell M. Phase behavior and coacervation of aqueous poly(acrylic acid)-poly(allylamine) solutions. Macromolecules 2010;43:2518–28. https://doi.org/10.1021/ma902144k.

[29] Rödig B, Denk P, Schürmann U, Kellermeier M, Kunz W. Nanoparticle formation utilizing simple polyacrylic acid-cation coacervates as template. RSC Adv 2026;16:8633–40. https://doi.org/10.1039/D6RA00330C.

[30] Becker R, Döring W. Kinetische Behandlung der Keimbildung in übersättigten Dämpfen. Ann Phys 1935;416:719–52. https://doi.org/10.1002/andp.19354160806.

[31] Gibbs JW. The collected works of J. Willard Gibbs. 2nd ed. New York: Longmans, Green and Co.; 1928.

[32] Polte J. Fundamental growth principles of colloidal metal nanoparticles - a new perspective. CrystEngComm 2015;17:6809–30. https://doi.org/10.1039/c5ce01014d.

[33] Thanh NTK, Maclean N, Mahiddine S. Mechanisms of nucleation and growth of nanoparticles in solution. Chem Rev 2014;114:7610–30. https://doi.org/10.1021/cr400544s.

[34] Arrhenius S. Über die Reaktionsgeschwindigkeit bei der Inversion von Rohrzucker durch Säuren. Zeitschrift Für Physikalische Chemie 1889;4U:226–48. https://doi.org/10.1515/zpch-1889-0416.

[35] Leite ER, Ribeiro C. Crystallization and Growth of Colloidal Nanocrystals. New York, NY: Springer New York; 2012. https://doi.org/10.1007/978-1-4614-1308-0.

[36] Kwon SG, Hyeon T. Formation mechanisms of uniform nanocrystals via hot-injection and heat-up methods. Small 2011;7:2685–702. https://doi.org/10.1002/smll.201002022.

[37] Vekilov PG. Nucleation. Cryst Growth Des 2010;10:5007–19. https://doi.org/10.1021/cg1011633.

[38] Cölfen H, Antonietti M. Mesocrystals: Inorganic superstructures made by highly parallel crystallization and controlled alignment. Angew Chem Int Ed 2005;44:5576–91. https://doi.org/10.1002/anie.200500496.

[39] Gebauer D, Raiteri P, Gale JD, Cölfen H. On classical and non-classical views on nucleation. Am J Sci 2018;318:969–88. https://doi.org/10.2475/09.2018.05.

[40] Wang T, Cölfen H, Antonietti M. Nonclassical crystallization: Mesocrystals and morphology change of CaCO3 crystals in the presence of a polyelectrolyte additive. J Am Chem Soc 2005;127:3246–7. https://doi.org/10.1021/ja045331g.

[41] Jun Y-S, Zhu Y, Wang Y, Ghim D, Wu X, Kim D, et al. Classical and Nonclassical Nucleation and Growth Mechanisms for Nanoparticle Formation. Annual Review of Physical Chemistry Annu Rev Phys Chem 2022 2022;73:35. https://doi.org/10.1146/082720.

[42] Gebauer D, Kellermeier M, Gale JD, Bergström L, Cölfen H. Pre-nucleation clusters as solute precursors in crystallisation. Chem Soc Rev 2014;43:2348–71. https://doi.org/10.1039/c3cs60451a.

[43] Vekilov PG. The two-step mechanism of nucleation of crystals in solution. Nanoscale 2010;2:2346–57. https://doi.org/10.1039/c0nr00628a.

[44] Sugimoto T. Preparation of monodispersed colloidal particles. Adv Colloid Interface Sci 1987;28:65–108. https://doi.org/10.1016/0001-8686(87)80009-X.

[45] Sugimoto Tadao. Monodispersed Particles. 2nd ed. Amsterdam: Elsevier; 2001. https://doi.org/10.1016/B978-0-444-89569-1.X5016-7.

[46] Rao CNR., Müller Achim, Cheetham AK. Nanomaterials Chemistry. Wiley; 2007. https://doi.org/10.1002/9783527611362.

[47] Reiss H. The Growth of Uniform Colloidal Dispersions. J Chem Phys 1951;19:482–7. https://doi.org/10.1063/1.1748251.

[48] Israelachvili JN. Intermolecular and Surface Forces. Elsevier; 2011. https://doi.org/10.1016/C2009-0-21560-1.

[49] Russel WB., Saville DA., Schowalter WR. Colloidal Dispersions. Cambridge University Press; 2012.

[50] Evans DF, Wennerström H. The Colloidal Domain. 2nd ed. New York, NY: John Wiley & Sons, INC.; 1999.

[51] Derjaguin B, Landau L. Theory of the stability of strongly charged lyophobic sols and of the adhesion of strongly charged particles in solutions of electrolytes. Prog Surf Sci 1941;43:30–59. https://doi.org/10.1016/0079-6816(93)90013-L.

[52] Verwey EJW. Theory of the Stability of Lyophobic Colloids. J Phys Colloid Chem 1947;51:631–6. https://doi.org/10.1021/j150453a001.

[53] Sennett Paul, Olivier JP. Colloidal dispersions, electrokinetic effects, and the concept of zeta potential. Ind Eng Chem 1965;57:32–50. https://doi.org/10.1021/ie50668a007.

[54] Hunter RJ., Ottewill RH., Rowell RL. Zeta Potential in Colloid Science: Principles and Applications. Elsevier Science; 2014.

[55] Clogston JD, Patri AK. Zeta Potential Measurement. In: McNeil SE, editor. Characterization of Nanoparticles Intended for Drug Delivery, vol. 1. 1st ed., New York, NY: Humana Press; 2011, p. 63–70. https://doi.org/10.1007/978-1-60327-198-1_6.

[56] Pomogailo AD, Kestelman VN, Dzhardimalieva GI. Monomeric and Polymeric Metal Carboxylates as Precursors of Nanocomposite Materials, 2010, p. 257–88. https://doi.org/10.1007/978-3-642-10574-6_9.

[57] LaMer VK, Dinegar RH. Theory, Production and Mechanism of Formation of Monodispersed Hydrosols. J Am Chem Soc 1950;72:4847–54. https://doi.org/10.1021/ja01167a001.

[58] Privman V. Mechanisms of Diffusional Nucleation of Nanocrystals and Their Self-Assembly into Uniform Colloids. Ann N Y Acad Sci 2009;1161:508–25. https://doi.org/10.1111/j.1749-6632.2008.04323.x.

[59] Ostwald W. Über die vermeintliche Isomerie des roten und gelben Quecksilberoxyds und die Oberflächenspannung fester Körper. Zeitschrift Für Physikalische Chemie 1900;34U:495–503. https://doi.org/10.1515/zpch-1900-3431.

[60] Lifshitz IM, Slyozov VV. The kinetics of precipitation from supersaturated solid solutions. Journal of Physics and Chemistry of Solids 1961;19:35–50. https://doi.org/10.1016/0022-3697(61)90054-3.

[61] Wagner C. Theorie der Alterung von Niederschlägen durch Umlösen (Ostwald-Reifung). Zeitschrift Für Elektrochemie, Berichte Der Bunsengesellschaft Für Physikalische Chemie 1961;65:581–91. https://doi.org/10.1002/bbpc.19610650704.

[62] Van Embden J, Sader JE, Davidson M, Mulvaney P. Evolution of colloidal nanocrystals: Theory and modeling of their nucleation and growth. Journal of Physical Chemistry C 2009;113:16342–55. https://doi.org/10.1021/jp9027673.

[63] Rempel JY, Bawendi MG, Jensen KF. Insights into the kinetics of semiconductor nanocrystal nucleation and growth. J Am Chem Soc 2009;131:4479–89. https://doi.org/10.1021/ja809156t.

[64] Xia Y, Gilroy KD, Peng H, Xia X. Seed-Mediated Growth of Colloidal Metal Nanocrystals. Angew Chem Int Ed 2017;56:60–95. https://doi.org/10.1002/anie.201604731.

[65] Lee J, Yang J, Kwon SG, Hyeon T. Nonclassical nucleation and growth of inorganic nanoparticles. Nat Rev Mater 2016;1. https://doi.org/10.1038/natrevmats.2016.34.

[66] Wu YA, McNulty I, Liu C, Lau KC, Liu Q, Paulikas AP, et al. Facet-dependent active sites of a single Cu2O particle photocatalyst for CO2 reduction to methanol. Nat Energy 2019;4:957–68. https://doi.org/10.1038/s41560-019-0490-3.

[67] Mourdikoudis S, Liz-Marzán LM. Oleylamine in Nanoparticle Synthesis. Chemistry of Materials 2013;25:1465–76. https://doi.org/10.1021/cm4000476.

[68] Yin Y, Alivisatos AP. Colloidal nanocrystal synthesis and the organic–inorganic interface. Nature 2005;437:664–70. https://doi.org/10.1038/nature04165.

[69] Sardar R, Shumaker-Parry JS. Spectroscopic and microscopic investigation of gold nanoparticle formation: Ligand and temperature effects on rate and particle size. J Am Chem Soc 2011;133:8179–90. https://doi.org/10.1021/ja107934h.

[70] Eastoe J, Hollamby MJ, Hudson L. Recent advances in nanoparticle synthesis with reversed micelles. Adv Colloid Interface Sci 2006;128–130:5–15. https://doi.org/10.1016/j.cis.2006.11.009.

[71] Uskokovic V, Drofenik M. Synthesis of materials within reverse micelles. Surface Review and Letters 2005;12:239–77. https://doi.org/10.1142/S0218625X05007001.

[72] López-Quintela M, Rivas J, Blanco & M, Tojo C. Nanoscale Materials. 1st ed. Boston, MA: Springer US; 2003. https://doi.org/10.1007/b101855.

[73] Li Y, Park CW. Particle Size Distribution in the Synthesis of Nanoparticles Using Microemulsions. Langmuir 1999;15:952–6. https://doi.org/10.1021/la980550z.

[74] Wolf S, Feldmann C. Mikroemulsionen: neue Möglichkeiten zur Erweiterung der Synthese anorganischer Nanopartikel. Angewandte Chemie 2016;128:15958–84. https://doi.org/10.1002/ange.201604263.

[75] Fan H, Zhou Y, Lopez GP. Stepwise assembly in three dimensions: Preparation and characterization of layered gold nanoparticles in porous silica matrices. Advanced Materials 1997;9:728–31. https://doi.org/10.1002/adma.19970090911.

[76] Morley KS, Marr PC, Webb PB, Berry AR, Allison FJ, Moldovan G, et al. Clean preparation of nanoparticulate metals in porous supports: A supercritical route. J Mater Chem 2002;12:1898–905. https://doi.org/10.1039/b111111f.

[77] Gröhn F, Kim G, Bauer BJ, Amis EJ. Nanoparticle formation within dendrimer-containing polymer networks: Route to new organic-Inorganic hybrid materials. Macromolecules 2001;34:2179–85. https://doi.org/10.1021/ma001489j.

[78] Kim CR, Uemura T, Kitagawa S. Inorganic nanoparticles in porous coordination polymers. Chem Soc Rev 2016;45:3828–45. https://doi.org/10.1039/c5cs00940e.

[79] Yi C, Yang Y, Liu B, He J, Nie Z. Polymer-guided assembly of inorganic nanoparticles. Chem Soc Rev 2020;49:465–508. https://doi.org/10.1039/c9cs00725c.

[80] Ledendecker M, Paciok P, Osowiecki WT, Pander M, Heggen M, Göhl D, et al. Engineering gold-platinum core-shell nanoparticles by self-limitation in solution. Commun Chem 2022;5. https://doi.org/10.1038/s42004-022-00680-w.

[81] Wu W, Njoki PN, Han H, Zhao H, Schiff EA, Lutz PS, et al. Processing core/alloy/shell nanoparticles: Tunable optical properties and evidence for self-limiting alloy growth. Journal of Physical Chemistry C 2011;115:9933–42. https://doi.org/10.1021/jp201151m.

[82] Lu J, Elam JW, Stair PC. Atomic layer deposition - Sequential self-limiting surface reactions for advanced catalyst “bottom-up” synthesis. Surf Sci Rep 2016;71:410–72. https://doi.org/10.1016/j.surfrep.2016.03.003.

[83] Natelson D. Nanostructures and Nanotechnology. 1. Cambridge: Cambridge University Press; 2015. https://doi.org/10.1017/CBO9781139025485.

[84] Shearer CJ, Slattery AD, Stapleton AJ, Shapter JG, Gibson CT. Accurate thickness measurement of graphene. Nanotechnology 2016;27. https://doi.org/10.1088/0957-4484/27/12/125704.

[85] Cayuela A, Soriano ML, Carrillo-Carrión C, Valcárcel M. Semiconductor and carbon-based fluorescent nanodots: The need for consistency. Chemical Communications 2016;52:1311–26. https://doi.org/10.1039/c5cc07754k.

[86] Nemade KR, Waghuley SA. Band gap engineering of CuS nanoparticles for artificial photosynthesis. Mater Sci Semicond Process 2015;39:781–5. https://doi.org/10.1016/j.mssp.2015.05.045.

[87] Kalt H, Klingshirn CF. Semiconductor Optics 1. 5th ed. Cham: Springer International Publishing; 2019. https://doi.org/10.1007/978-3-030-24152-0.

[88] Hinterding SOM, Salzmann BBV, Vonk SJW, Vanmaekelbergh D, Weckhuysen BM, Hutter EM, et al. Single Trap States in Single CdSe Nanoplatelets. ACS Nano 2021;15:7216–25. https://doi.org/10.1021/acsnano.1c00481.

[89] Bera D, Qian L, Tseng TK, Holloway PH. Quantum dots and their multimodal applications: A review. Materials 2010;3:2260–345. https://doi.org/10.3390/ma3042260.

[90] Babentsov V, Sizov F. Defects in quantum dots of IIB-VI semiconductors. Opto-Electronics Review 2008;16:208–25. https://doi.org/10.2478/s11772-008-0025-0.

[91] Rudan M. Physics of Semiconductor Devices. 1st ed. Cham: Springer International Publishing; 2018. https://doi.org/10.1007/978-3-319-63154-7.

[92] Thomas DG, Hopfield JJ, Augustyniak WM. Kinetics of Radiative Recombination at Randomly Distributed Donors and Acceptors. Physical Review 1965;140:A202–20. https://doi.org/10.1103/PhysRev.140.A202.

Chapter II. Surfactant-free Microemulsion as Template for Stöber Silica Nanoparticles Synthesis

2.1 Abstract

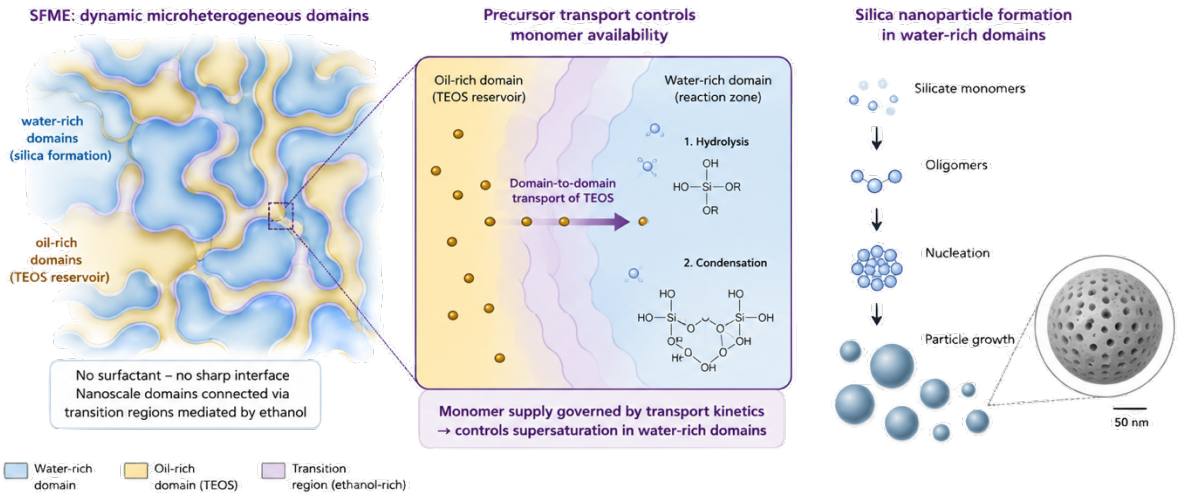


Figure II-1. Graphical Abstract: The oil-rich domains of the SFME act as precursor reservoirs, while the transport into water-rich domains across the ethanol-rich interphase regulates silicate monomer availability and thereby nanoparticle nucleation and growth.

Surfactant-free microemulsions (SFMEs) represent a potential structured reaction media for the synthesis of inorganic nanoparticles. This work investigates whether the ternary H_2O / EtOH / TEOS system forms SFME structures capable of directing silica particle formation via a self-templating mechanism. To this end, we systematically investigate this hypothesis and evaluate the influence of SFME structuring on the synthesis of Stöber silica nanoparticles. Ternary and pseudo-ternary phase diagrams of H_2O / EtOH / TEOS and H_2O / EtOH / (oil + TEOS) systems were established and characterized by dynamic light scattering (DLS), small- and wide-angle X-ray scattering (SWAXS), and transmission electron microscopy (TEM). The H_2O / EtOH / TEOS system was found to remain molecularly dispersed throughout the investigated monophasic region and showed no evidence of SFME aggregate formation. Consequently, silica particle formation in this system follows conventional Stöber-type kinetics rather than a self-templating mechanism. Nevertheless, synthesis at high water contents and low ammonia concentrations produced highly

monodisperse silica nanoparticles in the low-nanometer size range and enabled controlled particle growth through regrowth steps. In contrast, genuine SFME systems containing toluene or 1-octanol exhibited pronounced mesoscale structuring in the pre-Ouzo and bicontinuous regions, which strongly affected nucleation and growth behavior. Time-resolved DLS measurements revealed induction periods and growth regimes characteristic of compartmentalized reaction environments, yielding particle sizes ranging from a few to several hundred nanometers, depending on the microstructure and oil composition. The results demonstrate that SFME structures do not template particle formation in the H_2O / EtOH / TEOS system but can substantially modify Stöber kinetics when a genuine mesoscale organization is present. A mechanistic model is proposed in which diffusion of hydrolyzed silica species across the SFME interphase governs nucleation and growth, establishing interfacial mass transport as a key parameter for controlling silica nanoparticle formation in structured solvents. In this framework, the properties of the selected hydrophobic component then serve as new parameters that determine the characteristics of the resulting nanoparticles.

Parts of this chapter are published in *ACS Omega* (Rödig, B.; Schmauser, L.; Denk, P.; Kunz, W. Surfactant-Free Microemulsion as Template for Stöber Silica Nanoparticle Synthesis. ACS Omega 2026. https://doi.org/10.1021/acsomega.6c08994; Figures and text reproduced under the terms of the CC BY 4.0 license).
Contributions to experimental work:

- Bastian Rödig: Conceptualization, Experimental Work, Data Evaluation
- Lena Schmauser: Conceptualization, Experimental Work
- Patrick Denk, Olga Gebert, Julian Dolina: Experimental work

2.2 Introduction

The most widely known silica particle synthesis, often simply called the Stöber synthesis or sometimes the SFB synthesis, dates back to 1968, when Stöber, Fink, and Bohn first reported the controlled growth of silica spheres in aqueous alcoholic solutions [1]. This way, well-defined, highly monodisperse, uniform silica particles could be prepared. By varying simple reaction parameters such as water content, reactant concentrations, and catalyst concentration, the size of the resulting structures can be controlled [1]. In the first 30 years since the paper was published, interest in such particles was limited. Only in the last 20 years the synthesis and application of such particles have become a growing focus of scientific publications [2]. Additionally, silica offers excellent opportunities for surface modification and exhibits low toxicity, which explains its widespread use [3].

2.2.1 Chemistry of Silica

This bottom-up method is typically referred to as a sol-gel process, even though the reaction is usually terminated before the gel settles. The smallest building block of silica particles are the SiO_4^{4-} tetrahedra (**Figure II-2**). The oxygen atoms occupy the corners of the tetrahedron, whereas the center is occupied by a silicon atom (**Figure II-2a**). The actual radius of the oxygen ion (O^{2-}) is about 5 times as big as the silicon ion (Si^{4+}), resulting in contact between the oxygen ions. In contrast, the silicon ion is often considered a tetrahedral hole (**Figure II-2b**) [4]. These tetrahedra (simplified in **Figure II-2c**) can either be arranged periodically (**Figure II-2d**), resulting in a crystalline structure, or randomly (**Figure II-2e**), resulting in an amorphous structure. While the angle of the siloxane bonds may vary, the Si-O bond length of ~0.162 nm remains, and there are never more than two bonds per oxygen ion [5].

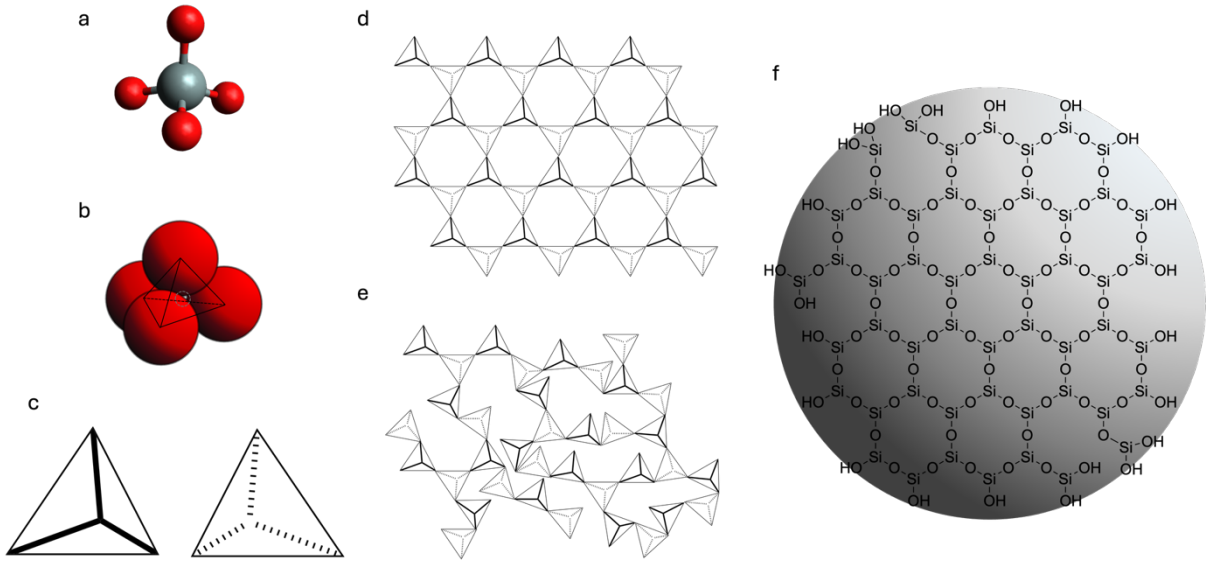


Figure II-2. (a) Ball and stick model, showing the tetrahedral coordination of silicon (grey) with oxygen (red), (b) space-filling model based on packed spheres for the silica tetrahedron, (c) solid tetrahedron model, (d) two-dimensional representation of SiO_4^{4-} tetrahedra packing for crystalline silica, (e) and for amorphous/random packing, (f) two-dimensional representation of fully hydroxylated silica colloid. For amorphous silica, the bond angles may vary, but the Si-O distances are constant, and oxygen is linked to no more than two silicon atoms. Reproduced with permission of refs [4,6].

To form particles (**Figure II-2f**) in the Stöber process, a basic catalyst, usually ammonia, is used first to hydrolyze and then polycondensate tetraalkylorthosilicates (TAOS), usually tetraethylorthosilicate (TEOS), in aqueous alcoholic solutions. [1] The primary reaction is the hydrolysis (**Figure II-3**, **Eqn II-1, II-2, II-3**), which involves the nucleophilic substitution of the alkoxy group (Si-OR) via a 5–bond transition state [7,8]. In general, hydrolysis takes place in water, but the poor nucleophilicity of water makes the addition of a base essential to ensure sufficiently fast reaction rates. The degree of hydrolysis varies, as 4 alkoxy groups can be converted to hydroxyl groups. The first hydrolysis step is the rate-determining step, as subsequent hydrolysis steps are favored due to the higher positive partial charge of the silicon. Also, the steric hindrance reduces with the OH^- replacement of the alkoxy groups (**Figure II-3**, **Eqn II-2**).

After the hydrolysis, the condensation reaction occurs, transforming the silanol (-Si-OH) groups of monomers/oligomers into siloxane (Si-O-Si) bonds (**Figure II-3**, **Eqn II-4, II-5, II-6**). The reaction rate of the condensation is much higher than that of hydrolysis, due to the easy deprotonation of the silanol groups. This increases the positive partial charge on the silicon, making nucleophilic attacks more favorable [7,9].

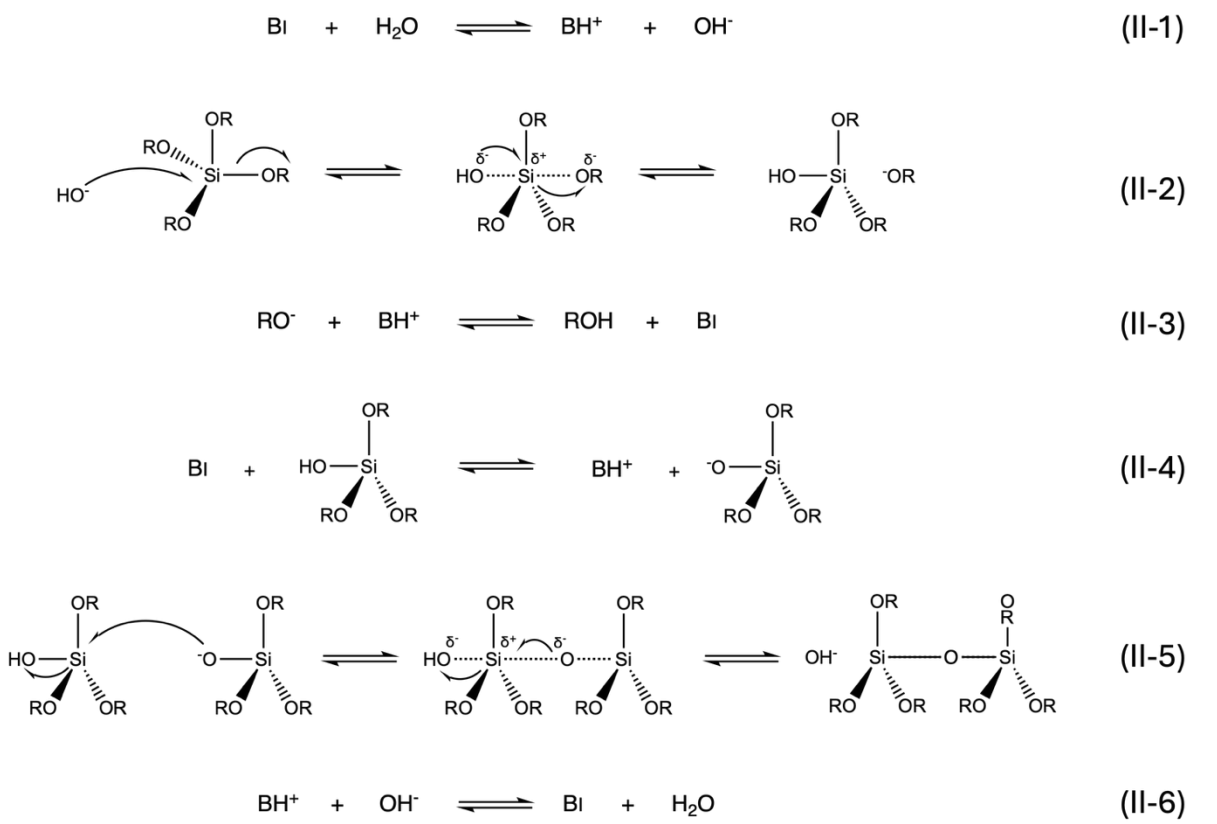


Figure II-3. Mechanism of base (BI) catalyzed hydrolysis (II-2) and condensation (II-5) of tetraalkylorthosilicates (TAOS).

Both reactions, hydrolysis and condensation, can also be acid-catalyzed (reactions not shown). The hydrolysis reaction rate decreases in the acidic region as the pH value increases, reaching a minimum at a pH value of 7. Under basic conditions, the reaction rate increases again. The rate of the condensation reaction increases with increasing pH values, with the slowest rate occurring at a pH of 2 [7,10,11]. The interplay of both reaction rates leads to weakly branched polymeric networks in acid catalysis, while basic catalysis leads to highly branched networks [10,11].

2.2.2 Parameter Dependence of the Stöber Synthesis

By variation of the initial reaction parameters, the structure and size of the final particles can be controlled. A few general statements can be made:

1. **Tetraalkylorthosilicate (TAOS) concentration**
   Since TEOS is used in classical Stöber synthesis, the data available here is the most extensive. Although certain trends can be transferred to other TAOS, the concentrations

do not correspond exactly. There are various reports on increasing/decreasing particle size with increasing TEOS concentration in the literature, which can be compared by using the hydrolysis ratio R = [H_2O]/[TEOS] [12].

First, in the synthesis without water (R = 0), the particle size decreases as TEOS concentration [13]. Then, at low R, as used in the original Stöber synthesis (R = 54-3), no apparent effect of TEOS concentration on size was observed (Stöber et al., 1968). At higher R, the particle size increases with increasing TEOS concentration (R = 120-50) [12,14], and at even higher R values (R = 1000-120), the size decreases again with increasing TEOS concentration [12,15].

2. Water content

As seen before, the hydrolysis ratio R strongly influences the size of the resulting particles, but the absolute concentration of water also plays a crucial role. The variation in water content directly influences the dielectric constant of the solvent and thus also the colloidal stability of the particles and the hydrolysis rate [15]. The higher the dielectric constant, the more polar the solvent, the better stabilized charged transition states in both hydrolysis and condensation (c.f. **Figure II-3**, **Eqn II-2**). Therefore, a solvent ratio S = [H_2O]/[EtOH] can be used to understand the behavior better.

As water content increases, the size of the resulting particles increases due to greater aggregation [16] until a maximum of S ~ 1 [1,16], after which the size decreases again [12,17]. The dielectric constant at a solvent ratio of S = 1 is around $\varepsilon \sim 65$ [18]. At higher water content, particle size and size distribution decrease, and particles become more spherical [17].

3. Ammonia/catalyst concentration

The catalyst, typically ammonia in the classical Stöber synthesis, significantly influences the resulting particle size. In the absence of ammonia, both hydrolysis and condensation proceed rather slowly, and the silica flocculates into irregularly shaped particles instead of forming clearly defined particles [1].

The influence of the ammonia concentration on particle size also depends on the solvent ratio S. Below S ~ 1, particle size increases with increasing ammonia concentration [1,15,16]. At higher solvent ratios (S > 1), the excess water can stabilize the formed nuclei through hydrogen bonding, and the higher ammonia content can in turn induce

more nuclei. This leads to faster hydrolysis/condensation rates and, thus, to smaller particles as the ammonia concentration increases [12].

4. **Alcohol chain length**

   As mentioned before, the dielectric constant plays a crucial role in influencing reaction rates, resulting in an increase in particle size with decreasing polarity [15]. The increasing steric hindrance of longer alkyl groups and the increasing viscosity of longer alcohol chains also reduce the reaction rates [19–21]. The decreasing polarity for longer alkyl groups results in weaker hydrogen bonding between the solvent and the silica, further slowing down the reaction rate [19].

   In general, decreasing polarity and increasing viscosity lead to bigger particles [22]. For primary alcohols, this directly implies that the resulting particle size increases with the molar mass of the alcohol [23–25]. Polydispersity, on the other hand, appears to be comparable in different solvents [1,20].

5. **Reaction temperature**

   Increased reaction temperatures (T) result in smaller particles, independent of reactant concentrations or the alcohol chain length used [12,15,17,26]. The higher temperature increases the reaction rates of both hydrolysis and condensation, resulting in more nuclei, which then in turn result in more but smaller particles [16].

The various reaction parameters can be ranked according to the strength of their influence on the final particle size: T > R = $[H_2O]/[TEOS]$ > S = $[H_2O]/[EtOH]$ > [NH3] [16].

2.2.3 Models for Particle Formation

Over the years, several models have been proposed for the growth of colloidal silica spheres. The two most commonly referred to are the monomer addition model and the controlled aggregation growth model.

The monomer addition model is based on the LaMer growth model (cf. **Chapter I**) [27] and on the assumption that particles, once nucleated, remain colloidally stable [27,28].

The ammonia-catalyzed growth in aqueous alcoholic solutions is controlled by the rate of TEOS hydrolysis, which is first order in c(TEOS) under excess water. The nucleation is then given by the condensation of two hydrolyzed silicic acid monomers [21]. Particle growth occurs via

monomer addition, with two possible growth pathways: diffusion and surface-reaction-limited addition. Predicts that precipitation increases monotonically, balanced by monomer production and particle growth. The model can capture the time rate of change in particle size [28].

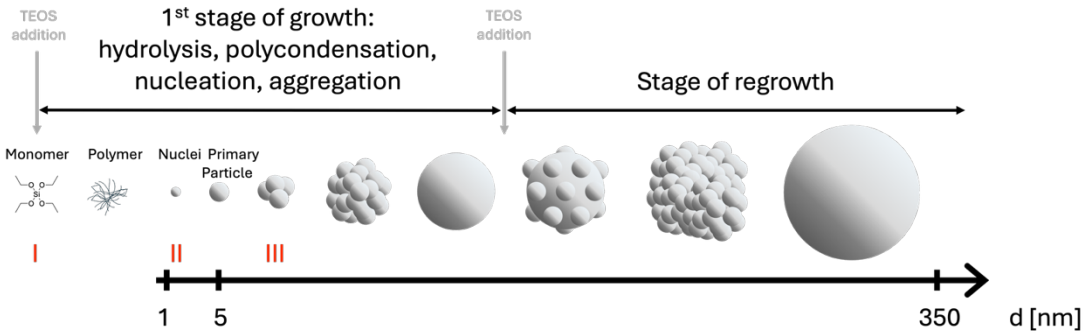


Figure II-4. Particle growth diagram during multistage growth by TEOS in water, EtOH, and ammonia medium. Adapted with permission from ref [29].

The controlled aggregation growth model is a simple extension of the LaMer model for colloidal unstable nuclei. Growth occurs solely by aggregation, and the absolute size of the final particle depends not only on reaction rates but also on the size and colloidal stability of the primary particle [30].

Particle formation starts with the aggregation of siloxane substructures and small oligomers. (cf. **Figure II-4 I**). These oligomers become colloidally unstable and phase-separate to form small, dense particles. This process, driven by a surface-reaction-limited condensation of hydrolyzed monomers/small oligomers, proceeds until colloidally stable sizes are attained (cf. **Figure II-4 II**) [17,31]. Again, a first-order kinetic relationship with respect to TEOS concentration emerges for the rate-determining hydrolysis step [31].

The induction phase (seed formation) is inversely related to the reaction rate and influenced by the same parameters. Nanometer-sized subunits form in the first reaction state, followed by controlled aggregation into larger structures [9,20]. Control over monodispersity is possible when the aggregation rate between large/large is lower than for large/small and small/small particle pairs [14,32].

Contrary to the monomer addition model, this model assumes continuous nucleation over the entire reaction time rather than burst nucleation at the beginning. A change in mechanism is possible, depending on overall reaction conditions [9,20]. Particles larger than 100 nm no

longer undergo monomer addition, indicating that regrown particles (c.f **Figure II-4b**) always react based on the controlled aggregative growth model [17,20].

2.2.4 Surfactant-free Microemulsion (SFME)

Ternary mixtures consisting of two immiscible compounds and an amphiphile exhibit interesting structural phenomena [33]. As their name suggests, amphiphiles consist of both hydrophilic and hydrophobic moieties. Depending on the amphiphilicity of the molecule, the amphiphiles are either considered as surfactants (surface active agents) or as hydrotropes [34]. When compared directly, the hydrophobic segment in hydrotropes is relatively small, resulting in reduced amphiphilic character, meaning that considerably higher amounts are necessary to achieve effects comparable to those of surfactants [35–38]. While both the solubility of hydrophobic species and the reduction in surface tension occur at millimolar concentrations for surfactants, hydrotropes must be present in the molar concentration range to achieve similar effects [38,39]. In other words, hydrotropes, such as short-chain alcohols, are weak surfactants that do not form (viscous) liquid crystals [39–41].

Analogous to water-surfactant-oil systems [42], ternary phase diagrams can be constructed for systems containing water, hydrotrope, and oil. (c.f. **Figure II-5**)

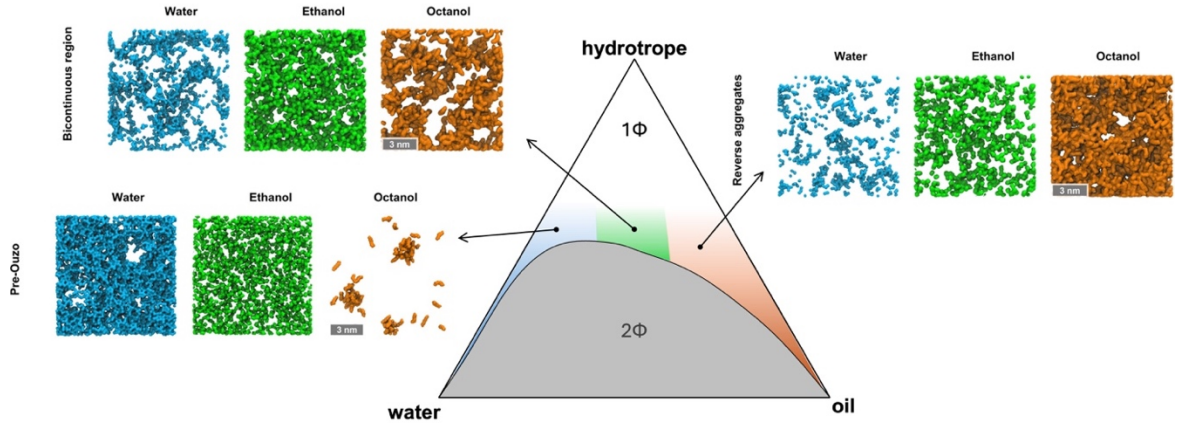


Figure II-5. Schematic ternary phase diagram for a solution containing water/hydrotrope/oil. The grey domain represents the two-phasic region. Above, one phasic structured phase can be found, like water-rich pre-Ouzo (direct micellar) (blue shade), bicontinuous (green shade), and oil-rich inverse micellar (orange shade). Further away from the phase boundary, the solution loses self-structuring, resulting in a molecularly dispersed solution. MD simulations show the distribution of pseudo-phases across the different structured regions in the H_2O/EtOH/1-Octanol system, reprinted with permission from ref [43].

These ternary mixtures, exhibiting different structured phases, partly similar to those of surfactant-containing mixtures, can be called surfactant-free microemulsions (SFMEs) [43,44]. (c.f. **Figure II-5**) Such structured solvents have attracted growing interest over the past decades due to their wide range of potential applications [41,45–48]. In SFMEs, the role of the amphiphilic component is covered by the hydrotrope, which offers several advantages over surfactant-based systems. They are usually more biodegradable, less toxic, exhibit less foaming capability, exhibit no liquid crystal formation, and are easier to remove [39,41].

For a typical SFME, different structural regimes can be identified, including oil in water microemulsion (o/w μE; c.f. pre-Ouzo MD in **Figure II-5**), bicontinuous structures (BIC; c.f. BIC MD in **Figure II-5**), and water in oil microemulsion (w/o μE; c.f. reverse aggregates MD in **Figure II-5**) [43]. The aggregates in SFMEs are assumed to be at least 10^3 times as dynamic as micellar aggregates and to exhibit sizes ranging from a few nanometers to ~100 nm [43,49–52]. Close to the phase boundary, the most pronounced structuring can be found, gradually fading with increasing distance (i.e., increasing hydrotrope concentration), resulting in a molecularly dispersed solution [43,49]. (c.f. **Figure II-5**) The hydrotrope is only weakly surface active, resulting in almost even distribution across the pseudo-phases and slight accumulation at the interphase [43,49,51,52]. The pre-Ouzo region is described as a single-phase, transparent, and thermodynamically stable area at lower oil concentrations. (c.f. **Figure II-5**; blue area) Within this area, aggregates of the hydrophobic component form and are swollen by the hydrotrope [53].

Not every ternary mixture containing water, oil, and hydrotrope is capable of forming structured SFMEs. Even though there is no comprehensive explanation yet, the choice of both, oil and hydrotrope, have strong influence on the resulting structure [54].

When the oil contains polar functional groups that interact with the hydrotrope, the structuring is primarily induced by the oil [54]. Two main factors favor the formation of structured regimes in this case. First, the enthalpic contribution due to weak interactions between the hydrotrope and the oil. Second, the entropic contribution due to the release of water molecules from the interface through the inclusion of the polar functional groups of the oil [39,55,56].

If the oil does not contain functional groups, the self-aggregation of the hydrotrope becomes the dominant factor, as interactions between the hydrotrope and the oil are limited to their aliphatic segments [54]. Due to the lack of functional groups in the oil, the hydrophobicity increases and the hydrotrope-oil interaction strength decreases. The oil is then solubilized within the pseudo-bulk phase of the hydrotrope [54]. The strength of prestructuring, i.e., the

self-aggregation of hydrotropes in water [57,58], determines the hydrotrope concentration required for the solubilization of oils in such systems [54].

As a result, SFMEs show considerable potential for applications in extraction processes [59], chemical reactions [60], and more generally for the solubilization of poorly water-soluble substances, including pharmaceuticals [46]. Further, the use of structured solvents appears to be an effective approach for performing template-based syntheses of both organic polymers [61,62] and inorganic particles [47,63–65].

2.2.5 H_2O / EtOH / TEOS a Ternary Mixture and a SFME?

Over the years, since the first publication on Stöber particles, many advancements have been made. Nevertheless, most of the used processes still rely on the use of ethanol as the main solvent, which is neither economically viable nor environmentally sustainable, as large quantities of organic solvent are wasted during the process. For better comparison, an overview of the ternary mixtures from the most relevant publications is presented in a ternary phase diagram. (cf. **Figure II-6**)

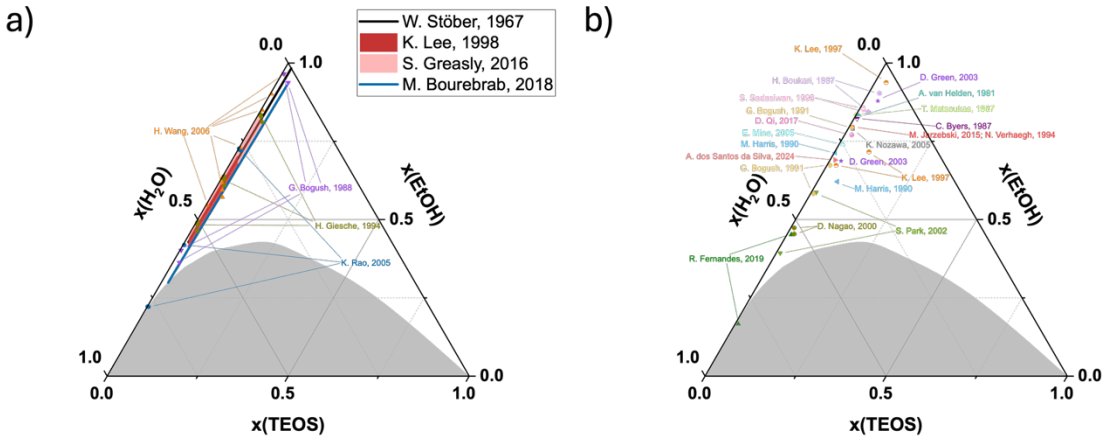


Figure II-6. Phase diagrams of the ternary mixture of H_2O / EtOH / TEOS expressed in molar fractions x. The positions in the ternary space of relevant publications on Stöber syntheses were plotted. (a) The highlighted areas correspond to screenings conducted by [1,66–68]. The single points were chosen as all references investigated rather different concentration ranges. [12,14,15,17] (b) The shown references only conducted experiments on a few points within the ternary phase diagram [13,16,19–21,23,24,28,30,31,66,69–76] Note that a majority of the conducted experiments are at reduced water concentrations ($x(H_2O) < 0.5$). This figure can be found in high resolution in the online repository.

What cannot be seen in these ternary phase diagrams is the catalyst (NH_3) concentration used at these points. Typically, the [TEOS]/[NH_3] does not exceed a value of 1, with few exceptions

[24,69,71,77] and the majority of the syntheses used in literature are characterized by a high ethanol content ($S < 1$).

The potential SFME character of the H_2O / EtOH / TEOS system is usually not considered, and a potential self-templating effect of the ternary system as SFME has been poorly investigated [65]. In other publications, the templating effect of an existing SFME on the synthesis of Stöber particles is investigated. First, Sun et al. [47] investigated the pseudo-ternary system H_2O / EtOH / dichloromethane+TEOS in the W/O region. They showed smaller particles with narrower distributions than those derived from similar ternary mixtures (at equal S). Later, Gudelj et al. [63,64] investigated the systems H_2O / EtOH / heptanol+TEOS and water / EtOH / pentanol+TEOS in the pre-Ouzo/BIC region and demonstrated the potential of these pseudo-ternary systems.

Three aspects should therefore be examined more closely in these systems. How does the classical Stöber process behave at low catalyst concentrations ($[TEOS]/[NH_3] > 1$) and high water content ($S \geq 1$)? How do the different regions/compositions of the SFMEs or the choice of the oil component influence the resulting particles? Does the ternary system of H_2O/EtOH/TEOS form a SFME with potential self-templating for particle synthesis?

2.3 Experimental

2.3.1 Materials

The following chemicals were used as received without further purification: 28 % ammonium hydroxide solution (NH_3, Supelco, p.A.), ethanol (EtOH, Sigma–Aldrich, ≥99.8%), L-arginine ($C_6H_{14}N_4O_2$, Sigma-Aldrich, p.A.), 1-octanol (TCI chemicals, >99.5%), tetraethyl orthosilicate (TEOS, Sigma–Aldrich, ≥98%), toluene (Fisher scientific, p.A.). Ultrapure water from a Millipore system (resistivity > 18 MΩ·cm).

2.3.2 Apparatus

2.3.2.1 Phase Diagram Construction

2 g of binary mixtures of water/hydrotrope or oil/hydrotrope were prepared in screwable glass tubes to record ternary phase diagrams. The samples were tempered to 25 °C with the heating thermostat A 111 and the immersion thermostat A 100 from Lauda (Lauda-Königshofen). After tempering, the third component is added drop by drop using a Pasteur pipette outside the thermostat and mixed thoroughly. The change in phase behavior was determined by the sample's turbidity as observed with the naked eye. The samples were tempered again to 25 °C. Changing the temperature can cause the system to become single-phase and clear again. For these samples, the process was repeated until the system remained turbid at 25 °C. The samples were weighed to determine the amount of the third component. Weight percentages and molar fractions were then calculated from the masses.

2.3.3 Methods

2.3.3.1 Dynamic Light Scattering (DLS)

Information about the structuring of the SFME samples and the size of the as-formed nanoparticles and their aggregates was obtained by dynamic light scattering measurements. To this end, 1 mL of each sample was filtered through 0.2 µm PTFE membranes and transferred into dust-free cylindrical borosilicate glass cells with a 10 mm outer diameter. The sealed DLS tubes were placed in the temperature-controlled toluene bath of a CGS-3 Compact Goniometer System from ALV, which was equipped with an ALV/LSE-5004 Multiple Tau Digital Correlator and a vertically polarized 22 mW He-Ne laser (λ = 632.8 nm). Measurements were performed

at 25 °C and a scattering angle of 90°. The sampling interval for all measurements, except kinetic studies, was 300 s. From the collected data, the mean intensities of the scattered light and the time-dependent self-correlation functions were determined. Average hydrodynamic diameters of the scattering species were extracted via a second-order cumulant analysis [78] and the CONTIN algorithm [79][80] However, we are aware that this procedure may be questionable for ternary or quaternary mixtures. Bimodal curves obtained in the kinetic measurements were fitted and evaluated according to Ref [81]. For batch evaluation, Python scripts were created and used; they can be found in the online repository.

2.3.3.2 Kinetic Measurements

Repeated DLS measurements were done for the kinetic experiments. To this purpose, 300 s measurements were taken every 15 mins for the samples of the ternary mixture H_2O / EtOH / TEOS until there was no more visible change in the obtained correlation function. For the samples containing oil and with arginine as catalysts, the same procedure was sufficient. Due to accelerated reaction rates with the added catalyst NH_3, the measurement was changed to 30 s measurements every 30 s for at least an hour or until visible precipitation occurred.

2.3.3.3 Small- and Wide-angle X-ray Scattering (SWAXS)

Small- and wide-angle X-ray scattering (SWAXS) data were recorded on a Nano-inXider from Xenocs (Grenoble, France), equipped with two detectors. A PILATUS3 R 100K from Dectris (Baden-Daettwil, Switzerland) with a sample-to-detector distance of 948 mm was used as SAXS detector without a beamstop, in principle covering a q range of 0.0057–4.47 nm^{-1}, where $q = 4\pi \cdot \lambda^{-1} \cdot \sin(\theta/2)$ is the magnitude of the wavevector and θ is the scattering angle. The transmission was measured simultaneously. Due to the beamstopless setup, the evaluable q range is limited by the direct beam, which influences the measured intensity up to $q = 0.2$ nm^{-1}. Another PILATUS3 R 100K detector from Dectris, centered at an angle of 33° with respect to the direct beam, with a sample-to-detector distance of 80 mm, was used as WAXS detector, covering a q range of 3.47–40.83 nm^{-1}. The WAXS detector was protected by a Mylar window, while the entire beam path from source to SAXS detector was windowless. A microfocus sealed tube (Cu, 30 W, 40 µm focus) generated X-rays with a wavelength of 0.154 nm (Cu K_α line). Measurements were performed under vacuum (≈0.1 mbar) in the "High Resolution" configuration of the Nano-inXider with a beam size on the sample of around 400 µm, a typical flux of 15 Mph·s-1, and a resolution of $\Delta q = 0.024$ nm^{-1}. Samples were measured at room

temperature (20–25°C, typically ≈23°C) in individual capillaries made of borosilicate glass (nominal outer ø 1.5 mm, wall thickness 0.01 mm, length 80 mm) from WJM-Glas/Müller GmbH (Berlin, Germany). Capillaries were sealed using a glue gun. The capillary thickness was measured with a precision of ±0.01 mm at the beam position using a spatial intensity scan perpendicular to the capillary and beam axes, achieved by moving the capillary, i.e., the sample stage, relative to the beam. Samples were measured in single acquisitions with exposure times of 1200 s or 10800 s, error-bars corresponding to the statistical error of the measured intensity. 1D data are radially averaged and normalized to the capillary thickness. Empty capillary scattering was subtracted as background from all sample data. Data were corrected for flat field, spatial distortion, electronic and dark noise, and transmitted flux. The Nano-inXider is regularly calibrated using glassy carbon to obtain absolute scale, as well as silver behenate and lanthanum hexaboride to ensure correct q-mapping for SAXS and WAXS, respectively. The "absolute" intensity obtained from the Xenocs Nano-inXider software (version 2.3.5) was manually corrected by a factor of 0.909 based on a Lupolen (thickness of 2.38 mm, reference absolute intensity $I(q) = 6.00\ cm^{-1}$ at $q = 0.37\ nm^{-1}$) reference measurement. The absolute intensity was also confirmed by measuring a water capillary, yielding a constant intensity for water around the reference value of $0.01642\ cm^{-1}$ (at 23 °C). The q-mapping was also checked and corrected by measuring silver behenate in a capillary.

2.3.3.4 Transmission Electron Microscopy (TEM)

To elucidate the nanostructure of the formed particles, 10 µL of the as obtained dispersions were placed on copper grids (400 mesh x 62 µm pitch) that were coated with a thin layer of graphite (using a Carbon Coater 208carbon from Cressington). After soaking for 20 s, excess liquid was removed by blotting with a filter paper. The fixed specimen on the grid was washed with 20 µL water and then dried again by blotting. Finally, the grid was left to dry in a closed Petri dish on a filter paper for at least 24 h, before it was transferred into the electron microscope using a Gatan cryo-holder.

Samples were screened and imaged with a 200-kV field-emitter TEM (JEM-2100F, JEOL) and a 16-megapixel complementary metal–oxide–semiconductor camera (F416, TVIPS). Microscope and imaging parameters were controlled using SerialEM software (version 3.8).

2.3.3.5 Artificial Intelligence (AI)

A generative AI system (OpenAI, model GPT-5, 24.06.2026) was used to create this graphical abstract, which visually represents a concept developed by the author. The author was solely responsible for the scientific content, the selection of the information presented, and verifying its factual accuracy.

2.3.3.6 Data Availability

Additional data, fit parameters, and associated scripts, are available in the online repository (Novel nanoparticle synthesis in self-organizing water–based systems - online repository, 10.5283/epub.80300). Representative data and fits are shown in the SI.

2.4 Results and Discussion

2.4.1 Ternary Phase Diagrams and Structuring of Different Mixtures

2.4.1.1 H_2O/EtOH/TEOS Phase Diagram und Structuring of Various Compositions

The phase diagram of the H_2O / EtOH / TEOS ternary system is shown in weight percentage (c.f. **Figure II-7a**) and in molar fractions (c.f. **Figure II-7b**). The grey areas in **Figure II-7** visualize the two-phase region with the single-phase region above, uncolored. The hydrolysis rate of TEOS at neutral pH is slow enough that it can be ignored for the duration of the phase diagram construction (< 20 mins) [7,65,82].

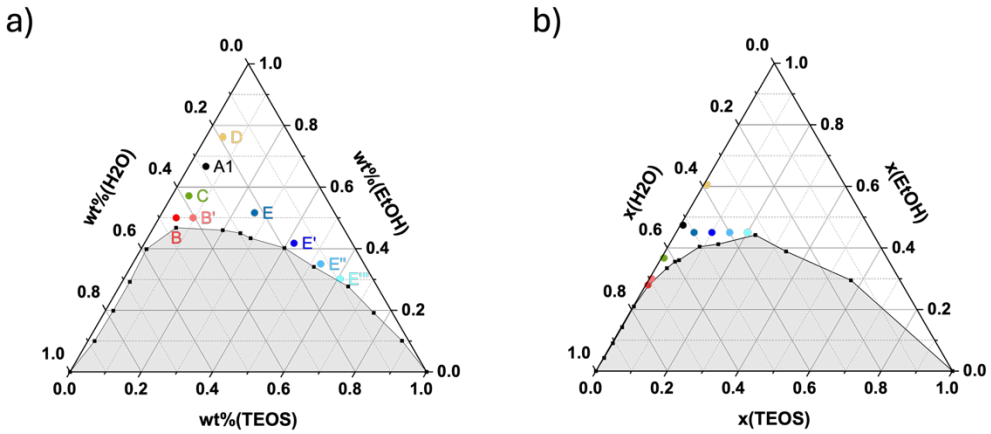


Figure II-7. Phase diagrams of the ternary mixture of H_2O / EtOH / TEOS expressed in weight percent wt% (a) and molar fraction x (b). The exact fractions of the various points visible in (a) and (b) are given in **Table SII-1**.

Various points are shown in **Figure II-7a** and **Figure II-7b** and their exact composition is given in **Table SII-1**. The chosen points are located in the part of the phase diagram which is used in most of the publications regarding Stöber silica particle formation (cf. **Figure II-6**) and are chosen in a way to directly compare the differing results to Lu et al. [65] A series of additional points (E to E’’’) near the phase boundary were chosen to further characterize the system at higher TEOS concentrations [43].

The time correlation function, and therefore the structuring, at these points can be seen in **Figure II-8a** and **Figure SII**-1 respectively. These are typical correlation functions of ternary mixtures with little to no structuring [52,83] and strongly contradict the results reported by Lu et al. [65] with “SFME” aggregate sizes of around 200 nm. Their methodology for crafting the

SFME samples, in particular the long stirring time and sonication, suggests that particles were already formed in an uncontrolled way before characterization. Typical SFME aggregate sizes are usually below 100 nm. [49,50] Further, the DLS is limited to analyzing these samples for roughly the aggregate size, as only the composition, but neither the viscosity nor the refractive index of the outer pseudo-phase are known.

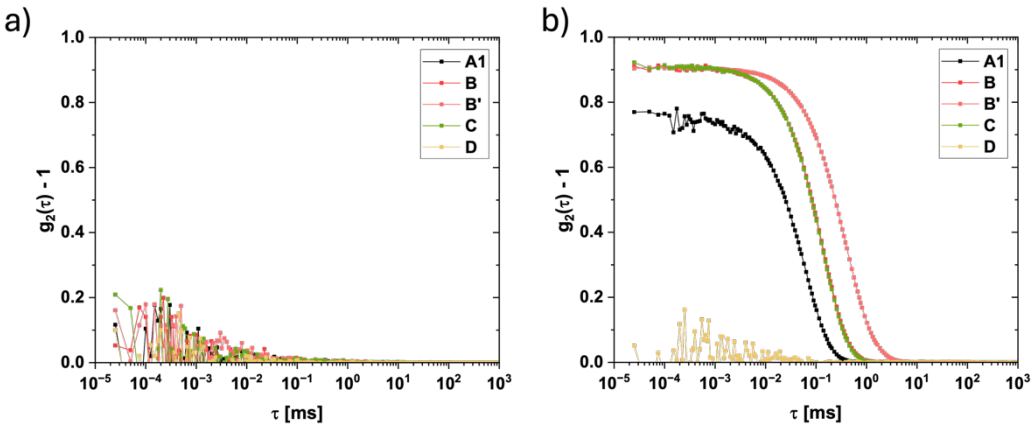


Figure II-8. Correlation functions of DLS measurements of the respective points A1, B, B‘, C, and D directly after preparation (a) and after 4 d without stirring (b). The exact compositions of the various points shown in (a) and (b) are given in **Table SII-1** and the sizes of the formed particles in **Table SII-2**.

To substantiate these claims, additional SAXS measurements (c.f. **Figure SII-2a**) of the points C and B were made. These points are the closest to the pre-Ouzo region and should, based on previous results, therefore be the most structured in **Figure II-7**. [49,50] Both methods combined show that little to no structuring occurs in this system, indicating that, instead of SFME formation, the system remains a molecular solution in the observed single-phase region. Also visible in **Figure II-8b** are the same samples as shown in **Figure II-8a** after a standing time of 4 days. In four of the five compositions, a substantial number of particles is formed after the waiting time shown by the unambiguous correlation function. The evaluated size, using cumulant analysis [78,84,85] is shown in **Table SII-2**. Even after four days, every sample shows significantly smaller particle sizes and narrower size distributions than what Lu et al. claim to be the aggregates of the SFME (c.f. **Table SII-2**) [65]. After further standing time, all samples were transformed into gels.

Nevertheless, typical trends for Stöber systems are visible, such as:

1. The lower the water content, and therefore the catalyst concentration (for the hydrolysis reaction), the slower is the reaction rate and the smaller are the formed particles (D<A1<C<B) [1,16].
2. The higher the TEOS content, the bigger the resulting particles (B' > B) [25,86].
3. Due to the neutral pH, there is no uniform nucleation followed by a subsequent growth phase; instead, an extended growth phase occurs throughout the volume until a uniform gel forms [1].

These results clarify that the H_2O / EtOH / TEOS ternary system does not form a SFME. This does not disqualify the system near the phase boundary for Stöber synthesis in general, but gives first hints that the mechanism proposed by Lu et al is incorrect [65]. SFME aggregates do not influence the size of formed particles in this ternary system, as there are no structures found in the solutions. The interest in the synthesis with high water concentrations remains unchanged, since limited experiments have been conducted in that area of the ternary phase diagram (c.f. **Figure II-6**) [12,72].

2.4.1.2 H_2O / EtOH / (Oil + TEOS) Phase Diagram and Structuring of Various Compositions

To actually evaluate the influence of SFME aggregates on Stöber particle synthesis, an existing SFME is used, and 10 vol% of TEOS is added to the oil before SFME formation. In comparable studies, TEOS is added after SFME formation, without accounting for the non-negligible shift of the point in the ternary phase diagram or the potential shift of the phase boundary. [47,63,64] To evaluate the actual positions of points used for Stöber synthesis pseudo-ternary phase diagrams of the systems H_2O / EtOH / toluene + TEOS (red) and H_2O / EtOH / 1-octanol + TEOS (green) were constructed (c.f. **Figure II-9**).

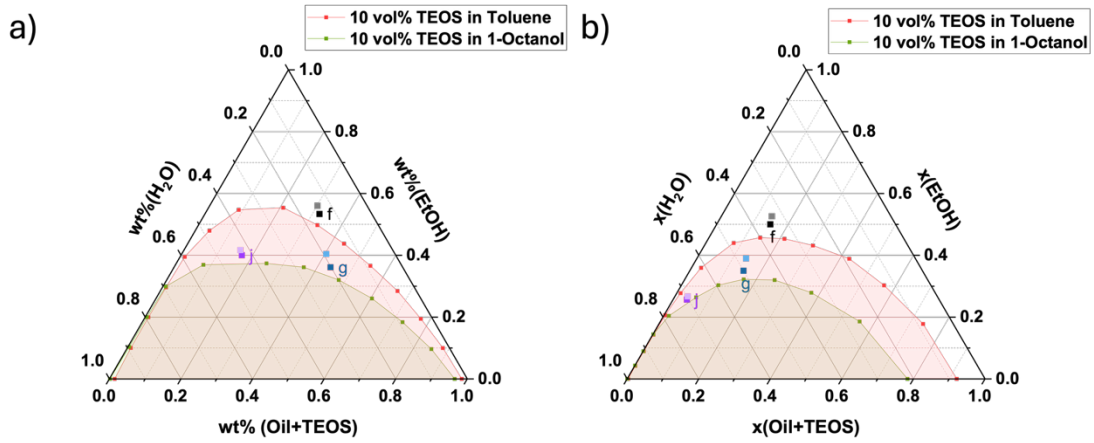


Figure II-9. Phase diagrams of the ternary mixture of H_2O / EtOH / Oil + TEOS expressed in weight percent wt% (a) and molar fraction x (b). The red phase boundary represents 10 vol% TEOS in Toluene and the green phase boundary represents 10 vol% TEOS in 1-Octanol. The exact fractions of the points f, j, g, f', j', and g' visible in (a) and (b) are shown in **Table SII-3**.

Again, the ternary phase diagram is shown in weight percentage (c.f. **Figure II-9a**), and in molar fractions (c.f. **Figure II-9b**). Compared to the ternary phase diagrams of pure toluene [87]/1-octanol [88,89], the biphasic area of the phase diagram decreases slightly (c.f. **Figure II-9**). The points f, g, and j (dark) and their respective counterparts f', g', and j' (theoretical shift after complete TEOS hydrolysis, light) are visualized in both ternary phase diagrams and their exact compositions are given in **Table SII-3**.

Point j was chosen because of its proximity to the phase boundary as well as to the Ouzo region (close to the critical point), which results in the highest amount of pre-Ouzo aggregates [49,50]. The H_2O/EtOH/Toluene system shows the most pronounced structuring around its critical point in the oil-rich region [89]. Since this region is not of interest here, and only very weak structuring is indicated in the water-rich region, f was chosen at a point with relatively high-water content, where structuring is still significant. g was chosen at the same oil+TEOS molar fraction as f with 1-octanol instead of toluene.

f', g', and j' represent the theoretical shift of the respective points f, g, and j after complete hydrolysis of TEOS (1 TEOS releases 4 EtOH). DLS and SWAXS measurements of these points are visualized in **Figure II-10a** and **Figure II-10b**, respectively.

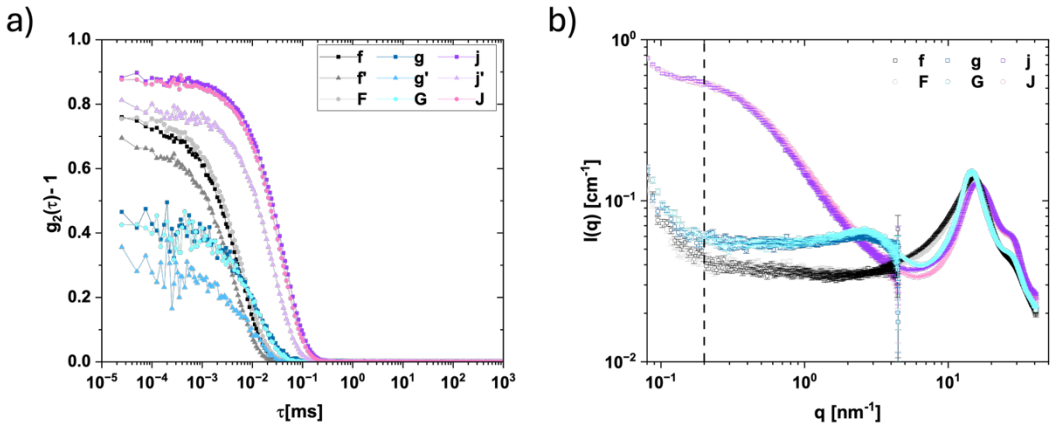


Figure II-10. (a) Correlation function of DLS measurements of the points f, g, and j and their respective alternated points after a theoretical complete TEOS hydrolysis f', g', and j'. The points F, G, and J represent the same points without the addition of TEOS. Samples were prepared immediately before the measurement. (b) SWAXS-spectra of the points f, F, g, G, j, and J. The increase at $q < 0.2$ nm^{-1} results from the X-ray beam (no beamstop).

The increase of the EtOH concentration through complete hydrolysis of the small amount of dissolved TEOS (10 vol% in oil) already results in a visible decrease in the correlation in all systems (c.f. **Figure II-10a**). This indicates a reduction in the amount of present scatterers and also hints, in combination with decreased decay times (τ), at reduced aggregate sizes. The hydrodynamic radius (r_H) could be evaluated, as the composition of the pseudo-phases can be estimated from the SAXS measurements [49,83]. (c.f. **Figure II-10b**, **Table SII-4**) However, the usefulness of such information is questionable given the dynamics of aggregates in an SFME system. Instead, the lag times (τ) derived from DLS, giving both, information about size and the fluctuation rate of the aggregates [35,49,90]. Therefore, the aggregates in j persist longer than in g and f, the latter having the highest dynamics and thus the shortest aggregate lifetime. Additional SWAXS-spectra (c.f. **Figure II-10b**) confirm that the incorporation of 10 vol% TEOS in the oil-rich pseudo-phase does not change the formed structures significantly for neither sample. While for the sample j direct pre-Ouzo aggregates are clearly visible in both the DLS measurement and SWAXS-spectra, the sample f shows ambiguous results. The missing indication for aggregates in the SWAXS spectra possibly results from the poor contrast between the pseudo-phases in this system (cf. **Figure SII-2b**), while the DLS measurement approves the existence of aggregates. The SWAXS-spectra for g clearly indicate a position in the BIC area of the ternary system, while the DLS measurement only confirms the existence of some kind of aggregates [43,49]. (cf. **Figure II-10**)

2.4.2 Kinetics of Stöber Nanoparticle Formation in the Different Mixtures (Refutation of Mechanisms Proposed in Literature)

2.4.2.1 Kinetics of Particle Formation at Point C (H_2O / EtOH / TEOS)

Point C (cf. **Figure II-7**) was chosen for further investigation, as only a few results with similarly high water contents are reported in the literature [12,72] (cf. **Figure II-6**). Time dependent DLS measurements were conducted without catalyst (cf. **Figure SII-3a**), with Arginine as catalyst (cf. **Figure SII-4**, [91]), and with NH_3 as catalyst (cf. **Figure II-11a**). In all cases, with and without catalyst, a change in the correlation functions is visible. From no scattering in the beginning (yellow) to a clearly defined correlation (purple) after different times, depending on the system.

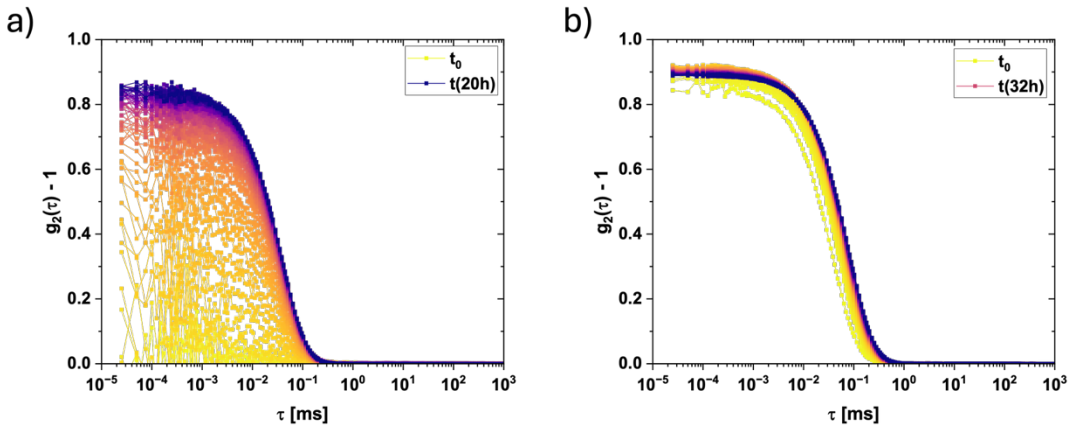


Figure II-11. Correlation function of multiple DLS measurements during the formation of particles in the ternary mixture H_2O / EtOH / TEOS at point C with the addition of NH_3 as catalyst (a) and a regrowth step after 24h (b). The gradient from yellow (t_0) to purple (t_{end}) visualizes the change of the samples over time. The hydrolysis ratio is R = 92.5 and the solvent ratio is S = 1.7.

The addition of NH_3 as catalyst not only reduces the reaction time but also induces a size restriction for the formed particles. (cf. **Figure II-11a** and **Figure SII-3a**) Instead of infinite growth to form a uniform gel, particles with a capped size are formed [1]. (cf. **Figure SII-5a**, **Figure SII-6a**) Contrary to the mechanism proposed by Lu et al [65], no SFME aggregates are present in the solution that can then be turned into particles of similar size or even coagulate into larger aggregates to form even larger particles. Instead, typical Stöber-like particle formation is observed. The used NH_3 concentration ([TEOS]/[NH_3]= 8.9) is significantly lower compared to particles synthesized in literature at comparable ternary mixtures ([TEOS]/[NH_3] = 0.6 [72] or 0.003 [12]), resulting in higher reaction times (~20 h vs. 1 h).

These slower reaction times generate further possibilities to control the size of the formed particles.

The addition of further TEOS, after equilibrium has been reached (approx. 24 h, cf. **Figure SII-6a**), results in uniform growth of the particles. Therefore, a visible shift of the correlation function to higher lag times (τ) is visible without emerging of a second correlation indicating growth instead of formation of new particles. (cf. **Figure II-11b**) After another 24 h, the particles can be doubled in size without any change in further parameters.

Even though the system does not form SFME aggregates, the investigation of particles formed at high water content ($S > 1$) and low catalyst concentrations ($[TEOS]/[NH_3] > 1$) appears interesting, especially given the limited data available in the literature [12,72].

2.4.2.2 Kinetics in Regular SFME Systems

After the addition of the catalyst NH_3, a change in all samples f, g, and j is visible. After some time (> 1 h), a white precipitate is visible for f and g, while j remains as a clear solution even after 3 d. The $[TEOS]/[NH_3]$ ratio equals 8.9, as before for point C, for all experiments. The hydrolysis ratio for g and f is similar at $R = 46$, but the solvent ratio is rather different at $S = 1.4$ and $S = 0.7$, respectively. j shows a significantly higher hydrolysis ratio of $R = 252$ and a solvent ratio of $S = 2.7$. Time-dependent DLS measurements were conducted after the addition of NH_3 to evaluate the particle growth. (cf. **Figure II-12**)

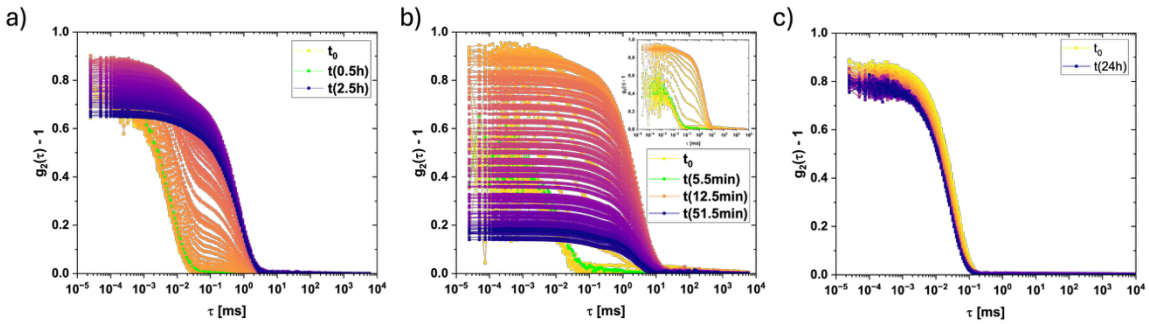


Figure II-12. Correlation function of multiple DLS measurements during the formation of particles after the addition of NH_3 to (a) f, (b) g, and (c) j. The gradient from yellow (t_0) to purple (t_{end}) visualizes the change of the samples over time. $[TEOS]/[NH_3] = 8.9$.

The three shown points exhibit vastly different reaction kinetics. The first change of the correlation function for sample f (cf. **Figure II-12a**) is visible after 30 mins, and a second fraction of scatterers emerges at τ values two orders of magnitude greater. While the correlation

function of sample g (cf. **Figure II-12b**) shows a similar trend after 5 mins, the sedimentation is faster, resulting in almost complete sedimentation after 50 mins. In contrast, the correlation function of sample j (cf. **Figure II-12c**) remains almost the same for over 24 h and appears to shift towards smaller lag times (τ).

All samples share that the scattering of the SFME structures / the fluctuations in these measurements remain visible. Instead of a shift in the correlation function, which would be expected with growing structures/aggregates, a second fraction of scattering centers appears after some time (f and g). The SFME structure remains visible until the number of large scattering centers becomes too large, as the scattering intensity is strongly size-dependent ($\sim r_H^6$) [92].

The change in sample j indicates that the second fraction of scatterers that emerges must be „smaller“ than the initial SFME aggregates, but less than one order of magnitude, which would lead to a shift of the correlation function (cf. **Figure II-12c**).

Size evaluations of these measurements can be found in **Figure SII-7** and **Table SII-5**. After the initial delay, the evaluated size remains almost constant for an extended period of time for all samples derived from the BIC area. This initial induction period is not observed for the classical Stöber process, but was seen before in synthesis in an O/W SFME system [47] and is typical of synthesis in microemulsions [93,94]. In analogy to Sun et al. [47], the induction period was followed by a nucleation burst with rapid growth and a slow increase stage. (cf. **Figure SII-7**) For f and g, the size stagnation stems from uniform growth and the onset of sedimentation, which appears to maintain the size balance of the dispersed particles. For j, the particles are so small that they neither aggregate nor sediment.

The difference between g and j, which are compositions of the same ternary system, is most likely due to the different SFME structures present. In j, pre-Ouzo aggregates are clearly prominent and therefore a high fraction of interphase is present, increasing the diffusion of the TEOS into the pseudo-water phase. Sample g is in the BIC area, which has less interphase, resulting in reduced TEOS diffusion into the pseudo-water phase. Also, the higher hydrolysis ratio in j (252 vs 46) increases the rate of hydrolysis, especially at the start of the reaction, resulting in more nuclei and, in turn, smaller particles.

2.4.2.3 Characterization / Comparison of Formed Stöber Nanoparticles

To evaluate the size and morphology of the formed particles after one hour reaction time, TEM micrographs were taken. (cf. **Figure II-13**)

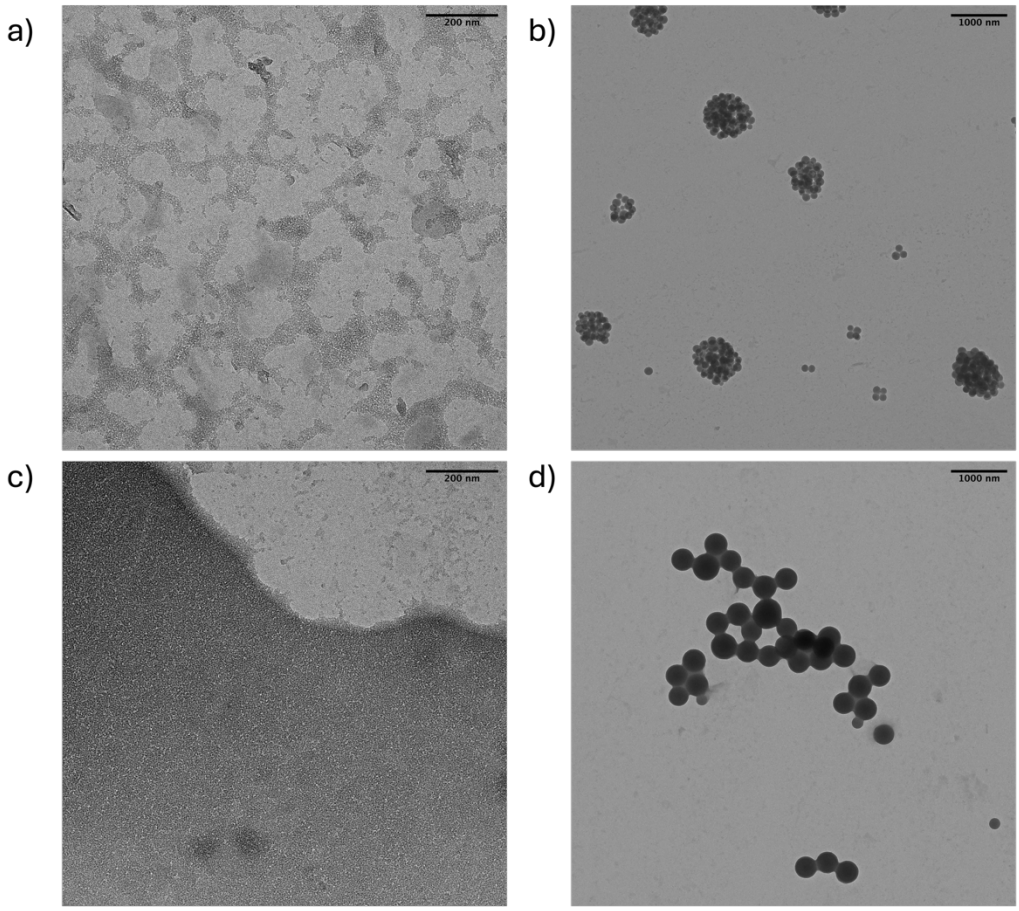


Figure II-13. (a) TEM micrograph of silica particles derived from point C in the H_2O / EtOH / TEOS system at a magnification of 40000x. The scale bar corresponds to 200 nm. (b) TEM micrograph of silica particles derived from point f in the H_2O / EtOH / toluene + TEOS system at a magnification of 6000x. The scale bar corresponds to 1000 nm. (c) TEM micrograph of silica particles derived from point j in the H_2O / EtOH / octanol + TEOS system at a magnification of 40000x. The scale bar corresponds to 200 nm (d) TEM micrograph of silica particles derived from point g in the H_2O / EtOH / octanol + TEOS system at a magnification of 6000x. The scale bar corresponds to 1000 nm

The particles derived from sample C (cf. **Figure II-13a**) are highly aggregated on the TEM grid but clearly visible. Information about the particle size can be derived from measurements of the FFT pictures (cf. **Figure SII-8a**) of the shown TEM micrograph. The visible particles are between 5 nm and 13 nm in size (cf. **Table SII-5**) and therefore continue the trend of reduced particle size for low NH_3 concentration at high hydrolysis ratio R, as shown in literature [12,72]. The particles derived from sample j (cf. **Figure II-13c**) are quite similar. They are also heavily aggregated on the grid, and size evaluation by measurements of the FFT (cf. **Figure SII-8b**) is comparable, suggesting slightly smaller aggregates. These particles are between 3 nm and 8 nm (cf. **Table SII-5**).

The particles derived from sample f (cf. **Figure II-13b**) and sample g (cf. **Figure II-13d**) show rather different results. The formed particles are significantly larger with ~58 nm and ~207 nm,

respectively (cf. **Table SII-5**). They are clearly spherical with sharp edges and are slightly aggregated.

The similarity between C and j indicates a similar particle formation process, even though j shows SFME (pre-Ouzo) aggregates, while C does not. The hydrolysis ratio of j is almost three times higher than that of C, and the solvent ratio is almost doubled. This results in faster hydrolysis/condensation kinetics, which in turn increases the number of nuclei capping the growth of the particles at a smaller final size [16,17].

Also, the overall TEOS concentration in j is halved, reducing the size due to a shorter growth phase. The point j significantly decreases the size and size distribution, hinting at no direct templating effect by pre-Ouzo aggregates compared to the system used in C.

In the other systems, the formation of the SFME beforehand seems to alter the resulting particles significantly. At the same hydrolysis ratio (~46), the particles derived from g are almost 4 times bigger than the particles derived from f (cf. **Table SII-5**). These size differences can not only be attributed to the solvent ratio or the hydrolysis ratio, but also to the influence of the oil component. Compared to SFME systems with primary alcohols [63,64], an interesting trend occurs, inverse to the trend visible in classical Stöber syntheses [23–25]. The particle size seems to decrease with increased viscosity (chain length) (cf. **Figure SII-10**) of the alcohol (pentanol [63] ~1000 nm > heptanol [64] ~700 nm > octanol ~500 nm) at similar points in the ternary system. Note that such comparisons are to be taken with a grain of salt, due to the inconsistencies and the lack of given values for R, S, or [NH_3]. Nevertheless, toluene (no primary alcohol, no hydrogen bonding) does not fit into this trend and instead results in smaller particles despite/due to its lower viscosity. It appears that the solubility of the hydrolyzed TEOS species and the solubility of the catalyst (cf. **Figure SII-4**) in the pseudo-oil phase and the interphase play a decisive role.

2.4.3 Proposed Mechanism of Nanoparticle Formation in the Regular SFME Systems

For both the pre-Ouzo region and the BIC region in the ternary phase diagram, a new mechanism can be proposed. Different from the existing mechanism [47], which describes particle formation in the O/W region, the condensation of TEOS most likely happens in the pseudo-water phase instead of the pseudo-oil phase. Part of the hydrolysis may happen in the pseudo-oil phase/interphase depending on the polarity, but the charged hydrolyzed TEOS

monomers tend to diffuse into the pseudo-water phase. (cf. **Figure II-14**) Based on Fick's First Law [95], the molar flux J across the interphase can be given by:

$$J = \frac{\Delta c}{\int_0^{\delta} \frac{1}{D(x)} dx} \tag{II-1}$$

With the concentration difference between inner and outer pseudo-phase Δc, the thickness of the interphase δ, and the diffusion coefficient function $D(x)$, depending on the variation of the viscosity across the interphase. As the diffusion rate depends on the viscosity of the pseudo-oil phase and of the interphase, the same applies for the reaction rates. The bigger the volume fraction of the interphase, which depends on the position in the ternary system (Pre-Ouzo > BIC), the faster the diffusion across the interphase. While the volume fraction of the interphase is the major factor in the size difference of g and j, the viscosity and polarity are the main factors for the difference between g and f. As the viscosity of the pseudo-oil phase and the interphase is much higher for g (cf. **Figure SII-10**), the diffusion is strongly hindered, inducing fewer nuclei at the start of the reaction, resulting in more extensive growth afterward.

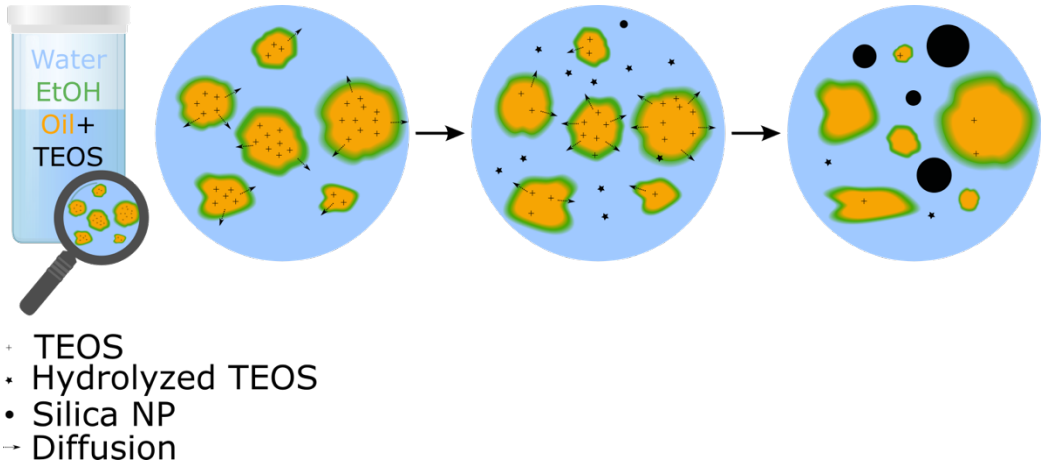


Figure II-14. Proposed mechanism of Stöber particle formation in SFME. The pseudo-oil phase acts as a reservoir for TEOS, which diffuses across the interphase. Hydrolysis and condensation occur in the pseudo-water phase.

Additionally, the reaction rate of the TEOS hydrolysis is reduced in the toluene system. The local coexistence of TEOS and NH_3 in the interphase is decreased, resulting in mass transfer potentially becoming the rate-determining step. In contrast, octanol promotes the distribution

of both species across the interphase, thereby increasing the effective contact probability and the observed reaction rate in the reactively coupled diffusion system.

Also, the dynamics of the aggregates play a crucial role, as the rate of forming and dissolving the SFME aggregates influences the contact time/probability of contact between TEOS and catalyst. This is mainly influenced by the position in the ternary system/closeness to the critical point, and the difference in polarity of water and used oil. Qualitatively, f shows the fastest fluctuations, followed by g and then by j (cf. **Figure II-10a**), even though the smallest particles were produced there. This indicates that the effect of the diffusion on the size of the final particles overshadows the effect of the fluctuation rates.

2.5 Conclusion

The ternary system H_2O / EtOH / TEOS does not form aggregates of a surfactant-free microemulsion. Instead, it is a molecularly dispersed solution throughout the ternary space. Stöber particle syntheses in such systems, characterized by high water content and low [NH_3], still remain comparatively underexplored. The formed particles are in the range of a few nanometers, exhibit high monodispersity, and the high-water content enhances the environmental friendliness compared to classical Stöber systems. The addition of regrowth steps allows easy size adjustment.

The incorporation of TEOS into existing SFME systems shows little change to the ternary phase diagrams and the aggregates contained. Depending on the microregion, the SFME structure can exhibit different effects on synthesized particles. It was evident that particles derived from the BIC area grew in three stages. First, the induction period for nucleation, followed by a nucleation burst and rapid growth, and finally subsequent slow growth [47].

Also, the chosen oil and, in particular, its viscosity and polarity, play an important role in affecting particle size, since TEOS diffusion across the interphase was identified as the rate-determining step.

SFME structures can induce interesting effects on the synthesis of Stöber particles. While the addition of a hydrophobic compound reduces the environmental friendliness of the system, it also introduces a new parameter that influences the particles' size, shape, and polydispersity. At similar R and S values, two oils, i.e., toluene and 1-octanol, already exhibited significant size differences. In connection with the pseudo-ternary systems in literature [63,64], new possibilities for size control and potential modification arise. Therefore, a study comparing syntheses in several different SFME forming ternary systems at similar R and S values would be interesting.

2.6 References

[1] Lu J, Peng L, Zhang A, Xu J, Wu M, Ma S. Fabrication of tetraethyl orthosilicate/ethanol–water surfactant-free microemulsions and their applications in self-templating synthesis of monodispersed silica colloidal spheres. RSC Adv 2024;14:39040–9. https://doi.org/10.1039/D4RA07679F.

[2] Stöber W, Fink A, Bohn E. Controlled growth of monodisperse silica spheres in the micron size range. J Colloid Interface Sci 1968;26:62–9. https://doi.org/10.1016/0021-9797(68)90272-5.

[3] Ghimire PP, Jaroniec M. Renaissance of Stöber method for synthesis of colloidal particles: New developments and opportunities. J Colloid Interface Sci 2021;584:838–65. https://doi.org/10.1016/j.jcis.2020.10.014.

[4] Rahman IA, Padavettan V. Synthesis of Silica Nanoparticles by Sol-Gel: Size-Dependent Properties, Surface Modification, and Applications in Silica-Polymer Nanocomposites—A Review. J Nanomater 2012;2012. https://doi.org/10.1155/2012/132424.

[5] Bergna HE. The Colloid Chemistry of Silica. vol. 234. Washington DC: American Chemical Society; 1994. https://doi.org/10.1021/ba-1994-0234.

[6] Unger KK. Porous silica : its properties and use as support in column liquid chromatography. Elsevier Scientific Pub. Co.; 1979.

[7] Iler RK. The Chemistry of Silica: Solubility, Polymerization, Colloid and Surface Properties and Biochemistry of Silica. Wiley; 1979.

[8] Cihlář J. Hydrolysis and polycondensation of ethyl silicates. 1. Effect of pH and catalyst on the hydrolysis and polycondensation of tetraethoxysilane (TEOS). Colloids Surf A Physicochem Eng Asp 1993;70:239–51. https://doi.org/10.1016/0927-7757(93)80298-S.

[9] Zerda TW, Hoang G. Effect of Solvents on the Hydrolysis Reaction of Tetramethyl Orthosilicate. Chemistry of Materials 1990;2:372–6. https://doi.org/10.1021/cm00010a012.

[10] Van Blaaderen A, Van Geest J, Vrij A. Monodisperse colloidal silica spheres from tetraalkoxysilanes: Particle formation and growth mechanism. J Colloid Interface Sci 1992;154:481–501. https://doi.org/10.1016/0021-9797(92)90163-G.

[11] Brinker CJ. Hydrolysis and condensation of silicates: Effects on structure. J Non Cryst Solids 1988;100:31–50. https://doi.org/10.1016/0022-3093(88)90005-1.

[12] Brinker CJ, Scherer GW. Hydrolysis and Condensation II. Sol-Gel Science 1990:96–233. https://doi.org/10.1016/b978-0-08-057103-4.50008-8.

[13] Rao KS, El-Hami K, Kodaki T, Matsushige K, Makino K. A novel method for synthesis of silica nanoparticles. J Colloid Interface Sci 2005;289:125–31. https://doi.org/10.1016/j.jcis.2005.02.019.

[14] Van Helden AK, Jansen JW, Vrij A. Preparation and characterization of spherical monodisperse silica dispersions in nonaqueous solvents. J Colloid Interface Sci 1981;81:354–68. https://doi.org/10.1016/0021-9797(81)90417-3.

[15] Bogush GH, Tracy MA, Zukoski CF. Preparation of monodisperse silica particles: Control of size and mass fraction. J Non Cryst Solids 1988;104:95–106. https://doi.org/10.1016/0022-3093(88)90187-1.

[16] Wang H-C, Wu C-Y, Chung C-C, Lai M-H, Chung T-W. Analysis of Parameters and Interaction between Parameters in Preparation of Uniform Silicon Dioxide Nanoparticles Using Response Surface Methodology. Ind Eng Chem Res 2006;45:8043–8. https://doi.org/10.1021/ie060299f.

[17] Park SK, Kim K Do, Kim HT. Preparation of silica nanoparticles: Determination of the optimal synthesis conditions for small and uniform particles. Colloids Surf A Physicochem Eng Asp 2002;197:7–17. https://doi.org/10.1016/S0927-7757(01)00683-5.

[18] Giesche H. Synthesis of monodispersed silica powders I. Particle properties and reaction kinetics. J Eur Ceram Soc 1994;14:189–204. https://doi.org/10.1016/0955-2219(94)90087-6.

[19] Wyman Jeffries. The dielectric constant of mixtures of ethyl alcohol and water from -5 to 40°C. J Am Chem Soc 1931;53:3292–301. https://doi.org/10.1021/ja01360a012.

[20] Sadasivan S, Dubey AK, Li Y, Rasmussen DH. Alcoholic Solvent Effect on Silica Synthesis—NMR and DLS Investigation. J Solgel Sci Technol 1998;12:5–14. https://doi.org/10.1023/A:1008659708390.

[21] Harris MT, Brunson RR, Byers CH. The base-catalyzed hydrolysis and condensation reactions of dilute and concentrated TEOS solutions. J Non Cryst Solids 1990;121:397–403. https://doi.org/10.1016/0022-3093(90)90165-I.

[22] Matsoukas T, Gulari E. Dynamics of growth of silica particles from ammonia-catalyzed hydrolysis of tetra-ethyl-orthosilicate. J Colloid Interface Sci 1988;124:252–61. https://doi.org/10.1016/0021-9797(88)90346-3.

[23] Bari AH, Jundale RB, Kulkarni AA. Understanding the role of solvent properties on reaction kinetics for synthesis of silica nanoparticles. Chemical Engineering Journal 2020;398:125427. https://doi.org/10.1016/j.cej.2020.125427.

[24] Mine E, Nagao D, Kobayashi Y, Konno M. Solvent Effects on Particle Formation in Hydrolysis of Tetraethyl Orthosilicate. J Solgel Sci Technol 2005;35:197–201. https://doi.org/10.1007/s10971-005-2289-x.

[25] Green DL, Lin JS, Lam Y-F, Hu MZ-C, Schaefer DW, Harris MT. Size, volume fraction, and nucleation of Stöber silica nanoparticles. J Colloid Interface Sci 2003;266:346–58. https://doi.org/10.1016/S0021-9797(03)00610-6.

[26] Yan Y, Fu J, Xu L, Wang T, Lu X. Controllable synthesis of SiO 2 nanoparticles: effects of ammonia and tetraethyl orthosilicate concentration. Micro Nano Lett 2016;11:885–9. https://doi.org/10.1049/mnl.2016.0434.

[27] Tan CG, Bowen BD, Epstein N. Production of Monodisperse Colloidal Silica Spheres: Effect of Temperature. J Colloid Interface Sci 1987;118:290–3. https://doi.org/doi.org/10.1016/0021-9797(87)90458-9.

[28] LaMer VK, Dinegar RH. Theory, Production and Mechanism of Formation of Monodispersed Hydrosols. J Am Chem Soc 1950;72:4847–54. https://doi.org/10.1021/ja01167a001.

[29] Bogush GH, Zukoski CF. Studies of the kinetics of the precipitation of uniform silica particles through the hydrolysis and condensation of silicon alkoxides. J Colloid Interface Sci 1991;142:1–18. https://doi.org/10.1016/0021-9797(91)90029-8.

[30] Masalov VM, Sukhinina NS, Kudrenko EA, Emelchenko GA. Mechanism of formation and nanostructure of Stöber silica particles. Nanotechnology 2011;22:275718. https://doi.org/10.1088/0957-4484/22/27/275718.

[31] Bogush GH, Zukoski CF. Uniform silica particle precipitation: An aggregative growth model. J Colloid Interface Sci 1991;142:19–34. https://doi.org/10.1016/0021-9797(91)90030-C.

[32] Nagao D, Satoh T, Konno M. A Generalized Model for Describing Particle Formation in the Synthesis of Monodisperse Oxide Particles Based on the Hydrolysis and Condensation of Tetraethyl Orthosilicate. J Colloid Interface Sci 2000;232:102–10. https://doi.org/10.1006/jcis.2000.7195.

[33] Verwey EJW. Theory of the Stability of Lyophobic Colloids. J Phys Colloid Chem 1947;51:631–6. https://doi.org/10.1021/j150453a001.

[34] Evans DF, Wennerström H. The Colloidal Domain. 2nd ed. New York, NY: John Wiley & Sons, INC.; 1999.

[35] Neuberg C. Hydrotropische Erscheinungen. Biochemie 1916;1:99–107.

[36] Hahn M, Krickl S, Buchecker T, Jošt G, Touraud D, Bauduin P, et al. Ab initio prediction of structuring/mesoscale inhomogeneities in surfactant-free microemulsions and hydrogen-bonding-free microemulsions. Physical Chemistry Chemical Physics 2019;21:8054–66. https://doi.org/10.1039/C8CP07544A.

[37] Hopkins Hatzopoulos M, Eastoe J, Dowding PJ, Rogers SE, Heenan R, Dyer R. Are hydrotropes distinct from surfactants? Langmuir 2011;27:12346–53. https://doi.org/10.1021/la2025846.

[38] Subramanian D, Anisimov MA. Phase behavior and mesoscale solubilization in aqueous solutions of hydrotropes. Fluid Phase Equilib 2014;362:170–6. https://doi.org/10.1016/j.fluid.2013.09.064.

[39] Eastoe J, Hatzopoulos MH, Dowding PJ. Action of hydrotropes and alkyl-hydrotropes. Soft Matter 2011;7:5917–25. https://doi.org/10.1039/c1sm05138e.

[40] Kunz W, Holmberg K, Zemb T. Hydrotropes. Curr Opin Colloid Interface Sci 2016;22:99–107. https://doi.org/10.1016/j.cocis.2016.03.005.

[41] Mehringer J, Kunz W. Carl Neuberg's hydrotropic appearances (1916). Adv Colloid Interface Sci 2021;294:102476. https://doi.org/10.1016/j.cis.2021.102476.

[42] Hou W, Xu J. Surfactant-free microemulsions. Curr Opin Colloid Interface Sci 2016;25:67–74. https://doi.org/10.1016/j.cocis.2016.06.013.

[43] Nakama Y. Surfactants. Cosmetic Science and Technology, Elsevier; 2017, p. 231–44. https://doi.org/10.1016/B978-0-12-802005-0.00015-X.

[44] Lopian T, Schöttl S, Prévost S, Pellet-Rostaing S, Horinek D, Kunz W, et al. Morphologies observed in ultraflexible microemulsions with and without the presence of a strong acid. ACS Cent Sci 2016;2:467–75. https://doi.org/10.1021/acscentsci.6b00116.

[45] Smith GD, Donelan CE, Barden RE. Oil-continuous microemulsions composed of hexane, water, and 2-propanol. J Colloid Interface Sci 1977;60:488–96. https://doi.org/10.1016/0021-9797(77)90313-7.

[46] Abrar I, Bhaskarwar AN. Performance and emission characteristics of constant speed diesel engine fueled by surfactant-free microemulsions. Sustainable Energy Technologies and Assessments 2021;47. https://doi.org/10.1016/j.seta.2021.101414.

[47] Han Y, Liu S, Du Y, Li D, Pan N, Chai J, et al. A new application of surfactant-free microemulsion: Solubilization and transport of drugs and its transdermal release properties. J Taiwan Inst Chem Eng 2022;138:104473. https://doi.org/10.1016/j.jtice.2022.104473.

[48] Sun B, Chai J, Chai Z, Zhang X, Cui X, Lu J. A surfactant-free microemulsion consisting of water, ethanol, and dichloromethane and its template effect for silica synthesis. J Colloid Interface Sci 2018;526:9–17. https://doi.org/10.1016/j.jcis.2018.04.072.

[49] Schmauser L, Müller E, Touraud D, Kunz W. Applications of surfactant-free microemulsions. Curr Opin Colloid Interface Sci 2026;83:102001. https://doi.org/10.1016/j.cocis.2026.102001.

[50] Zemb TN, Klossek M, Lopian T, Marcus J, Schöettl S, Horinek D. How to explain microemulsions formed by solvent mixtures without conventional surfactants 2016:1–6. https://doi.org/10.1073/pnas.1515708113.

[51] Schöttl S, Lopian T, Prévost S, Touraud D, Grillo I, Diat O, et al. Combined molecular dynamics (MD) and small angle scattering (SAS) analysis of organization on a nanometer-scale in ternary solvent solutions containing a hydrotrope. J Colloid Interface Sci 2019;540:623–33. https://doi.org/10.1016/j.jcis.2019.01.037.

[52] Krickl S, Jurko L, Wolos K, Touraud D, Kunz W. Surfactant-free microemulsions with cleavable constituents. J Mol Liq 2018;271:112–7. https://doi.org/10.1016/j.molliq.2018.08.120.

[53] Krickl S. Investigation of Potential Applications of Surfactant-free Microemulsions - Solubilisation, Separation and Extraction Processes and Reaction Media 2018:1–205. https://doi.org/10.5283/epub.38134.

[54] Schöttl S, Touraud D, Kunz W, Zemb T, Horinek D. Consistent definitions of “the interface” in surfactant-free micellar aggregates. Colloids Surf A Physicochem Eng Asp 2015;480:222–7. https://doi.org/10.1016/j.colsurfa.2014.11.029.

[55] Buchecker T, Krickl S, Winkler R, Grillo I, Bauduin P, Touraud D, et al. The impact of the structuring of hydrotropes in water on the mesoscale solubilisation of a third hydrophobic component. Physical Chemistry Chemical Physics 2017;19:1806–16. https://doi.org/10.1039/c6cp06696h.

[56] Booth JJ, Omar M, Abbott S, Shimizu S. Hydrotrope accumulation around the drug: The driving force for solubilization and minimum hydrotrope concentration for nicotinamide and urea. Physical Chemistry Chemical Physics 2015;17:8028–37. https://doi.org/10.1039/c4cp05414h.

[57] Shimizu S, Matubayasi N. The origin of cooperative solubilisation by hydrotropes. Physical Chemistry Chemical Physics 2016;18:25621–8. https://doi.org/10.1039/c6cp04823d.

[58] Choi S, Parameswaran S, Choi JH. Understanding alcohol aggregates and the water hydrogen bond network towards miscibility in alcohol solutions: Graph theoretical analysis. Physical Chemistry Chemical Physics 2020;22:17181–95. https://doi.org/10.1039/d0cp01991g.

[59] Dixit S, Crain J, Poon WCK, Finney JL, Soper AK. Molecular segregation observed in a concentrated alcohol–water solution. Nature 2002;416:829–32. https://doi.org/10.1038/416829a.

[60] Degot P, Huber V, Hofmann E, Hahn M, Touraud D, Kunz W. Solubilization and extraction of curcumin from Curcuma Longa using green, sustainable, and food-approved surfactant-free microemulsions. Food Chem 2021;336:127660. https://doi.org/10.1016/j.foodchem.2020.127660.

[61] Xenakis A, Zoumpanioti M, Stamatis H. Enzymatic reactions in structured surfactant-free microemulsions. Curr Opin Colloid Interface Sci 2016;22:41–5. https://doi.org/10.1016/j.cocis.2016.02.009.

[62] Blahnik J, Schuster J, Müller R, Müller E, Kunz W. Surfactant-free microemulsions (SFMEs) as a template for porous polymer synthesis. J Colloid Interface Sci 2024;655:371–82. https://doi.org/10.1016/j.jcis.2023.10.162.

[63] Blahnik J, Krickl S, Schmid K, Müller E, Lupton J, Kunz W. Microemulsion and microsuspension polymerization of methyl methacrylate in surfactant-free microemulsions (SFME). J Colloid Interface Sci 2023;648:755–67. https://doi.org/10.1016/j.jcis.2023.06.025.

[64] Gudelj M, Kranjac M, Hajdin I, Tomšič M, Cerar J, Prkić A, et al. Design of Surfactant-Free Microemulsions Composed of n-Pentanol, Ethanol, and Water: Application in Silica Nanoparticle Synthesis. Inorganics (Basel) 2025;13:392. https://doi.org/10.3390/inorganics13120392.

[65] Gudelj M, Kranjac M, Jurko L, Tomšič M, Cerar J, Prkić A, et al. Structure and Potential Application of Surfactant-Free Microemulsion Consisting of Heptanol, Ethanol and Water. Colloids and Interfaces 2024;8:53. https://doi.org/10.3390/colloids8050053.

[66] Lee K, Sathyagal AN, McCormick A V. A closer look at an aggregation model of the Stöber process. Colloids Surf A Physicochem Eng Asp 1998;144:115–25. https://doi.org/10.1016/S0927-7757(98)00566-4.

[67] Greasley SL, Page SJ, Sirovica S, Chen S, Martin RA, Riveiro A, et al. Controlling particle size in the Stöber process and incorporation of calcium. J Colloid Interface Sci 2016;469:213–23. https://doi.org/10.1016/j.jcis.2016.01.065.

[68] Bourebrab MA, Oben DT, Durand GG, Taylor PG, Bruce JI, Bassindale AR, et al. Influence of the initial chemical conditions on the rational design of silica particles. J Solgel Sci Technol 2018;88:430–41. https://doi.org/10.1007/s10971-018-4821-9.

[69] Boukari H, Lin JS, Harris MT. Small-Angle X-Ray Scattering Study of the Formation of Colloidal Silica Particles from Alkoxides: Primary Particles or Not? J Colloid Interface Sci 1997;194:311–8. https://doi.org/10.1006/jcis.1997.5112.

[70] Qi D, Lin C, Zhao H, Liu H, Lü T. Size regulation and prediction of the SiO 2 nanoparticles prepared via Stöber process. J Dispers Sci Technol 2017;38:70–4. https://doi.org/10.1080/01932691.2016.1143373.

[71] dos Santos da Silva A, dos Santos JHZ. Stöber method and its nuances over the years. Adv Colloid Interface Sci 2023;314:102888. https://doi.org/10.1016/j.cis.2023.102888.

[72] Fernandes RS, Raimundo IM, Pimentel MF. Revising the synthesis of Stöber silica nanoparticles: A multivariate assessment study on the effects of reaction parameters on the particle size. Colloids Surf A Physicochem Eng Asp 2019;577:1–7. https://doi.org/10.1016/j.colsurfa.2019.05.053.

[73] Byers CH, Harris MT, Williams DF. Controlled microcrystalline growth studies by dynamic laser-light-scattering methods. Ind Eng Chem Res 1987;26:1916–23. https://doi.org/10.1021/ie00069a033.

[74] Jarzębski M, Śliwa T, Jarzębska M, Szutkowski K. Fabrication of Size-Tunable Silica Particles During Seed-Growth Process. Current Topics in Biophysics 2015;37:35–41. https://doi.org/10.2478/ctb-2014-0072.

[75] Verhaegh NAM, Van Blaaderen A. Dispersions of Rhodamine-Labeled Silica Spheres: Synthesis, Characterization, and Fluorescence Confocal Scanning Laser Microscopy. Langmuir 1994;10:1427–38. https://doi.org/10.1021/la00017a019.

[76] Nozawa K, Gailhanou H, Raison L, Panizza P, Ushiki H, Sellier E, et al. Smart control of monodisperse stöber silica particles: Effect of reactant addition rate on growth process. Langmuir 2005;21:1516–23. https://doi.org/10.1021/la048569r.

[77] Lee K, Look J-L, Harris MT, McCormick A V. Assessing Extreme Models of the Stöber Synthesis Using Transients under a Range of Initial Composition. J Colloid Interface Sci 1997;194:78–88. https://doi.org/10.1006/jcis.1997.5089.

[78] Frisken BJ. Revisiting the method of cumulants for the analysis of dynamic light-scattering data. Appl Opt 2001;40:4087. https://doi.org/10.1364/AO.40.004087.

[79] Provencher SW. A constrained regularization method for inverting data represented by linear algebraic or integral equations. Comput Phys Commun 1982;27:213–27. https://doi.org/10.1016/0010-4655(82)90173-4.

[80] Provencher SW. Contin: A general purpose constrainded regularization program for inverting noisy linear algebraic and integral equations. Comput Phys Commun 1984;35:C-818-C–819. https://doi.org/10.1016/S0010-4655(84)82935-5.

[81] Litmanovich EA, Ivleva EM. The problem of bimodal distributions in dynamic light scattering: Theory and experiment. Polymer Science - Series A 2010;52:671–8. https://doi.org/10.1134/S0965545X10060143.

[82] Malay O, Yilgor I, Menceloglu YZ. Effects of solvent on TEOS hydrolysis kinetics and silica particle size under basic conditions. J Solgel Sci Technol 2013;67:351–61. https://doi.org/10.1007/s10971-013-3088-4.

[83] Klossek ML, Touraud D, Zemb T, Kunz W. Structure and Solubility in Surfactant-Free Microemulsions. ChemPhysChem 2012;13:4116–9. https://doi.org/10.1002/cphc.201200667.

[84] Koppel DE. Analysis of macromolecular polydispersity in intensity correlation spectroscopy: The method of cumulants. J Chem Phys 1972;57:4814–20. https://doi.org/10.1063/1.1678153.

[85] Koppel DE. Analysis of macromolecular polydispersity in intensity correlation spectroscopy: The method of cumulants. J Chem Phys 1972;57:4814–20. https://doi.org/10.1063/1.1678153.

[86] Wang XD, Shen ZX, Sang T, Cheng X Bin, Li MF, Chen LY, et al. Preparation of spherical silica particles by Stöber process with high concentration of tetra-ethyl-orthosilicate. J Colloid Interface Sci 2010;341:23–9. https://doi.org/10.1016/j.jcis.2009.09.018.

[87] Washburn ER, Beguin AE, Beckord OC. The Ternary System: Ethyl Alcohol, Toluene and Water at 25°. J Am Chem Soc 1939;61:1694–5. https://doi.org/10.1021/ja01876a018.

[88] Moriyoshi T, Sakamoto T. (Liquid + liquid) equilibria of (water + ethanol + a C , alkanol) from 0.1 to 200 MPa at 298.15 K 1989;954:947–54. https://doi.org/https://doi.org/10.1016/0021-9614(89)90153-5.

[89] Prevost S, Lopian T, Pleines M, Diat O, Zemb T. Small-angle scattering and morphologies of ultra-flexible microemulsions. J Appl Crystallogr 2016;49:2063–72. https://doi.org/10.1107/S1600576716016150.

[90] Malayil Kalathil F, Plazanet M, Koza MM, Falus P, Czakkel O, Fouquet P, et al. How the formation of ultra-soft microemulsions affects dynamical properties at different lengthscales. J Mol Liq 2025;432:127684. https://doi.org/10.1016/j.molliq.2025.127684.

[91] Hartlen KD, Athanasopoulos APT, Kitaev V. Facile Preparation of Highly Monodisperse Small Silica Spheres (15 to >200 nm) Suitable for Colloidal Templating and Formation of Ordered Arrays. Langmuir 2008;24:1714–20. https://doi.org/10.1021/la7025285.

[92] Babick F. Dynamic light scattering (DLS). Characterization of Nanoparticles, Elsevier; 2020, p. 137–72. https://doi.org/10.1016/B978-0-12-814182-3.00010-9.

[93] Ganguli AK, Ganguly A, Vaidya S. Microemulsion-based synthesis of nanocrystalline materials. Chem Soc Rev 2010;39:474–85. https://doi.org/10.1039/B814613F.

[94] Abarkan I, Doussineau T, Smaïhi M. Tailored macro/microstructural properties of colloidal silica nanoparticles via microemulsion preparation. Polyhedron 2006;25:1763–70. https://doi.org/10.1016/j.poly.2005.11.031.

[95] Tyrrell HJV. The origin and present status of fick's diffusion law. J Chem Educ 1964;41:397–400. https://doi.org/10.1021/ed041p397.

[96] Rohr L, Denk P, Blahnik J, Müller E, Sztucki M, Kunz W. The Influence of Surface-active Compounds on Surfactant-free Microemulsions. Aggregate, Submitted 2026.

[97] Cano-Gómez JJ, Iglesias-Silva GA, Ramos-Estrada M, Hall KR. Densities and Viscosities for Binary Liquid Mixtures of Ethanol + 1-Propanol, 1-Butanol, and 1-Pentanol from (293.15 to 328.15) K at 0.1 MPa. J Chem Eng Data 2012;57:2560–7. https://doi.org/10.1021/je300632p.

[98] Nikam PS, Jagdale BS, Sawant AB, Hasan M. Densities and viscosities of binary mixtures of toluene with methanol, ethanol, propan-1-ol, butan-1-ol, pentan-1-ol, and 2-methylpropan-2-ol at (303.15, 308.15, 313.15) K. J Chem Eng Data 2000;45:559–63. https://doi.org/10.1021/je990317i.

[99] Rauf MA, Stewart GH, Farhataziz. Viscosities and Densities of Binary Mixtures of 1-Alkanois from 15 to 55 °C. J Chem Eng Data 1983;28:324–8. https://doi.org/10.1021/je00033a012.

[100] Shan Z, Asfour AFA. Viscosities and densities of nine binary 1-alkanol systems at 293.15 K and 298.15 K. J Chem Eng Data 1999;44:118–23. https://doi.org/10.1021/je980177x.

2.7 Supporting Information

Table SII-1. Weight percentage and molar fraction of various points of the ternary mixture H_2O / EtOH / TEOS as shown in **Figure II-7a**, **Figure II-8**, and **Figure SII-1**.

	wt%(H_2O)	wt%(EtOH)	wt%(TEOS)	x(H_2O)	x(EtOH)	x(TEOS)
A1	0.286	0.667	0.048	0.519	0.474	0.007
B	0.476	0.476	0.048	0.714	0.279	0.006
B'	0.452	0.500	0.048	0.694	0.300	0.006
B''	0.405	0.500	0.095	0.665	0.321	0.014
B'''	0.357	0.500	0.143	0.632	0.346	0.022
B''''	0.310	0.500	0.190	0.593	0.375	0.032
C	0.381	0.571	0.048	0.626	0.367	0.007
D	0.190	0.762	0.048	0.387	0.605	0.008
E	0.224	0.516	0.259	0.500	0.450	0.050
E'	0.163	0.417	0.419	0.450	0.450	0.100
E''	0.122	0.350	0.528	0.400	0.450	0.150
E'''	0.092	0.302	0.606	0.350	0.450	0.200

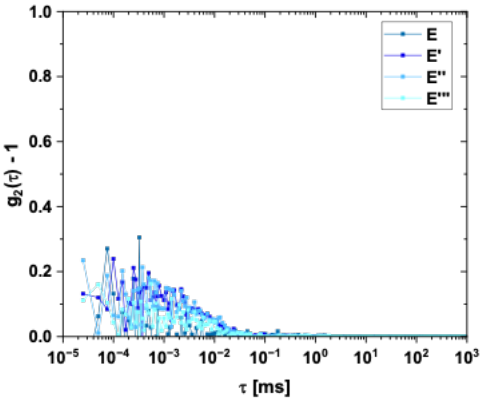


Figure SII-1. Correlation functions of DLS-measurements of the respective points E, E‘, E’’, and E’’’ directly after preparation. The exact fractions of the various are shown in **Table SII-1**.

Table SII-2. Hydrodynamic radius (r_H) derived from the DLS measurements shown in **Figure II-8b**. These sizes correspond to particles/aggregates formed after 4d in the respective solutions without catalyst/stirring. For evaluation the viscosity and refractive index of the corresponding water/ethanol mixture (x(EtOH) = 0.477; 0.281; 0.302; 0.370; 0.610) was used. As the composition D formed no clear correlation function, fitting was not possible.

	r_H [nm]	width [nm]	PD.I.
A1	4.83	2.23	0.213
B	9.37	4.54	0.235
B’	26.67	16.68	0.391
C	9.57	4.55	0.226
D	-	-	-

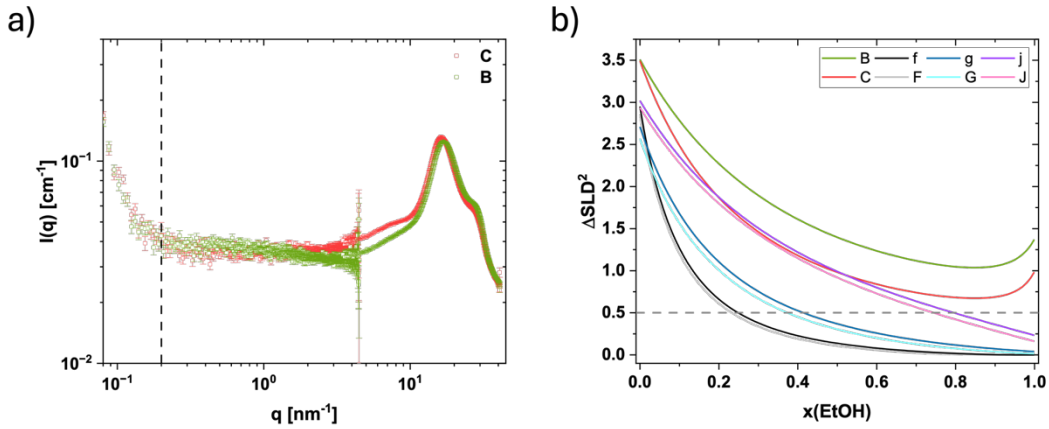


Figure SII-2. (a) SWAXS spectra of a) point B and C in the H_2O/EtOH/TEOS system. The increase at $q < 0.2$ nm^{-1} results from the X-ray beam. (b) Visualization of the contrast (ΔSLD^2) in the SWAXS measurements relative to the distribution of the hydrotrope ethanol in the pseudo-phases. The molar fraction x(EtOH) indicates the amount of ethanol in the aqueous pseudo-phase. In this simplified assumption no oil is solubilized in the aqueous pseudo-phase and no water in the oil pseudo-phase. The dashed line at $\Delta SLD^2 = 0.5$ shows the threshold below which the resolution of the SWAXS measurements is questionable. For J/j a value of literature was found to be x(EtOH) = 0.6 [96].

Table SII-3. Weight percentage and molar fraction of various points of the ternary mixture H_2O / EtOH / Oil + TEOS. The point f represents the mixture containing toluene and f' the total hydrolyzed state of the same point. For the points g and j the same is true in the mixtures containing 1-octanol [96].

	wt%(H_2O)	wt%(EtOH)	wt%(Oil+TEOS)	x(H_2O)	x(EtOH)	x(Oil+TEOS)
f	0.146	0.534	0.320	0.350	0.500	0.150
f'	0.139	0.560	0.301	0.332	0.526	0.141
g	0.202	0.361	0.437	0.500	0.350	0.150
g'	0.192	0.404	0.404	0.473	0.389	0.138
j	0.430	0.400	0.170	0.705	0.256	0.039
j’	0.426	0.417	0.157	0.698	0.267	0.036

Table SII-4. Estimated x(EtOH) for the points f, g, and j from SWAXS-measurements and their respective hydrodynamic radius evaluated from the DLS measurements. The value for j was taken from literature [96] whereas the values for f and g were estimated to be around 0.4 due to their contrast (**Figure SII-**2b) and their position near the critical point.

sample	x(EtOH)	r_H [nm]	width [nm]	PD.I.
f	0.4	0.45	0.17	0.151
g	0.4	0.81	0.38	0.221
j	0.6	3.73	0.59	0.0247

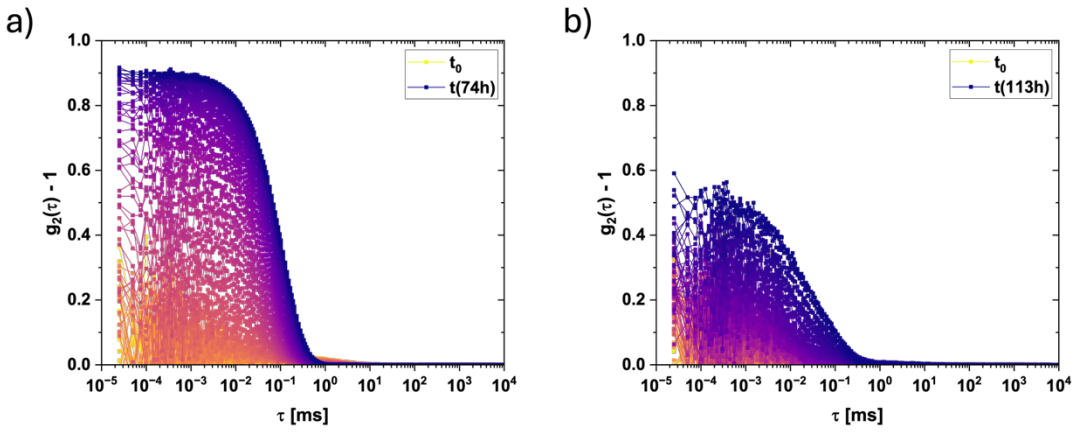


Figure SII-3. Correlation function of multiple DLS measurements during the formation of particles in the ternary mixture H_2O / EtOH / TEOS at point C (a) without the addition of a catalyst and (b) with arginine as catalyst (b). The gradient from yellow (t_0) to purple (t_{end}) visualizes the change of the samples over time. The hydrolysis ratio R = 92.5 and the solvent ratio S = 1.7.

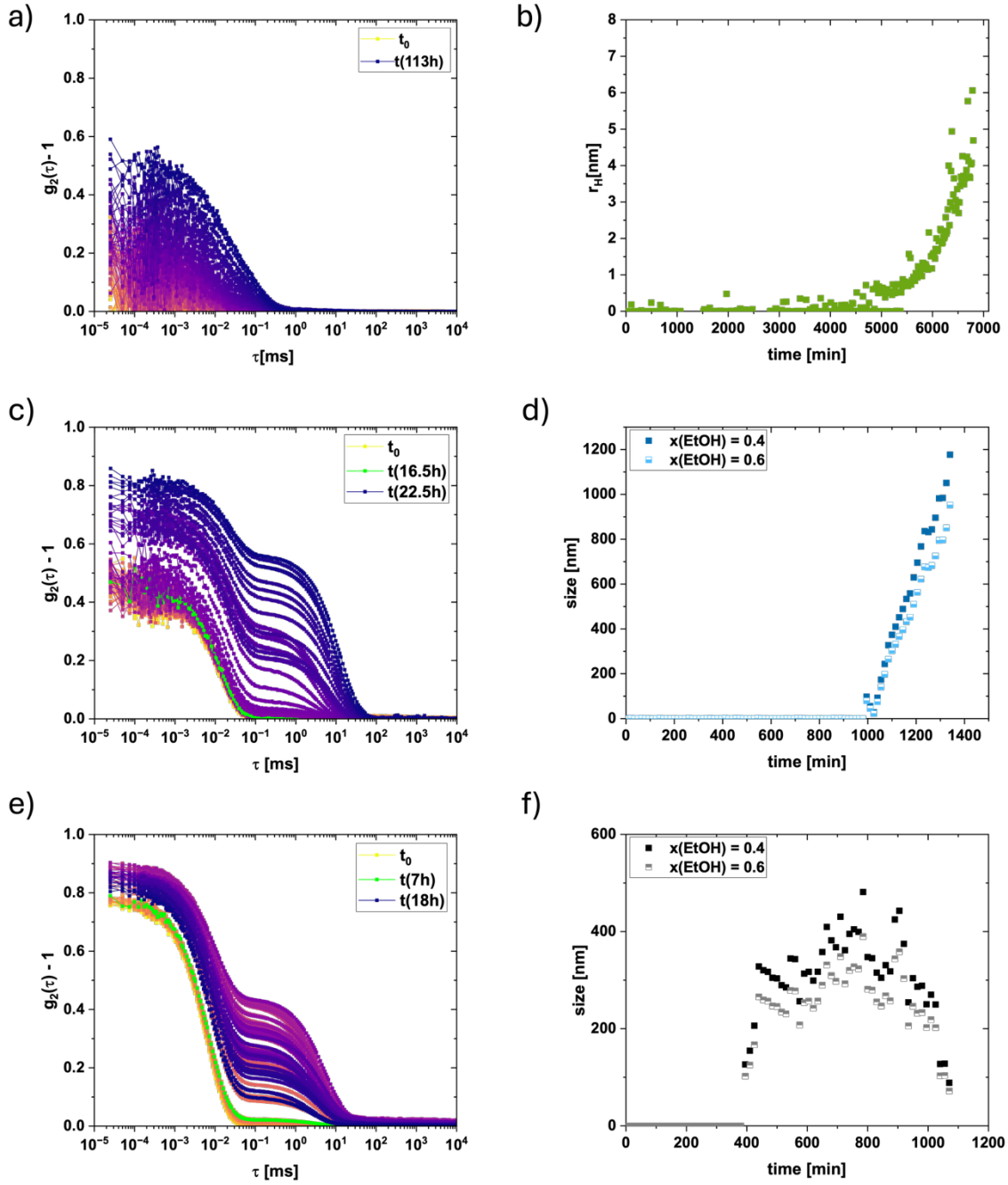


Figure SII-4. Correlation function of multiple DLS measurements during the formation of particles in the ternary mixtures (a) H_2O / EtOH / TEOS at point C, (c) H_2O / EtOH / 1-octanol + TEOS at point g and (d) H_2O / EtOH / toluene + TEOS at point f with the addition of arginine as catalyst. The gradient from yellow (t_0) to purple (t_{end}) visualizes the change of the samples over time. The respective change in hydrodynamic radius over time is shown in (b), (d), and (f).

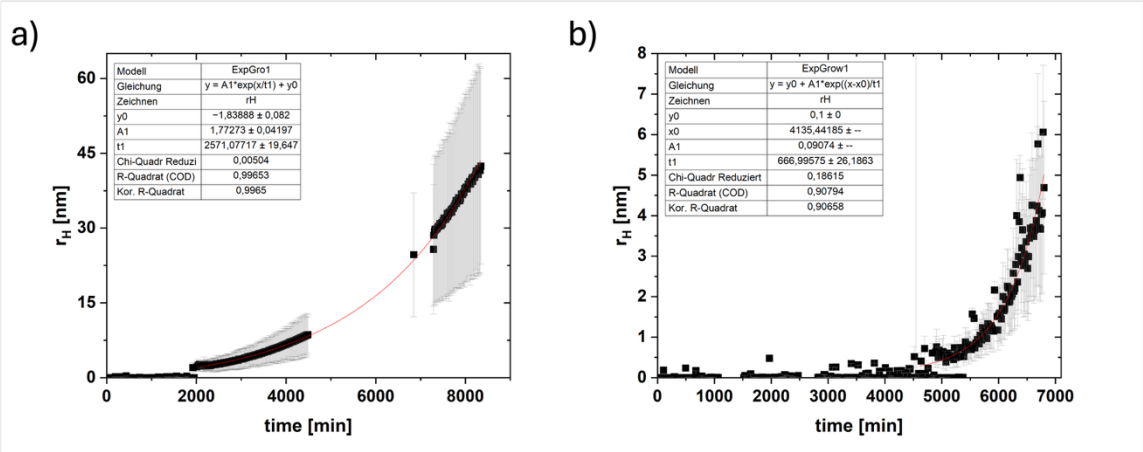


Figure SII-5. Hydrodynamic radius (r_H) derived from time dependent DLS measurements of the point C in the H_2O / EtOH / TEOS ternary mixture with (a) no catalyst and (b) arginine as catalyst. The corresponding correlation functions can be found in **Figure SII-3a** and **Figure SII-3b**, respectively.

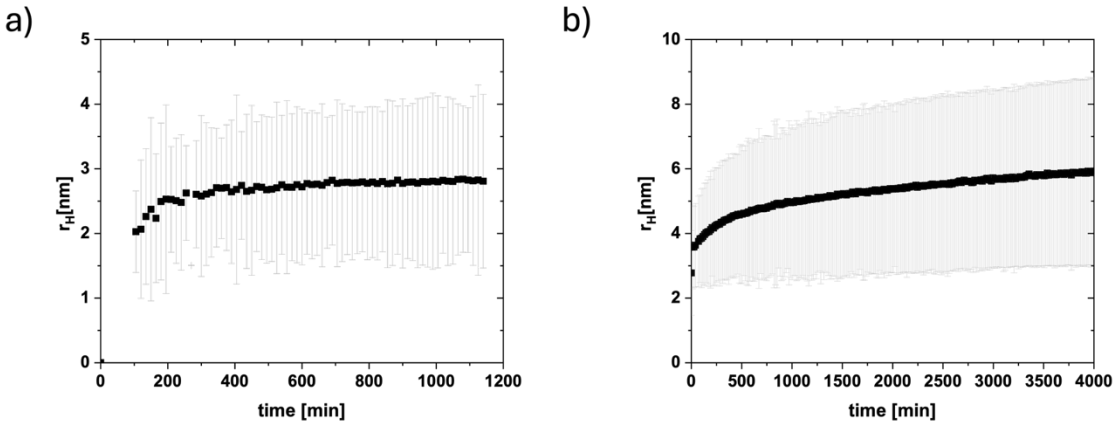


Figure SII-6. Hydrodynamic radius (r_H) derived from time dependent DLS measurements of the point C in the H_2O / EtOH / TEOS ternary mixture with (a) NH_3 as catalyst ([TEOS]/[NH_3] = 8.9) and (b) further addition of TEOS after reaching equilibria (~24h) in (a). The corresponding correlation functions can be found in **Figure II-11a** and **Figure II-11b**, respectively.

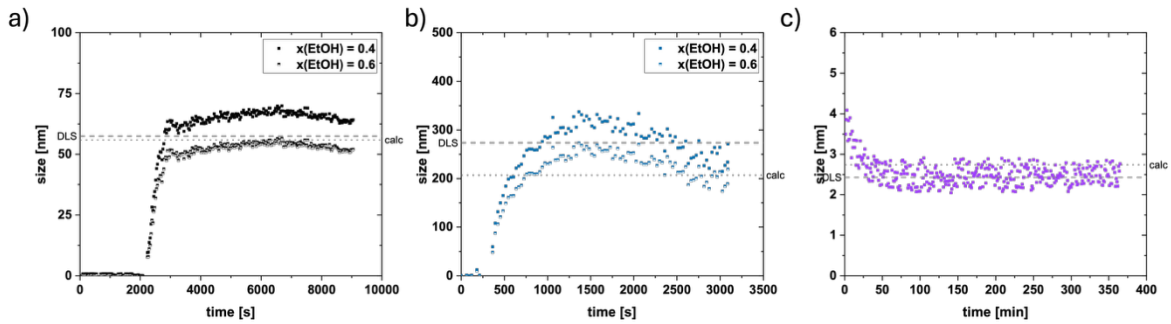


Figure SII-7. Hydrodynamic radius (r_H) derived from time dependent DLS measurements of the points (a) f in the H_2O / EtOH / toluene+TEOS ternary mixture, (b) g in the H_2O / EtOH / octanol+TEOS pseudo-ternary mixture, and (c) f in the H_2O / EtOH / octanol+TEOS pseudo-ternary mixture with NH_3 as catalyst ([TEOS]/[NH_3] = 8.9). The corresponding correlation functions can be found in **Figure II-12**. The dashed (DLS) and the dotted (calculated) lines correspond to the values shown in **Table SII-5**. As the exact distribution of ethanol changes as the reaction progresses, only the boundaries of the range, within which the x(EtOH) is most likely, were plotted.

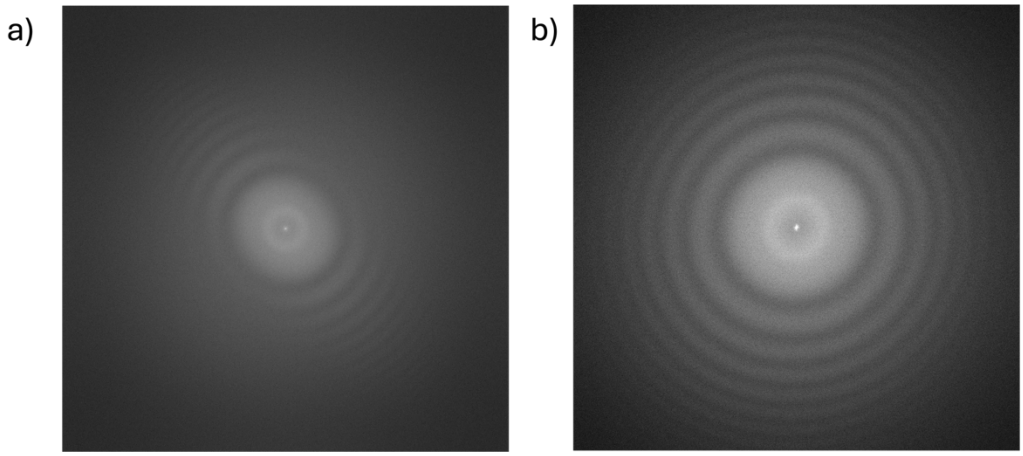


Figure SII-8. (a) FFT of the micrograph shown in **Figure II-13a**. The white circle corresponds to the distance between individual particles giving an estimate for their size between 5.51 nm and 12.81 nm after radial integration. (b) FFT of the micrograph shown in **Figure II-13c**. The white circle corresponds to the distance between individual particles giving an estimate for their size between 3.53 nm and 7.43 nm after radial integration.

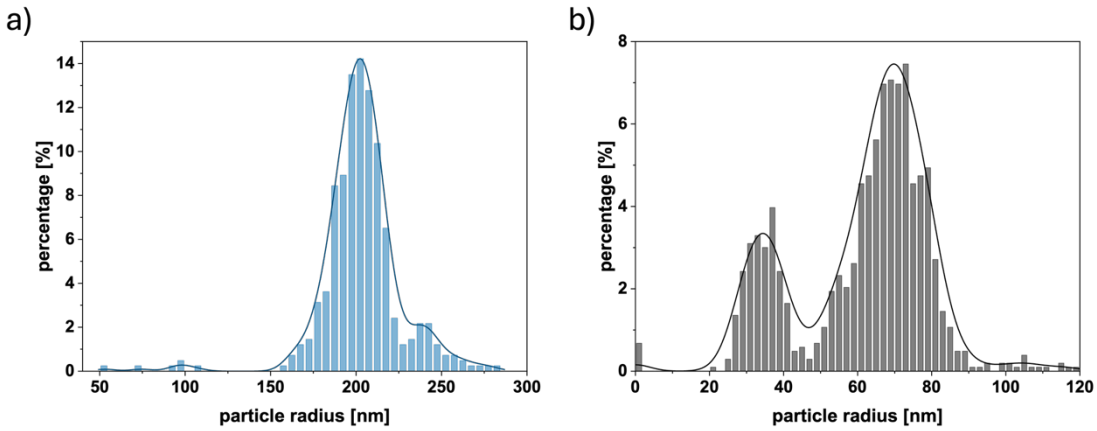


Figure SII-9. Histograms of measured particles from TEM micrographs. (a) 415 particles were measured for g and (b) 1026 particles were measured for f. Corresponding TEM micrographs can be found in **Figure II-1**3b and **Figure II-1**3d.

Table SII-5. Hydrodynamic radii of particles synthesized in the different systems. Values derived from DLS measurements and calculated from distribution fits of the histograms or are derived from the FFTs of the respective micrographs (cf. **Figure SII-8** and **Figure SII-9**). x(EtOH) was estimated to be around 0.6 for all samples except C. For C the composition of a fully hydrolyzed solution was used with x(EtOH) = 0.37.

	Derived from DLS			calculated		
	r_H [nm]	**width [nm]**	**PD.I.**	**r_H [nm]**	**width [nm]**	**PD.I.**
C	2.91	1.28	0.194	4.58	2.15	0.111
f	55.95	33.17	0.352	57.49	43.09	0.101
g	273.41	129.48	0.224	207.12	42.49	0.008
j	2.43	0.61	0.062	2.74	1.15	0.032

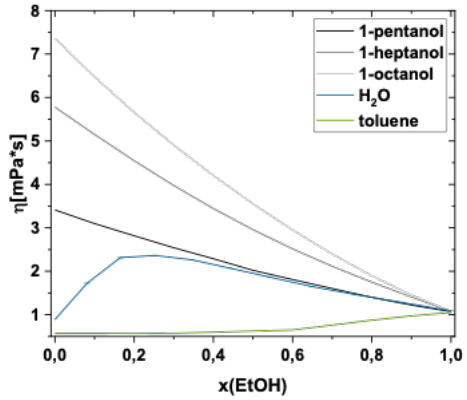


Figure SII-10. Viscosities of various binary mixtures of ethanol and the used solvents in the SFME systems as functions of the molar fraction of ethanol (x(EtOH)). While the value of the water ethanol mixture was measured, the others were taken from literature [97–100].

Chapter III. Nanodots of Transition Metal Sulfides, Carbonates and Oxides Obtained by Spontaneous Co-Precipitation with Silica

3.1 Abstract

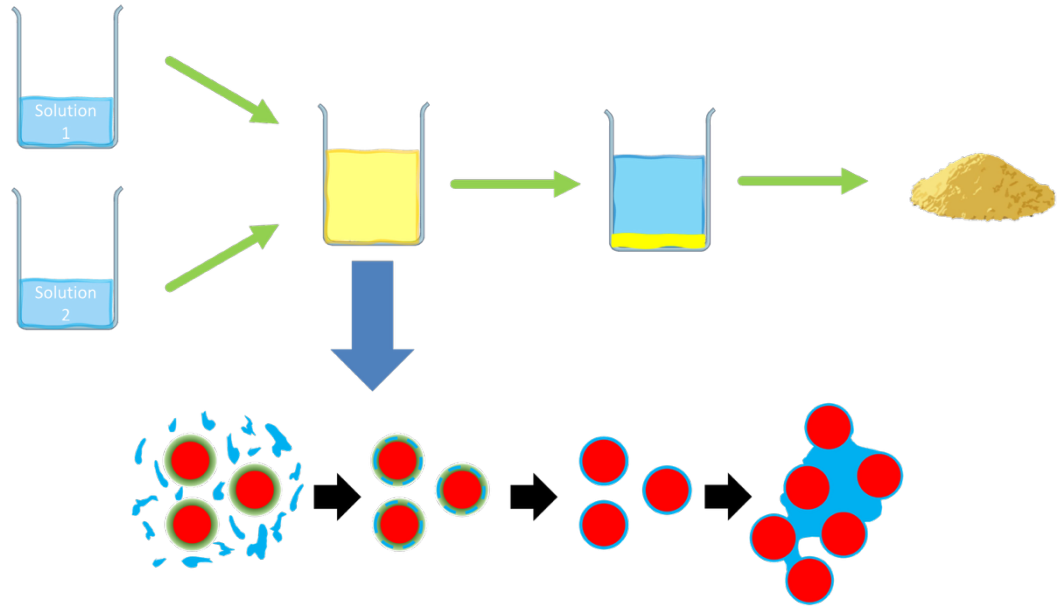


Figure III-1. Graphical Abstract: The combination of two aqueous solutions results in spontaneous coprecipitation of transition metal sulfides/carbonates and silica resulting in core-shell like aggregates. The precipitate can be centrifuged and lyophilized to obtain nanoparticle powder.

The controlled formation and stabilization of nanoparticles is of fundamental relevance for materials science and key to many modern technologies. Common synthetic strategies to arrest growth at small sizes and prevent undesired particle agglomeration often rely on the use of organic additives and require non-aqueous media and/or high temperatures, all of which appear critical with respect to production costs, safety and sustainability. In the present work, we demonstrate a simple one-pot process in water under ambient conditions that can produce particles of various transition metal carbonates and sulfides with sizes of only a few nanometers embedded in a silica shell, similar to particles derived from more elaborate synthesis routes, like the sol-gel process. To this end, solutions of soluble salts of metal cations (e.g., chlorides) and the respective anions (e.g., sodium carbonate or sulfide) are mixed in the presence of different amounts of sodium silicate at elevated pH levels. Upon mixing, metal

carbonate/sulfide particles nucleate and their subsequent growth causes a sensible decrease of pH in the vicinity. Dissolved silicate species respond to this local acidification by condensation reactions, which eventually lead to the formation of amorphous silica layers that encapsulate the metal carbonate/sulfide cores and thus effectively inhibit any further growth. The as-obtained carbonate nanodots can readily be converted into the corresponding metal oxides by secondary thermal treatment, during which their nanometric size is maintained. Although the described method clearly requires optimization towards actual applications, the results of this study highlight the potential of bottom-up self-assembly for the synthesis of functional nanoparticles at mild conditions.

The first part of this chapter is published in *MDPI nanomaterials* (Rödig, B.; Funkner, D.; Frank, T.; Schürmann, U.; Rieder, J.; Kienle, L.; Kunz, W.; Kellermeier, M. Nanodots of Transition Metal Sulfides, Carbonates, and Oxides Obtained Through Spontaneous Co-Precipitation with Silica. Nanomaterials 2024, 14 (24), 2054. https://doi.org/10.3390/nano1424205. Figures and text reproduced under the terms of the CC BY 4.0 license) [1].

Contributions to experimental work:

- Bastian Rödig: Conceptualization, Experimental Work, Data Evaluation
- Diana Funkner, Thomas Frank, Julian Rieder, Ulrich Schürmann: Experimental Work, Data Evaluation

3.2 Introduction

Nanoparticles continue to be an important type of material for a broad range of applications, including catalysis [2], electronics [3], energy storage [4], (bio-)sensors [5], functional coatings [6,7], and many more [8]. While a variety of different approaches to the synthesis of defined nanoparticles have been developed (such as sol-gel chemistry [9], hydrothermal [10], and solvothermal [11] processes, or mechanochemical concepts [12]), it is still a challenge to control their size, composition, structure (e.g., crystalline vs. amorphous) and surface functionalities (which are key to interactions and thus final properties). In addition, nanoparticle systems inherently suffer from their tendency to agglomerate, and hence, means to achieve sufficient colloidal stabilization need to be found [13]. In many cases, organic additives like surfactants, polymers, or small molecules are used to influence the size and shape of the forming nanoparticles and improve their colloidal stability in the targeted formulation [14–17]. However, in view of actual applications, these additives often have the disadvantage of high costs related to their synthesis or purification, possible contamination of the environment (since the additive can be released from the nanoparticle at some point), and/or the fact that controlled nanoparticle formation only occurs under particular conditions [18]. Given these limitations, robust methods based on self-organizing simple and harmless components at mild conditions appear highly desirable.

In this context, one particularly interesting but rather rarely considered case is the inorganic-inorganic route to self-assembled nanostructures, most notably the spontaneous stabilization of nanoparticles by silica. Indeed, there is a vast body of literature on coating various types of nanomaterials with silica to improve stability and achieve other beneficial effects [19–23]. However, instead of depositing a silica shell around preformed nanoparticles in a secondary step, silicate species dissolved in aqueous solutions can also be used as primary "capping agents" to preserve growing particles at nanometric dimensions by chemically coupled coprecipitation [24,25]. For this dynamic spontaneous process to occur, the material in question needs to show inverse trends in solubility as a function of pH compared to silica, and its constituent ions (or molecules) should exist in a partially protonated state under the chosen synthesis conditions [26]. One prominent example meeting these criteria is the precipitation of alkaline-earth metal cations ($M^{2+} = Ca^{2+}$ or Ba^{2+}) with carbonate anions from water at moderately alkaline pH levels in a typical range of 9-11 [27,28], which can be written as follows:

$$HCO_3^- \rightleftharpoons CO_3^{2-} + \mathbf{H}^+ \xrightarrow{M^{2+}} MCO_3 \downarrow \qquad \text{(III-1)}$$

The release of protons ($\mathbf{H}^+$) caused by re-establishment of the carbonate/bicarbonate equilibrium results in a decrease of the local pH near growing metal carbonate surfaces, which in turn triggers polycondensation of dissolved silicate species according to:

$$-Si-O^- + \mathbf{H}^+ \rightleftharpoons -Si-OH + HO-Si \xrightarrow{-H_2O} -Si-O-Si-\rightarrow\rightarrow "SiO_2" \downarrow \qquad \text{(III-2)}$$

The complete TEOS hydrolysis and condensation reactions can be found in **Chapter II**. This pH-based coupling of the chemistries of carbonate and silicate eventually leads to spontaneous coating of MCO_3 particles with SiO_2 shells, as illustrated by **Figure III-2**. The response of silicate species to changes in the local microenvironment around forming carbonate particles has three important consequences: first, growth of the cores is arrested soon after nucleation, such that nanoparticles of tunable sizes are obtained; second, local polycondensation yields continuous layers of amorphous silica around the carbonate cores in the same step, with thicknesses that can likewise be readily tuned by proper choice of the bulk silicate concentration and/or the pH of the solution; third the surface energy of the formed nanodots is minimized stabilizing them at very small sizes [27–29].

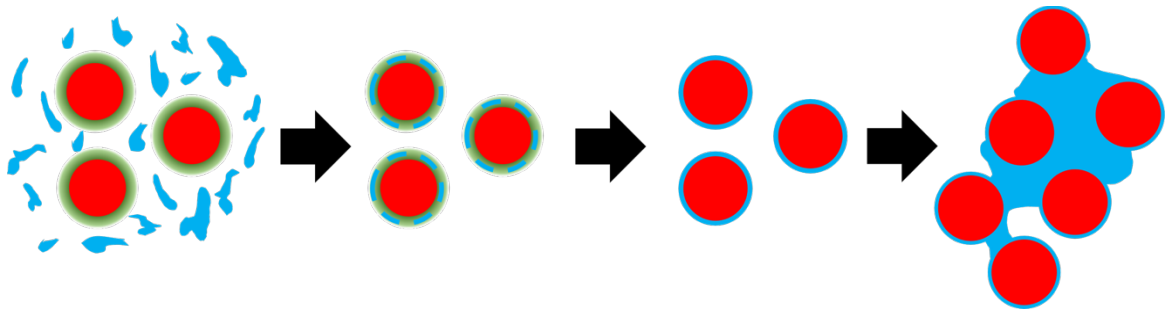


Figure III-2. Spontaneous coating of metal carbonate particles (red circles) with shells of amorphous silica (blue rims) as a consequence of local pH gradients (green halos) in alkaline solutions, caused by bicarbonate dissociation and triggering polycondensation of dissolved silicate species (blue shreds) in the immediate vicinity of growing particles. Redrawn according to the concept introduced in ref [27].

In the case of alkaline-earth metal carbonates, this concept of spontaneous stabilization of nanodots by a coprecipitation of both the core and the stabilizing silica shell could readily be realized by simple mixing of calcium or barium chloride solutions (at typical concentrations of 10 mM) with alkaline sols containing sodium silicate. At silicate concentrations of up to

33.3 mM in the final mixture, nanoparticles of amorphous $CaCO_3$ cores with typical sizes of 30-150 nm and silica shells with thicknesses in the range of 2-10 nm were obtained [27], whereas SiO_2-$BaCO_3$-SiO_2 core-shell-shell structures formed when barium cations were used under similar conditions [28]. Subsequent studies performed at higher silicate concentrations (≥50 mM as SiO_2) have further shown that $CaCO_3$ clusters of only a few nanometers in diameter could be stabilized by the same approach [29], confirming the notion that silica can effectively capture the earliest precursors of inorganic crystallization processes.

Regarding the model of chemically coupled spontaneous coprecipitation described above, there is no apparent reason why the underlying interactions should be limited to alkaline-earth metal cations. Likewise, anions other than carbonate may engage in chemical coupling with silicate, provided that they exist at least partially in a protonated state under the chosen conditions. Indeed, both of these hypotheses have been sustained by the results of a recent study, in which silica-coated cadmium sulfide (as well as zinc sulfide and cadmium selenide) quantum dots were successfully synthesized by coprecipitation from aqueous solutions at ambient temperature [30]. In this case, the reaction leading to nucleation and growth of the metal sulfide cores can be written as:

$$HS^- \rightleftharpoons S^{2-} + \mathbf{H}^+ \xrightarrow{M^{2+}} MS\downarrow \qquad \text{(III-3)}$$

Building upon these findings, the goal of the present work was to test the generality of the concept and extend the range of nanoparticles accessible via spontaneous stabilization with silica by self-assembly. To this end, various transition metal salts were precipitated with carbonate or sulfide in the presence of silicate, and the outcome of the reaction was characterized using transmission electron microscopy (TEM). It will be shown that despite the simplicity of the approach, well-defined metal carbonate and sulfide particles with diameters of less than 5 nm (hereinafter referred to as "nanodots") can be obtained and, in the case of carbonates, converted into corresponding oxides by secondary thermal treatment. Overall, the described procedures devise a straightforward and sustainable strategy towards the synthesis of functional nanomaterials with potential for applications in the areas of catalysis, biomedicine, and beyond.

3.3 Experimental

3.3.1 Materials

The following substances were used as received without further purification:
ammonium carbonate ($(NH_4)_2CO_3$; AppliChem, analytical grade), ammonium chloride (NH_4Cl, Merck, ≥98 %), 28 % ammonium hydroxide solution (NH_3 in H_2O, Merck, ≥99.99 %), cadmium chloride ($CdCl_2$; Sigma-Aldrich, 99.99 %), cobalt chloridehexahydrate ($CoCl_2 \cdot 6H_2O$; Sigma-Aldrich, 98 %), copper chloride dihydrate ($CuCl_2 \cdot 2H_2O$; Riedel-de Haën, ≥99 %), glycerol ($C_3H_8O_3$, Fisher, ≥98 %), glycine ($C_2H_5NO_2$, Sigma-Aldrich, ≥98 %), guanidnium hydrochloride (CH_6N_3Cl, Sigma-Aldrich, ≥98 %),hydrochloric acid (32 % HCl in water; Sigma-Aldrich, analytical grade), lithium metasilicate (Li_2SiO_3, TCI Chemicals, ≥98 %), 20 % lithium polisilicate solution ($Li_2Si_5O_{11}$, Sigma-Aldrich, ≥98 %), manganese chloride tetrahydrate ($MnCl_2 \cdot 4H_2O$; Sigma-Aldrich, ≥99 %), nickel chloride hexahydrate ($NiCl_2 \cdot 6H_2O$; Merck, ≥98 %), potassium chloride (KCl, Carl Roth, ≥98 %), sodium carbonate (Na_2CO_3; Riedel-de Haën, ≥99.8 %), sodium chloride (NaCl; Carl Roth, ≥99.8 %), sodium hexametaphosphate (SHMP, $Na_6(PO_3)_6$, sodium hydrogenphosphate ($NaHPO_4$, Merck, ≥99 %), sodium hydroxide (NaOH; Sigma-Aldrich, ≥98 %), sodium iodide (NaI, Sigma-Aldrich, ≥98 %), sodium silicate solution ("water glass", containing 27 % SiO_2 and 14 % NaOH; Sigma-Aldrich, reagent grade), sodium sulfate (Na_2SO_4, Merck, ≥99 %), sodium sulfide trihydrate ($Na_2S \cdot 3H_2O$; VWR International, analytical grade), sodium thiocyanate (NaSCN, Sigma-Aldrich, ≥98 %), tetraethyl orthosilicate (TEOS; Sigma-Aldrich, 98 %), trehalose dihydrat ($C_{12}H_{22}O_{11} \cdot 2H_2O$, Carl Roth, ≥98 %), and zinc chloride ($ZnCl_2$; Merck, ≥98 %).
All solutions and dilutions were prepared using water taken from a Millipore system.

3.3.2 Apparatus

3.3.2.1 Synthesis of Nanoparticles

First, aqueous solutions containing 0-33.3 mM sodium silicate were prepared by diluting commercial sodium silicate solution ("water glass") or hydrolyzing tetraethyl orthosilicate (t = 1h) with ammonia at pH 11, using plastic beakers to avoid potential covalent attachment to the surface of glass vessels by silica condensation reactions. Then, 10–20 mM of sodium sulfide, sodium carbonate, or ammonium carbonate were dissolved in the silicate solution. To 50 mL of the resulting mixtures, the same volume of a solution of divalent transition metal

chloride was quickly added under vigorous stirring (600 rpm) at room temperature. The amounts of transition metal (M) cation and sulfide or carbonate were chosen to be equimolar, while the silicate content was varied. Typical final concentrations thus were 5-10 mM MS/MCO_3 and 0-30 mM SiO_2. Immediately after mixing, colored suspensions of more or less finely dispersed precipitates were obtained. After stirring for 5 min, the formed particles were separated from dissolved salt (mainly NaCl or NH4Cl) by centrifugation in a Sigma 3-18KS centrifuge at 4700 rpm (4248 g) for 5 min at room temperature. Unless separation was not possible under these conditions, a few drops of 5 M sodium chloride solution were added before centrifugation. The sedimented material was washed three times with water to further remove any residues of sodium/ammonium chloride unreacted residues. Finally, the purified particles were re-dispersed in water using an ultrasonic processor (Hielscher UP200Ht). To convert the as-formed silica-coated transition metal carbonates into oxides, corresponding dispersions were lyophilized to obtain a dry powder, which was calcined in a Thermicon T oven from Heraeus under atmospheric pressure. The following calcination temperatures and times were applied, following procedures described in the literature [31–35]: $CdCO_3$ – 500 °C for 2 h, $CoCO_3$ – 500 °C for 3 h, $CuCO_3$–400 °C for 2 h, $MnCO_3$ – 400 °C for 4 h, $NiCO_3$ – 500 °C for 2 h, $ZnCO_3$ – 600 °C for 2 h.

3.3.2.2 Variation of Synthesis Parameters

3.3.2.2.1 Variation of the Silica Source

For experiments with differing silica sources, the synthesis of $ZnSxSiO_2$ was carried out as described before with one of the following silica sources used: sodium silicate, TEOS, lithium silicate, lithium polysilicate. The pH of the silica solution was then set to 11 or 12 prior to synthesis. Final concentrations of both silica and zinc sulfide were 5 mM.

3.3.2.2.2 Variation in TEOS Pre-Hydrolysis Time

For differing hydrolysis times, the TEOS solution was hydrolyzed between 1 min and 6 h before the addition of sodium sulfide and pH adjustment. Otherwise, the synthesis was carried out as described above.

3.3.2.2.3 Variation of the Synthesis pH

For differing pH values the pH value of the silica solution was set to the desired pH value (10, 11, 12) after the sulfide addition before combination with the metal chloride solution. As the metal cation would precipitate as hydroxide only the silica solutions pH is set. The final pH value after synthesis is around 0.5-0.7 smaller than the set value.

3.3.2.2.4 Buffering the Synthesis Solutions

A 100 mM glycin buffer, and a 100 mM ammonia buffer were prepared and used instead of water for the silica solution. Again, the pH value was adjusted after the addition of sodium sulfide and immediately before combination with the metal chloride solution.

3.3.2.2.5 Variation of Synthesis Temperature

The hydrolysis of TEOS was carried out as before. Directly before the combination of the individual solutions, both were tempered to the desired temperature (variation between 10 °C and 80 °C).

3.3.2.2.6 Addition of Hofmeister Salts

Salts of differing positions in the Hofmeister series were added to the silica solution prior to synthesis in various differing concentrations ranging from a final concentration of 5 mM to 100 mM.

3.3.2.2.7 Synthesis Using Microfluidics

Two different microfluidic devices with differing flow geometries have been used, a serpentine mixer and a tesla valve mixer. For syntheses using microfluidics the concentration of the individual solutions had to be adjusted to the respective flow rates (0.01 mL/min – 0.1 mL/min). Typically, the silica solution had twice the flow rate of the metal chloride solution and therefore half the concentration. Final concentrations of silica varied between 5 and 15 mM, whereas the final metal sulfide concentration was always 5 mM.

3.3.2.2.8 Particle Workup Using Centrifugation, Dialysis, and Lyophilization

The particles can be fractionated using centrifugation. Therefore, the nanoparticle supensions were filled into 50 mL centrifugal tubes and were centrifuged at differing rotational

speeds / differing centrifugal force (5000g, 10000g, 15000g, 20000g) for 20 mins. Then the supernatant was further analyzed.

When centrifugal filters were used (Pall Macrosep Advance with a MWCO of 3k, 10k, or 30k), 15 mL of the nanoparticle suspension was filled into the filters and placed in the centrifuge for 1h at 3000g. The supernatant and the filtrate were then analyzed separately.

For dialysis, the desired volume of the nanoparticle suspension was filled in a dialysis tube (Servapor 16 mm diameter with a MWCO of 3.5k) and placed in a water reservoir. The water was changed 3 times after 2h each and then the dialysis tube was kept in last reservoir for 18 h.

The lyoprotective agents trehalose/glycerin were added to the nanoparticle suspension before lyophilization in multiples (0.5, 1, 2, 4) of the total silica concentration. The same amount of water was then added to the dry powder to test for redispersibility.

3.3.2.2.9 Addition of Sodium Hexametaphosphate (SHMP)

Equimolar (to silica) amounts of SHMP were first added to the different solutions to evaluate the influence of SHMP on the different synthesis parameters. Afterwards differing concentrations of SHMP in multiples (0.1-3) of the used silica concentration were tested. Therefore, SHMP was present in the silica solution prior to synthesis.

3.3.3 Methods

3.3.3.1 Dynamic Light Scattering (DLS)

Information about the size of the as-formed nanoparticles and their aggregates was obtained by dynamic light scattering measurements. 0.5 mL of the re-dispersed samples were diluted with 2.0 mL water, filtered through 0.45 μm cellulose acetate membranes, and transferred into dust-free cylindrical borosilicate glass cells of 10 mm outer diameter. The sealed DLS tubes were placed in the temperature-controlled toluene bath of a CGS-3 Compact Goniometer System from ALV, which was equipped with an ALV/LSE-5004 Multiple Tau Digital Correlator and a vertically polarized 22 mW He-Ne laser ($\lambda = 632.8$ nm). Measurements were performed at 25 °C and a scattering angle of 90°. The sampling time for sulfide and carbonate nanoparticles was 300 s. As suspensions of oxide nanoparticles were less stable, the sampling time for these systems was reduced to 60 s. From the collected data, the mean intensities of the scattered light and the time-dependent self-correlation functions were determined. Average hydrodynamic diameters of the scattering species were extracted via a second-order cumulant analysis [36]

and the CONTIN algorithm [37,38]. As many of the studied systems showed rather high polydispersity, the derived apparent sizes should be considered as rough estimates of the dimensions of nanostructures occurring in solution.

3.3.3.2 Nanoparticle Tracking Analysis (NTA)

NTA measurements were carried out to further enhance the information about the size distribution of the NPs and clusters. For the measurement, the NP suspension was diluted 1:400 for the typical synthesis, and 1 mL of this diluted sample was filled into a syringe. The samples were injected into the sample chamber of a NanoSight NS300 from Malvern (Malvern, UK) equipped with a 30 mW diode laser ($\lambda = 532$ nm). The syringe was placed higher than the sample chamber to provide a constant flow of the suspension through the chamber. Three measurements for 1 mins each were taken, and the associated software then tracks each particle and determines via their movement the hydrodynamic radius. From the three measurements, the mean size distribution for each particle size with error is created. Note that the particle concentration is selected so that not more than 40 particles are detected simultaneously.

3.3.3.3 Transmission Electron Microscopy (TEM)

To elucidate the nanostructure of the formed precipitates, the obtained dispersions were diluted with water to particle volume densities low enough to enable meaningful TEM analyses. For this purpose, 20 µL dilute sample were placed on copper grids (400 mesh x 62 µm pitch) that were coated with a thin layer of graphite (using a Carbon Coater 208carbon from Cressington) and hydrophilized by treatment in a PDC-3XG plasma cleaner from Harrick Plasma. After soaking for 20 s, excess liquid was removed by blotting with a filter paper. The fixed specimen on the grid was washed with 20 µL water and then dried again by blotting. Finally, the grid was left to dry in a closed Petri dish on a filter paper for at least 24 h, before it was transferred into the electron microscope using a Gatan cryo-holder. TEM studies were performed on a CM12 microscope from FEI/Philips, equipped with a tungsten cathode operating at an accelerating voltage of 120 kV. Images were taken with a TVIPS digital camera and processed using the software EMMenu4. Electron diffraction patterns were carried out, measured on a Tecnai F30 G2 STwin from FEI (300 kV) equipped with an EDX detector (Si/Li, EDAX). ADF-STEM micrographs and EDX elemental mapping were conducted on a probe Cs-corrected JEM-ARM200F NEOARM from JEOL (200 kV) equipped with two front and entry side positioned silicon drift EDX (100 mm2 area each) detectors.

3.3.3.4 Scanning Electron Microscopy / Energy Dispersive X-ray Spectroscopy

Field emission scanning electron microscopy (SEM) images were recorded on a Phenom ProX scanning electron microscope (FEI Company, Hillsboro, OR, US) equipped with an EDX and a backscattering detector. Lyophilized samples were prepared on a sample holder and sputtered with Au/Pd for 30 s (2.45 kV, 22 mA) under an Argon atmosphere using a Polaron E 510 Series II Sputter Coater (Polaron Instruments, London, UK).

3.3.3.5 Fluorescence Spectroscopy

Fluorescence spectra were recorded using a Cary Eclipse Fluorescence spectrometer from Agilent Technologies (Santa Clara, CA, USA). The temperature was held constant at 25°C. Because of the multi-sample holder, reference and sample can be measured simultaneously. The NPs were suspended in water to obtain the sample, and the reference is the corresponding solvent. 3 mL of these suspensions and the respective references were inserted into a quartz glass fluorescence cuvette with a 10 mm path length. To obtain the relevant range of the spectrum, multiple measurements were performed. The excitation filter and the emission filter were adjusted after each measurement to the maximum of the opposite spectrum until the value remained constant. Then the final excitation and emission spectrum can be measured.

To estimate the proportion of defect-induced emission, the photoluminescence spectra were deconvoluted using a bimodal model consisting of a Gaussian component and a log-normal component. The Gaussian component was attributed to emission near the band edge, while the asymmetric component described by the log-normal function was attributed to the long-wavelength region of defect-induced (trap state) emission, which is consistent with previous reports on CdS- and ZnS-based quantum dots [39–43]. The fraction of DE (f_D) was then calculated from the integrated area of the defect-related contribution ($\int I_D(\lambda)d\lambda$) relative to the total emission ($\int I_{BE}(\lambda)d\lambda + \int I_D(\lambda)d\lambda$):

$$f_D = \frac{\int I_{defect}(\lambda)d\lambda}{\int I_{BE}(\lambda)d\lambda + \int I_D(\lambda)d\lambda} \quad \text{(III-4)}$$

3.3.3.6 UV/Vis Spectroscopy

Absorption of UV/Vis light (700-200 nm) by selected nanoparticle dispersions (CdS/SiO_2 and CuS/SiO_2) was measured using a Lambda 18 UV/Vis Spectrometer from Perkin-Elmer, after

dilution with water to suitable optical densities in cells of 10 mm path length. From the acquired spectra, the wavelength at the onset of significant light absorption was determined and converted into mean radii of the nanoparticle cores using the Brus equation [44,45]. The required values for the band gap energy of the semiconductors, as well as the effective masses of their excited electrons and holes, were taken from the literature [42,46].

3.3.3.7 Data Availability

Additional data, fit parameters, and associated scripts are available in the online repository (Novel nanoparticle synthesis in self-organizing water–based systems - online repository, 10.5283/epub.80300). Representative data and fits are shown in the SI.

3.4 Results

3.4.1 Coprecipitation of Various Transition Metal Sulfides and Carbonates and their Transition into Oxides

The experiments performed in this work were utterly simple: typically, 10 mM aqueous solutions of chloride salts of the chosen metal cations were mixed in equal volumes with a solution containing the same molar amount of the anion in question, i.e., carbonate or sulfide as their sodium or ammonium salts. To the latter solution, varying concentrations of sodium silicate were added, as obtained by

(i) dilution of conventional sodium silicate solution ("water glass"),

(ii) dissolution of sodium metasilicate, or

(iii) prior hydrolysis of tetraethyl orthosilicate (TEOS) with ammonia.

Whereas solutions containing sodium meta silicate were the easiest to prepare, the hydrolysis of TEOS with constant hydrolysis times led to the best reproducibility. First experiments were done using sodium metasilicate due to the simplicity of the synthesis process. All the structures shown below can be obtained regardless of which silica source is used. The pH established after mixing of the reagents was either left unadjusted or set to 9.0 or 11.0 by dosing aliquots of HCl or NaOH (in order to test the influence of pH on colloidal stability). The effect of added silica on the precipitation of metal carbonates and sulfides from water at ambient conditions becomes evident already from the visual appearance of samples, as illustrated in **Figure III-3** for the case of cobalt carbonate obtained from $CoCl_2$ and NH_4CO_3. In the absence of silica and at low concentrations (e.g., 0.83 mM SiO_2 after mixing), relatively large solid particles are nucleated and aggregate to form a flocculated material that sediments to the bottom of the sample container. The color of this material varies as a function of silica concentration and pH, arguably due to a change in primary particle size. By contrast, at final SiO_2 contents of ≥5 mM (pH 9.0) or respectively ≥2.5 mM (pH 11.0), no visual precipitation occurs anymore, and homogeneous solutions with a slight violet color are obtained. This suggests that small nanoparticles of $CoCO_3$ have formed and remain finely dispersed in their mother medium due to the stabilizing influence of silicate.

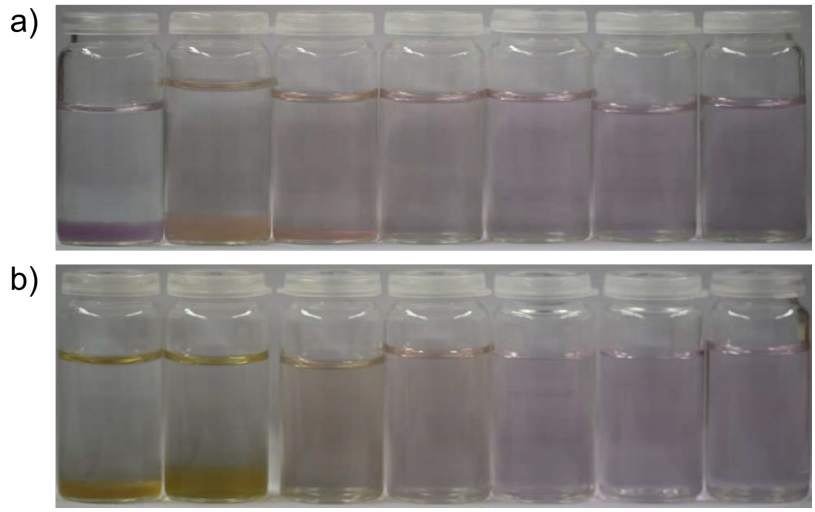


Figure III-3. Photographs of samples obtained by mixing equal volumes of 10 mM solutions of $CoCl_2$ and $(NH_4)_2CO_3$, with the latter containing different amounts of dissolved sodium silicate (from left to right): 0, 0.83, 4.99, 11.65, 16.64, 24.97, and 33.29 mM SiO_2. The pH was adjusted to (a) 9.0 and (b) 11.0 after mixing by addition of HCl and NaOH.

Analyses of the size of the species present in the colloidally stable systems by means of dynamic light scattering (DLS) indicate the formation of primary particles with diameters of less than 10 nm, which coexist with a certain fraction of larger entities (typically up to 100 nm; cf. **Table SIII-1**). The measured sizes of the primary particles and their secondary aggregates do not show clear systematic trends with pH and/or silicate concentration, probably as a consequence of different, partly opposing effects: higher levels of pH will increase the supersaturation of the solutions with respect to metal carbonate formation (potentially leading to larger particles), but also enhance the degree of charges at siliceous species [47], which should impede particle aggregation due to electrostatic repulsion. However, the latter effect may also be mitigated or even reversed by association and bridging of free divalent cations. On the other hand, higher silicate concentrations should be more effective at capturing $CoCO_3$ cores at small sizes, but will also favor particle aggregation through polycondensation (which again depends intimately on the pH value).

Further insights into the nature of the formed particles can be gained by TEM analyses, as shown in **Figure III-4** for $CoCO_3$ precipitated in the presence of 10 mM SiO_2 and isolated from the aqueous mother solution by centrifugation. At this point, it is important to note that the aforementioned ability of divalent metal cations to trigger silica polycondensation by charge screening [47] can lead to the formation of nanosized colloidal species consisting of amorphous silica with some coordinated metal cations but no explicit metal carbonate (or sulfide) components. An example of these colloidal silica structures observed during precipitation of

$CdCO_3$ from silicate-containing solution is shown in **Figure III-4a**. Indeed, such byproducts of the reaction were occasionally found in all the investigated samples, but their amounts relative to metal carbonate (or sulfide) bearing structures were generally low. Even though the dimensions of the latter are similar to the condensed siliceous networks, they can clearly be distinguished based on morphology and texture, as shown by **Figure III-4b**.

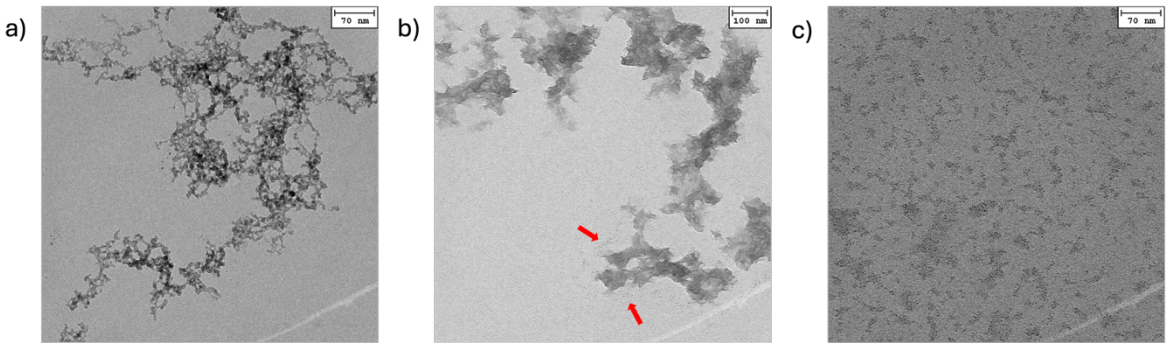


Figure III-4. TEM micrographs of typical reaction products obtained from mixtures containing 10 mM each of $CoCl_2$, Na_2CO_3 and SiO_2 at native pH. (a) Colloidal aggregates formed by cation-induced condensation of silicate species. (b) Structures of diffuse silica matrix with multiple embedded nanodots. (c) Numerous $CoCO_3$ nanodots (dark spots), partially embedded in diffuse silica matrices (areas of lower contrast), typically found in the near vicinity of the structure shown in **(b),** indicated by the red arrows. Scale bars: 70 nm and 100 nm, respectively.

In such images, nanodots of, arguably, $CoCO_3$ can clearly be discerned and are found to be embedded in cloud-like domains of lower electron contrast, arguably silica matrices, which interconnect multiple individual cores. In fact, the two types of structure shown in **Figure III-4a** and **Figure III-4b** can also exist in mixed forms, for example colloidal silica aggregates with attached and/or occluded metal carbonate nanodots. The third type of structure, visible in **Figure III-4c**, resembles less aggregated/fused particles shown in **Figure III-4b**. The nanodots of $CoCO_3$ and the surrounding silica matrix are clearly visible and distinguishable. These particles are usually found in the near vicinity of the structure shown in **Figure III-4b** (indicated by the red arrows) and form cloud-like shapes around them (cf. **Figure SIII-2**).

Imaging nanodot-rich structures as those in **Figure III-4b** by annular dark-field scanning transmission electron microscopy (ADF-STEM, **Figure III-5**) reveals extended networks (likely formed by forced aggregation upon centrifugation), which appear to consist of a continuous matrix of amorphous silica with multiple embedded $CoCO_3$ cores (**Figure III-5a**). This but cannot be proven directly as the small particles are destroyed during STEM measurement with high resolution, or respectively are contaminated by carbon impurities during EDX mapping. Individual cores can be discerned at the edges and in the middle of the

agglomerates with sizes of a few nanometers, in good agreement with the DLS data (cf. **Table SIII-1**).

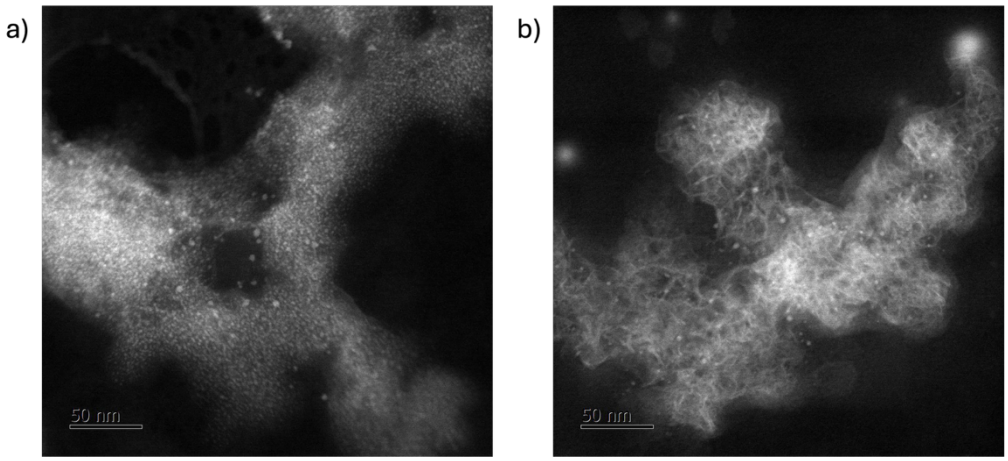


Figure III-5. ADF-STEM micrographs of nanostructures obtained by mixing equal volumes of 10 mM solutions of $CoCl_2$ and Na_2CO_3, with the latter containing 5 mM SiO_2 at native pH of 10.35. Scale bars: 50 nm.

Interestingly, the ADF-STEM analyses also reveal the occasional formation of another type of structure, consisting of a network of plate-like particles along with randomly distributed nanodots (**Figure III-5b**). This suggests that in some cases, the stabilization of nanodots by silica is insufficient and allows partial $CoCO_3$ crystallization to occur. For both types of structure, the presence of cobalt and carbonate, along with silica, is confirmed by EDX (energy–dispersive X–ray spectroscopy) elemental mapping (see **Figure SIII-3**).

Based on the observations made for $CoCO_3$ as a function of pH and silicate concentration (cf. **Figure III-3**), a screening of different transition metal cations was performed at fixed conditions of 10 mM metal chloride, 10 mM sodium carbonate, and 10 mM sodium silicate at the respective native pH. Representative TEM images of samples prepared by direct blotting of diluted aqueous solutions on carbon-filmed copper grids are summarized in **Figure III-6**. It is evident that cores with high electron contrast and diameters below 10 nm were formed with all metal cations investigated. Interestingly, the degree of aggregation can be classified into three groups, where the nanoparticles exist

(i) mostly separated from one another with low affinity to aggregate (Co^{2+} ($pK_A = 9.7$) and Mn^{2+} ($pK_A = 10.6$)),

(ii) as loose agglomerates in which individual particles retain certain mutual distances (Cd^{2+} ($pK_A = 10.1$) and Zn^{2+} ($pK_A = 9.0$)), or

(iii) embedded in a matrix of silica that encompasses multiple cores (Cu^{2+} (pK_A = 7.5) and Ni^{2+} (pK_A = 9.8)).

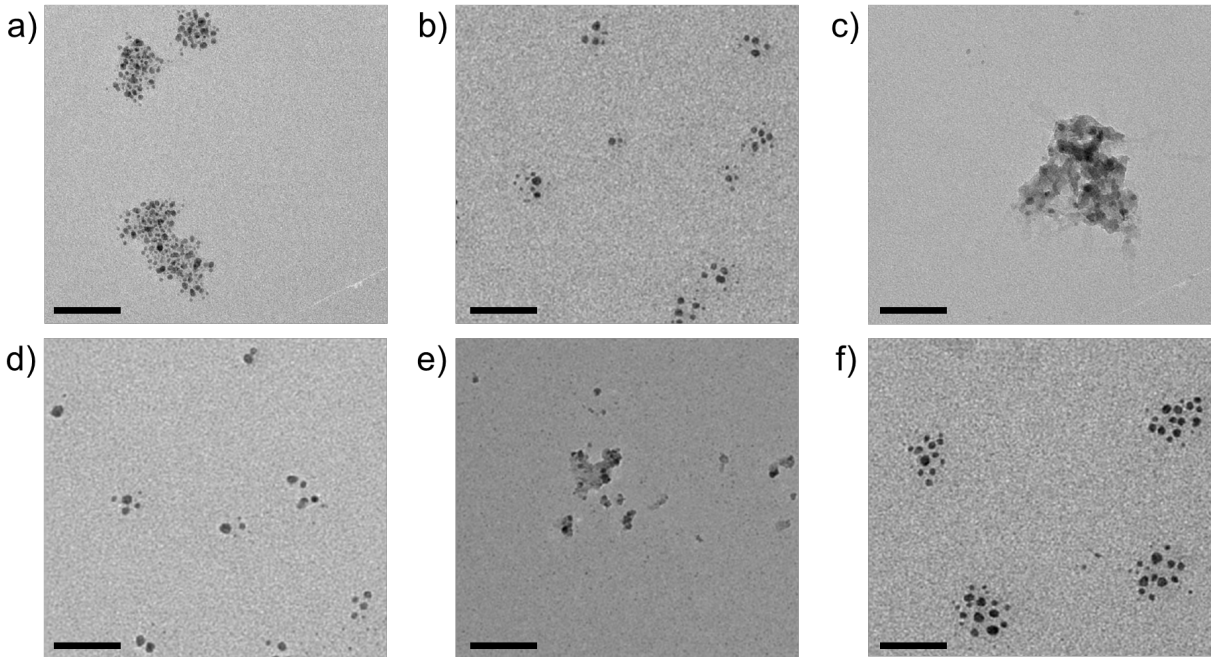


Figure III-6. TEM micrographs of silica-coated nanoparticles of a) $CdCO_3$, b) $CoCO_3$, c) $CuCO_3$, d) $MnCO_3$, e) $NiCO_3$, and f) $ZnCO_3$, obtained by spontaneous coprecipitation from solutions containing 10 mM each of metal chloride, Na_2CO_3, and sodium silicate, at the respective native pH of around 10.5. Scale bars: 50 nm.

The influence of metal cations on the degree of silica polycondensation around nucleated and growing metal carbonate nanoparticles should depend on

(i) the concentration of cations remaining in solution after initial nanoparticle formation and

(ii) their affinity to bind to silicate species and catalyze condensation via charge screening and bridging.

The latter effect may be expected to scale with cation acidity; however, there is no clear relationship between the reported pK_A values (as given above [48]) and the observed aggregation behavior, likely due to a convolution of cation properties and concentration. The amount of residual dissolved cations after nucleation is, in turn, difficult to estimate. One possible approach would be to use the solubility products; however, reported solubilities for the respective bulk mineral likely do not apply to nanometric particles [49] and per se, the nature of phases formed in the present experiments is not unambiguous. For example, precipitation of Cu^{2+} should result in basic copper carbonate (i.e., $Cu_2CO_3(OH)_2$ instead of $CuCO_3$) under the given conditions [50]. Based on the available data, we can thus only speculate about the actual

composition of the cores and the effects underlying the observed differences in nanoparticle aggregation and silica polycondensation. Nonetheless, it can safely be concluded that the presence of silica during precipitation leads to drastic miniaturization of the formed solid phase, yielding nanodots with typical diameters in the range of 3-20 nm, as measured from TEM images and summarized in **Table III-1**.

Table III-1. Mean diameters (d) determined from TEM micrographs like those shown in **Figure III-6**, **Figure III-7**, and **Figure III-8** for silica-stabilized nanoparticles of different metal cations with different anions. Carbonate and sulfide samples were obtained via spontaneous coprecipitation from solutions containing 10 mM each of metal chloride, sodium silicate, and sodium carbonate or sodium sulfide. Oxide particles were formed upon calcination of their carbonate counterparts. For each system, a statistically relevant number (n) of nanoparticles was analyzed, giving reliable mean diameters with corresponding standard deviations. Note that calcination leads to a decrease in the average size, with relative changes ranging from 12 (Cu^{2+}) to 47 % (Zn^{2+}).

Metal cation	d(CO_3^{2-}) [nm]	d(O^{2-}) [nm]	d(S^{2-}) [nm]
Cd^{2+}	4.8 ± 1.1 (n = 90)	3.5 ± 0.9 (n = 55)	5.3 ± 2.2 (n = 68)
Co^{2+}	4.1 ± 1.2 (n = 140)	2.8 ± 0.7 (n = 70)	4.4 ± 1.5 (n = 47)
Cu^{2+}	4.8 ± 1.1 (n = 10)	4.3 ± 1.4 (n = 86)	5.5 ± 1.3 (n = 29)
Mn^{2+}	5.7 ± 1.7 (n = 70)	3.7 ± 1.0 (n = 230)	4.5 ± 1.7 (n = 40)
Ni^{2+}	4.4 ± 1.1 (n = 21)	2.9 ± 0.7 (n = 107)	4.7 ± 1.0 (n = 45)
Zn^{2+}	4.7 ± 1.4 (n = 90)	2.5 ± 0.5 (n = 133)	3.3 ± 0.7 (n = 38)

In a subsequent step, the carbonate (and/or hydroxocarbonate) particles obtained via mixing of metal chloride and sodium carbonate/silicate solutions were calcined according to procedures described in the literature for the respective (hydroxo)carbonate phases [31–35], in order to convert the cores of the nanodots into (catalysis-relevant) oxides. **Figure III-7** provides an overview of representative TEM micrographs showing typical nanostructures resulting from the thermal treatment. Nanodots were observed after calcination for all metal cations investigated, yet again with different degrees of aggregation and silica-mediated crosslinking. Here, well-dispersed individual nanoparticles occur for oxides derived from $NiCO_3$, $ZnCO_3$, and (to a lesser extent) $CdCO_3$. At the same time, loose agglomerates of multiple cores characterize samples obtained via calcination of $CuCO_3$ and $MnCO_3$, and the most pronounced embedding in remaining silica matrices is observed for $CoCO_3$. As expected, the average core size decreases upon calcination, with relative degrees of shrinkage (due to decarboxylation and/or dehydration) ranging from 12 to 47 % (cf. **Table III-1**).

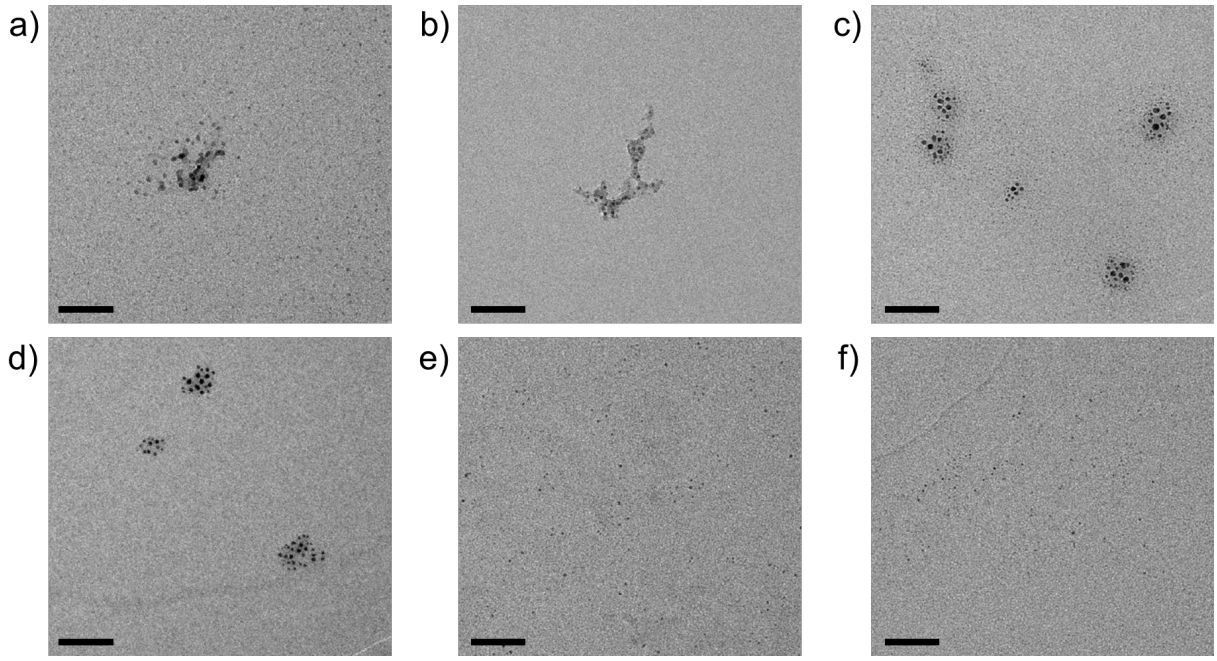


Figure III-7. TEM micrographs of oxide nanoparticles obtained by calcination of silica-coated precursors of a) $CdCO_3$, b) $CoCO_3$, c) $CuCO_3$, d) $MnCO_3$, e) $NiCO_3$, and f) $ZnCO_3$, as shown in **Figure III-6**. Note that numerous individual nanodots can be observed across the entire fields of view in (e) and (f). Scale bars: 50 nm.

As in the case of the carbonate precursor systems (cf. **Figure III-5**), stabilization by silica proved to be sufficient to protect most of the nanodots against strong agglomeration and/or crystallization, but failed in singular instances, as shown for the product of $CoCO_3$ calcination by **Figure SIII-4**. Indeed, TEM and ADF-STEM analyses reveal the local formation of cobalt oxide crystals with sizes in the range of 100-200 nm. Their crystallinity could be confirmed by electron diffraction (**Figure SIII-5**). Although such recrystallization events were generally scarce and only occurred upon ageing in air, further studies will have to be performed to improve the robustness of the process.

The approach described above for metal carbonates can be used in complete analogy to prepare fairly well-defined nanostructures of metal sulfides, as illustrated in **Figure III-8**. While the size of the formed cores is comparable to the corresponding (hydroxo)carbonates (as determined from TEM images, cf. Table 1, and confirmed by UV-Vis measurements, see **Figure SIII-6**), the aggregation behavior again shows interesting differences. For CdS, CoS, CuS, and MnS, multiple primary nanodots assembled into larger secondary structures (typically 20-50 nm in diameter), with morphologies and aggregation numbers that are quite uniform for a given metal cation but differ significantly from cation to cation. In all of these cases, individual cores maintain certain distances from one another within the aggregates and seem to be interspersed by a matrix of lower electron density, most likely

consisting of amorphous silica. The "cloud-like" appearance of these secondary structures suggests a self-limiting aggregation process, driven and arrested by the amount of residual free metal cations and their influence on local silica polycondensation.

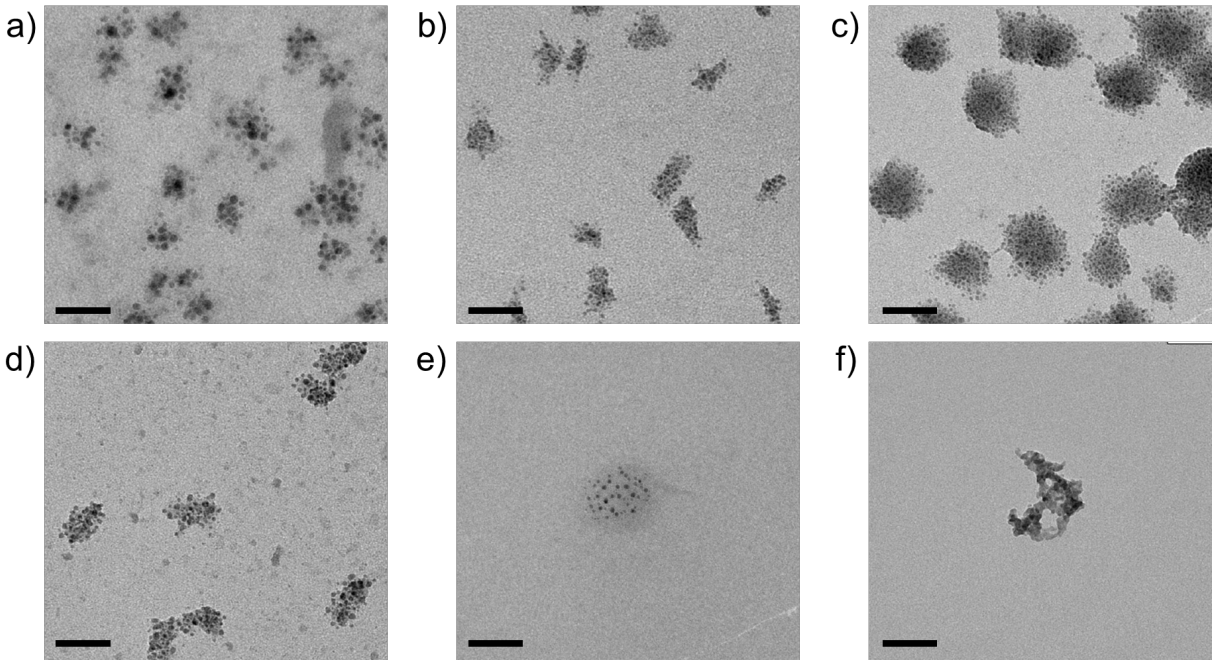


Figure III-8. TEM micrographs of silica-coated nanoparticles of a) CdS, b) CoS, c) CuS, d) MnS, e) NiS, and f) ZnS, obtained by spontaneous coprecipitation from solutions containing 10 mM each of metal chloride, Na_2S, and sodium silicate, at the respective native pH. Scale bars: 50 nm.

3.4.2 Influence on the Formed Particles by Synthesis Parameter Variation and Addition of Small Molecules

3.4.2.1 Variation of the Silica Source

Given their specific applications, the following study will focus on zinc and cadmium sulfides (bioimaging/fluorescence, cf. online repository) and iron sulfides (catalysis, cf. **Chapter IV**). First, it was examined how different silicate sources influence the size and optical properties of co-precipitated $ZnSxSiO_2$ nanoparticles. In addition to a molecular precursor (TEOS, details on hydrolysis and condensation reactions can be found in **Chapter II**), short-chain sodium/lithium metasilicates (NaSi, LiSi), and oligomeric lithium polysilicate (LiPol) were investigated. If only the average values of the hydrodynamic radii are compared, all silicate sources appear to result in similar secondary cluster sizes. (cf. **Figure III-9a**) However, upon closer examination of the distributions (cf. **Figure SIII-11a**), a broader distribution is observed for LiPol, while the other samples yield size distributions that are virtually identical. The pH value also appears to have little effect on the secondary cluster size in this unoptimized synthesis. The most significant difference is observed in the concentration of the resulting particles, which is higher in samples derived from LiSi and LiPol when compared directly.

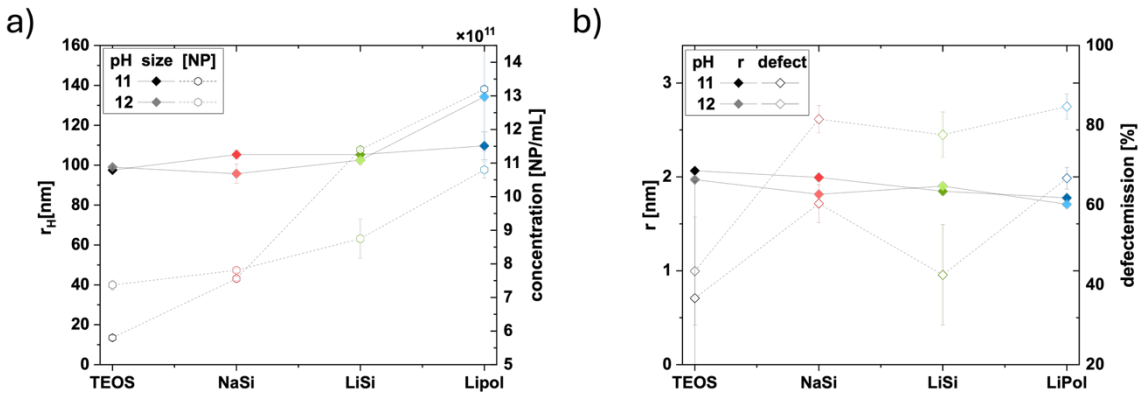


Figure III-9. (a) Hydrodynamic radius and concentration for $ZnSxSiO_2$ particles derived from mixtures with [Si]/[Zn] = 1, but differing in silica source and synthesis pH. Shown values are averages of multiple measurements to highlight trends. The more detailed NTA derived size distributions can be found in **Figure SIII-11a**. (b) QD radius derived from calculation using the Brus equation and DE determined by fitting the emission tail of the transformed emission spectra (cf. **Figure SIII-11b**).

Based on the fluorescence properties (cf. **Figure SIII-11b**), a comparison can be made of the sizes of the primary particles and their passivation. Starting with TEOS, through NaSi and LiSi, and ending with LiPol, the excitation wavelength decreases, and so does the QDs size

determined by the Brus equation. (cf. **Figure III-9b**) At the same time, there has been a noticeable increase in the proportion of DE. While the pH value had little effect on the particle size, DE was significantly higher for samples synthesized at a pH value of 12.

The increased DE observed for samples at higher pH values is a direct result of the degree of coupling between the two precipitation reactions. (cf. **Figure SIII-1**) In systems employing partially condensed polysilicate species rather than molecular TEOS, the larger silicate clusters exhibit reduced diffusivity and reduced accessibility to the particle surface, which can hinder homogeneous shell formation [51–53]. At elevated particle number concentrations, the substantially increased total surface area further amplifies this effect, promoting incomplete surface coverage and locally insufficient passivation. As a consequence, a higher density of interfacial trap states and structural defects is generated, resulting in enhanced DE [39,41].

Based on these results, TEOS was selected as the silicate source for further experiments. Nevertheless, the question arose as to how long pre-hydrolysis is beneficial and at what point excessive condensation might lead to poorer surface passivation.

Generally, increasing hydrolysis times (up to 6 hours) increases the size and size distribution of the secondary clusters, after an initial decrease for low hydrolysis times. (cf. **Figure SIII-13**) Only after sufficient hydrolysis can QDs be captured sufficiently. To determine the optimal pre-hydrolysis time, the fluorescence behavior of $ZnSxSiO_2$ synthesized at differing hydrolysis times (< 2 h) was investigated. (cf. **Figure SIII-12a**) A slight size increase of the primary QDs can be observed. (cf. **Figure III-10**)

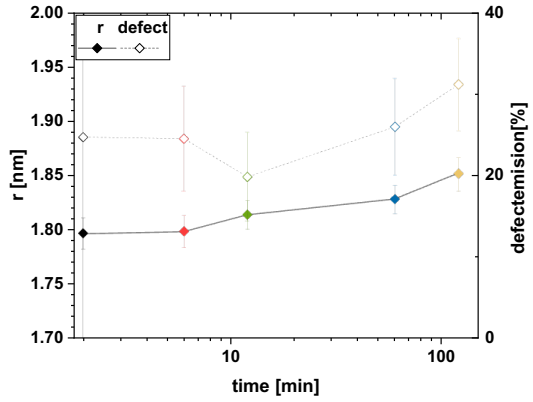


Figure III-10. QD radius derived from calculation using the Brus equation and DE determined by fitting the emission tail of the transformed emission spectra (cf. **Figure SIII-12b**).

After a hydrolysis time of 10 mins, a minimum in DE is reached in the observed timeframes. Also, the size between 10 mins and 60 mins remains almost constant. Additionally, the shift of

the emission maximum towards longer wavelengths (cf. **Figure SIII-12a**), while maintaining identical excitation conditions, is consistent with enhanced relaxation through surface- or defect-associated electronic states prior to radiative recombination [39,41]. Prolonged pre-hydrolysis of tetraethyl orthosilicate leads to increased condensation of the silicate species even before the synthesis. The resulting formation of oligomeric/cluster-like structures reduces the mobility and diffusivity of the reactive species [52–54]. This leads to a more incomplete surface passivation and an increased density of interfacial defect states, which manifests as enhanced DE and the red shift of the emission peak.

Therefore, hydrolysis times between 10 mins and 1 h are considered to be the optimum, and all further experiments were conducted with hydrolysis times of 1 h.

3.4.2.2 Effects of the Synthesis pH on Resulting Particles

As previously observed, the synthesis pH significantly influences the size of the secondary clusters. The pH value can be used to influence the equilibrium position and the strength of the coupling in precipitation reactions. Therefore, it was investigated how the pH value and the silicate concentration affect the secondary cluster sizes of both $ZnSxSiO_2$ and $CdSxSiO_2$. (cf. **Figure III-11**)

For both ZnS and CdS, synthesis at pH 11 results in a reduction in the size of the secondary clusters as the silica content increases. At the same time, the concentration of particles increases until a [Si]/[M] ratio of 3, after which it drops slightly again.

In comparison, fewer $ZnSxSiO_2$ particles are generated at pH 10 and pH 12, up to a [Si]/[Zn] ratio of 4, at which point the concentration increases again. Clear size-dependent trends are only partially evident. While the size increases from a [Si]/[Zn] ratio of 1 to 2 at pH 10, it subsequently decreases again as the silicate content rises. At pH 12, the smallest secondary clusters are formed for the lowest silicate content. (cf. **Figure III-11a**)

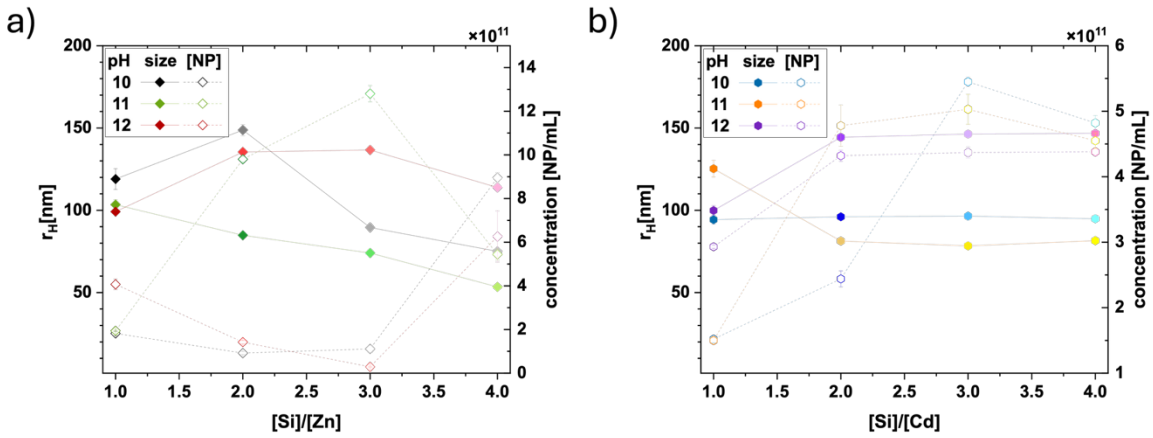


Figure III-11. Hydrodynamic radius and concentration for (a) $ZnSxSiO_2$ and (b) $CdSxSiO_2$ particles derived from mixtures at differing pH values and increasing silica concentrations. Shown values are averages of multiple measurements to highlight trends. The more detailed NTA derived size distributions can be found in **Figure SIII-14a** and **Figure SIII-14b** respectively.

$CdSxSiO_2$ exhibits partly similar trends. However, when synthesized at pH 10, the size of the secondary clusters hardly changes. At pH 12, on the other hand, the size increases at a [Si]/[Cd] ratio of 2 and then remains relatively constant. The concentrations for both, pH 10 and pH 12, increase with increasing silica content. (cf. **Figure III-11b**)

When examining the fluorescence behavior, two things immediately stand out. For $ZnSxSiO_2$, typical spectra can be recorded, (cf. **Figure SIII-16a**) but with a relatively broad emission, which suggests a significant component of DE [39,41]. No typical spectra could be recorded for $CdSxSiO_2$. (cf. **Figure SIII-15a**) This can potentially be attributed to one of two factors. First, the QDs being captured exceed a radius of 6 nm [55,56], or second the fluorescence is effectively quenched by the solvent which would imply unsuccessful silica coating of the QDs [57]. Additional TEM micrographs (cf. online repository) confirm successful coating and the QD size. Hence, a majority of the CdS appears to exceed the size required for quantum-effect-induced fluorescence, possibly due to faster precipitation kinetics of CdS compared to ZnS [58,59].

Both the excitation and emission wavelengths decrease for $ZnSxSiO_2$ with increasing silica concentration for samples derived from pH 10 and 11. (cf. **Figure III-12a**) While for particles derived from pH 12, a decrease in the excitation wavelength is observable, the emission wavelength shifts to slightly higher wavelengths. At the same time, a significantly higher fluorescence intensity is observed in samples derived from pH 10 compared to those derived from pH 11 and 12. (cf. **Figure SIII-16a**)

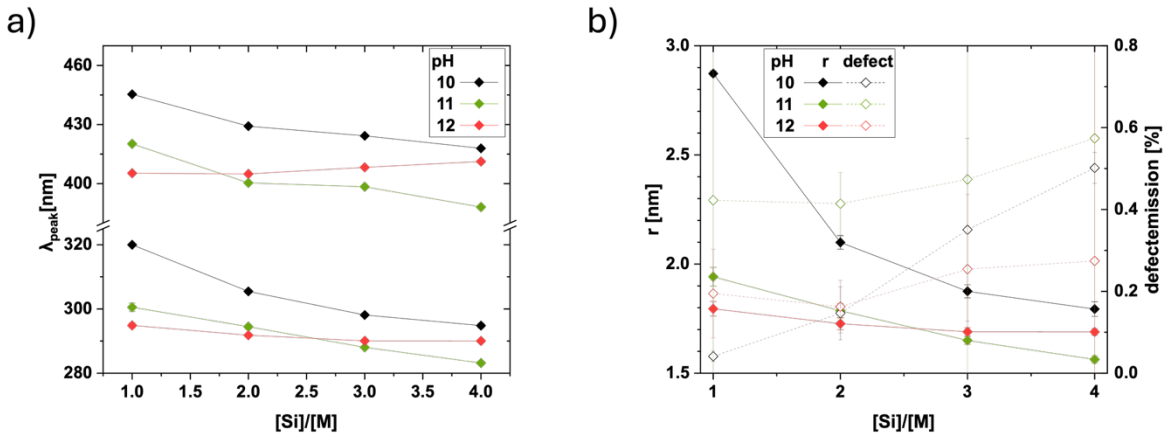


Figure III-12. (a) Emission and excitation peak of fitted fluorescence spectra (cf. **Figure SIII-16a**). (b) QD radius derived from calculation using the Brus equation and DE determined by fitting the emission tail of the transformed emission spectra (cf. **Figure SIII-16b**).

The size of the QDs decreases as the silicate concentration increases, with the most pronounced decrease occurring at pH 10 and the least pronounced at pH 12. At the same time, DE increases with increasing silicate concentration. (cf. **Figure III-12b**)

As the silicate concentration increases, the ZnS nanocrystals are confined by the silicate network at an earlier stage, and further growth is limited. The resulting smaller nanocrystals have a higher proportion of surface and interface atoms, as well as potentially fewer opportunities for defect healing during growth [60,61]. This leads to an increased density of defect states and thus to stronger DE.

The observed pH-dependent intensity decrease may not solely originate from size-dependent effects, but could also reflect the higher local packing density of ZnS nanocrystals within the silica matrix [62]. (cf. online repository) Increased interparticle interactions may promote exciton migration, self-absorption, and quenching processes, thereby reducing the luminescence efficiency [41,43,57].

Overall, at a pH of 11, the smallest, most stable, and most evenly distributed particles are produced compared to the other pH levels. (cf. **Figure SIII-14**) This confirms the expectation that the optimal coupling of the precipitation reactions occurs at this pH. (cf. **Figure SIII-1**) At a pH of 12, metal sulfide can precipitate without requiring HS^- (using S^{2-} instead), thereby preventing/suppressing silica condensation on the surface. At pH 10, the pH drops too quickly, e.g., leaves the optimal range too quickly, so that the existing silica species are no longer able to capture the forming QDs efficiently enough. Therefore, they can grow larger, especially at lower silica concentrations.

3.4.2.3 Various Attempts to Enhance Synthesis Control and Sample Workup

Several optimization strategies were explored to improve control over particle formation and properties, including size, colloidal stability, and surface chemistry. These parameters are also relevant to potential applications, such as catalysis (see **Chapter IV**) or bioimaging (see online repository), although the primary focus remains understanding and controlling the synthesis procedure. These included synthesis with additional buffer systems (cf. **Figure SIII-17**), synthesis in alcoholic mixtures (data not shown, cf. ref [62]), temperature control during synthesis (cf. **Figure SIII-18** and **Figure SIII-19**), addition of Hofmeister ions during synthesis (cf. **Figure SIII-20**), and the use of microfluidic reactors (cf. **Figure SIII-21**). Also, post-synthetic modifications of the formed secondary clusters have been attempted, including reduction of silica shell by HF addition (data not shown, cf. ref [62], see **Chapter IV**), regrowth experiments (data not shown, cf. online repository) and surface modification (data not shown, cf. ref [62] & online repository). In addition, attempts were made to fractionate the synthesized particles by sequential centrifugation (cf. **Figure SIII-22**), improve redispersibility after freeze-drying (cf. **Figure SIII-23**), and purify the particles using dialysis and ultracentrifuge filters (cf. **Figure SIII-24**).

Only the key findings are summarized here. Detailed experimental procedures, datasets and additional characterization results are provided in the Supporting Information and the accompanying online repository.

Further optimizing the coupling of the two precipitation reactions (cf. **Figure SIII-1**), the particle synthesis was carried out in buffered solutions, using a glycine buffer (pKa = 9.60) and an ammonia buffer (pKa = 9.24).

In the buffered solutions at pH 10 and 11, the size of the secondary clusters could be reduced. (cf. **Figure SIII-17a** and b) At pH 12, there was hardly any noticeable effect, probably due to the marginal buffering capacity of the buffer used at this pH value, as well as the suboptimal coupling conditions at this pH value. A significantly reduced concentration is observed for particles originating from glycin buffered solutions. This may be due, on the one hand, to kinetic interference of the buffer (see **Chapter V**) on the other hand, it may also be attributable to the detection threshold of the NTA. (cf. **Figure SIII-17a**)

When TEOS is used as silica source, usually ammonia initially acts as a base catalyst for TEOS hydrolysis. After sulfide addition and pH adjustment, the NH_3/NH_4^+ equilibrium can additionally contribute to the overall buffering capacity of the reaction medium. Together with the HS^-/S^{2-} equilibrium and surface silanol groups, this moderates local pH fluctuations during

metal sulfide precipitation and the subsequent silica condensation process. This way, it was possible to buffer the solutions to maintain the set pH value sufficiently. This enables the beneficial effects of a buffered solution to be achieved without undesirable interactions between the buffer and the forming particles.

Syntheses in aqueous alcoholic solutions have been conducted, inspired by various Stöber syntheses (cf. **Chapter II**) using short-chain alcohols (≤ 4C) with and without the addition of sodium hexametaphosphate (SHMP). (data not shown but can be found in ref [62]) It was demonstrated that the use of alcohols broadens the size distribution and reduces the overall colloidal stability of the formed particles. At the same time, the use of alcohols as solvents reduces the environmental friendliness of the synthesis. Therefore, these pathways were not investigated further.

The temperature dependence of coprecipitation and the effect of temperature on the coupling of precipitation reactions were investigated. The size of the resulting secondary clusters varies but remains within the same order of magnitude, with nearly identical size distributions. (cf. **Figure SIII-18a** and b) With increasing temperature, both the peak emission and excitation wavelengths increase. (cf. **Figure SIII-18c**) The amount of DE increases up to about 40 °C synthesis temperature and then decreases again. (cf. **Figure SIII-18d**) The radius of the formed QDs increases with increasing temperature (cf. **Figure SIII-18f** and **Figure SIII-19**). As the temperature rises, the precipitation reaction accelerates; the primary particles can grow larger before they are trapped, giving them more time to heal defects. At moderate temperatures, they are trapped more quickly and are less able to heal defects, resulting in higher amounts of DEs. Overall, while temperature can influence the reaction, it primarily affects the fluorescence properties. Nevertheless, for potential applications, a synthesis carried out between room temperature and 40°C is likely to be optimal.

The effect of various salts on coprecipitation was investigated. Regardless of their position in the Hofmeister series [63], the added salts primarily caused colloidal destabilization. This occurred already during synthesis, resulting in increased secondary cluster sizes. When sufficiently low concentrations were used to suppress colloidal destabilization, there was no effect on either the secondary cluster size or the primary QD size. (cf. **Figure SIII-20**)

Two different microfluidic [64] chips were used: a serpentine mixer and a mixer in the form of a Tesla valve. (cf. **Figure SIII-21a**, respective SCAD files can be found in the online repository. Various flow rates and concentration variations have been tested. Overall, only a marginal reduction in the size of the secondary clusters, with a slight increase in concentration, was achieved under the best conditions tested, and no effect on fluorescence behavior was observed.

(cf. **Figure SIII-21b-f**) The use of microfluidic reactors complicates the synthesis compared to the simple batch method, with little to no additional control over size/optics.

A post-synthetic reduction of the silica shell is possible by the addition of small amounts of HF. Addition mostly resulted in immediate aggregation and proved to be only of limited use for most possible applications. (cf. ref [62], see **Chapter IV**) The elegance of the one-pot process is transformed into a multi-step process relying on quite toxic chemicals, reducing the environmental friendliness drastically.

Regrowth attempts have been made to increase the shell thickness and enhance the colloidal stability. Even though a size increase of the particles was achievable, seemingly no colloidal stability improvement was achieved.

Multiple attempts have been conducted to increase the colloidal stability of coprecipitated particles, including surface modification during synthesis [62] and post-synthesis (cf. online repository). Differing strategies of surface modification have been tested, including covalently bound silanes and adsorbed polymers. Overall, only a very limited improvement in colloidal stability was achieved, despite a variety of methods confirming surface occupation. Usually, upon transfer to physiological media (physiological salt content), aggregation occurred, while other samples even exhibited generally reduced stability. (cf. online repository)

Using sequential centrifugation enabled limited size separation. The concentration of bigger clusters can be reduced, while no change in the optical behavior is detectable. The found structures remain the same at lower concentrations, indicating the possibility of removing potential byproducts and QD-poor silica clusters.

Addition of lyoprotective agents, such as trehalose and glycerol, was tested to enhance the redispersibility of coprecipitated particles in differing concentrations. Relative to the total amount of silica, at least a [La]/[Si] ratio of 1 is required to quantitatively redisperse the lyophilized particles and maintain the colloidal stability. Similar to results found in literature, glycerol performs overall worse than trehalose [65]. (cf. **Figure SIII-23**)

Attempts were made to purify the particles and narrow the size distribution by extracting fractions using techniques such as dialysis and ultracentrifugation. When dialyzed, the particles lose their colloidal stability due to pH neutralization, loss of surface charge, and therefore reduction of electrostatic repulsion. This results in broader size distributions due to aggregation and redshifts the fluorescence spectra slightly. Filtration, on the other hand, reduces the size distribution but also loses a majority of secondary clusters with embedded QDs, resulting in significantly less photoluminescence (PL) intensity and a simultaneous blueshift (smaller QDs remain). (cf. **Figure SIII-24**)

Overall, the investigated parameter space indicates high robustness of the coupled precipitation process to external perturbations. While certain trends in particle size, shell morphology, and optical properties could be identified, the system shows limited non-generalizable tunability under the applied conditions.

3.4.2.4 Effects of SHMP as an Additive

To prevent the primary shells from coalescing into secondary clusters, the condensation reaction was specifically targeted. One molecule that can effectively control or suppress/delay the TEOS condensation reaction is sodium hexametaphosphate (SHMP) [66–69]. In previous experiments (data not shown), a reduction in the size of the secondary clusters was observed for $CdSxSiO_2$ [62]. Nevertheless, no consideration was given to how the position of the SHMP before synthesis affects the resulting particles. For this reason, syntheses were carried out using SHMP in the metal solution, the silica solution, and both solutions, and were compared to a synthesis without SHMP addition. Again, the synthesis pH values of 10, 11, and 12 were investigated. The synthesis of $ZnSxSiO_2$ in the presence of SHMP reduces the size of the formed secondary clusters in all cases. (cf. **Figure III-13**) While a decrease in particle size is observed as the pH increases in syntheses without SHMP, this trend does not apply to syntheses in which SHMP is added. The size reduction effect is most pronounced when SHMP is present in the metal solution, followed by the silicate solution, and finally, 50/50 in both solutions, before synthesis.

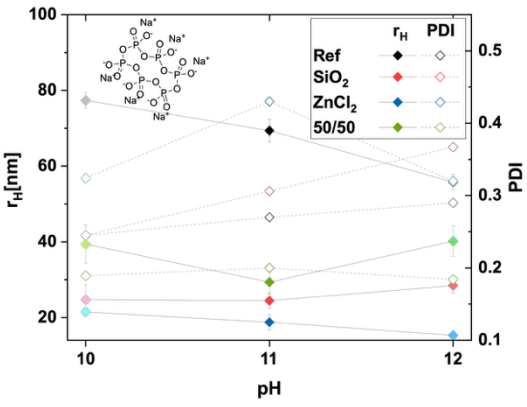


Figure III-13. Hydrodynamic radius and PDI for $ZnSxSiO_2$ particles derived from mixtures with [Si]/[M] = 2, at differing pH values and [SHMP]/[Si] = 2. Shown values are averages of multiple measurements to highlight trends. The more detailed CONTIN [37,38] derived size distributions and the respective correlation functions can be found in **Figure SIII-25**. The structural formula of SHMP is shown in the top left corner.

SHMP slows down the hydrolysis of TEOS by complexing Si species via its multiply negatively charged phosphate groups, thereby inhibiting their spontaneous condensation. At the same time, it stabilizes the resulting silanol intermediates, making the condensation kinetics more controlled and homogeneous. Overall, SHMP leads to finer, better-dispersed silica networks, as it effectively suppresses uncontrolled growth and aggregation [69,70].

When examining the fluorescence behavior (cf. **Figure SIII-26a**), it is evident that in all cases the addition of SHMP redshifts the peak excitation/emission slightly. The effect is more pronounced in the excitation for SHMP in the metal-containing solution and the 50/50 solution. Accordingly, this effect is particularly pronounced when SHMP has time to complex the cation beforehand. Also, the PL intensity increases for particles derived from SHMP containing syntheses. For both SHMP in silica solution and 50/50, a decrease in PL intensity with increasing pH is observable. The reference remains at a constant PL intensity, while the particles from the SHMP-containing silica solution actually exhibit an increase in intensity as the pH rises. (cf. **Figure III-14a**)

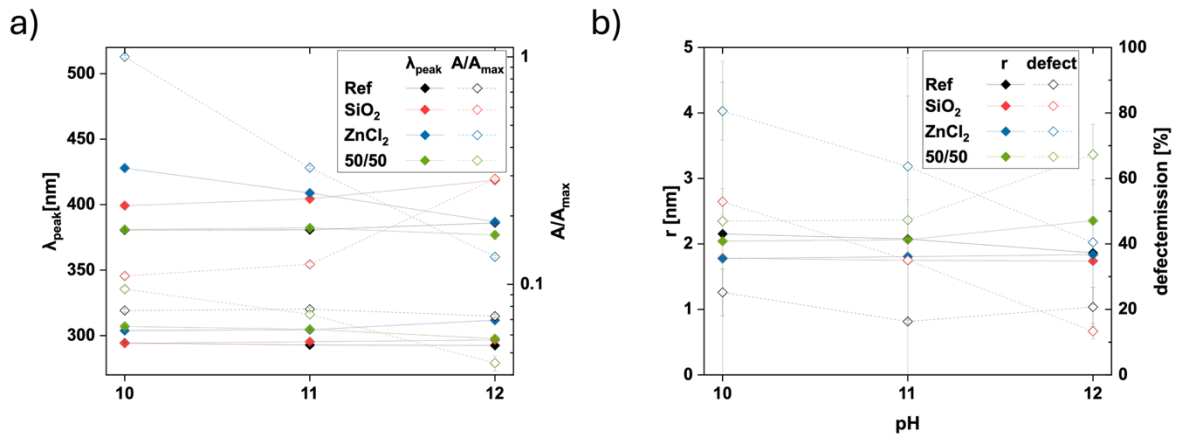


Figure III-14. (a) Emission and excitation peak of fitted fluorescence spectra (cf. **Figure SIII-26a**). (b) QD radius derived from calculation using the Brus equation and DE determined by fitting the emission tail of the transformed emission spectra (cf.**Figure SIII-26b**).

The size of the QDs hardly changes with pH and remains in the same size range. The larger QDs (> 2 nm) are seen for the reference sample and SHMP in a 50/50 mixture, while the smaller QDs (< 2 nm) are exhibited for particles derived from syntheses with SHMP in the silica or metal-containing solution. Particles synthesized in the presence of SHMP exhibit higher DEs. At the same time, however, DE decreases as the pH value increases. (cf. **Figure III-14b**)

SHMP likely adsorbs on the growing ZnS nanocrystal surfaces and acts as a multidentate coordinating species that kinetically hinders growth (cf. **Chapter V**) while simultaneously disrupting surface reconstruction and passivation processes. This leads to kinetically trapped, less-relaxed nanocrystals, in which incomplete defect healing and heterogeneous surface coordination result in an increased density of DE centers despite the reduced particle size [39,41]. This effect seems to be dominating the inhibition of the condensation reaction. Deviations at pH 12 can be attributed primarily to the hydrolysis of SHMP, which can be hydrolyzed under basic conditions, with an increasing hydrolysis rate with increasing pH value [66–68].

Based on this, a screening was conducted to determine the optimal [SHMP]/[Si] ratio for synthesizing the smallest particles with optimal stability and optical properties. Syntheses were made with SHMP in the silica-containing solution to minimize complexation of Zn and maximize the delay in silica condensation.

A synthesis pH value of 12 results in the largest particles. Overall, the size of formed particles increases with increasing [SHMP]/[Si] ratio, especially if [SHMP]/[Si] exceeds a value of 1. Below this value, a size reduction down to 10 nm is possible. The polydispersity index remains between 0.2 and 0.3 and also increases with increasing [SHMP]/[Si] ratio. (cf. **Figure III-15**) The size distributions are similarly narrow and significantly shifted toward smaller radii compared with syntheses without SHMP. (cf. **Figure SIII-30**)

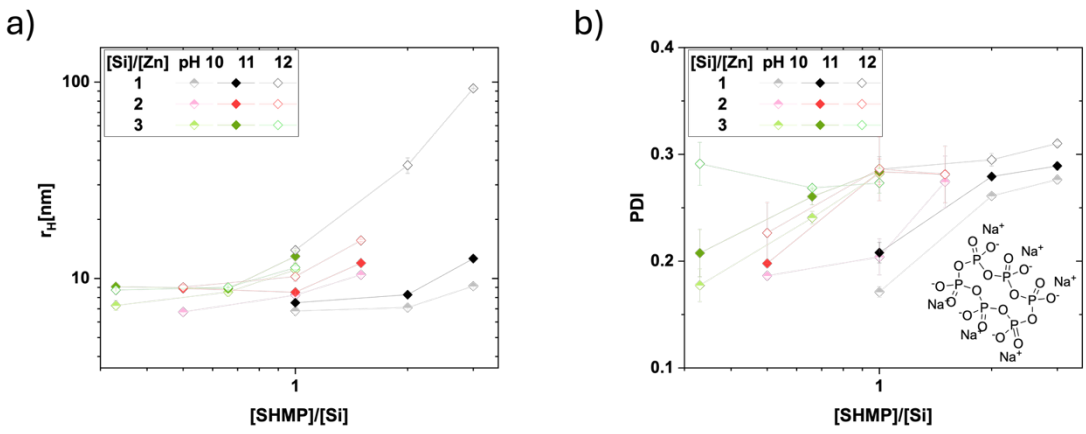


Figure III-15. (a) Hydrodynamic radius and (b) polydispersity index (PDI) for $ZnSxSiO_2$ particles derived from mixtures with differing [Si]/[Zn] ratios, at differing pH values and added SHMP in differing [SHMP]/[Si] ratios. Shown values are averages of multiple measurements to highlight trends. Correlation functions and the more detailed size distributions derived from CONTIN analysis can be found in **Figure SIII-30**. The structural formula of SHMP is shown in the bottom right corner of (b).

The fluorescence behavior of the particles, particularly those derived from pH 11, exhibits relatively constant excitation and emission peak wavelengths. With increasing [SHMP]/[Si] ratios, the excitation peak wavelengths tend to slightly blueshift, while the emission peak wavelengths tend to slightly redshift. At comparable [SHMP]/[Si] ratios, the trend of decreasing excitation/emission peak wavelength with increasing silica concentration remains true. Additionally, a decrease in PL intensity is observable for increasing [SHMP]/[Si] ratios. (cf. **Figure III-16**a)

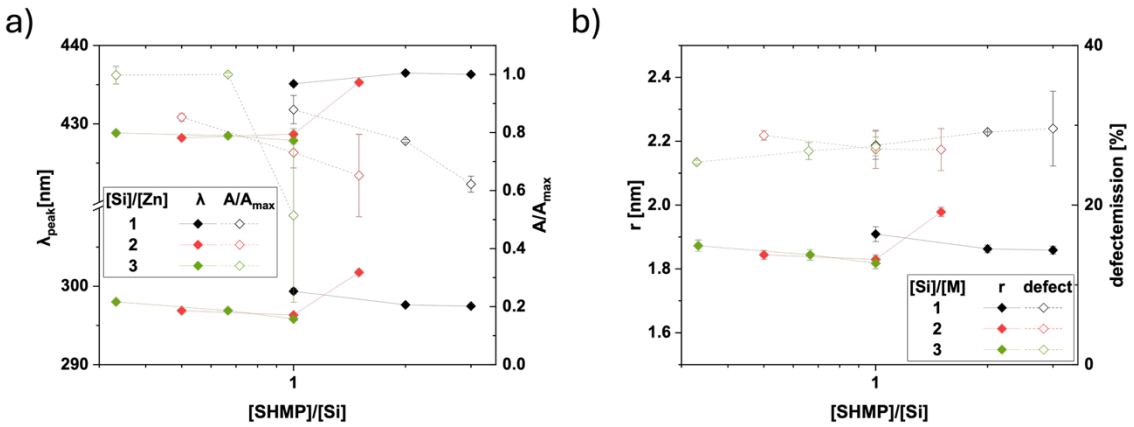


Figure III-16. (a) Emission and excitation peak of fitted fluorescence spectra for samples derived from syntheses at pH 11(cf. **Figure SIII-28a**). (b) QD radius derived from calculation using the Brus equation and DE determined by fitting the emission tail of the transformed emission spectra (cf. **Figure SIII-28c**).

When examining the resulting QD sizes determined using the Brus equation, two trends become apparent. First, as noted earlier, QD sizes decrease with increasing silicate content. Second, the QD size continues to decrease slightly as the [SHMP]/[Si] ratio increases. As observed before, the addition of SHMP tends to increase DE, with the effect increasing as the [SHMP]/[Si] ratio increases. (cf. **Figure III-16a**) Similar trends can be observed for particles derived from different synthesis pH. (cf. **Figure SIII-29**)

SHMP also incorporates an additional buffering system that further reduces the overall change in pH and ensures more consistent conditions throughout the synthesis. Simultaneously, as described before, a kinetic hindrance in silica polycondensation occurs, combined with surface complexation, and therefore reduced growth kinetics. The optimal pH for small, uniform, colloidally stable, and fluorescent particles was found to be around 11. A [SHMP]/[Si] ratio below 1 was found to be most effective at slowing condensation kinetics and thereby reducing the formation of secondary clusters, while maintaining significant fluorescence signals.

3.5 Discussion

The data collected in this work provide compelling evidence that direct spontaneous coprecipitation of various transition metal cations with carbonate and sulfide ions from silicate-rich solutions can lead to the spontaneous formation of primary nanoparticles with typical QD sizes below 5 nm. These self-assembled nanodots are obtained as a consequence of the miniaturizing influence of silica, likely facilitated by local co-mineralization, as illustrated in **Figure III-2**. The fundamental feasibility of reducing the dimensions of nanoparticles to such small sizes by chemically coupled processes has previously been reported for clusters of calcium carbonate [29] and was proposed to occur intrinsically during the growth of self-assembled silica/barium carbonate structures [71]. Very recently, we showed that the same principle can be used to prepare silica-coated quantum dots of cadmium, zinc, and mixed cadmium/zinc sulfides and selenides in simple one-pot procedures [30]. In this regard, the experimental results of the present study can be considered an extension of the approach toward a broader range of functional materials, thus confirming the initial hypothesis that pH-based chemical coupling may serve as a general strategy for synthesizing (silica-coated) nanoparticles.

The role of pH in the current system goes beyond its usual function as a simple control parameter for solubility and supersaturation. It links silicate speciation, thereby managing polymerization balances and surface charge development of new colloidal phases. This complex role matches previous findings in silica-mediated mineralization systems, where changes in pH affected the transition between monomeric and oligomeric silicate species [47,52,72]. The emergence of a narrow optimal pH range, around $pH \approx 11$, is especially important. It shows a careful balance between competing kinetic constraints. Similar non-linear behaviors have been noted in related coprecipitation systems, where the highest colloidal stability occurred only in a specific range of overlapping reaction kinetics involving inorganic nucleation and matrix formation [73–75]. Outside this range, either early phase separation or insufficient silicate reactivity results in a loss of structural control and wider particle distributions.

The comparison of different silica precursors further demonstrates that not only the silica concentration but also the structural state of the silicate species influences the coupled precipitation process. As established for silica condensation in general, monomeric silicates exhibit considerably higher mobility and reactivity than pre-condensed oligomeric species [54,76–78]. The present results suggest that this higher mobility promotes more homogeneous

encapsulation of freshly nucleated nanocrystals, whereas increasingly condensed silicates reduce coupling efficiency and lead to less effective surface passivation. The dependence on TEOS pre-hydrolysis time further supports this interpretation. While a certain degree of hydrolysis is required to generate sufficient reactive silanol species, prolonged pre-condensation decreases their mobility, thereby reducing the efficiency of nanoparticle encapsulation [51,79]. The existence of an optimum hydrolysis time thus supports the concept that efficient coprecipitation is governed by a balance between silicate reactivity and diffusional accessibility rather than by the maximum degree of silica condensation.

While (hydroxo)carbonate (cf. **Figure III-6**) and sulfide (cf. **Figure III-8**) phases of different (transition) metals are directly accessible through spontaneous coprecipitation at ambient conditions, corresponding oxides can be obtained via thermal post-treatment of the carbonate nanoparticles (cf. **Figure III-7**). In principle, both oxides and hydroxides should also be suitable anions to induce pH-based chemical coupling due to the release of protons upon mineralization, as exemplified below for the cases of zinc and manganese:

$$Zn^{2+} + 2H_2O \rightarrow Zn(OH)_2 + 2\,\mathbf{H}^+ \rightarrow ZnO + H_2O + 2\,\mathbf{H}^+ \qquad \text{(III-5)}$$

$$2\,MnO_4^- + 3\,Mn^{2+} + 2\,H_2O \rightarrow 5\,MnO_2 + 4\,\mathbf{H}^+ \qquad \text{(III-6)}$$

However, tests have shown that the absence of a buffer equilibrium (as provided by both carbonates and sulfides) results in uncontrolled conditions that prevent the formation of uniform nanoparticles via direct coprecipitation. Also, this direct reaction path is not suitable for all transition metals investigated. Therefore, we chose to prepare the oxides by calcinating the corresponding carbonate salts for the present work.

Although further characterization of the obtained nanodots is certainly required (especially concerning the structure of the cores and the presence of a silica shell around them), the observed miniaturization and presumed coating of the resulting particles by silicate species have the following beneficial effects on the properties of the nanomaterials:

(I) Enlargement of their specific surface area. (see **Chapter IV**)

(II) Protection of the surface of individual nanodots through thin layers of silica (e.g., to prevent oxidation in air or to shield dipole-dipole interactions in case of magnetic particles) while at the same time, the silica layer can still be permeable for solutes (e.g., in catalysis) or gradually release the encapsulated material (e.g., for delivery applications); both is essentially controlled by the thickness of the shell, which can

easily be tuned by adjusting the concentration of silica in solution [27]. (see **Chapter IV**)

(III) Higher colloidal stability: as a consequence of their large surface-to-volume ratios, nanosized particles are inherently unstable with a high tendency to aggregate to minimize surface energy; a negatively charged coating (e.g., silica) could enhance Coulomb as well as steric repulsion and thus decrease their tendency to agglomerate [80]. (cf. **Figure III-3** & online repository)

(IV) Surface functionalization: another general advantage of silica coatings is the well-established silane chemistry for surface modification; the free silanol groups at the surface can thus be chemically modified to afford different functionalities, such as amines or carboxylates [81]. (see online repository)

(V) Control over crystallinity and/or polymorphism: as in the case of the alkaline-earth carbonates [27–29], rapid encapsulation of early (hydroxo)carbonate/sulfide particles could allow for the isolation and stabilization of otherwise transient precursor phases, like for instance, amorphous states. (see **Chapter V**)

The addition of sodium hexametaphosphate (SHMP) suggests that the system is sensitive to subtle variations in interfacial coordination chemistry and reaction kinetics. Similar to observations in other kinetically confined precipitation systems, SHMP likely stabilizes early-stage intermediates, thereby shifting the system away from diffusion-limited cluster growth toward a more kinetically regulated regime [68–70]. The persistence of pronounced DE despite reduced particle sizes indicates that such kinetic confinement may come at the expense of surface relaxation and defect annealing processes [41,60,61]. A phenomenon that has also been reported for ligand-stabilized semiconductor nanocrystals under non-equilibrium growth conditions [82,83]. This suggests that structural and optical properties are not solely governed by size confinement but are significantly influenced by the dynamic accessibility of surface reconstruction pathways during particle formation.

Particular interest in capturing and preserving transient disordered phases originates from the finding that such materials often show higher catalytic activity than their crystalline counterparts [84,85]. The procedure described herein could thus provide easy access to these promising phases and stabilize them against transformation, as shown for, e.g., amorphous calcium and barium carbonate [27,28]. On a more fundamental level, the approach might also be utilized to study crystallization mechanisms in detail with respect to short-lived intermediates [29]. Current work is therefore focused on a profound characterization of the

obtained nanodots at high resolution as well as to testing their potential in selected catalytic applications.

Indeed, there is a vast body of literature available on the synthesis of nanodots, most notably those based on carbon [86], but also different types of transition metal oxides [87–89] and their use for catalysis [90,91] and other areas [92,93]. Likewise, previous studies have reported various ways to obtain metal sulfide quantum dots [23] or transition metal oxide nanoparticles [94–98] with a coating of amorphous silica. Compared to all these existing concepts for the preparation of functional core-shell nanoparticles, the present approach is clearly distinguished by its simplicity, along with the versatility in terms of core composition (as highlighted by the results of this study) and shell properties (e.g., thickness, porosity, and condensation of silica layers, still to be demonstrated). Altogether, the described method for nanodot preparation appears attractive as it:

(I) relies on plain mixing of two solutions (with no need for the use of complex templates or exfoliation procedures);

(II) takes place in a one-pot reaction utilizing self-assembly (in contrast to many other reported protocols for core-shell structures, where nanoparticles are typically prepared first and subsequently coated with silica in a second step, e.g. via the Stöber process);

(III) does not require any specific organic additives such as capping or exfoliation agents;

(IV) can be carried out in water (i.e. no organic solvents needed) at standard pressure and room temperature, and

(V) gives straightforward access to a variety of nanodots by reaction of (transition) metal cations with either sulfides or carbonates, whereby secondary calcination of the latter can be used to transform the initially obtained compositions into their corresponding oxides.

Given these advantages, simple coprecipitation from silicate-containing solutions seems to be a promising strategy for the sustainable synthesis of functional nanostructures, warranting further detailed studies of the obtained products (e.g., by high-resolution TEM) and their potential in catalytic processes and other applications. (cf. **Chapter IV** and online repository)

3.6 Conclusion

In the present work, a series of straightforward precipitation experiments were performed, in which selected transition metal chlorides were reacted with sulfides and carbonates under the influence of dissolved silicate at elevated pH in a purely aqueous system at ambient conditions. Phenomenological characterization of the obtained products utilizing conventional transmission electron microscopy showed that this simple procedure resulted in defined nanometric structures containing nanodots of the desired metal carbonate/sulfide coated in a silica matrix and other predominantly silicate-containing structures. Apart from offering a possible alternative to existing experimental routines for synthesizing and coating nanoparticles with silica, our approach has several advantages compared to others. Most importantly, our syntheses are simple and nevertheless offer large degrees of freedom in terms of their output. They only involve one reaction step, and no elaborate precursors [99] or sacrificial templates [100] have to be prepared in advance. Instead, the process solely relies on mixing aqueous solutions of commercially available reactants in a simple one-pot route. Additionally, all experiments can be conducted at ambient conditions, i.e., standard pressure and room temperature. The systematic variation of reaction parameters further revealed that the coupled precipitation process is predominantly governed by reaction kinetics rather than equilibrium considerations alone. In particular, pH, the structural state of the silicate species, and the condensation kinetics determine the efficiency of nanoparticle encapsulation and ultimately the structural and optical properties of the obtained nanomaterials. These findings establish a framework for the rational design of future coupled precipitation systems. Even further, by adjusting these handles carefully, the thickness and permeability of the silica shell, as well as the size of the coated nanoparticles, can be tuned. The spontaneous encapsulation of functional (e.g., catalytically active) nanoparticles in layers of silica is expected to improve the performance of corresponding materials by increasing the specific surface area, providing colloidal stability, hindering aggregation, and offering the possibility of straightforward chemical modification.

Particles produced in this unelaborate spontaneous coprecipitation can be used in a variety of applications. Particularly in areas such as catalysis or bioimaging, where usually particles produced in an elaborate sol-gel process are used. For such applications, however, individual optimization is still required (see **Chapter IV** & **Chapter V** & online repository). Nevertheless, the simplicity of the synthesis combines many individual steps of other syntheses and significantly accelerates the process of nanoparticle production.

3.7 References

[1] Rödig B, Funkner D, Frank T, Schürmann U, Rieder J, Kienle L, et al. Nanodots of Transition Metal Sulfides, Carbonates, and Oxides Obtained Through Spontaneous Co-Precipitation with Silica. Nanomaterials 2024;14:1–15. https://doi.org/10.3390/nano14242054.

[2] Astruc D. Introduction: Nanoparticles in Catalysis. Chem Rev 2020;120:461–3. https://doi.org/10.1021/acs.chemrev.8b00696.

[3] Payal, Pandey P. Role of Nanotechnology in Electronics: A Review of Recent Developments and Patents. Recent Pat Nanotechnol 2021;16:45–66. https://doi.org/10.2174/1872210515666210120114504.

[4] Pomerantseva E, Bonaccorso F, Feng X, Cui Y, Gogotsi Y. Energy storage: The future enabled by nanomaterials. Science (1979) 2019;366. https://doi.org/10.1126/science.aan8285.

[5] Sabela M, Balme S, Bechelany M, Janot JM, Bisetty K. A Review of Gold and Silver Nanoparticle-Based Colorimetric Sensing Assays. Adv Eng Mater 2017;19:1–24. https://doi.org/10.1002/adem.201700270.

[6] Jiang C cong, Cao Y ke, Xiao G yong, Zhu R fu, Lu Y peng. A review on the application of inorganic nanoparticles in chemical surface coatings on metallic substrates. RSC Adv 2017;7:7531–9. https://doi.org/10.1039/c6ra25841g.

[7] Kumar S, Ye F, Dobretsov S, Dutta J. Nanocoating Is a New Way for Biofouling Prevention. Frontiers in Nanotechnology 2021;3:1–16. https://doi.org/10.3389/fnano.2021.771098.

[8] Khondakar KR, Kaushik AK. Nanotechnology in Cancer Management. Elsevier; 2021. https://doi.org/10.1016/C2018-0-02630-4.

[9] Parashar M, Shukla VK, Singh R. Metal oxides nanoparticles via sol–gel method: a review on synthesis, characterization and applications. Journal of Materials Science: Materials in Electronics 2020;31:3729–49. https://doi.org/10.1007/s10854-020-02994-8.

[10] Hayashi H, Hakuta Y. Hydrothermal Synthesis of metal oxide nanoparticles in supercritical water. Materials 2010;3:3794–817. https://doi.org/10.3390/ma3073794.

[11] Jaji ND, Othman MBH, Lee HL, Hussin MH, Hui D. One-pot solvothermal synthesis and characterization of highly stable nickel nanoparticles. Nanotechnol Rev 2021;10:318–29. https://doi.org/10.1515/ntrev-2021-0019.

[12] Tsuzuki T. Mechanochemical synthesis of metal oxide nanoparticles. Commun Chem 2021;4. https://doi.org/10.1038/s42004-021-00582-3.

[13] Kister T, Monego D, Mulvaney P, Widmer-Cooper A, Kraus T. Colloidal Stability of Apolar Nanoparticles: The Role of Particle Size and Ligand Shell Structure. ACS Nano 2018;12:5969–77. https://doi.org/10.1021/acsnano.8b02202.

[14] Alexandridis P. Gold Nanoparticle Synthesis, Morphology Control, and Stabilization Facilitated by Functional Polymers. Chem Eng Technol 2011;34:15–28. https://doi.org/10.1002/ceat.201000335.

[15] Kang H, Buchman JT, Rodriguez RS, Ring HL, He J, Bantz KC, et al. Stabilization of Silver and Gold Nanoparticles: Preservation and Improvement of Plasmonic Functionalities. Chem Rev 2019;119:664–99. https://doi.org/10.1021/acs.chemrev.8b00341.

[16] Franconetti A, Carnerero JM, Prado-Gotor R, Cabrera-Escribano F, Jaime C. Chitosan as a capping agent: Insights on the stabilization of gold nanoparticles. Carbohydr Polym 2019;207:806–14. https://doi.org/10.1016/j.carbpol.2018.12.046.

[17] Zhu H, Prince E, Narayanan P, Liu K, Nie Z, Kumacheva E. Colloidal stability of nanoparticles stabilized with mixed ligands in solvents with varying polarity. Chemical Communications 2020;56:8131–4. https://doi.org/10.1039/d0cc02592e.

[18] Drummer S, Madzimbamuto T, Chowdhury M. Green synthesis of transition-metal nanoparticles and their oxides: A review. Materials 2021;14. https://doi.org/10.3390/ma14112700.

[19] Liz-Marzán LM, Giersig M, Mulvaney P. Synthesis of Nanosized Gold−Silica Core−Shell Particles. Langmuir 1996;12:4329–35. https://doi.org/10.1021/la9601871.

[20] Guerrero-Martínez A, Pérez-Juste J, Liz-Marzán LM. Recent progress on silica coating of nanoparticles and related nanomaterials. Advanced Materials 2010;22:1182–95. https://doi.org/10.1002/adma.200901263.

[21] Liu S, Han MY. Silica-coated metal nanoparticles. Chem Asian J 2010;5:36–45. https://doi.org/10.1002/asia.200900228.

[22] Yang SA, Choi S, Jeon SM, Yu J. Silica nanoparticle stability in biological media revisited. Sci Rep 2018;8:1–9. https://doi.org/10.1038/s41598-017-18502-8.

[23] Pham XH, Park SM, Ham KM, Kyeong S, Son BS, Kim J, et al. Synthesis and application of silica-coated quantum dots in biomedicine. Int J Mol Sci 2021;22. https://doi.org/10.3390/ijms221810116.

[24] García-Ruiz JM, Melero-García E, Hyde ST. Morphogenesis of self-assembled nanocrystalline materials of barium carbonate and silica. Science (1979) 2009;323:362–5. https://doi.org/10.1126/science.1165349.

[25] Kellermeier M, Cölfen H, García-Ruiz JM. Silica biomorphs: Complex biomimetic hybrid materials from "sand and chalk." Eur J Inorg Chem 2012:5123–44. https://doi.org/10.1002/ejic.201201029.

[26] Kellermeier M, Glaab F, Melero-García E, García-Ruiz JM. Experimental Techniques for the Growth and Characterization of Silica Biomorphs and Silica Gardens. Methods Enzymol., vol. 532, 2013, p. 225–56. https://doi.org/10.1016/B978-0-12-416617-2.00011-4.

[27] Kellermeier M, Melero-García E, Glaab F, Klein R, Drechsler M, Rachel R, et al. Stabilization of amorphous calcium carbonate in inorganic silica-rich environments. J Am Chem Soc 2010;132:17859–66. https://doi.org/10.1021/ja106959p.

[28] Eiblmeier J, Kellermeier M, Deng M, Kienle L, García Ruiz JM, Kunz W. Bottom-up self-assembly of amorphous core-shell-shell nanoparticles and biomimetic crystal forms in inorganic silica-carbonate systems. Chemistry of Materials 2013;25:1842–51. https://doi.org/10.1021/cm4003959.

[29] Kellermeier M, Gebauer D, Melero-García E, Drechsler M, Talmon Y, Kienle L, et al. Colloidal stabilization of calcium carbonate prenucleation clusters with silica. Adv Funct Mater 2012;22:4301–11. https://doi.org/10.1002/adfm.201200953.

[30] Funkner D, Frank T, Kohlmann N, Zahnweh D, Rieder J, Kienle L, et al. Functional nanoparticles from chemically coupled precipitation processes. Mater Today Chem 2023;29:101438. https://doi.org/10.1016/j.mtchem.2023.101438.

[31] Shaheen WM, Selim MM. Effect of thermal treatment on physicochemical properties of pure and mixed manganese carbonate and basic copper carbonate. Thermochim Acta 1998;322:117–28. https://doi.org/10.1016/S0040-6031(98)00486-9.

[32] Guo Z, Li M, Liu J. Highly porous CdO nanowires: Preparation based on hydroxy- and carbonate-containing cadmium compound precursor nanowires, gas sensing and optical properties. Nanotechnology 2008;19. https://doi.org/10.1088/0957-4484/19/24/245611.

[33] Cong HP, Yu SH. Shape control of cobalt carbonate particles by a hydrothermal process in a mixed solvent: An efficient precursor to nanoporous cobalt oxide architectures and their sensing property. Cryst Growth Des 2009;9:210–7. https://doi.org/10.1021/cg8003068.

[34] Spinner N, Mustain WE. Effect of nickel oxide synthesis conditions on its physical properties and electrocatalytic oxidation of methanol. Electrochim Acta 2011;56:5656–66. https://doi.org/10.1016/j.electacta.2011.04.023.

[35] Pourmortazavi SM, Marashianpour Z, Karimi MS, Mohammad-Zadeh M. Electrochemical synthesis and characterization of zinc carbonate and zinc oxide nanoparticles. J Mol Struct 2015;1099:232–8. https://doi.org/10.1016/j.molstruc.2015.06.044.

[36] Frisken BJ. Revisiting the method of cumulants for the analysis of dynamic light-scattering data. Appl Opt 2001;40:4087. https://doi.org/10.1364/AO.40.004087.

[37] Provencher SW. A constrained regularization method for inverting data represented by linear algebraic or integral equations. Comput Phys Commun 1982;27:213–27. https://doi.org/10.1016/0010-4655(82)90173-4.

[38] Provencher SW. Contin: A general purpose constrainded regularization program for inverting noisy linear algebraic and integral equations. Comput Phys Commun 1984;35:C-818-C–819. https://doi.org/10.1016/S0010-4655(84)82935-5.

[39] Hinterding SOM, Salzmann BBV, Vonk SJW, Vanmaekelbergh D, Weckhuysen BM, Hutter EM, et al. Single Trap States in Single CdSe Nanoplatelets. ACS Nano 2021;15:7216–25. https://doi.org/10.1021/acsnano.1c00481.

[40] Bera D, Qian L, Tseng TK, Holloway PH. Quantum dots and their multimodal applications: A review. Materials 2010;3:2260–345. https://doi.org/10.3390/ma3042260.

[41] Babentsov V, Sizov F. Defects in quantum dots of IIB-VI semiconductors. Opto-Electronics Review 2008;16:208–25. https://doi.org/10.2478/s11772-008-0025-0.

[42] Oliva AI, Solís-Canto O, Castro-Rodríguez R, Quintana P. Formation of the band gap of CdS thin films growth by different techniques. Modern Physics Letters B, vol. 15, 2001, p. 671–4. https://doi.org/10.1142/S0217984901002269.

[43] Lee GJ, Lee Y, Lim H, Cheong H, Kil B-H, Han S-H. Photoluminescence and Nonlinear Optical Properties of Semiconductor Nanocomposites Consisting of ZnO Nanorods and CdS Nanodots. Journal of the Korean Physical Society 2011;58:1290–4. https://doi.org/10.3938/jkps.58.1290.

[44] Brus LE. Electron-electron and electron-hole interactions in small semiconductor crystallites: The size dependence of the lowest excited electronic state. J Chem Phys 1984;80:4403–9. https://doi.org/10.1063/1.447218.

[45] Nemade KR, Waghuley SA. Band gap engineering of CuS nanoparticles for artificial photosynthesis. Mater Sci Semicond Process 2015;39:781–5. https://doi.org/10.1016/j.mssp.2015.05.045.

[46] Sheardy AT, Arvapalli DM, Wei J. Novel microwave synthesis of near-metallic copper sulfide nanodiscs with size control: experimental and DFT studies of charge carrier density. Nanoscale Adv 2020;2:1054–8. https://doi.org/10.1039/d0na00069h.

[47] Iler RK. The Chemistry of Silica: Solubility, Polymerization, Colloid and Surface Properties and Biochemistry of Silica. Wiley; 1979.

[48] Lide DR. Handbook of chemistry and physics. 10th ed. Boca Raton, FL, USA: CRC Press; 2005.

[49] Navrotsky A. Energetic clues to pathways to biomineralization: Precursors, clusters, and nanoparticles. Proc Natl Acad Sci U S A 2004;101:12096–101. https://doi.org/10.1073/pnas.0404778101.

[50] Seidel H, Ehrhardt H, Viswanathan K, Johannes W. Darstellung, Struktur und Eigenschaften von Kupfer(II)-Carbonat. ZAAC - Journal of Inorganic and General Chemistry 1974;410:138–48. https://doi.org/10.1002/zaac.19744100207.

[51] Harris MT, Brunson RR, Byers CH. The base-catalyzed hydrolysis and condensation reactions of dilute and concentrated TEOS solutions. J Non Cryst Solids 1990;121:397–403. https://doi.org/10.1016/0022-3093(90)90165-I.

[52] Matsoukas T, Gulari E. Monomer-addition growth with a slow initiation step: A growth model for silica particles from alkoxides. J Colloid Interface Sci 1989;132:13–21. https://doi.org/10.1016/0021-9797(89)90210-5.

[53] Han Y, Lu Z, Teng Z, Liang J, Guo Z, Wang D, et al. Unraveling the growth mechanism of silica particles in the stöber method: In situ seeded growth model. Langmuir 2017;33:5879–90. https://doi.org/10.1021/acs.langmuir.7b01140.

[54] Bogush GH, Zukoski CF. Uniform silica particle precipitation: An aggregative growth model. J Colloid Interface Sci 1991;142:19–34. https://doi.org/10.1016/0021-9797(91)90030-C.

[55] Chukwuocha EO, Onyeaju MC, Harry TST. Theoretical Studies on the Effect of Confinement on Quantum Dots Using the Brus Equation. World Journal of Condensed Matter Physics 2012;02:96–100. https://doi.org/10.4236/wjcmp.2012.22017.

[56] Rossetti R, Ellison JL, Gibson JM, Brus LE. Size effects in the excited electronic states of small colloidal CdS crystallites. J Chem Phys 1984;80:4464–9. https://doi.org/10.1063/1.447228.

[57] Reshchikov MA. Mechanisms of Thermal Quenching of Defect-Related Luminescence in Semiconductors. Physica Status Solidi (A) Applications and Materials Science 2021;218. https://doi.org/10.1002/pssa.202000101.

[58] Fan C, Chen J, Chen Y, Ji J, Teng HH. Relationship between solubility and solubility product: The roles of crystal sizes and crystallographic directions. Geochim Cosmochim Acta 2006;70:3820–9. https://doi.org/10.1016/j.gca.2006.06.011.

[59] Kolthoff IM. The solubilities and solubility products of metallic sulfides in water. Journal of Physical Chemistry 1931;35:2711–21. https://doi.org/10.1021/j150327a019.

[60] Lu J, Carvalho A, Chan XK, Liu H, Liu B, Tok ES, et al. Atomic healing of defects in transition metal dichalcogenides. Nano Lett 2015;15:3524–32. https://doi.org/10.1021/acs.nanolett.5b00952.

[61] Marino E, Kodger TE, Crisp RW, Timmerman D, MacArthur KE, Heggen M, et al. Repairing Nanoparticle Surface Defects. Angew Chem Int Ed 2017;56:13795–9. https://doi.org/10.1002/anie.201705685.

[62] Rödig B. Silicate structures - spontaneous formation in structured media and application. Master Thesis. University of Regensburg, 2022.

[63] Kunz W, Henle J, Ninham BW. "Zur Lehre von der Wirkung der Salze" (about the science of the effect of salts): Franz Hofmeister's historical papers. Curr. Opin. Colloid Interface Sci., vol. 9, 2004, p. 19–37. https://doi.org/10.1016/j.cocis.2004.05.005.

[64] Squires TM, Quake SR. Microfluidics: Fluid physics at the nanoliter scale. Rev Mod Phys 2005;77:977–1026. https://doi.org/10.1103/RevModPhys.77.977.

[65] Sameti M, Bohr G, Ravi Kumar MNV, Kneuer C, Bakowsky U, Nacken M, et al. Stabilisation by freeze-drying of cationically modified silica nanoparticles for gene delivery. Int J Pharm 2003;266:51–60. https://doi.org/10.1016/S0378-5173(03)00380-6.

[66] de Morais SC, de Lima DF, Ferreira TM, Domingos JB, de Souza MAF, Castro BB, et al. Effect of pH on the efficiency of sodium hexametaphosphate as calcium carbonate scale inhibitor at high temperature and high pressure. Desalination 2020;491. https://doi.org/10.1016/j.desal.2020.114548.

[67] Yang S, Luo X, Zhou H, Tang X, Liu Z, Guo J, et al. Effect of sodium hexametaphosphate on the flotation separation of lepidolite and quartz: MD study. Physicochemical Problems of Mineral Processing 2024;60. https://doi.org/10.37190/ppmp/192882.

[68] Jia Y, Wang B, Wu Z, Han J, Zhang T, Vandeperre LJ, et al. Role of sodium hexametaphosphate in MgO/SiO2 cement pastes. Cem Concr Res 2016;89:63–71. https://doi.org/10.1016/j.cemconres.2016.08.003.

[69] Torresan MF, Parra-Florez L, Sorbello C, Azcárate JC, Etchenique R, Wolosiuk A. Sodium Hexametaphosphate: An Inexpensive Inorganic Polyelectrolyte “Primer” For Upconverting Nanoparticles/Mesoporous Silica Core-Shell Synthesis. ChemistrySelect 2020;5:5210–6. https://doi.org/10.1002/slct.202000287.

[70] Lu J, Sun M, Yuan Z, Qi S, Tong Z, Li L, et al. Innovative insight for sodium hexametaphosphate interaction with serpentine. Colloids Surf A Physicochem Eng Asp 2019;560:35–41. https://doi.org/10.1016/j.colsurfa.2018.09.076.

[71] Knoll P, Steinbock O. Nanodot-to-Rod Transition and Particle Attachment in Self-Organized Polycrystalline Aggregates. Cryst Growth Des 2019;19:4218–23. https://doi.org/10.1021/acs.cgd.9b00085.

[72] Matsoukas T, Gulari E. Dynamics of growth of silica particles from ammonia-catalyzed hydrolysis of tetra-ethyl-orthosilicate. J Colloid Interface Sci 1988;124:252–61. https://doi.org/10.1016/0021-9797(88)90346-3.

[73] Kellermeier M, Melero-García E, Kunz W, García-Ruiz JM. Local autocatalytic co-precipitation phenomena in self-assembled silica-carbonate materials. J Colloid Interface Sci 2012;380:1–7. https://doi.org/10.1016/j.jcis.2012.05.009.

[74] Voinescu AE, Kellermeier M, Carnerup AM, Larsson AK, Touraud D, Hyde ST, et al. Co-precipitation of silica and alkaline-earth carbonates using TEOS as silica source. J Cryst Growth 2007;306:152–8. https://doi.org/10.1016/j.jcrysgro.2007.03.060.

[75] Taheri-Ledari R, Salehi MM, Esmailzadeh F, Mohammadi A, Kashtiaray A, Maleki A. A brief survey of principles of co-deposition method as a convenient procedure for preparation of metallic nanomaterials. J Alloys Compd 2024;980. https://doi.org/10.1016/j.jallcom.2024.173509.

[76] Bogush GH, Zukoski CF. Studies of the kinetics of the precipitation of uniform silica particles through the hydrolysis and condensation of silicon alkoxides. J Colloid Interface Sci 1991;142:1–18. https://doi.org/10.1016/0021-9797(91)90029-8.

[77] Bogush GH, Tracy MA, Zukoski CF. Preparation of monodisperse silica particles: Control of size and mass fraction. J Non Cryst Solids 1988;104:95–106. https://doi.org/10.1016/0022-3093(88)90187-1.

[78] Bogush GH, Zukoski Iv CF. Uniform Silica Particle Precipitation: An Aggregative Growth Model. 1991. https://doi.org/10.1016/0021-9797(91)90030-C.

[79] Malay O, Yilgor I, Menceloglu YZ. Effects of solvent on TEOS hydrolysis kinetics and silica particle size under basic conditions. J Solgel Sci Technol 2013;67:351–61. https://doi.org/10.1007/s10971-013-3088-4.

[80] Schubert J, Chanana M. Coating Matters: Review on Colloidal Stability of Nanoparticles with Biocompatible Coatings in Biological Media, Living Cells and Organisms. Curr Med Chem 2018;25:4553–86. https://doi.org/10.2174/0929867325666180601101859.

[81] Kango S, Kalia S, Celli A, Njuguna J, Habibi Y, Kumar R. Surface modification of inorganic nanoparticles for development of organic-inorganic nanocomposites - A review. Prog Polym Sci 2013;38:1232–61. https://doi.org/10.1016/j.progpolymsci.2013.02.003.

[82] Sartinska L. Surface-driven electrostatic, luminescent, and paramagnetic features of freshly synthesized BN nanopowders under concentrated light. Vacuum 2026;244. https://doi.org/10.1016/j.vacuum.2025.114898.

[83] Zeng H, Duan G, Li Y, Yang S, Xu X, Cai W. Blue luminescence of ZnO nanoparticles based on non-equilibrium processes: Defect origins and emission controls. Adv Funct Mater 2010;20:561–72. https://doi.org/10.1002/adfm.200901884.

[84] Hong WT, Risch M, Stoerzinger KA, Grimaud A, Suntivich J, Shao-Horn Y. Toward the rational design of non-precious transition metal oxides for oxygen electrocatalysis. Energy Environ Sci 2015;8:1404–27. https://doi.org/10.1039/c4ee03869j.

[85] Iyer A, Del-Pilar J, King'Ondu CK, Kissel E, Garces HF, Huang H, et al. Water oxidation catalysis using amorphous manganese oxides, octahedral molecular sieves (OMS-2), and octahedral layered (OL-1) manganese oxide structures. Journal of Physical Chemistry C 2012;116:6474–83. https://doi.org/10.1021/jp2120737.

[86] Li H, Kang Z, Liu Y, Lee ST. Carbon nanodots: Synthesis, properties and applications. J Mater Chem 2012;22:24230–53. https://doi.org/10.1039/c2jm34690g.

[87] Nakamura K, Oaki Y, Imai H. Monolayered nanodots of transition metal oxides. J Am Chem Soc 2013;135:4501–8. https://doi.org/10.1021/ja400443a.

[88] Han U Bin, Lee JS. Bottom-up synthesis of ordered metal/oxide/metal nanodots on substrates for nanoscale resistive switching memory. Sci Rep 2016;6:1–8. https://doi.org/10.1038/srep25537.

[89] Suzuki N, Tanaka H, Yamanaka S, Kanai M, Lee BK, Lee HY, et al. Epitaxial Nanodot Arrays of Transition-Metal Oxides Fabricated by Dry Deposition Combined with a Nanoimprint-Lithography-Based Molybdenum Lift-Off Technique. Small 2008;4:1661–5. https://doi.org/10.1002/smll.200800734.

[90] Jana B, Reva Y, Scharl T, Strauss V, Cadranel A, Guldi DM. Carbon Nanodots for All-in-One Photocatalytic Hydrogen Generation. J Am Chem Soc 2021;143:20122–32. https://doi.org/10.1021/jacs.1c07049.

[91] Chen X, Xu X, Fei Z, Xie X, Lou J, Tang J, et al. CeO2 nanodots embedded in a porous silica matrix as an active yet durable catalyst for HCl oxidation. Catal Sci Technol 2016;6:5116–23. https://doi.org/10.1039/c5cy02300a.

[92] Sivasankarapillai VS, Vishnu Kirthi A, Akksadha M, Indu S, Dhiviya Dharshini U, Pushpamalar J, et al. Recent advancements in the applications of carbon nanodots: Exploring the rising star of nanotechnology. Nanoscale Adv 2020;2:1760–73. https://doi.org/10.1039/c9na00794f.

[93] Koutavarapu R, Tamtam MR, Rao MC, Peera SG, Shim J. Recent progress in transition metal oxide/sulfide quantum dots-based nanocomposites for the removal of toxic organic pollutants. Chemosphere 2021;272:129849. https://doi.org/10.1016/j.chemosphere.2021.129849.

[94] Santra S, Tapec R, Theodoropoulou N, Dobson J, Hebard A, Tan W. Synthesis and characterization of silica-coated iron oxide nanoparticles in microemulsion: The effect of nonionic surfactants. Langmuir 2001;17:2900–6. https://doi.org/10.1021/la0008636.

[95] Bumb A, Brechbiel MW, Choyke PL, Fugger L, Eggeman A, Prabhakaran D, et al. Synthesis and characterization of ultra-small superparamagnetic iron oxide nanoparticles thinly coated with silica. Nanotechnology 2008;19. https://doi.org/10.1088/0957-4484/19/33/335601.

[96] Yang H, Zhuang Y, Hu H, Du X, Zhang C, Shi X, et al. Silica-coated manganese oxide nanoparticles as a platform for targeted magnetic resonance and fluorescence imaging of cancer cells. Adv Funct Mater 2010;20:1733–41. https://doi.org/10.1002/adfm.200902445.

[97] Chia SL, Leong DT. Reducing ZnO nanoparticles toxicity through silica coating. Heliyon 2016;2. https://doi.org/10.1016/j.heliyon.2016.e00177.

[98] Basu P, De K, Das S, Mandal AK, Kumar A, Jana TK, et al. Silica-Coated Metal Oxide Nanoparticles: Magnetic and Cytotoxicity Studies. ChemistrySelect 2018;3:7346–53. https://doi.org/10.1002/slct.201801254.

[99] Gui Z, Liu J, Wang Z, Song L, Hu Y, Fan W, et al. From muticomponent precursor to nanoparticle nanoribbons of ZnO. Journal of Physical Chemistry B 2005;109:1113–7. https://doi.org/10.1021/jp047088d.

[100] Liu J, Fu S, Yuan B, Li Y, Deng Z. Toward a universal “adhesive nanosheet” for the assembly of multiple nanoparticles based on a protein-induced reduction/decoration of graphene oxide. J Am Chem Soc 2010;132:7279–81. https://doi.org/10.1021/ja100938r.

3.8 Supporting Information

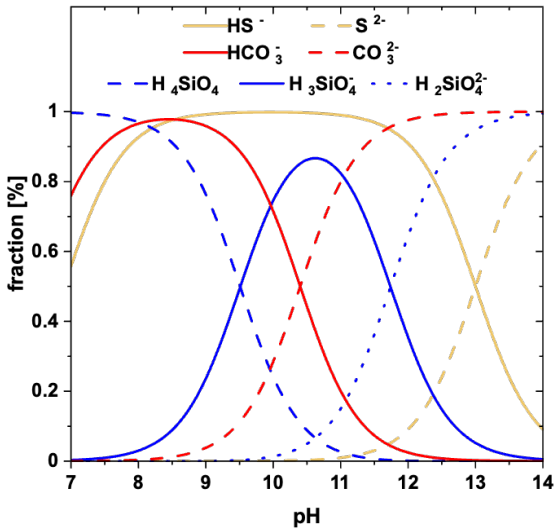


Figure SIII-1. Bjerrum-plot of the HS^-/S^{2-} system (yellow), the HCO_3^-/CO_3^{2-} system (red), and the $H_4SiO_4/H_3SiO_4^-/H_2SiO_4^{2-}$ system (blue). Suitable for coprecipitation is thepH range where the overlap between the HS^-/HCO_3^- and the $H_3SiO_4^-$ is the greatest.

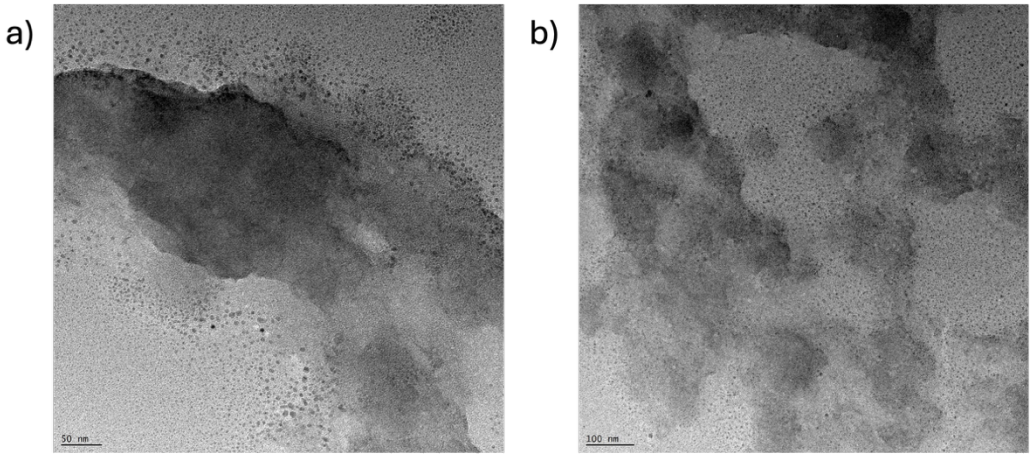


Figure SIII-2. TEM micrographs of particles derived from a synthesis containing 10 mM of each Na_2S, $CoCl_2$, and sodium silicate. a) Cloud-like appearance of the formed particle around bigger aggregates. Scale bar: 50 nm. b) Scale bar: 100 nm.

Table SIII-1. Apparent particle and aggregate sizes determined by dynamic light scattering for $CoCO_3$ dispersions obtained by mixing equal volumes of 10 mM $CoCl_2$ and $(NH_4)_2CO_3$ solutions in the presence of different amounts of silicate at varying final pH. Average diameters were derived from the DLS data using the cumulants method and the CONTIN algorithm, which gives apparent sizes for both the primary particles and their aggregates. Note that corresponding analyses of samples containing 2.5 or 5.8 mM SiO_2 did not yield meaningful results due to the formation of large particles, which subsequently aggregated and sedimented (as shown in **Figure III-3** of the main text). (The oddity of the selected values comes from the conversion from ppm to mM.)

[SiO_2] / mM	**pH**	**DLS (Cumulants) d / nm**	**DLS (CONTIN) d / nm**
2.5	8.4 (native)	n.d.	29.4 (100 %)
	9.0	65.7	1.6 (97.2 %)
			8.2 (2.8 %)
	11.0	52.7	1.2 (98.4 %)
			15.6 (1.6 %)
5.8	9.0	43.9	8.1 (100%)
	9.2 (native)	48.6	5.6 (96.8 %)
			19.2 (3.2 %)
	11.0	36.0	6.8 (100 %)
8.3	9.0	41.4	6.5 (99.6 %)
			18.4 (0.4 %)
	9.6 (native)	51.9	12.3 (99.7 %)
			44.3 (0.3 %)
	11.0	19.4	2.4 (97.3 %)
			8.6 (2.7 %)
12.5	9.0	12.4	3.0 (100 %)
	10.0 (native)	10.8	4.2 (98.3 %)
			16.3 (2.7 %)
	11.0	40.2	1.2 (99.3 %)
			13.6 (0.7 %)
16.6	9.0	7.6	3.0 (100 %)
	10.3 (native)	36.1	3.0 (98.8 %)
			12.1 (1.2 %)
	11.0	26.9	3.5 (99.2 %)
			14.2 (0.8 %)

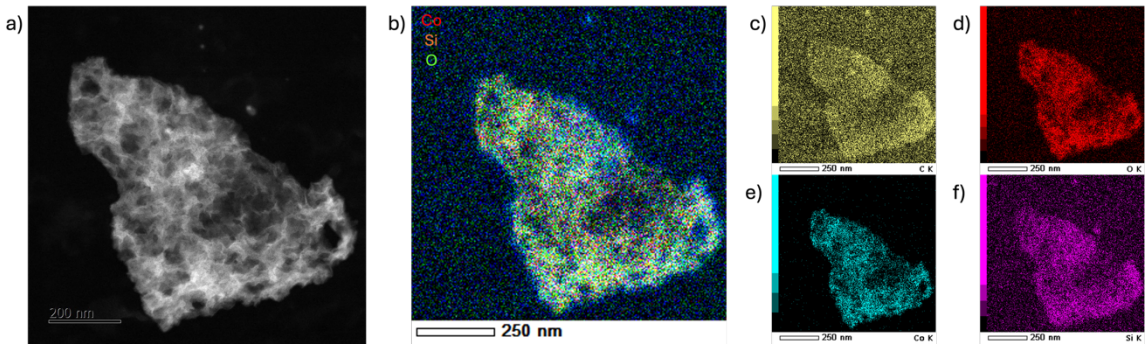


Figure SIII-3. Elemental mapping of nanostructures as shown by **Figure III-5b** in the main text: (a) HAADF-STEM micrograph, (b) elemental map, (c) carbon, (d) oxygen, (e) cobalt and (f) silicon. Scale bars: 250 nm.

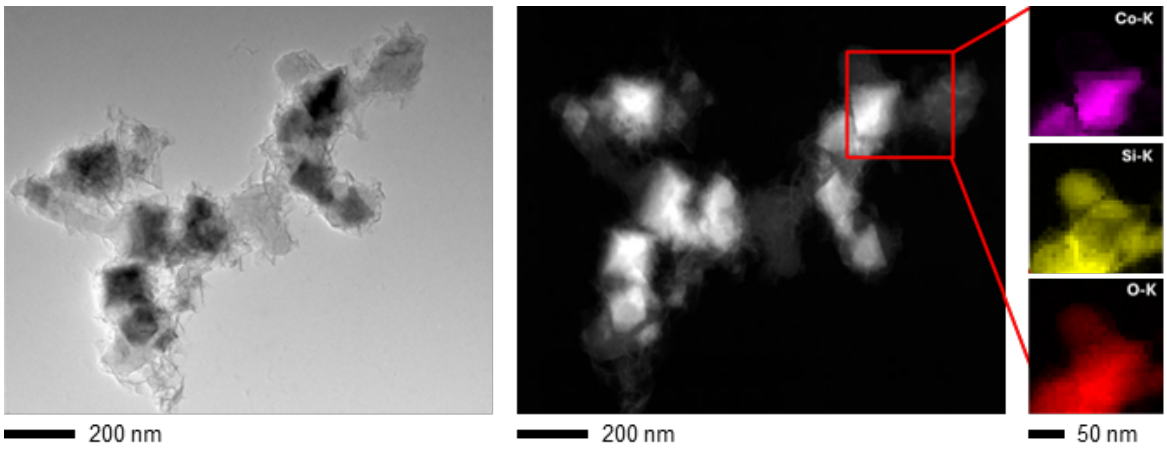


Figure SIII-4. TEM (left) and HAADF-STEM (middle) micrographs of nanostructures formed upon calcination of silica-stabilized cobalt carbonate precursors as shown in **Figure III-6b** of the main text and obtained by mixing equal volumes of 10 mM solutions of $CoCl_2$ and Na_2CO_3, with the latter containing 10 mM SiO_2. Elemental maps (right) confirm the presence of Co, Si and O, consistent with silica-coated cobalt oxide nanocrystals.

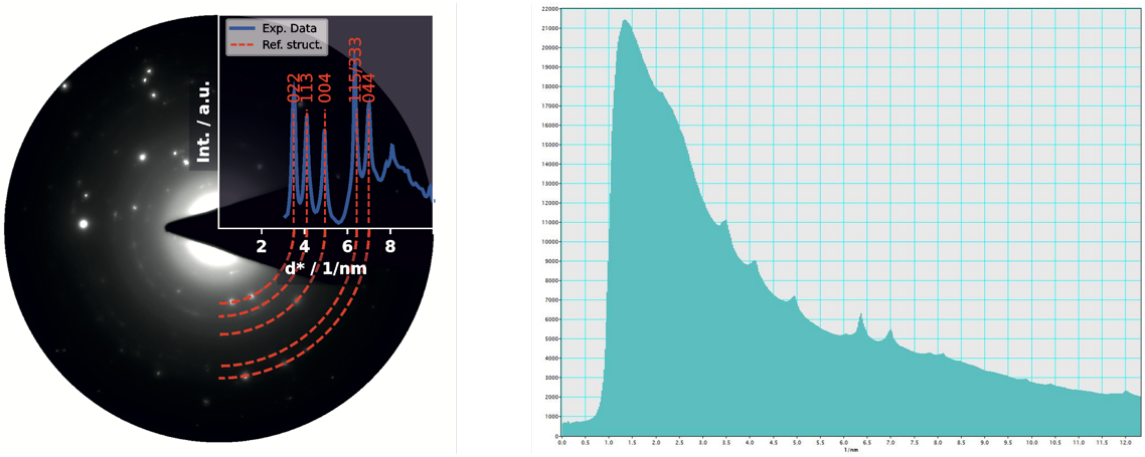


Figure SIII-5. Electron diffraction (ED) pattern (left) and the corresponding diffractogram obtained by radial integration (right) from the nanostructures shown in **Figure SIII-4**. The observed reflections suggest a spinel structure, probably Co_3O_4.

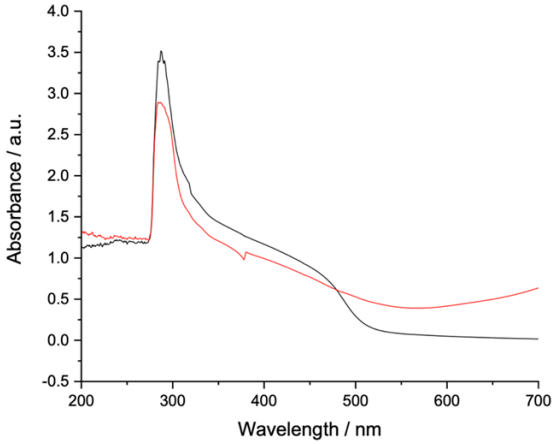


Figure SIII-6. UV/Vis spectra of CdS (black) and CuS (red) particles formed from aqueous solutions containing 10 mM each of transition metal chloride, sodium sulfide, and sodium silicate. Using the Brus equation with an onset of absorption of 312 nm for CdS and 304 nm for CuS, diameters of 2.51 nm and 2.56 nm can be calculated, respectively.

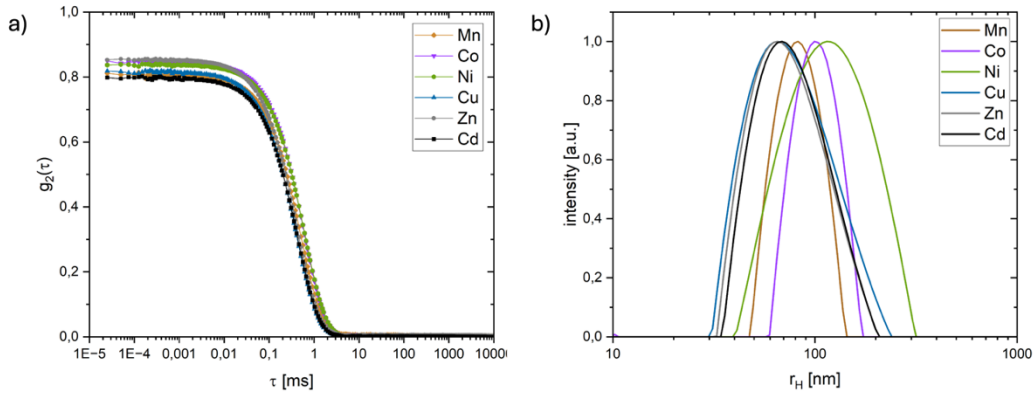


Figure SIII-7. DLS measurements of particles derived by mixing equal volumes of 10 mM solutions of metal chloride and Na_2CO_3, with the latter containing 5 mM SiO_2, at native pH of 10.41 (Mn), 10.35 (Co), 10.40 (Ni), 10.22 (Cu), 10.10 (Zn), and 10.51 (Cd). (a) DLS correlation function of particles derived from various transition metal cations. b) Size distributions derived from correlation functions shown in a).

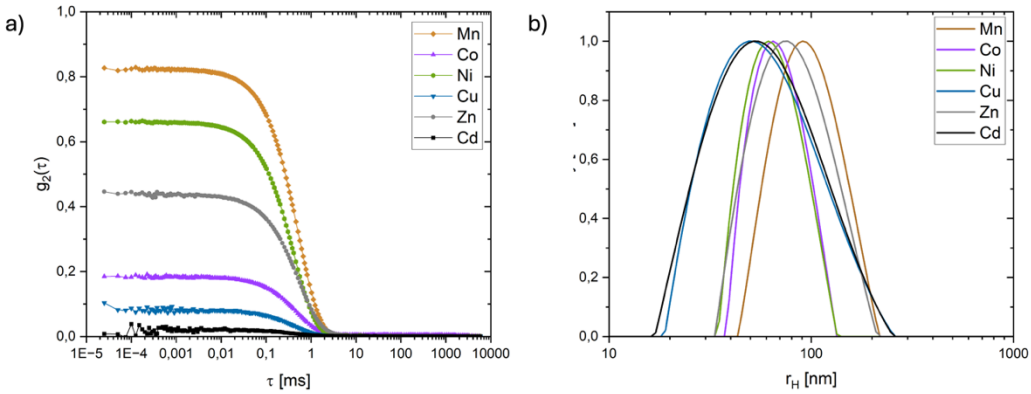


Figure SIII-8. DLS measurements of particles derived by calcination of the carbonates obtained by mixing equal volumes of 10 mM solutions of metal chloride and Na_2CO_3, with the latter containing 5 mM SiO_2, at native pH of 10.41 (Mn), 10.35 (Co), 10.40 (Ni), 10.22 (Cu), 10.10 (Zn), and 10.51 (Cd). (a) DLS correlation function of particles derived from various transition metal cations. (b) Size distributions derived from correlation functions shown in (a).

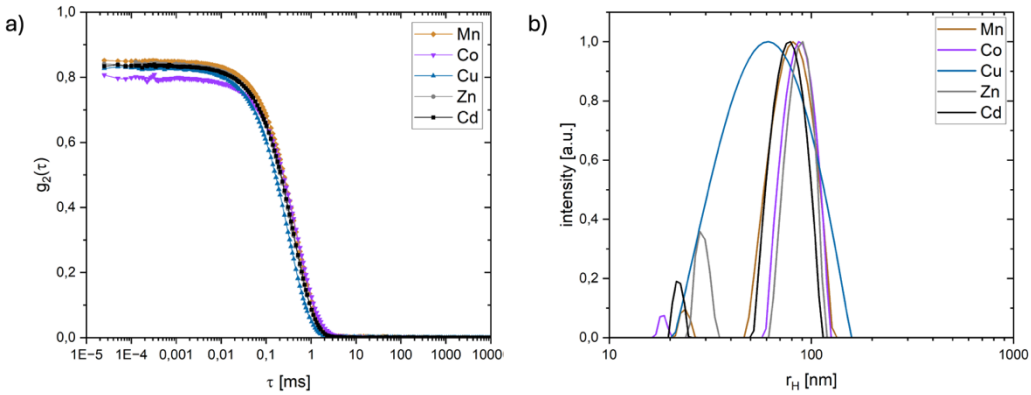


Figure SIII-9. DLS measurements of particles derived by mixing equal volumes of 10 mM solutions of metal chloride and Na_2S, with the latter containing 5 mM SiO_2, at native pH of 10.82 (Mn), 11.14 (Co), 11.21 (Ni), 10.87 (Cu), 10.92 (Zn), and 11.15 (Cd). a) DLS correlation function of particles derived from various transition metal cations. b) Size distributions derived from correlation functions shown in a).

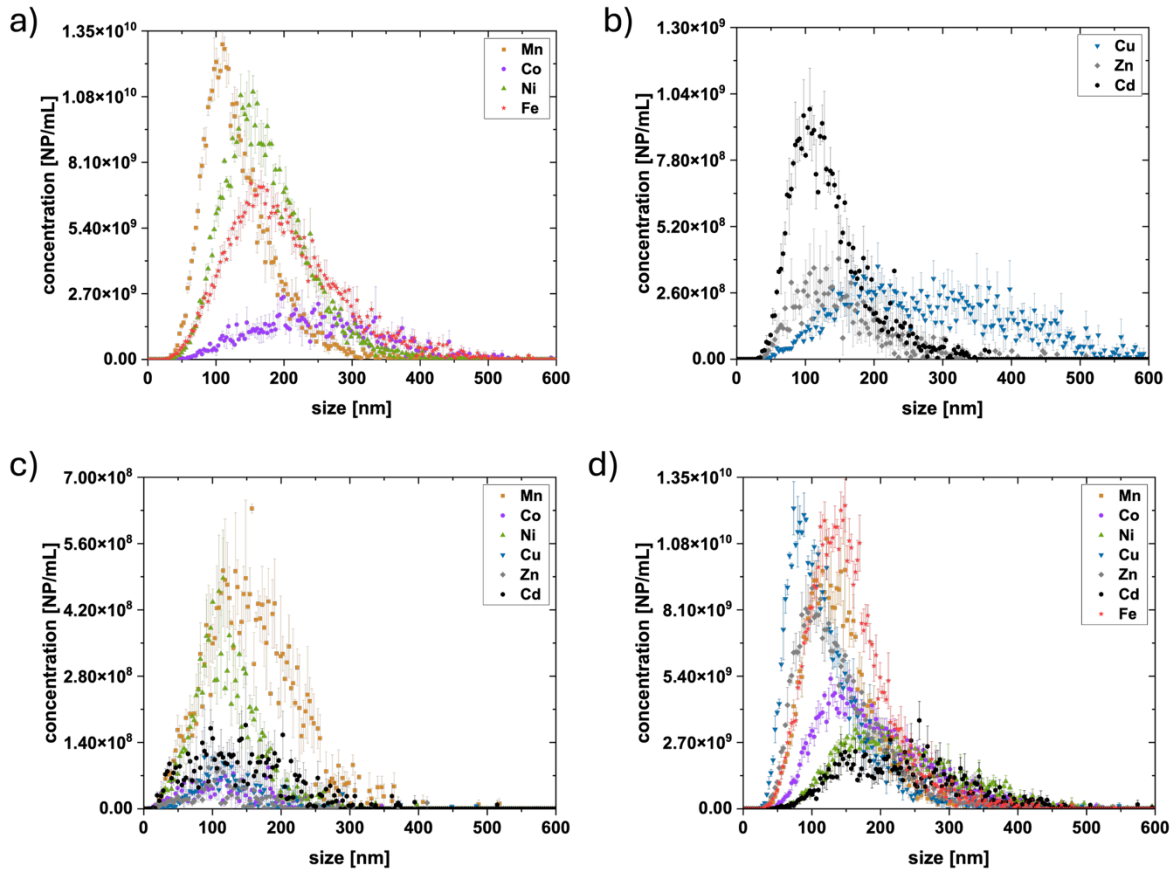


Figure SIII-10. NTA measurements of particles derived by mixing equal volumes of 10 mM solutions of metal chloride and Na_2S/Na_2CO_3, with the latter containing 5 mM SiO_2. a) Size distributions of carbonate samples at dilutions of 1:500. b) Size distributions of carbonate samples at dilutions of 1:100. c) Size distributions of calcinated carbonate samples at dilutions of 1:100. d) Size distributions of sulfide samples at dilutions of 1:1000.

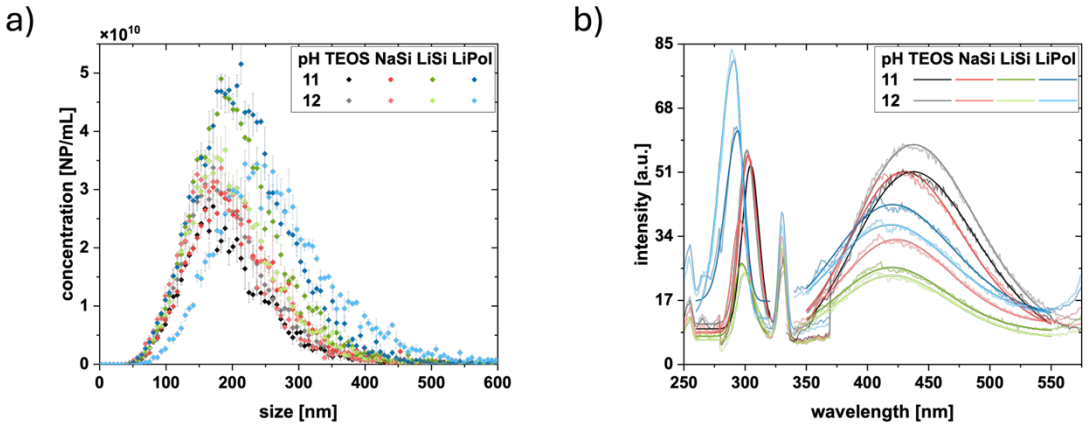


Figure SIII-11. (a) NTA measurements of $ZnSxSiO_2$ particles derived from mixtures with [Si]/[M] = 1, but differing in silica source and synthesis pH. (b) Fluorescence measurements (λ_{exc} = 300 nm, λ_{em} = 430 nm) and corresponding fit functions.

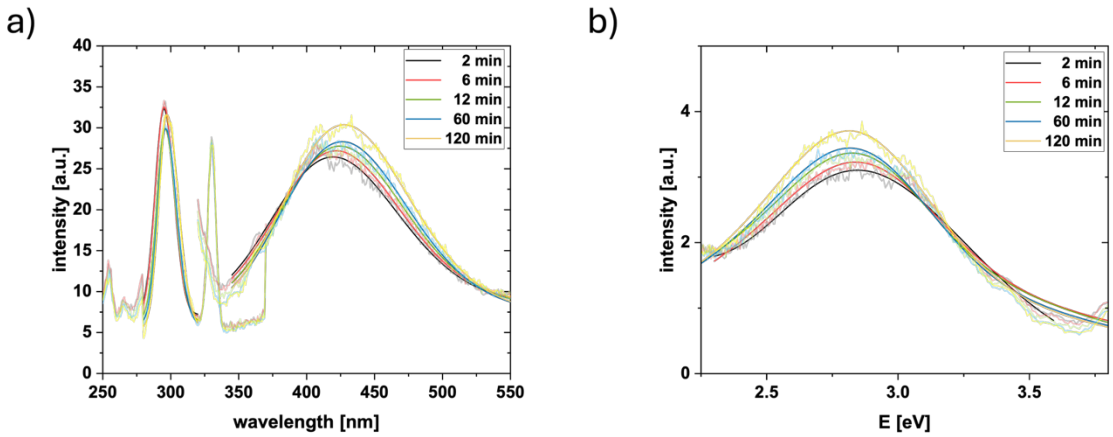


Figure SIII-12. (a) Fluorescence measurements (λ_{exc} = 300 nm, λ_{em} = 430 nm) of $ZnSxSiO_2$ particles derived from mixtures with [Si]/[M] = 1, TEOS as silica source, a pH of 11, but differing hydrolysis times. (b) Respective transformed emission spectra and corresponding fit functions.

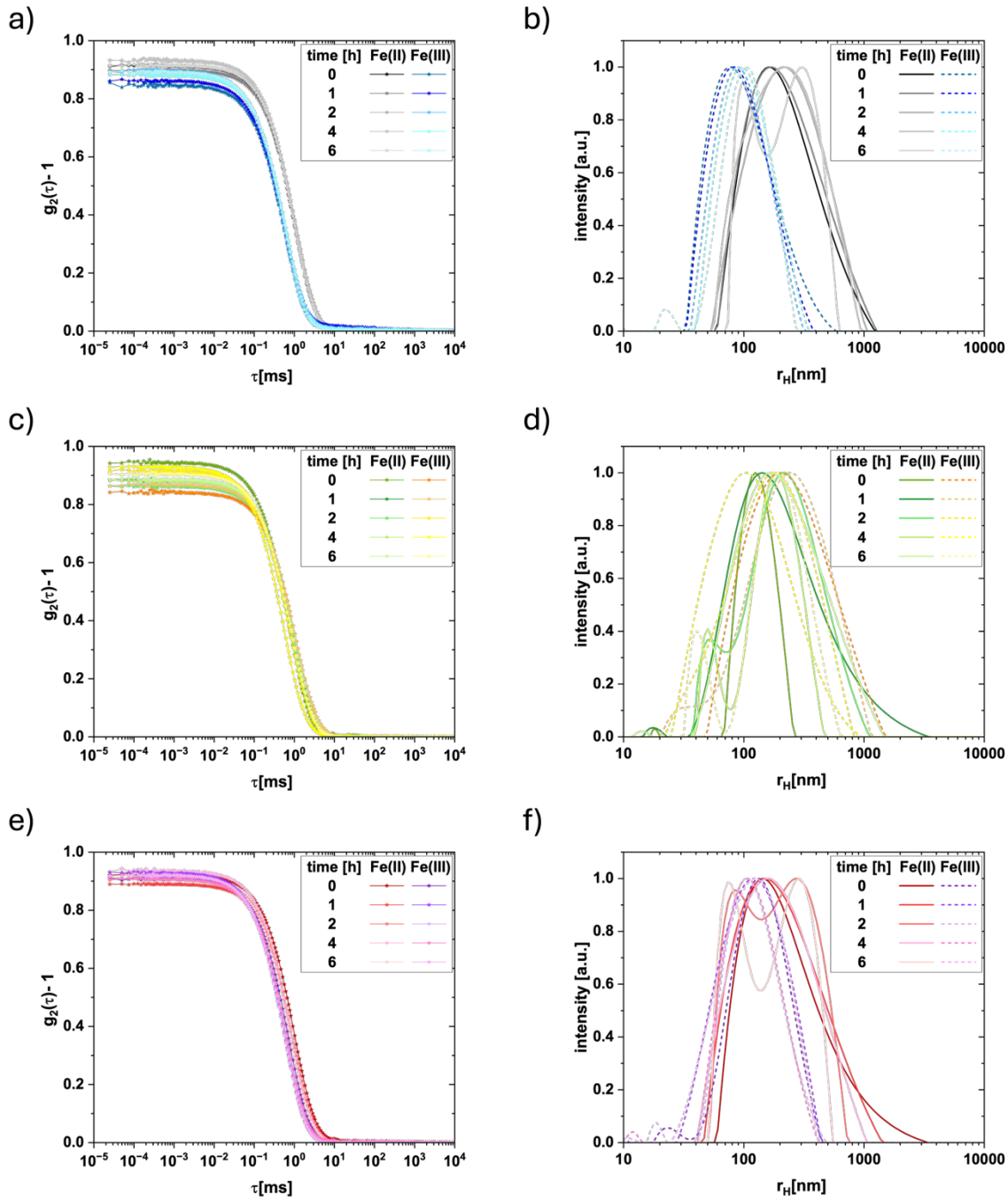


Figure SIII-13. DLS measurements of $FeSxSiO_2$ samples derived from a synthesis at a pH of 11 and [Si]/[Fe]-ratio. (a) [Si]/[Fe] = 0.5, (c) [Si]/[Fe] = 1, and (e) [Si]/[Fe] = 2. (b), (d), and (f) unweighted size distribution derived from the respective DLS measurements shown in (a), (c), and (e) using the CONTIN algorithm [38].

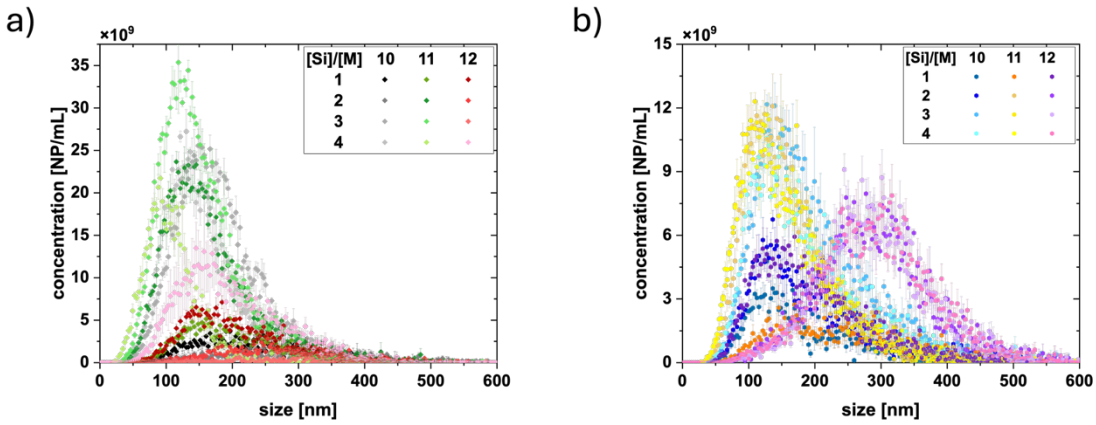


Figure SIII-14. NTA measurements of (a) $ZnSxSiO_2$ and (b) $CdSxSiO_2$ particles derived from mixtures with differing [Si]/[M] ratio at differing pH values.

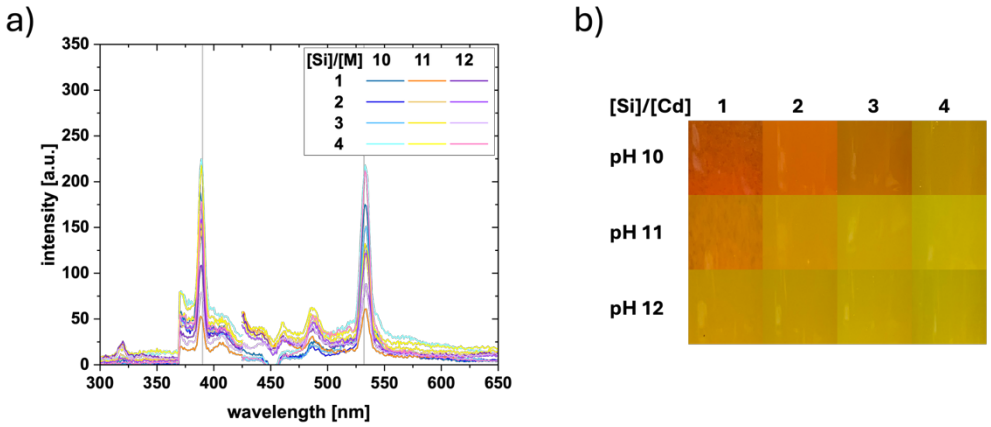


Figure SIII-15. (a) Fluorescence spectra (λ_{exc} = 390 nm, λ_{em} = 532 nm) for $CdSxSiO_2$ particles derived from mixtures with differing [Si]/[M] ratio at differing pH values. (b) Visual appearance of the synthesized samples dispersed in their native solution.

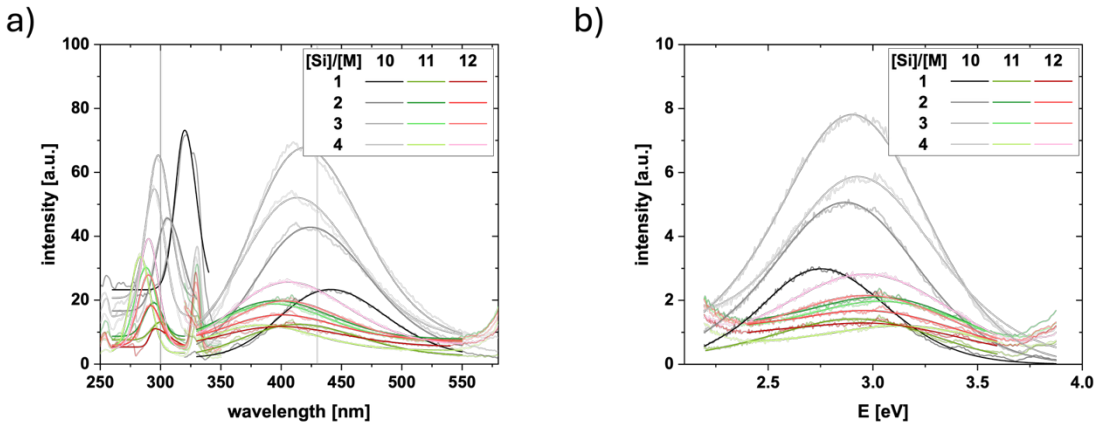


Figure SIII-16. (a) Fluorescence spectra (λ_{exc} = 300 nm, λ_{em} = 430 nm) for $ZnSxSiO_2$ particles derived from mixtures with differing [Si]/[M] ratio at differing pH values. (b) Respective transformed emission spectra and fit functions.

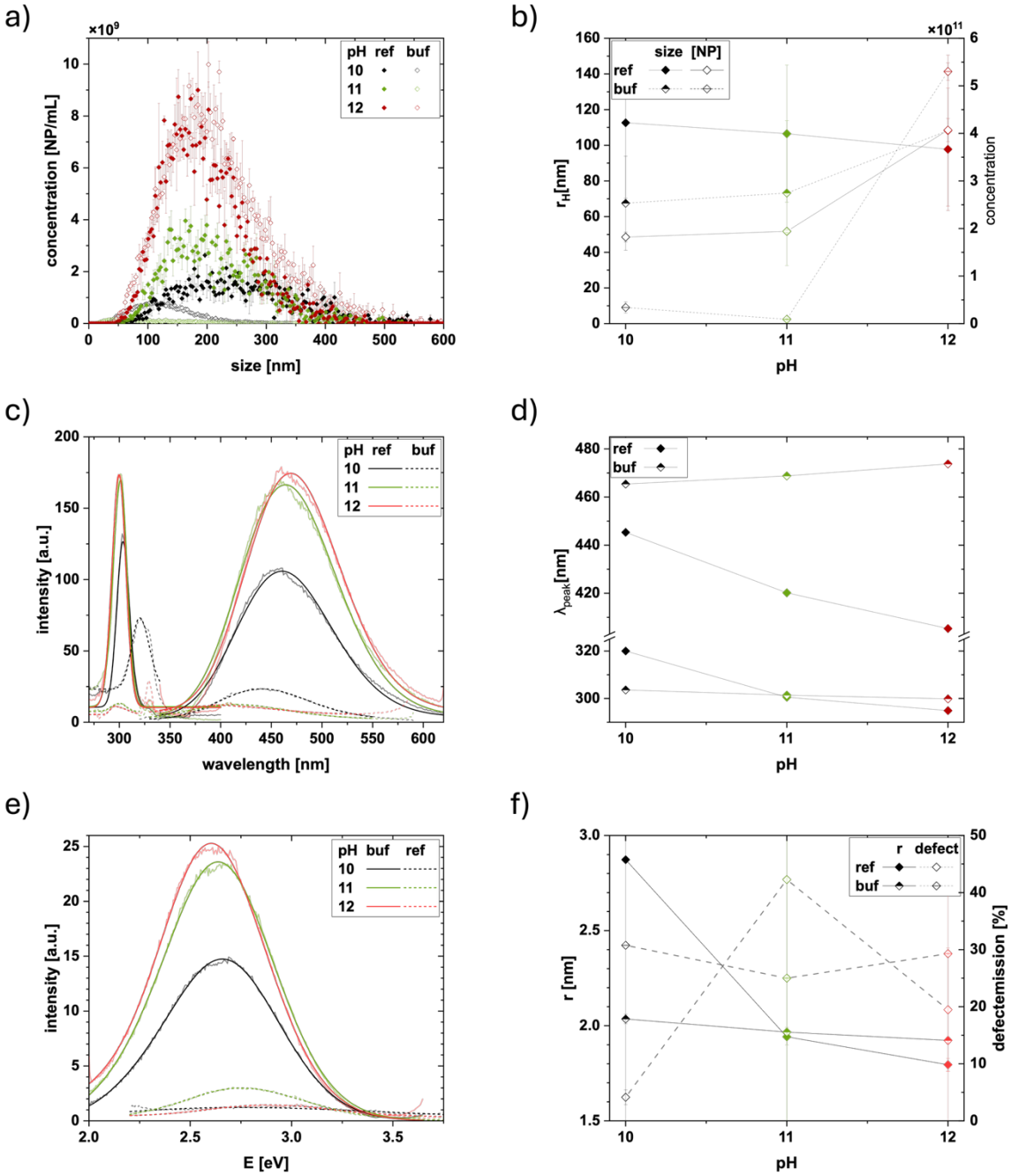


Figure SIII-17. (a) NTA measurements for $ZnSxSiO_2$ particles derived from solutions with [Si]/[Zn] = 1, at differing pH values in buffered and unbuffered solutions. (b) Evaluated hydrodynamic radii and concentrations derived from the NTA measurements. (c) Fluorescence (λ_{exc} = 300 nm, λ_{em} = 440 nm) measurement with corresponding fits and (d) evaluation of peak emission/excitation wavelengths. (d) Transformed emission spectra and corresponding fits. (e) QD size calculated using the Brus equation and DE determined by fitting the tail of the transformed emission spectra.

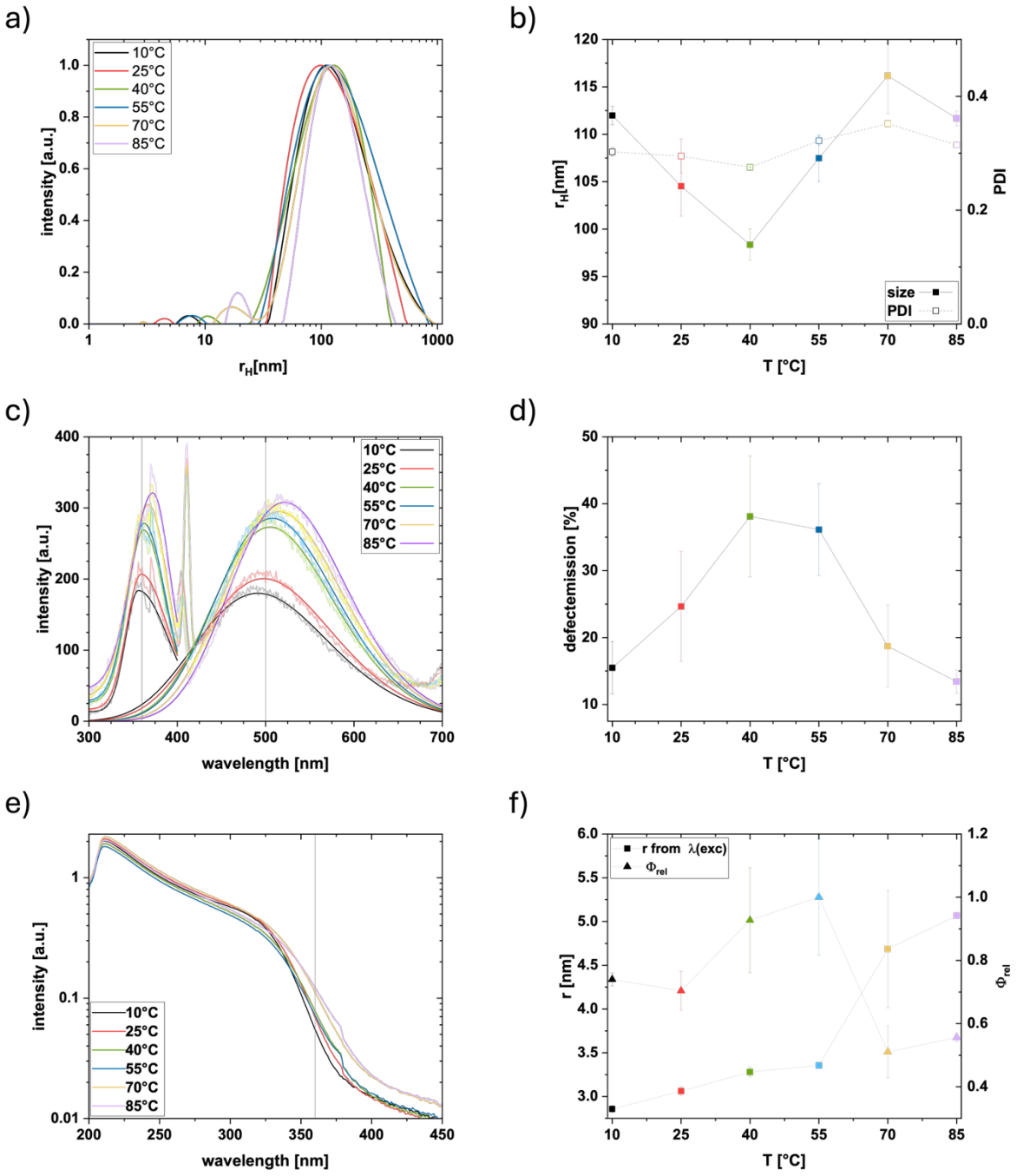


Figure SIII-18. Measurements for $Zn_{0.8}Cd_{0.2}SxSiO2$ particles derived from solutions with [Si]/[Zn] = 1, a pH value of 11 at differing synthesis temperatures. (a) Unweighted size distributions derived from DLS measurements using the CONTIN algorithm. (b) Hydrodynamic radius and PDI derived from DLS measurements. Shown values are averages of multiple measurements to highlight trends. (c) Fluorescence (λ_{exc} = 360 nm, λ_{em} = 500 nm) measurements and corresponding fits. (d) DE determined by fitting the emission tail of the transformed emission spectra. (e) UV/vis measurement. (f) QD size determined using the Brus equation and relative quantum yield.

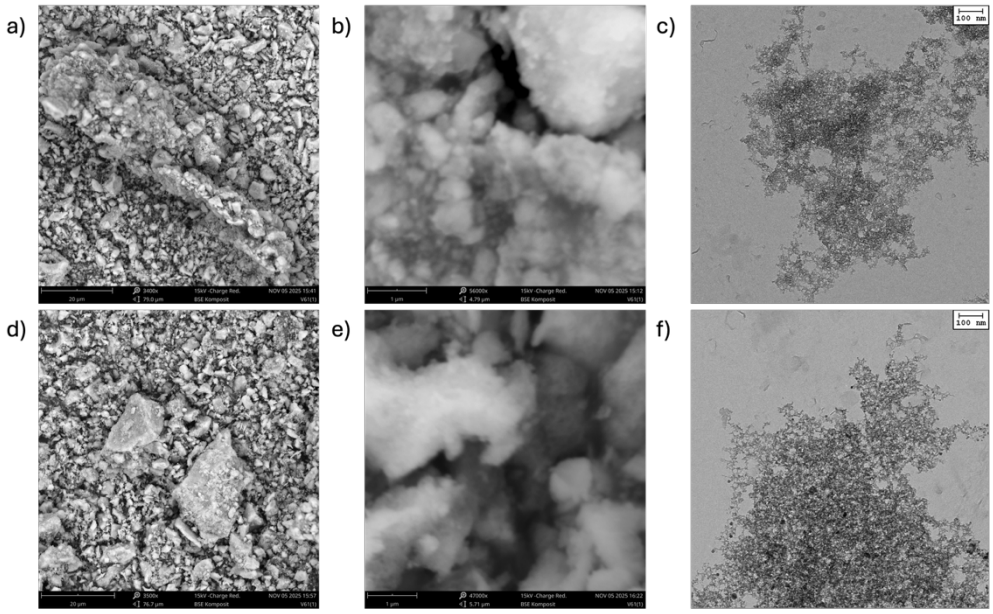


Figure SIII-19. SEM and Tem micrographs for $ZnCdSxSiO_2$ particles derived from solutions with [Si]/[Zn] = 2, a pH value of 11 at (a), (b), (c) 10°C and (d), (e), (f) 85°C. The scale bars correspond to (a) and (d) 20 µm, (b) and (e) 1 µm, and (c) and (f) 100 nm, respectively.

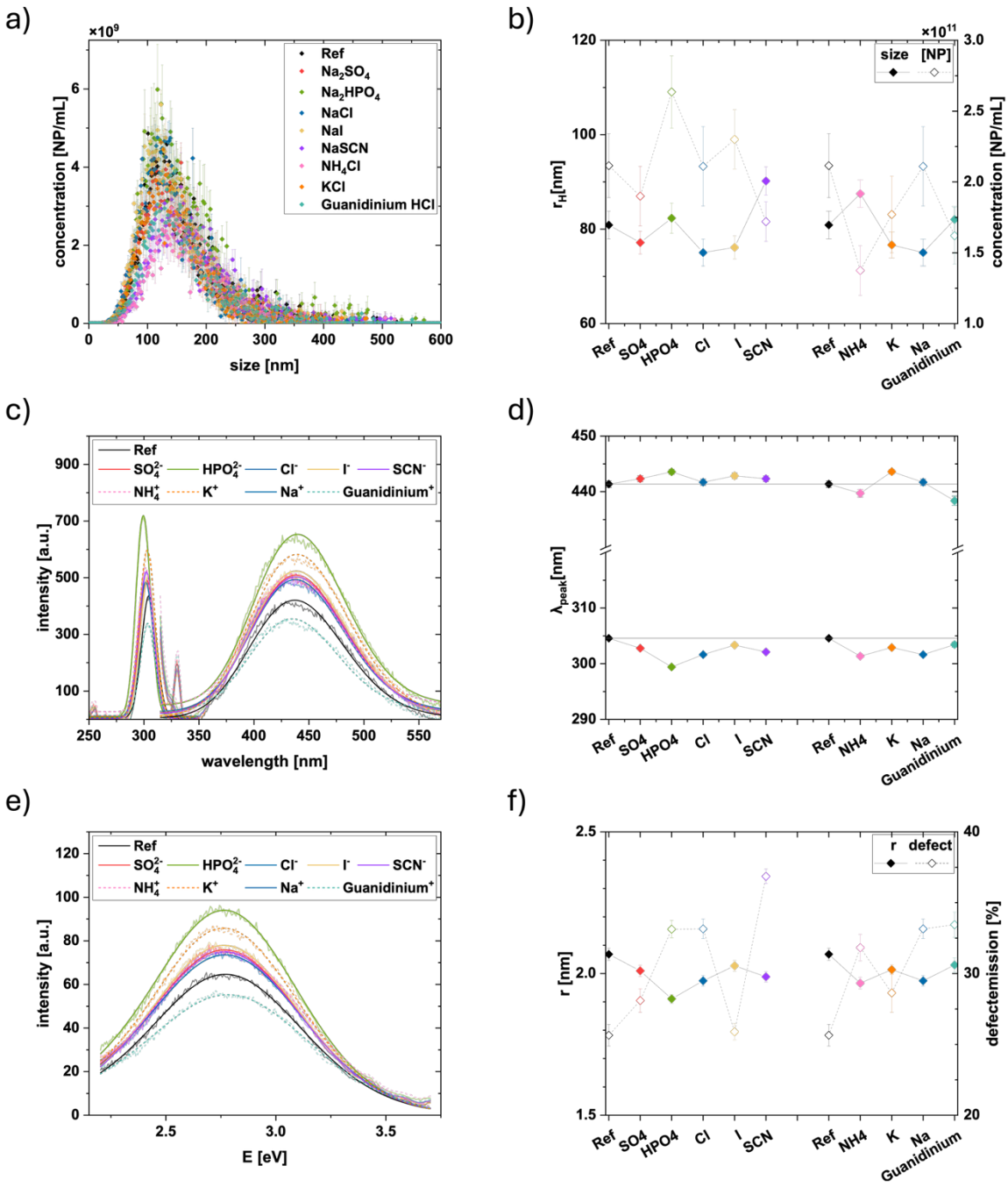


Figure SIII-20. (a) NTA measurements for $ZnSxSiO_2$ particles derived from solutions with [Si]/[Zn] = 2, a pH value of 11 and differing added ions from differing positions in the Hofmeister series. (b) Evaluated hydrodynamic radii and concentrations derived from the NTA measurements. (c) Fluorescence (λ_{exc} = 300 nm, λ_{em} = 440 nm) measurement and corresponding fits and (d) evaluation of peak emission/excitation wavelengths. (e) Transformed emission spectra and corresponding fits. (f) QD size calculated using the Brus equation and DE determined by fitting the tail of the transformed emission spectra.

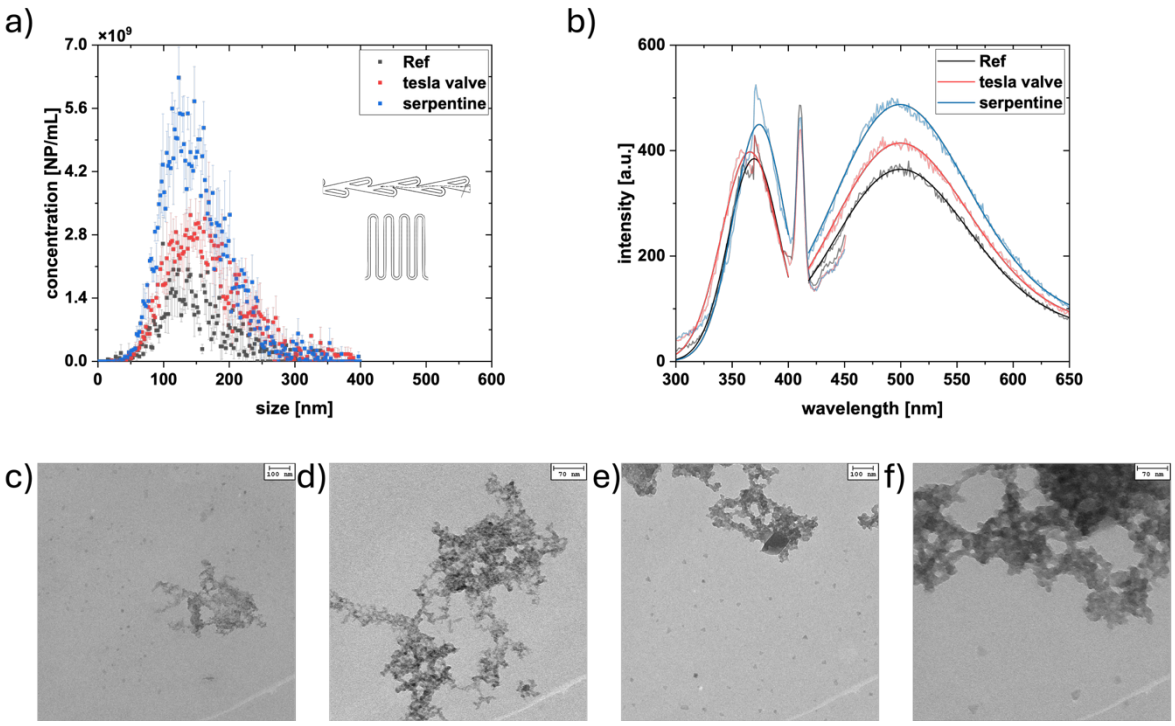


Figure SIII-21. (a) NTA measurements for $Zn_{0.8}Cd_{0.2}SxSiO_2$ particles derived from a modified synthesis using a microfluidic system (Q_S = 0.05 mL/min, Q_M = 0.1 mL/min) at a pH value of 11 with a final ratio of [Si]/[M] = 2. Schematic depictions of the used microfluidic device (flow from left to right) from top to bottom: tesla valve, serpentine. (b) Fluorescence (λ_{exc} = 360 nm, λ_{em} = 500 nm) measurement and corresponding fits. (c-f) TEM micrographs of the particles derived from (c), (d) tesla valve and (e), (f) serpentine. The scale bars correspond to 100 nm for (c) and (e) and 70 nm for (d) and (f), corresponding to a magnification of 13000x and 28000x respectively.

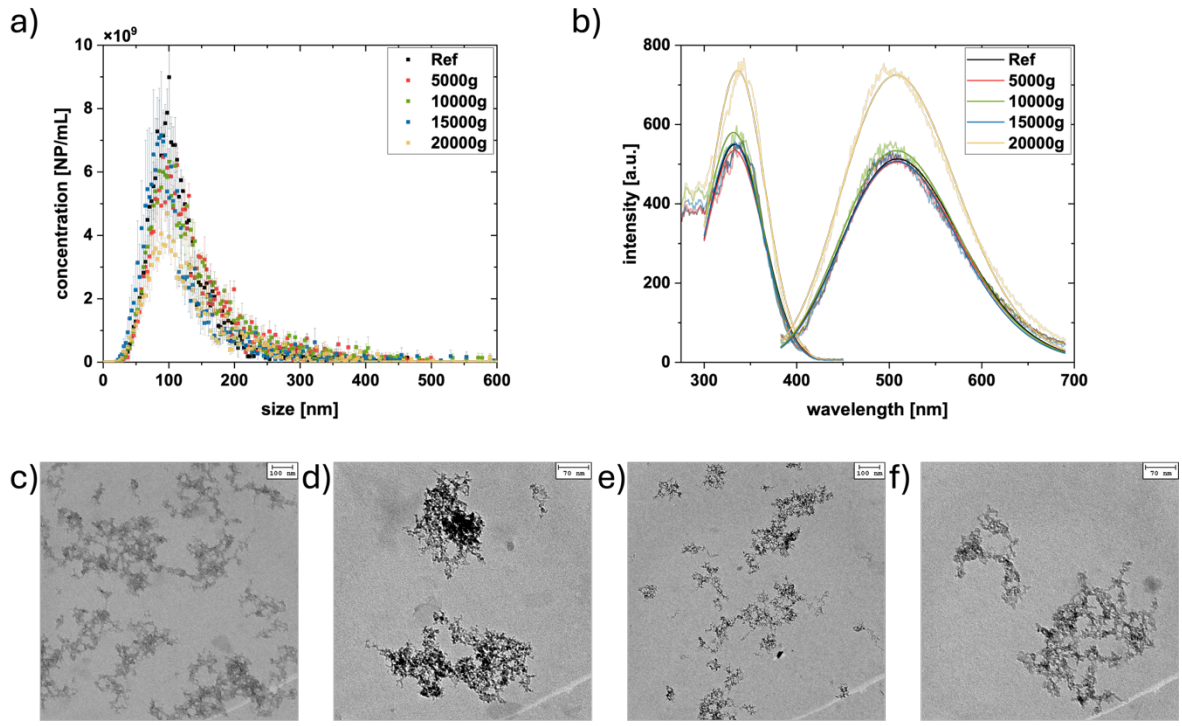


Figure SIII-22. (a) NTA measurements for $Zn_{0.8}Cd_{0.2}SxSiO_2$ particles derived from solutions with [Si]/[M] = 2 at a pH value of 11 before and after sequential centrifugation at increasing rotational speeds. (b) Fluorescence (λ_{exc} = 360 nm, λ_{em} = 500 nm) measurement and corresponding fits. (c-f) TEM micrographs of particles derived from centrifugation steps at (c), (d) 5000g and (e), (f) 20000g. The scale bars correspond to 100 nm for (c) and (e) and 70 nm for (d) and (f), corresponding to a magnification of 13000x and 28000x respectively.

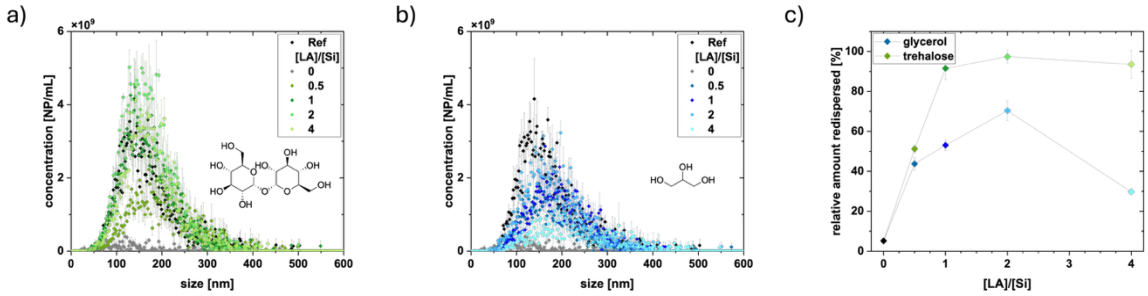


Figure SIII-23. NTA measurements for $ZnSxSiO_2$ particles derived from solutions with [Si]/[M] = 2 at a pH value of 11 before and after lyophilization. Differing amounts of lyoprotective agent (LA) (a) trehalose, (b) glycerol were added before the lyophilization. The structural formulas of the used LA are shown in (a) and (b). (c) Relative redispersed amount of particles after lyophilization at differing [LA]/[Si] ratios.

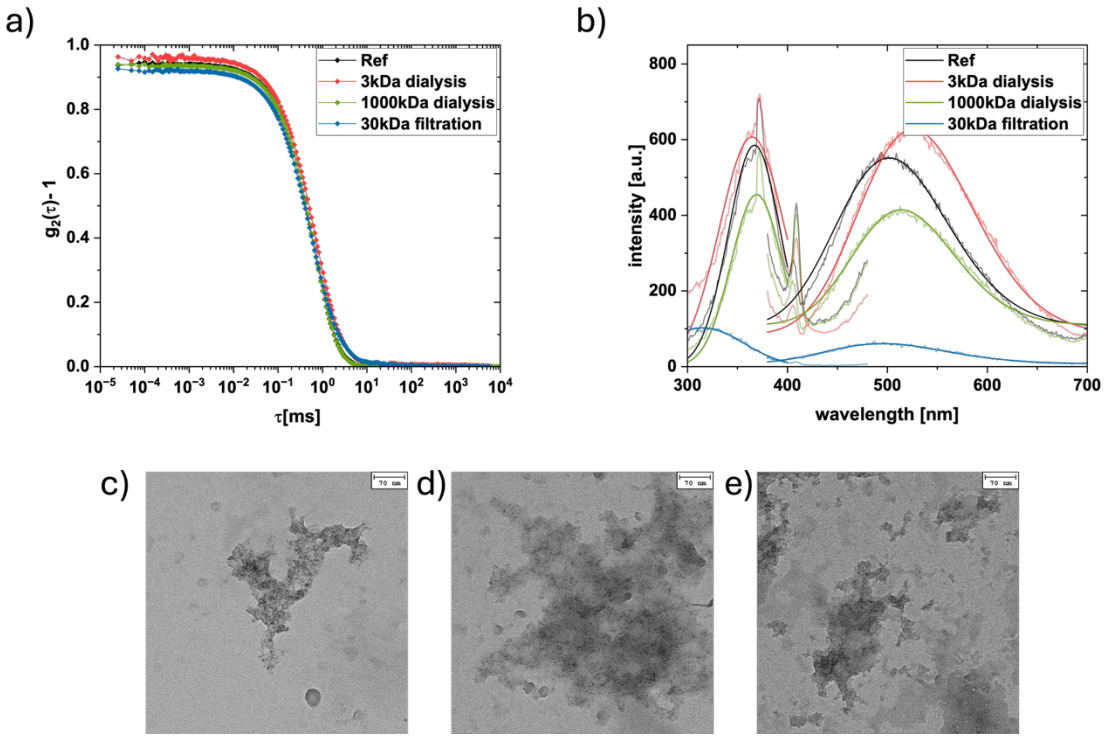


Figure SIII-24. (a) DLS measurements of $Zn_{0.8}Cd_{0.2}SxSiO_2$ particles derived from mixtures with [Si]/[Zn] = 2 at a pH value of 11 before and after dialysis/filtration. (b) Fluorescence (λ_{exc} = 360 nm, λ_{em} = 500 nm) measurement and corresponding fits. (c-e) TEM micrographs of dialyzed particles at a MWCO of (c) 3kDa, (d) 1000kDa and of filtrated particles (e) using a 30kDa ultracentrifuge filter. Scale bars correspond to 70 nm and a magnification of 28000x.

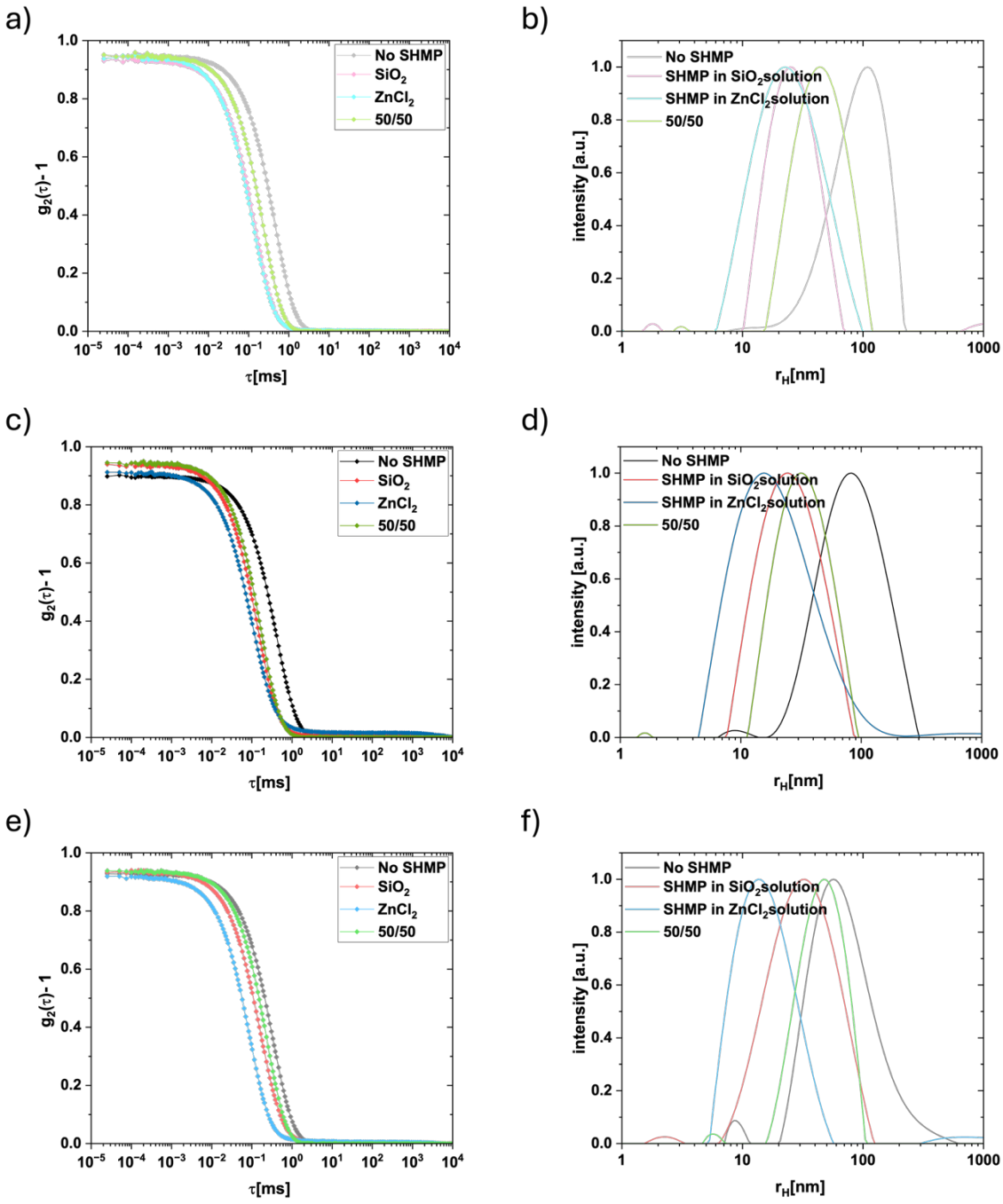


Figure SIII-25. DLS measurements of $ZnSxSiO_2$ samples derived from a synthesis with a [Si]/[Zn] = 2 at (a) pH 10, (b) pH 11, and (c) pH 12. Unweighted size distribution derived from the respective DLS measurements shown in (a), (b), and (c) using the CONTIN algorithm [38].

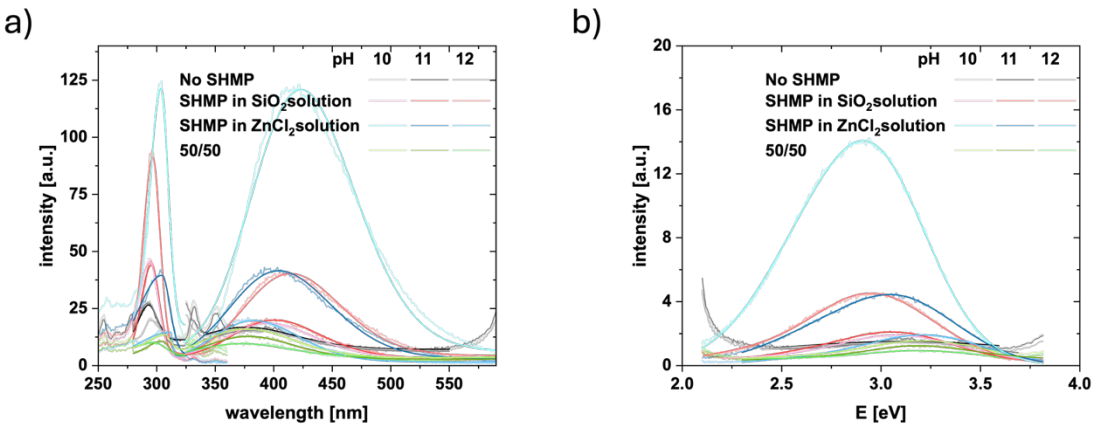


Figure SIII-26. Fluorescence spectra (λ_{exc} = 300 nm, λ_{em} = 430 nm) for $ZnSxSiO_2$ particles derived from mixtures with [Si]/[M] = 2 and [SHMP]/[Si] = 2 with differing SHMP positions at differing pH values. (b) Respective transformed emission spectra and fit functions.

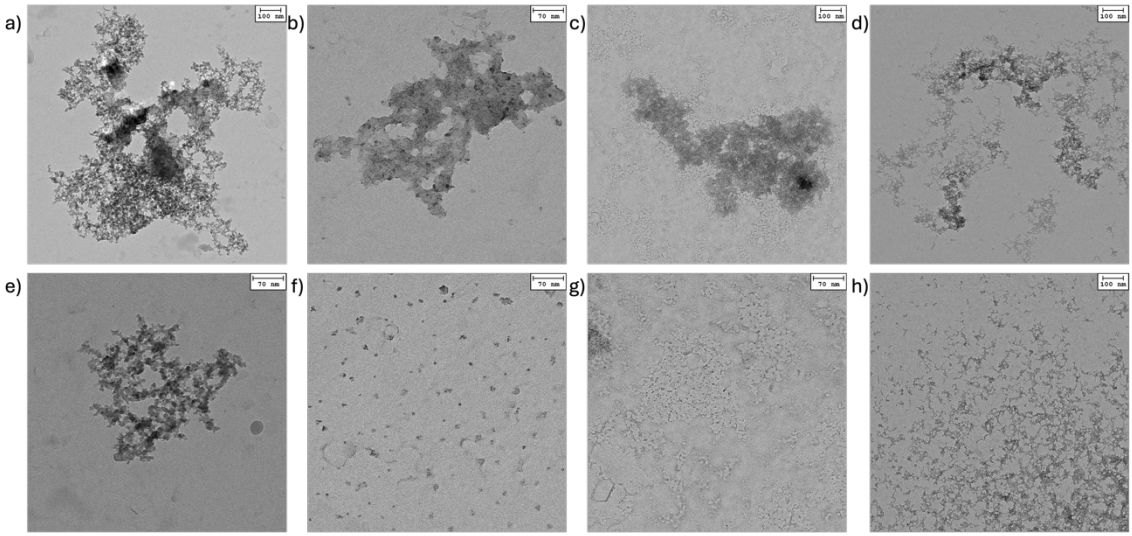


Figure SIII-27. TEM micrographs for $ZnSxSiO_2$ particles derived from mixtures with [Si]/[M] = 2 and [SHMP]/[Si] = 2 with differing SHMP positions. (a) and (e) reference, (b) and (f) SHMP in silica containing solution, (c) and (g) SHMP in metal containing solution, and (d) and (h) 50/50 in both, silica and metal containing solution. The scale bar corresponds to 100 nm for (a), (c), (d), and (h) with a magnification of 13000x, and to 70 nm for (b), (e), (f), and (g) with a magnification of 28000x.

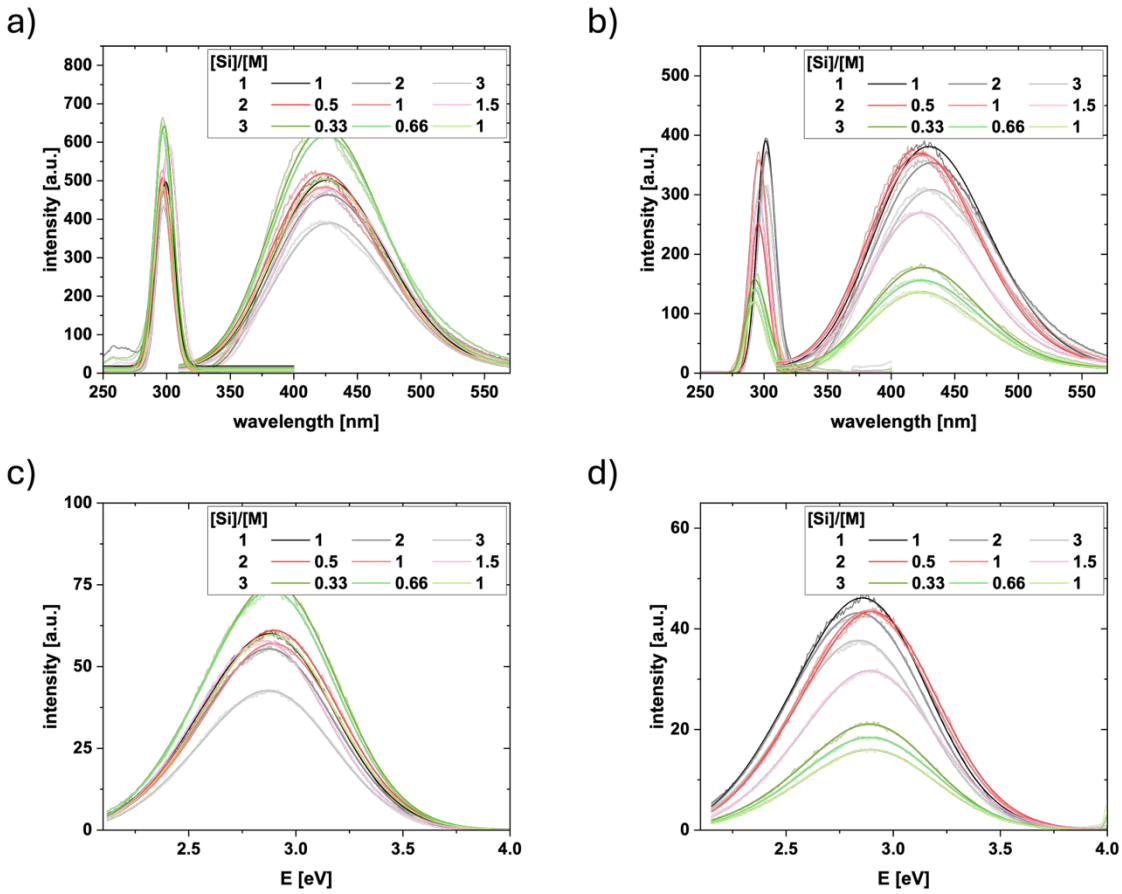


Figure SIII-28. Fluorescence spectra (λ_{exc} = 300 nm, λ_{em} = 430 nm) for $ZnSxSiO_2$ particles derived from mixtures with differing [Si]/[M] ratio and differing [SHMP]/[Si] ratios at (a) pH 11 and (b) pH 12. (c) and (d) Respective transformed emission spectra and fit functions.

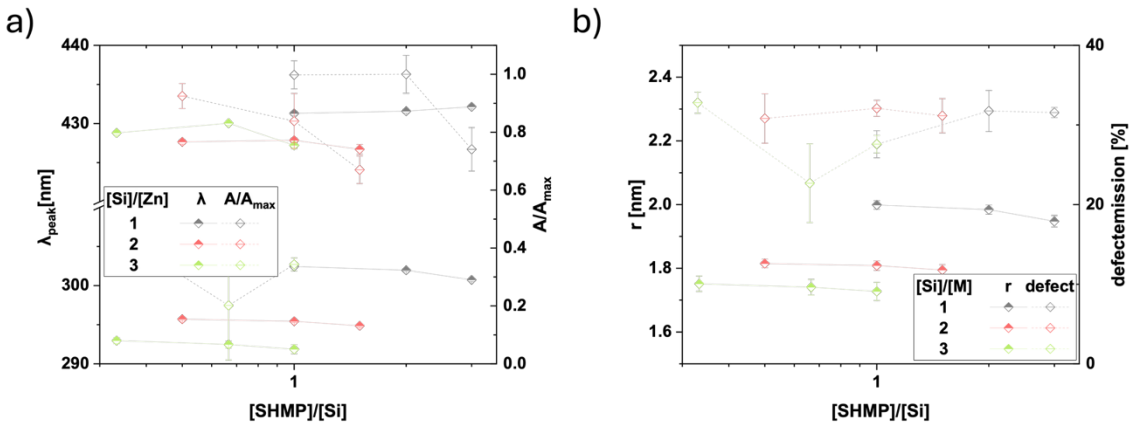


Figure SIII-29. Emission and excitation peak of fitted fluorescence spectra for samples derived from syntheses at pH 12 (cf. **Figure SIII-28b**). (b) QD radius derived from calculation using the Brus equation and DE determined by fitting the emission tail of the transformed emission spectra (cf. **Figure SIII-28d**).

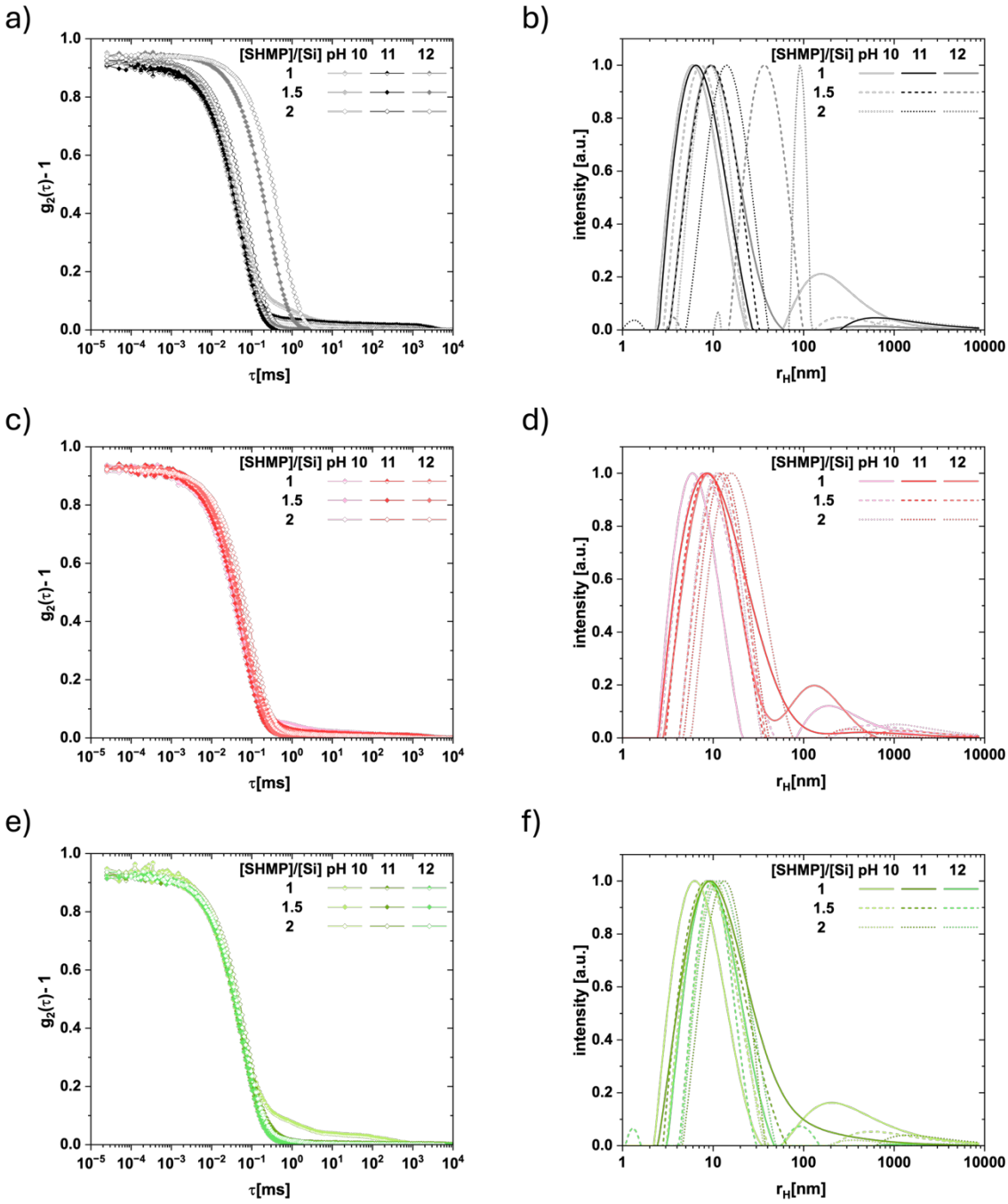


Figure SIII-30. DLS measurements of $ZnSxSiO_2$ samples derived from a synthesis with varying pH and [SHMP]/[Si]-ratio. (a) [Si]/[Zn] = 1, (b) [Si]/[Zn] = 2, and (c) [Si]/[Zn] = 3. Unweighted size distribution derived from the respective DLS measurements shown in (a), (b), and (c) using the CONTIN algorithm [38].

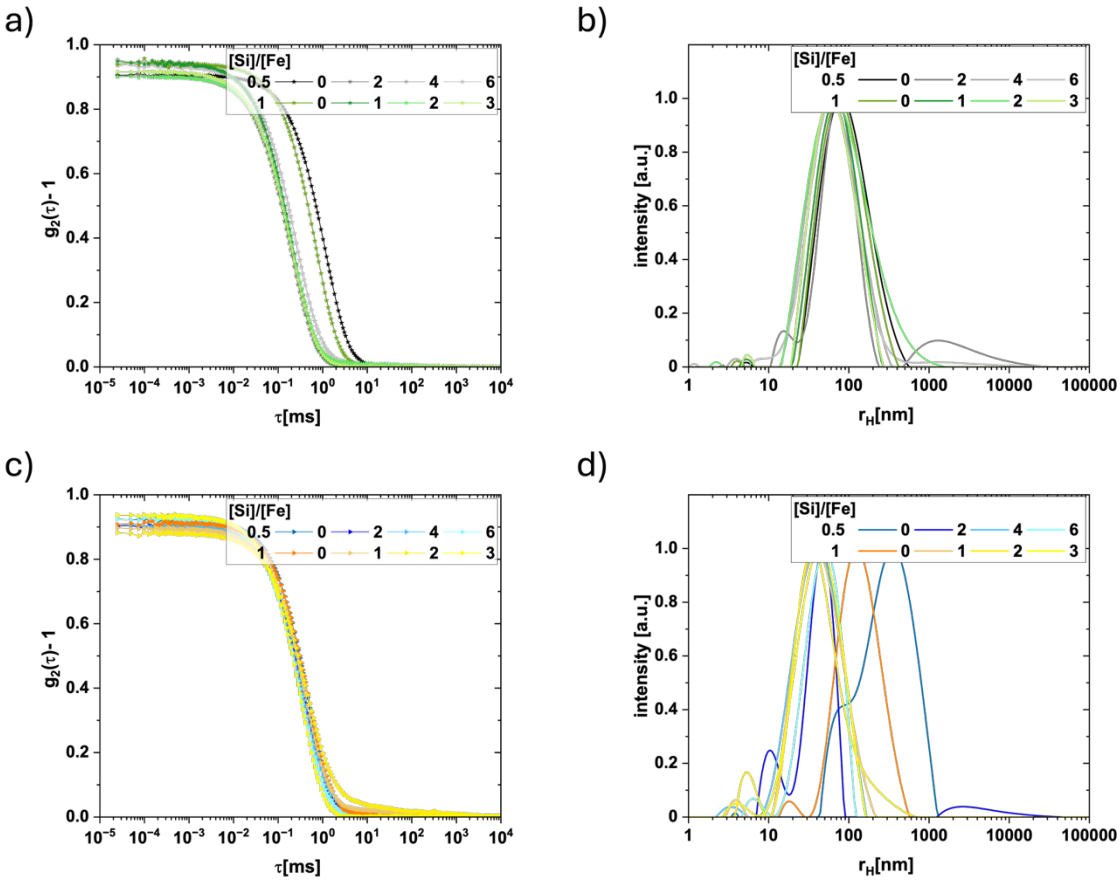


Figure SIII-31. DLS measurements of $FeSxSiO_2$ samples derived from a synthesis with varying pH and [SHMP]/[Si]-ratio. (a) particles derived from Fe(II), (c) particles derived from Fe(III). Unweighted size distribution derived from the respective DLS measurements shown in (b), and (d) using the CONTIN algorithm [38].

Chapter IV. Heterogeneous Fenton Reaction at Neutral pH Values Catalyzed by One-Pot Synthesized Iron Oxide/Silica Core Shell Nanoparticles

4.1 Abstract

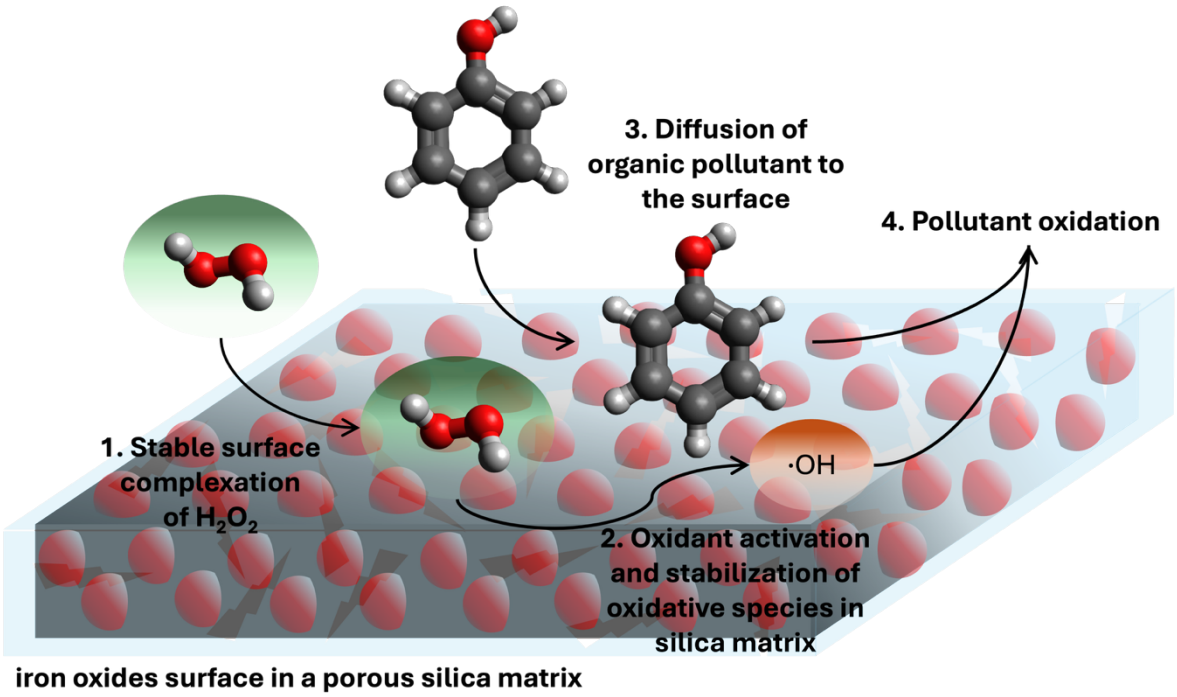


Figure IV-1. Graphical Abstract: Visualization of surface Fenton reaction on a silica coated iron oxide surface at circumneutral pH values. The hydroxyl radicals are generated on the iron oxides surface and the oxidants are stabilized afterwards by the silica matrix. They can then be used to oxidize organic pollutants such as phenol. Inspired by ref [1].

The use of iron oxide catalysts in advanced oxidation processes (AOP) such as the conversion of hydrogen peroxide to hydroxyl radicals, is relatively inefficient at circumneutral pH values. Silica containing iron oxide nanoparticles derived from a one pot process show higher conversion rates and greater harness of oxidative species compared to those made of plain iron oxide. The formed particles (50-200 nm) were characterized by TEM, SEM, BET, DLS and used in a reaction to degrade phenol. In a period of 8 h, all particles investigated showed higher phenol degradation while degrading significantly less hydrogen peroxide. The higher

conversion rate is attributable to the interaction of iron with the silica shell that alters the redox processes favoring the formation of more strong oxidants during H_2O_2 decomposition. Production of such nanomaterials by a unelaborate, environmentally friendly, upscalable route is particularly appealing due to its simplicity in a one-pot process.

Parts of this chapter are published in *ACS Omega* (Rödig, B.; Nagin, D.; Müller, R.; Kunz, W. Heterogeneous FentonReaction at Circumneutral pHValues Catalyzed by Novel One-Pot Synthesized Iron Oxide/Silica Core–ShellNanoparticles. ACS Omega 2026. https://doi.org/10.1021/acsomega.6c06904, Figures and text reproduced under the terms of the CC BY 4.0 license).

Contributions to experimental work:

- Bastian Rödig: Conceptualization, Data Evaluation, Experimental work
- Lukas Vala, Daniel Nagin, Anita Fuchs, Verena Schlüter, Elias Wild, Anna Selmeier, Anna Mändl, Olga Gebert, Rainer Müller: Experimental work

4.2 Introduction

4.2.1 The Fenton Reaction

Iron is the fourth most common element in the earth's crust and occurs in various oxides/hydroxides, which can be used as catalysts in countless reactions [2]. One of the possible applications is the use as catalyst for advanced oxidation processes (AOPs) to oxidize pollutants in water, especially useful in the treatment of wastewater [3,4]. AOPs are typically characterized by the hydroxyl radical ($\cdot OH$) which bears a high standard reduction potential of E^0 = 2.80 V which is even higher than that for atomic oxygen (E^0 = 2.42 V). Therefore, it is very effective in the degradation of contaminants, that are difficult to break up in conventional methods [2]. A prominent example for AOPs is the so-called Fenton reaction, a reaction of iron and H_2O_2 first discovered in 1894. In this reaction, a soluble iron salt, most commonly iron (II) sulfate, is the catalyst for the decomposition of the H_2O_2 at acidic pH values of 3 or less. At higher pH values iron hydroxide formation occurs, while at lower pH value iron complexes form that reduce their activity [5]. The commonly accepted mechanism of the catalytic decomposition of H_2O_2 in the presence of solubilized Fe^{2+} has been described in the literature on the basis of the classical Haber Weiss mechanism [2,6].

$$H_2O_2 + Fe^{2+} \rightarrow Fe^{3+} + OH^- + HO\cdot \qquad \text{(IV-1)}$$

When Fe^{3+} serves as the initial iron species, the process is referred to as Fenton-like process. Numerous different decomposition mechanisms initiated by Fe^{3+}, such as the Weiss mechanism for decomposition of H_2O_2 on metal surfaces [7], have been proposed in the past. Typically, these reactions cannot appropriately describe the mechanism over iron oxide surfaces (surface bound iron: $\equiv Fe^{III}/\equiv Fe^{II}$). The more complex and more accurate descriptions can be simplified into the following reactions [8]:

$$\equiv Fe^{III} - OH + H_2O_2 \rightleftharpoons (H_2O_2)_S \qquad \text{(IV-2)}$$

$$(H_2O_2)_S \rightarrow \equiv Fe^{II} + H_2O + HO_2\cdot \qquad \text{(IV-3)}$$

$$\equiv Fe^{II} + H_2O_2 \rightarrow \equiv Fe^{III} - OH + \cdot OH \qquad \text{(IV-4)}$$

$$HO_2\cdot \rightleftharpoons H^+ + O_2^{\cdot -} \qquad \text{(IV-5)}$$

$$\equiv Fe^{III} - OH + HO_2\cdot/O_2^{\cdot -} \rightarrow Fe^{II} + H_2O/OH^- + O_2 \qquad \text{(IV-6)}$$

In both cases the decomposition results in reactive oxygen species (ROS), including hydroxyl radicals ($\cdot OH$), hydroperoxyl radicals ($HO_2\cdot$), and potentially surface-associated oxidizing intermediates (e.g. $(H_2O_2)_S$), which can be used for further oxidation of organic compounds [8–10]. The reaction can be differentiated into homogeneous and heterogeneous Fenton-(like) reactions for soluble and insoluble iron species such as iron sulfate and iron (hydr)oxides, respectively.

The main limitation of the homogeneous reaction is the strict control of the pH, which should not exceed a value of 3 to prevent the formation of iron sludge. During the reaction the continuous neutralization has to be countered by the continuous addition of acid [11]. The heterogeneous reaction can overcome these drawbacks but also has its own problems. As the iron (hydr)oxides are stable in a broader pH range, the heterogeneous reaction can be carried out in a broader pH range and even at neutral pH, sparing the need for acidification and avoiding the formation of iron sludge completely. Also, the catalyst can be easily recycled and regenerated [2]. Although heterogeneous reactions are considered dominant under circumneutral conditions, dissolution of iron species may contribute to the overall oxidation processes. This aspect is especially relevant when evaluating catalyst performance.

For the heterogeneous Fenton(-like) reactions, various properties of the catalysts are important, such as the oxidation state of the iron [12], the crystallinity [13–15], and the surface area [14,15]. These can already be optimized during synthesis. Also, the doping with other transition metals or the implementation of the iron oxide in secondary structures is possible and can improve the catalytic ability. Attempts of incorporating iron oxides into silica/aluminum bearing secondary structures greatly increases the lifetime of ROS through stabilization by surface complexation [1,16,17].

4.2.2 Reaction Kinetics of Heterogeneous Fenton Reactions

For heterogeneous Fenton reactions, a sequence of adsorption, electron-transfer, and oxidation occurs at the catalysts surface. The observed reaction rate depends not only on the iron reactivity but also on the surface properties such as the number of active sites, crystallinity, and adsorption behavior of the peroxide [13–15,18].

The catalytic decomposition of hydrogen peroxide is the first step of the heterogeneous Fenton process. Although several elementary steps have been proposed, the overall decomposition on iron oxides is described using a Langmuir-Hinshelwood approach. This model simplifies to a pseudo-first-order kinetic with respect to the hydrogen peroxide concentration [8,19,20].

As the hydrogen peroxide adsorbs onto the catalysts surface, adsorption phenomena influence the observable reaction kinetics. Heterogeneous Fenton reactions are frequently described using the Langmuir-Hinshelwood model, assuming the adsorption of reactants before reaction with a rate r [19,20]:

$$r = \frac{kKc}{1 + Kc} \tag{IV-12}$$

with the intrinsic surface reaction constant k, the adsorption equilibrium constant K, and the reactant concentration c. Usually employed concentrations in Fenton reactions are in the low concentration regime ($Kc << 1$) resulting in pseudo-first-order kinetics ($r = kKc$) The reaction can then be reduced to a pseudo-first-order kinetics, as the rate-limiting step has been proposed to be the diffusion of the phenol to the surface complex [1,21]. For equal catalyst loading the reaction rate can be approximated by:

$$-\frac{d[H_2O_2]}{dt} = k_{obs,H_2O_2}[H_2O_2] \tag{IV-7}$$

$$\ln\left(\frac{[H_2O_2]}{[H_2O_2]_0}\right) = -k_{obs,H_2O_2}t \tag{IV-8}$$

with k_{obs,H_2O_2} as the apparent first-order constant.

The reactive oxygen species, including hydroxyl radicals and other surface-associated oxidants, can oxidize organic contaminants. The oxidation of organic pollutants can be expressed generally as:

$$\mathrm{RH + HO\cdot \rightarrow R\cdot + H_2O \rightarrow\rightarrow CO_2 + H_2O} \tag{IV-9}$$

The organic pollutant reacts with the hydroxyl radical creating water and a destabilized pollutant radical that then further decomposes via various rather complex steps until complete mineralization [22].

The degradation of pollutants is commonly described as pseudo first order kinetics. This approximation is justified when the concentration of reactive surface species remains constant throughout the reaction. Under these conditions, pollutant degradation becomes limited by the

transport of pollutant to the reactive surface rather than by the generation of hydroxyl radicals themselves [1,17].

$$-\frac{d[RH]}{dt} = k_{obs,RH}[RH] \quad \text{(IV-10)}$$

$$ln\left(\frac{[RH]}{[RH]_0}\right) = -k_{obs,RH}t \quad \text{(IV-11)}$$

with $k_{obs,RH}$ as the apparent first-order constant.

The resulting apparent rate constants can be used to compare the catalytic activities of different iron oxide materials. However, they do not represent the intrinsic reaction constants independent of adsorption effects [8]. Ultimately, any modification to the heterogeneous catalyst that alters adsorption equilibria, surface reactivity, or the lifetime of oxidizing species, may significantly influence the reaction kinetics.

4.2.3 Mechanism of Hydrogen Peroxide Activation on Silica-supported Iron Oxides

Silica-supported iron oxides can alter the adsorption and the lifetime of surface associated ROS. Consequently, the apparent decomposition rates differ substantially from those observed for unsupported iron oxides. Numerous studies reported significantly enhanced oxidant utilization efficiency for silica-supported iron oxides compared to unsupported iron oxides. Nevertheless, the underlying mechanism remains controversial [1,17,23,24].

One explanation for the enhanced performance is the increased dispersion of iron centers. Silica inhibits aggregation and reduces the particles size, resulting in a higher density of accessible surface iron sites. Consequently, a larger fraction of iron atoms participates in the hydrogen peroxide activation compared to bulk iron oxides [16,25].

Silica also may directly influence the interfacial reaction. Silanol groups near the iron surface site participate in hydrogen bonding with adsorbed peroxide and reactive iron species. This may delay desorption kinetics and facilitate charge transfer processes at the oxide-water interface. Additionally, silica surfaces exhibit lower reactivity towards radical scavenging, thereby reducing unproductive side reactions and increasing oxidant utilization [21,26–28]. Further, it was demonstrated that this way the diffusion of the pollutant to the surface-bound ROS can become the rate-determining step for the oxidation reaction [1]. (cf. **Figure IV-1**)

This concept differs significantly from typical Fenton catalysis, in which hydroxyl radicals are assumed to react immediately upon formation because of their extremely short lifetime in solution. The overall oxidation rate for silica-supported iron oxides is determined not only by the generation of the ROS but also by their stabilization and accessibility on the catalysts surface [23,29].

The exact nature of oxidizing species remains under debate. Nevertheless, the effects of silica are a combination of colloidal stabilization, enhanced iron dispersion, radical scavenging suppression, and stabilization of ROS on the surface [1,23,24,26].

4.2.4 Silica-supported Iron Oxides Derived from a One-Pot Coprecipitation Reaction

The synthesis of such particles usually includes multiple steps [12,17]. In this work, variations of a simple one-pot approach are used for the synthesis of silica-coated iron sulfide/carbonate nanoparticles [30,31]. (see **Chapter III**)

The as-formed particles can then be further processed into iron oxides by either calcination of the carbonates [32,33] (**Eqn. IV-13** & **IV-14**) or with a reaction of atmospheric oxygen at elevated pH values for the sulfides [34] (**Eqn IV-15** & **IV-17**).

$$2\ FeCO_3 \xrightarrow{600°C} 2\ FeO\ + 2CO_2 \uparrow + \frac{1}{2}\ O_2 \xrightarrow{600°C} \alpha - Fe_2O_3 \quad \text{(IV-13)}$$

$$Fe_2(CO_3)_3 \xrightarrow{600°C} Fe_2O_3 + 3\ CO_2 \uparrow \quad \text{(IV-14)}$$

Depending on the temperature used for the calcination, different crystal structures of iron oxide can form even from amorphous starting material [32]. At elevated temperatures, the iron will also be oxidized by atmospheric oxygen resulting at a calcination temperature of 600°C in the most stable iron oxide α-Fe_2O_3, called hematite [32,35].

$$2\ FeS + 3\ O_2 + 4\ OH^- \longrightarrow 2\ Fe(OH)_2 + 2\ SO_4^{2-} \quad \text{(IV-15)}$$

$$4\ Fe(OH)_2 + O_2 + 2\ H_2O \longrightarrow 4\ Fe(OH)_3 \quad \text{(IV-16)}$$

$$Fe_2S_3 + 6\ O_2 + 6\ OH^- \longrightarrow 2\ Fe(OH)_3 + 3\ SO_4^{2-} \quad \text{(IV-17)}$$

$$2\ Fe(OH)_3 \longrightarrow Fe_2O_3 + 3\ H_2O \quad \text{(IV-18)}$$

For the iron sulfides, the reaction to the oxides occurs via the hydroxides. (**Eqn. IV-15** & **IV-17**) Depending on the starting oxidation state, a further oxidation takes place (**Eqn. IV-16**), before the condensation of the hydroxides results in the oxides (**Eqn. IV-18**) [34].

These reactions result in mostly amorphous iron oxide covered in a silica shell, which increases the total surface area and the colloidal stability, and allows size control of the primary iron oxide particles [31]. The optimal synthesis parameters for this application are determined by variation of pH, silicate concentration, addition of small molecules, change of iron precursors (Fe^{2+} or Fe^{3+}), and variation of primary precipitated particles.

The heterogeneous Fenton reaction, as a well-established catalytic system, was selected as a model reaction. Its performance strongly depends on the accessibility and reactivity of surface iron sites. Therefore, it is used for the evaluation of the catalytic accessibility with differing silica concentrations. Further, the reaction allows a quantitative assessment of catalytic activity by the individual decomposition rates. Consequently, it provides a convenient proof-of-concept to assess the functional applicability of the synthesized particles as oxidation catalysts.

4.3 Experimental

4.3.1 Materials

The following substances were used as received without further purification: ammonia solution 25% (NH_4OH, Supelco, >99%), citric acid monohydrate ($C_6H_8O_7$; Merck, >99.5), hydrochloric acid (1M HCl in water; Sigma-Aldrich, analytical grade), hydrogen peroxide (35% in water; Sigma-Aldrich), iron(II) chloride tetrahydrate ($FeCl_2 \cdot 4H_2O$; Sigma-Aldrich, ≥99%), iron(III) chloride hexahydrate ($FeCl_3 \cdot 6H_2O$; Carl Roth, >99%), methanol (CH_3OH; Sigma-Aldrich, >99.8%), 1,10-phenantroline ($C_{12}H_8N_2$, Sigma–Aldrich, ≥99%), phenol (Sigma-Aldrich, >99.9%), sodium carbonate (Na_2CO_3; Sigma-Aldrich, ≥99.8 %), sodium chloride (NaCl; Carl Roth, ≥99.8 %), sodium hexametaphosphate ($Na_6[(PO_3)_6]$, Fluka, >99.8%), sodium hydroxide (NaOH; Sigma-Aldrich, ≥98 %), sodium metasilicate (Na_2SiO_3; Sigma-Aldrich, >97%), sodium sulfide trihydrate ($Na_2S \cdot 3H_2O$; VWR, >60%), sulfuric acid (0.5M in water; Supelco, >95%), tetraethylorthosilicate ($Si[C_2H_5O]_4$, Sigma–Aldrich, >98%), trifluoroacetic acid (CF_3COOH; Sigma-Aldrich, >99%), and titanium(IV) oxysulfate solution (15% in water, Sigma-Aldrich, >99%). All solutions and dilutions were prepared using water taken from a Millipore system.

4.3.2 Apparatus

4.3.2.1 Synthesis of Particles

To avoid potential covalent attachment to the surface of glass vessels by silica condensation reactions, synthesis was carried out using plastic beakers. To 50 mL aqueous solutions containing varying amounts (5-20 mM) of sodium silicate or TEOS and 10 mM sodium sulfide or sodium carbonate the same volume of an aqueous solution of 10 mM iron chloride (Fe^{2+} or Fe^{3+}) was quickly added under vigorous stirring (700 rpm) at room temperature. Immediately after mixing, black (iron sulfide) or greenish (iron carbonate) suspensions of more or less finely dispersed precipitates were obtained.

In some variations, the pH of the silica containing solution is adapted to 9-12 and/or 5-15 mM SHMP was added. Also, for some samples small amounts of 35w% HF solution were added to etch up to 100% of the initial silica shell. Afterwards, the resulting particles were separated from synthesis residues by centrifugation in a Sigma 3-18KS centrifuge at 14000 rpm (20379 g) for 5 min at room temperature. After repeated washing with water they were redispersed using

an ultrasonic probe UP200Ht from Hielscher and the corresponding dispersions were lyophilized to obtain a dry powder. To convert the as-formed silica-coated iron carbonates into oxides, they were calcined in a Thermicon T oven from Heraeus under atmospheric pressure at 650 °C for at least 6 h. To convert the iron sulfides into oxides, they were stirred for at least 48 h to react with oxygen from the air before their workup.

4.3.2.2 Fenton Reactions

4.3.2.2.1 Oxidation of Phenol

All reactions were carried out at room temperature in 20 mL reaction medium with open reaction vessels. Reactions were buffered with 1 mM citric acid at pH 5.3 adjusted using 1M NaOH or 0.5 M H_2SO_4. The initial phenol concentration was 0.5 mM and a catalyst concentration of 3 mg/mL FeO was used. The reaction started with the addition of H_2O_2 solution resulting in a total H_2O_2 concentration of 50 mM. Experiments were carried out at least in triplicate, and average values and deviations are presented in this work.

4.3.2.2.2 HPLC Reaction Analysis

Every 2h over a total period of 8 h, 2 mL were withdrawn from the reaction vessel, filtered using a 0.22 µm nylon filter, and transferred into an HPLC vial. 100 µL of methanol were added to the vial to quench remaining radicals. Samples were measured in a high-performance liquid chromatography (HPLC) using a Waters Alliance HPLC system equipped with a 4.6 mm x 250 mm Altmann Analytik C18 5 µm column. A flow rate of 0.8 mL/min was set with a mobile phase consisting of 49.5 vol% water, 49.5 vol% methanol, and 1 vol% trifluoroacetic acid.

4.3.2.2.3 H_2O_2 Determination

H_2O_2 was determined by the titanium sulfate method [36], using the absorption of UV/Vis light (at 402 nm) by the formed titanium complex measured using a U-1000 spectrophotometer from Hitatchi (Tokyo, Japan) after dilution with water to suitable optical densities in cells of 10 mm path length.

4.3.2.2.4 Leached Iron Determination

Leached iron into the solution during the reaction was measured using 1,10-phenanthroline as a complexing agent [37], by measuring the absorption (λ = 510 nm) of the formed iron complex measured using a U-1000 spectrophotometer from Hitatchi (Tokyo, Japan) after dilution with water to suitable optical densities in cells of 10 mm path length.

4.3.3 Methods

4.3.3.1 X-ray Diffraction Analysis (XRD)

X-ray diffraction analysis (XRD) was carried out using a STADI-P device from STOE & Cie GmbH (Darmstadt, Germany), with $CuK_{\alpha 1}$ radiation (λ=1.540598 Å). The samples were ground to form a homogeneous powder and scanned from 2° to 92° in 0.015° steps. Raw data were processed with the WinXPOW software package (Stoe & Cie) Powder X-ray diffraction patterns were compared with reference data from the Powder Diffraction File (PDF) database of the International Centre for Diffraction Data (ICDD).

4.3.3.2 Dynamic Light Scattering (DLS)

For dynamic light scattering (DLS) measurements, a CGS-3 Compact Goniometer System from ALV (Langen, Germany) combined with an ALV/LSE-5004 Multiple Tau Digital Correlator and a vertically polarized 22 mW HeNe laser (λ = 632.9 nm), was used. Suspensions as obtained after synthesis were filtered using a 450 µm CA-membrane and measured at a scattering angle of 90° with a constant temperature of 25 °C for 300 s. Using the 2nd order cumulant analysis [38,39] of the ALV-7004 Correlator software, the hydrodynamic radius and size distributions can be calculated from the autocorrelation function. Also, the CONTIN algorithm [40,41] was used to gather information from noisier measurements.

4.3.3.3 Transmission Electron Microscopy (TEM)

The structure and size of the particles were evaluated using a CM-12 transmission electron microscope from FEI/Phillips (Dreieich, Germany) with a tungsten cathode and 120 kV acceleration voltage. For this purpose, 10 µL diluted (usually 1:20) sample was placed on carbon-coated copper grids from Plano GmBH (S160) hydrophilized by treatment in a PDC-3XG plasma cleaner from Harrick Plasma. After soaking for 30s, excess liquid was removed

by blotting with a filter paper, and the grids were left on another filter paper to dry for 24h. Pictures were taken with the digital camera 1kx1k from TVIPS (Gauting, Germany). The images were processed and evaluated with the software EMMenu4.

4.3.3.4 Scanning Electron Microscopy (SEM)

Field emission scanning electron microscopy (SEM) images were recorded on a Phenom Pro X scanning electron microscope (FEI Company, Hillsboro, OR, US) equipped with an EDX and a backscattering detector. Lyophilized samples were prepared on a sample holder and sputtered with Au/Pd for 30 s (2.45 kV, 22 mA) under an Argon atmosphere using a Polaron E 510 Series II Sputter Coater (Polaron Instruments, London, UK).

4.3.3.5 Brunauer-Emmett-Teller (BET) Adsorption Measurements

The specific surface areas of selected, dried particle samples were determined by nitrogen adsorption following the BET adsorption model using an Accelerated Surface Area and Porosimetry System ASAP 2010 of Micromeritics (Norcross, GA, USA).

4.3.3.6 Cyclic Voltammetry (CV)

To investigate the electrochemical behavior of the NPs, cyclic voltammograms were created. To provide sufficient conductivity, all observed NPs were redispersed after lyophilization in 0.1 M KCl solution. The concentration of the NPs was selected so that there was 1 mM of the metal sulfide in the suspension. The samples were ultrasonicated for about 1 min before one drop was placed on a single-use DRP-C550 electrode from Metrohm DropSens (Asturias, Spain). The working and auxiliary electrodes are made of platinum, whereas the reference electrode is made of silver. The measurements were performed with a µStat 200 Bipotentiostat from Metrohm DropSens and evaluated with the associated software DropView 200. Usually, up to 5 cycles were measured with the potential ranging from -1.3 V up to 0.0 V with a scan rate of 0.01 V/s.

4.3.3.7 Data Availability

Additional data, including fit parameters and associated scripts, are available in the online repository (Novel nanoparticle synthesis in self-organizing water–based systems - online repository, 10.5283/epub.80300). Representative data and fits are shown in the SI.

4.4 Results and Discussion

4.4.1 Structural Overview

The optimal synthesis conditions for obtaining catalytically active particles via the one-pot approach [30,31] were systematically investigated. First, the structure of the particles was investigated and then their efficiency as heterogeneous catalyst in a Fenton reaction at circumneutral pH values was tested.

Typically, the structures formed in this coupled precipitation process result in small primary particles embedded in diffuse silica matrices forming the secondary particles [31]. (cf. **Figure IV-2a**, section III)

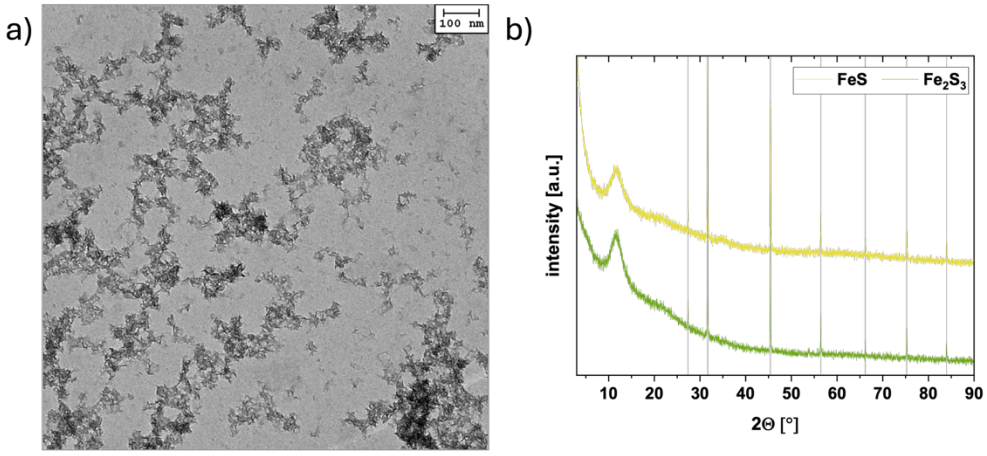


Figure IV-2. (a) TEM micrograph of particles derived from Fe(II) at 5 mM TEOS and a pH value of 11. The scale bar corresponds to 100 nm. (b) XRD spectra of FeS derived from Fe(II) and Fe(III), respectively. The vertical lines indicate the crystal structure of the synthesis residue NaCl.

While particles derived from the same iron precursor appear quite similar, rather different structures occur when using different precursors. (cf. **Figure SIV-1a**) An increase in the [Si]/[Fe] ratio results in smaller secondary particles in the observed range. Particles derived from Fe(III) are significantly smaller than those derived from Fe(II). Hydrodynamic radii derived from DLS are summarized in the supporting information. (cf. **Table SIV-1**) Generally, for divalent cations the hydrodynamic radius decreases with increasing silica concentration or increasing pH during synthesis due to increased colloidal stability already in early stages of the particle formation [31]. (see **Chapter III**)

No representative reflexes for iron oxides could be found in XRD measurements, but a broad peak at small angles, which indicates the existence of amorphous crystal structures, highly disordered, or nanocrystalline material [42,43]. (cf. **Figure IV-2b**) The visible reflexes derive

from the synthesis residue NaCl. Neither the XRD nor the TEM provides information about the crystal structure of the formed iron oxides except that a certain proportion may be amorphous. Synthesizing iron carbonates first, with subsequent calcination after lyophilization, results in more pronounced crystal structures compared to the particles derived from the sulfides. While the XRD spectrum of the precipitated iron carbonate shows no reflections apart from a slight indication of amorphous structures, several reflections can be seen after calcination, which indicate various iron (hydr)oxides. (cf. **Figure SIV-2**) During the calcination/sintering process the particles rearrange into a classical lattice [43,44].

Because of the chosen calcination temperature (650°C), the main component should be α-Fe_2O_3, also known as hematite [45], which is frequently used in literature as highly reactive heterogeneous Fenton catalyst [13–15,46]. The indication of amorphous structures vanishes for the particles derived from Fe(III) species but remains for the Fe(II) derived particles. The reflexes in both spectra can be attributed to hematite and to magnetite Fe_3O_4 [43]. TEM micrographs of iron carbonates and calcinated samples can be found in the supporting information. (cf. **Figure SIV-3**)

4.4.2 Catalytic Difference in Sulfide and Carbonate Derived Materials

Particles derived from both pathways, oxidation of FeS (cf. **Figure IV-3a**) and the calcination of $FeCO_3$ (cf. **Figure IV-3b**), were used as catalysts for phenol degradation in a heterogeneous Fenton reaction. Therefore, a series of particles was produced, obtained at different pH values and with different amounts of silica. Hematite was used as a reference [13–15], which always resulted in a total of around 12% decomposed phenol after 8 h. Only a few particles derived from $FeCO_3$ exhibit poorer conversion rates, whereas particles derived from FeS consistently exhibit higher conversion rates. (cf. **Figure IV-3**)

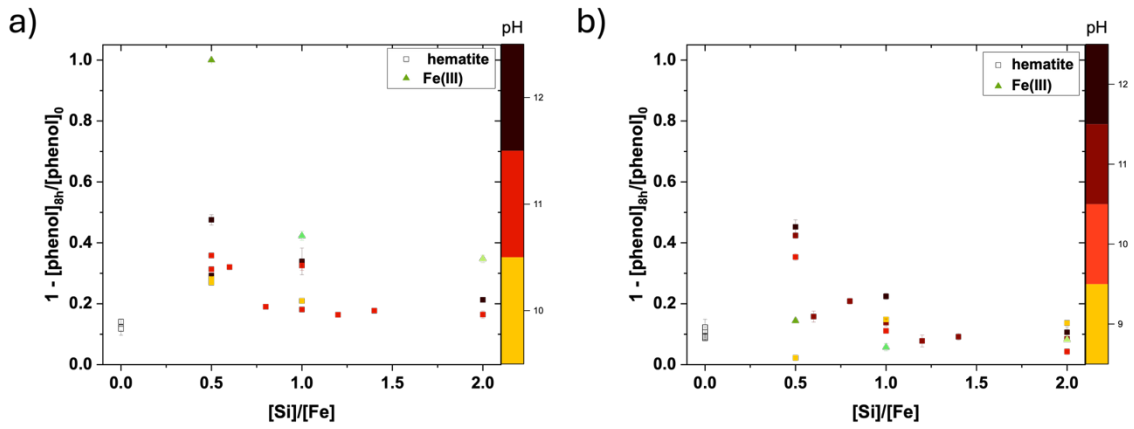


Figure IV-3. Relative amount of phenol degraded after 8 h reaction time for particles derived from modified syntheses. The white squares represent the reference hematite. In (a) particles derived from FeS and in (b) particles derived from $FeCO_3$ are shown. The green triangles represent particles derived from a synthesis from Fe(III) at a pH value of 11.

A trend visible for all particles is a reduction in phenol decomposition with increasing silica content. (cf. **Figure IV-3**) This can be directly attributed to the surfaces of the catalytically active cores being better shielded, as previously shown in **Chapter III**. In other words, the density and thickness of the silica shell increase, thereby preventing more oxidant-releasing reactions on the iron oxide surfaces [31].

Another trend is the increased phenol degradation for particles originating from syntheses at higher pH values. (cf. **Figure IV-3**) This applies to both particles originating from FeS and those originating from $FeCO_3$. Due to chemical equilibria, the synthesis of $FeCO_3$ can be carried out at a lower pH value than FeS. (see **Chapter III**) Only at pH 12 and higher silica concentrations is this trend no longer strictly true.

When directly compared, particles derived from FeS exhibit higher phenol degradation. While the difference is small at low silica content, it increases significantly toward higher silica content. At an [Si]/[Fe] ratio of 1, twice as much phenol is converted using FeS derived particles as with particles derived from $FeCO_3$. Even more evident is the difference between Fe(III) and Fe(II) derived particles. While for FeS the change in the iron precursor leads to particles with increased phenol degradation capacity, particles obtained from $FeCO_3$ exhibit poorer catalytic properties. (cf. **Figure IV-3**)

Based on these results, no further experiments were conducted on particles derived from $FeCO_3$, as particles derived from FeS appear more promising. In addition, the preparation of FeS derived particles is less time-consuming.

4.4.3 Effective Utilization of Oxidative Species by the Nanomaterial?

The [Si]/[Fe] ratio and the specific surface area of selected lyophilized FeS derived particles determined by BET are listed in **Table IV-1**.

Table IV-1. Specific surface area per gram of nanoparticles measured with BET. Particles derived from an FeS synthesis at different silicate concentrations.

[Si]/[Fe] ratio	A($Fe^{(II)}$) [m^2/g]	A($Fe^{(III)}$) [m^2/g]
0.5	296.19 ± 10.66	273.73 ± 12.32
1	318.41 ± 3.12	231.42 ± 12.29
2	331.71 ± 4.64	203.78 ± 3.84

The surface area determined by BET measurements shows that the synthesis with Fe(II) always results in a higher surface area, regardless of the silica concentration used for the synthesis. Also, the surface area increases for increased silica concentrations, whereas for Fe(III), the surface area decreases with increased silica concentrations. This seems to be a direct result of classical nucleation theory and the increased insolubility of Fe(III) sulfides over Fe(II) sulfides (cf. **Table SIV-3**) and corresponds to the sizes determined by DLS (cf. **Table SIV-1**). Faster precipitation results in more primary particles and less diffuse silica matrix, which induces the majority of the measurable surface for BET. Also, the sizes of the particles derived from Fe(III) do not change significantly, indicating increased density of the shell due to closure of inner surfaces with the addition of more silica during synthesis [47].

Evaluation of SEM (cf. **Figure SIV-4**) highlights the porous surface of the material and the aforementioned trend. EDX measurements indicate that the actual ratios for the particles are reduced to about two-thirds compared to the theoretical value. (cf. **Table SIV-2**)

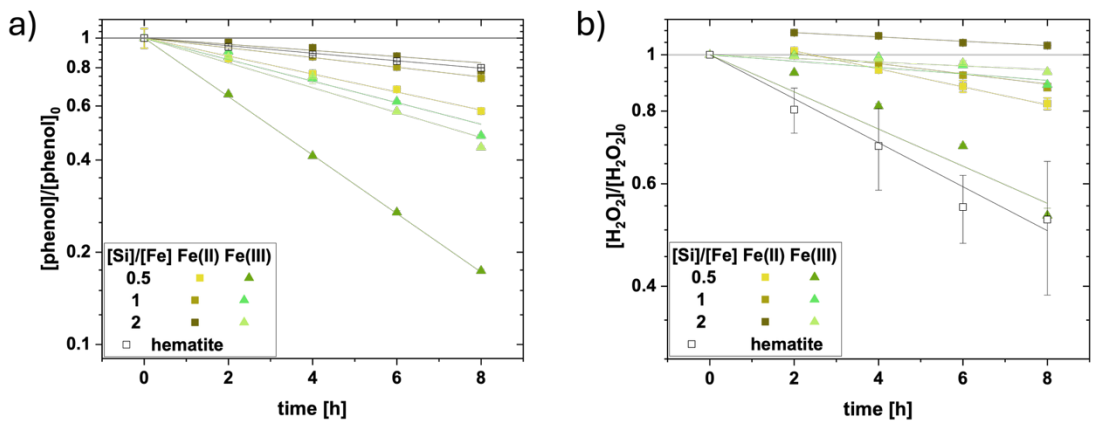


Figure IV-4. a) Normalized degradation of phenol over the reaction time of 8 h for different particles derived from Fe(II) or Fe(III) and the reference, hematite. First-order linear fit to determine reaction rates. b) Normalized degradation of H_2O_2 over the reaction time of 8 h for different particles derived from Fe(II) or Fe(III) and the reference, hematite, including first-order linear fits. pH values (cf. **Figure SIV-5a**) and reaction rates (cf. **Figure SIV-5b**) can be found in the SI.

Several trends were observed when the catalytic activity of the synthesized particles was evaluated in heterogeneous Fenton reactions at near-neutral pH. First, all particles used induce higher phenol degradation after 8 h compared to the hematite used as reference [17]. Secondly, Fe(III) derived particles outperform Fe(II) derived particles in phenol degradation. And third, phenol degradation increases for particles with lower [Si]/[Fe] ratios than for higher ratios. (cf. **Figure IV-4a**)

Similar and different trends can be observed in the degradation of H_2O_2. Here, the reference hematite causes the highest rate of H_2O_2 degradation. A higher [Si]/[Fe] ratio again leads to less reactant conversion, with Fe(III) at [Si]/[Fe] = 0.5 reducing the H_2O_2 concentration similarly to the reference hematite. All other particles cause a smaller H_2O_2 reduction with a similar course over a period of 8 hours. (cf. **Figure IV-4b**)

Another key factor for reaction rates (cf. **Figure SIV-5b**) in Fenton reactions is the pH value. In this case, the pH was above 5.3 for all samples (cf. **Figure SIV-5a**), in a semi-neutral range, where the oxidant-releasing pathway for H_2O_2 decomposition is already less favored [8].

The overall surface area of the particles after lyophilization increases with increasing silica concentration for synthesis derived from Fe(II) but decreases for Fe(III). (cf. **Table IV-1**) At the highest silica to iron ratio (2), the cores are effectively shielded, which is visible in their poor catalytic efficiency, and also explains their little electrochemical accessibility (c.f. online repository & **Figure SIV-17**). At lower ratios (1 or 0.5) the particles show electrochemical accessibility as well as catalytic H_2O_2 decomposition. The leakage or dissolution of iron is almost neglectable and does not significantly increase for lower [Si]/[Fe] ratios. After 8 h, only

a small percentage (< 0.5%) of the total used iron was dissolved into the reaction media. (cf. **Figure IV-5a**) This also proves that even though negligible amounts of iron are in solution, the majority of the catalyst remains insoluble, and the catalysis remains heterogeneous. This ensures easy removal of the catalyst after the reaction.

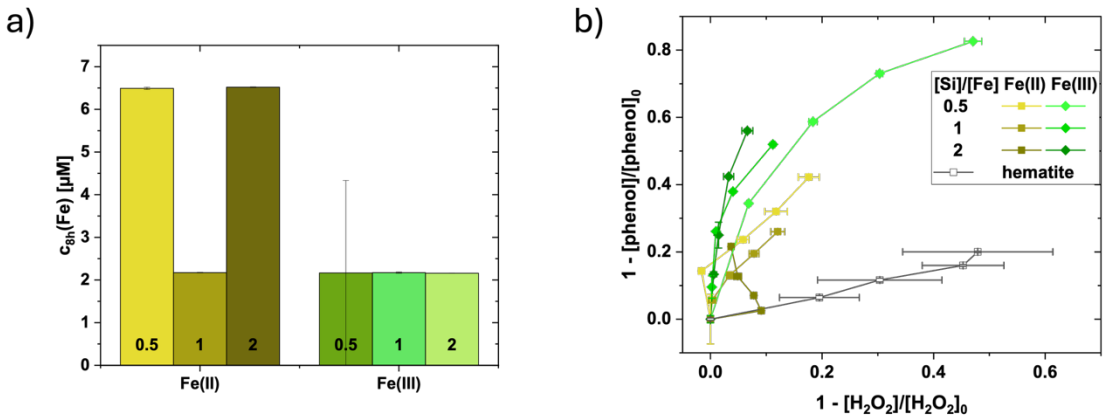


Figure IV-5. (a) Concentration of Fe(II) in solution after 8 h of reaction time for different particles derived from Fe(II) or Fe(III). Note that only a small portion of approximately 0.5% is leached out in relation of the total amount of Fe. (b) Normalized degradation of phenol respective to the normalized degradation of H_2O_2 for different particles derived from Fe(II) or Fe(III) at different [Si]/[Fe] ratios and the reference, hematite.

When the degradation of phenol and H_2O_2 is compared directly, a pattern becomes apparent. (cf. **Figure IV-5b**) Even though all used particles induced less H_2O_2 degradation than hematite, the phenol degradation was higher compared to the reference hematite. In fact, all particles derived from Fe(III) induce a higher phenol degradation with less H_2O_2 used compared to Fe(II). While the reaction rate for H_2O_2 degradation is higher than that for phenol degradation for hematite, this relationship is reversed for all particles with silica shells. (cf. **Figure SIV-5b**) Therefore, higher [Si]/[Fe] ratios reduce the amount of degraded phenol and also require less H_2O_2. Overall, fewer oxidizing species are generated, and they are utilized more effectively for phenol degradation.

The degradation of the peroxide is much more controlled, and the reactive oxygen species (ROS) are harnessed much more efficiently on the silica surfaces. The superiority of Fe(III) derived materials has been proven before for more elaborately prepared iron oxide silica core-shell nanoparticles [48]. Numerous studies reported significantly enhanced oxidant utilization efficiency for silica-supported iron oxides compared to unsupported iron oxides. Nevertheless, the underlying mechanism remains controversial [1,17,23,24].

One explanation for the enhanced performance is the increased dispersion of iron centers. Silica inhibits aggregation and reduces the particle size, resulting in a higher density of accessible surface iron sites. Consequently, a larger fraction of iron atoms participates in the hydrogen peroxide activation compared to bulk iron oxides [16,25].

Silica also may directly influence the interfacial reaction. Silanol groups near the iron surface site participate in hydrogen bonding with adsorbed peroxide and reactive iron species. This may delay desorption kinetics and facilitate charge transfer processes at the oxide-water interface. Additionally, silica surfaces exhibit lower reactivity towards radical scavenging, thereby reducing unproductive side reactions and increasing oxidant utilization [21,26–28]. It was also demonstrated that this way the diffusion of the pollutant to the surface-bound ROS can become the rate-determining step for the oxidation reaction [1].

4.4.4 Tuning Silica Shell Formation and Accessibility

4.4.4.1 Effects of Increasing TEOS Hydrolysis Time Prior to Particle Synthesis

The hydrolysis time of TEOS before the synthesis of the particles has only little effect on the size (r_H) of the secondary particle clusters for both Fe(II) and Fe(III). (cf. **Figure SIV-6**) Nevertheless, a clear difference can be seen when the catalytic properties are considered. Therefore, samples were examined with different hydrolysis times of 0, 1, 2, and 4 hours, respectively. (cf. **Figure IV-6**) Samples with 0 h TEOS hydrolysis time are hardly reproducible (see **Chapter III**) and are therefore not used as catalysts in the reactions.

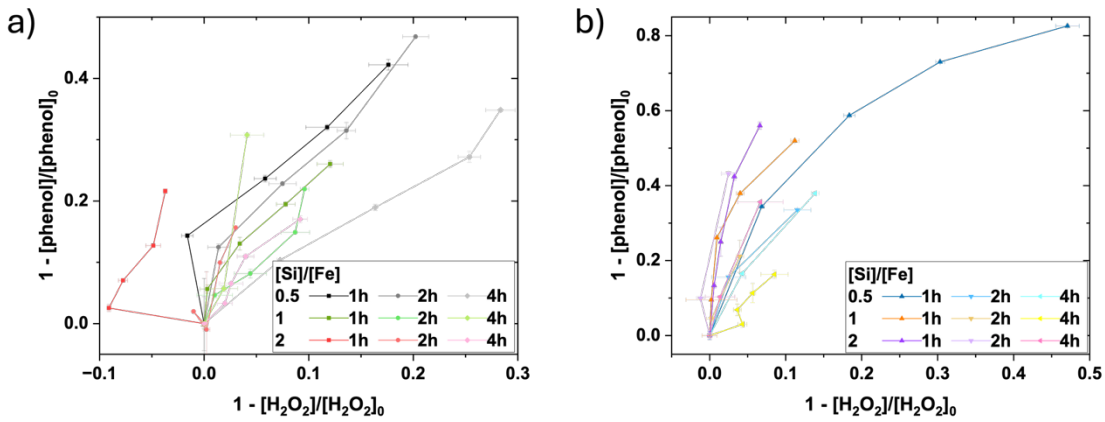


Figure IV-6. Normalized degradation of phenol respective to the normalized degradation of H_2O_2 for different particles derived from (a) Fe(II) and (b) Fe(III) with different [Si]/[Fe] ratios and differing TEOS hydrolysis times before particle synthesis. pH values (cf. **Figure SIV-7**) and reaction rates (cf. **Figure SIV-8**) can be found in the supporting information. Note that negative values result from a very slight H_2O_2 degradation over the time period with a magnitude similar to the measurement accuracy.

For both Fe(II) and Fe(III) derived particles, similar trends can be seen. For increased hydrolysis times, the curves shift to the bottom right, i.e., less phenol degradation, although increased H_2O_2 degradation occurs. This indicates a decrease not necessarily in the catalytic ability but in the ability to stabilize the formed oxidative species in the silica matrix. (cf. **Figure IV-6**) This can also be seen considering the leaching of iron from the catalyst into the reaction solution. While even for the highest iron concentration (~100 µM) less than 1% of the total iron was dissolved, the concentration tends to increase more for samples with higher hydrolysis times, especially expressed for Fe(III). (cf. **Figure SIV-9a**)

Some samples seem to deviate from these trends, such as the particles with [Si]/[Fe] = 1 and 4 h of TEOS hydrolysis or Fe(II), and multiple samples for Fe(III) with hydrolysis times >1 h except [Si]/[Fe] = 1 with 4 h of hydrolysis time. For these samples, a rapid increase in phenol degradation can be seen after 4 h of reaction time. (cf. **Figure SIV-10a**) Also, a steep decrease in pH (cf. **Figure SIV-10b**) and an increase in the leached iron concentration (cf. **Figure SIV-9b**) can be observed in the same timeframe. When only the first 4 h of reaction are compared to samples that maintained the pH value in the desired range, the aforementioned trends apply. This trend is also evident when comparing reaction rates, particularly in the first four hours before deviations from linear first-order behavior occur. (cf. **Figure SIV-8**)

A pH decrease below a value of 5 enhances the oxidant-forming pathway of H_2O_2 degradation and also enhances the potential dissolution of the iron oxides. Also, the silica shell seems to be less dense at higher hydrolysis times, further enhancing the dissolution and acidification. The combination of these effects results in supposedly higher catalytic ability, but as the catalyst is dissolved, the reaction deviates from heterogeneous catalysis.

Considering these results, 1 h of TEOS hydrolysis results in particles with higher oxidative species harness than particles with higher hydrolysis times. Further, as noted earlier, Fe(III) derived materials outperform Fe(II) derived materials, and while a higher [Si]/[Fe] ratio reduces reaction rates, it increases the efficient harness of the oxidative species.

4.4.4.2 Partial Removal of the Silica Shell Utilizing HF

Since lower silica contents in previous experiments resulted in higher phenol degradation, it was investigated whether subsequent removal with hydrogen fluoride (HF) could improve the catalytic properties. Particles with low degradation themselves, i.e., denser silicate shells, were used for this investigation.

The addition of HF leads to two opposing effects when considering pure catalytic activity. First, a thinner silica shell reduces colloidal stability. (cf. **Figure SIV-11a**) This leads to increased aggregation and thus impairs access of the reactants to the catalytically active surfaces. At the same time, however, a reduction in shell thickness/density improves access to the catalytically active surface. (cf. **Figure SIV-11b**) Additional TEM micrographs can be found in the online repository.

In order to improve the catalytic properties, some silicate must be removed, but not too much. (cf. **Figure IV-7**)

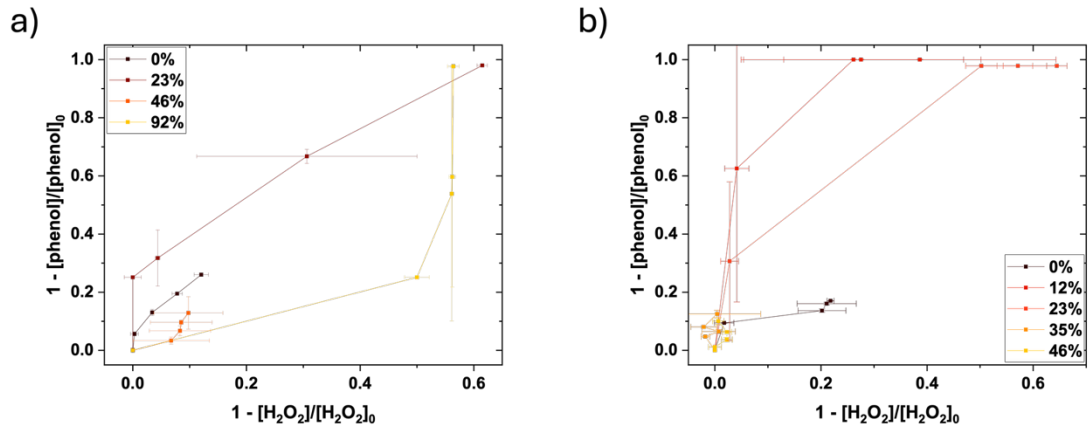


Figure IV-7. Normalized degradation of phenol respective to the normalized degradation of H_2O_2 for different particles derived from Fe(II) with different [Si]/[Fe] ratios and subsequent silica removal by HF addition. The sample names correspond to the etched percentage of silica. (a) Particles derived from FeS at pH 10 and [Si]/[Fe] = 1. (b) Particles derived from FeS at pH 10 and [Si]/[Fe] = 2. The corresponding pH values (cf. **Figure SIV-12**) and reaction rates (cf. **Figure SIV-13**) can be found in the supporting information.

For particles with [Si]/[Fe] = 1 (cf. **Figure IV-7a**) both samples, with 23 % and 92 % removal of the total silica, result in a complete degradation of phenol. Thus, both show greater phenol degradation than the unetched reference sample. The sample in between, with 46% of the silica removed, performs worse than the reference. Looking at the entire progression, it is clear that 23 % and 92 % show a significantly different reaction pattern. While the sample with 23 % etched silica can use H_2O_2 more effectively at the beginning, the reaction of phenol degradation accelerates significantly for the sample with 92 % etched silica, especially towards the end. Note that the rapid increase in phenol degradation between 4 h and 8 h for the sample with 92 % can be attributed to the decreased pH value (< 5) in this sample. The decreased pH also caused the rapid H_2O_2 degradation between 0h and 2h, most likely via non-oxidant-releasing pathways.

(cf. **Figure SIV-12a**) Also, the reaction rate for H_2O_2 degradation is higher than that for phenol degradation as it was seen before only for hematite. (cf. **Figure SIV-13**)

For particles with [Si]/[Fe] = 2 (cf. **Figure IV-7b**), less silica was removed relatively. The samples with 12 % or 23 % etched silica, respectively, already resulted in total degradation of phenol after 4 h. Both samples, therefore, exhibit higher phenol degradation than the unetched reference. Especially for 12 % etched silica, the reaction rate for phenol degradation is strongly increased. The removal of more silica worsens the catalytic ability, again resulting in less degraded phenol and H_2O_2 than for the reference. The reaction rates also decrease to the same order of magnitude as those of unetched samples. (cf. **Figure SIV-13**)

Therefore, the samples with [Si]/[Fe] = 2 and 12 % etched silica performed best. Although the colloidal stability was disrupted here, the particles did not yet aggregate significantly. (cf. **Figure SIV-11a**) The sample is able to break down the full phenol content after just 4 h, but only needs about 25 % of the available H_2O_2 to do so. This is roughly the same amount that the unetched reference sample needed to break down about 20 % phenol after 8 h. (cf. **Figure IV-7b**)

For both [Si]/[Fe] ratios, it is clear that small amounts of HF significantly improve the catalytic properties. In line with previous results, the existence of the silicate shell is relevant for stabilizing oxidative species and using them effectively for phenol degradation. If too much silica is removed, H_2O_2 is broken down in a more diversified manner, especially via non-oxidant releasing pathways, deviating from the pseudo-first-order kinetics. This results in significantly higher H_2O_2 degradation with simultaneous low phenol degradation. In addition, excessive silica removal causes aggregation and thus poorer access of the reactants to the catalytically active surface, slowing the phenol degradation further.

4.4.4.3 Addition of SHMP During Synthesis

Another strategy to influence the silica shell is the addition of sodium hexametaphosphate (SHMP) during synthesis (see **Chapter III**). Whilst the influence on the size of the secondary particle clusters is immediately apparent for Fe(II) derived materials (> 100 nm vs. ~30 nm), the effect on Fe(III) derived materials is not (~75 nm vs. ~60 nm). (cf. **Figure SIV-14**)

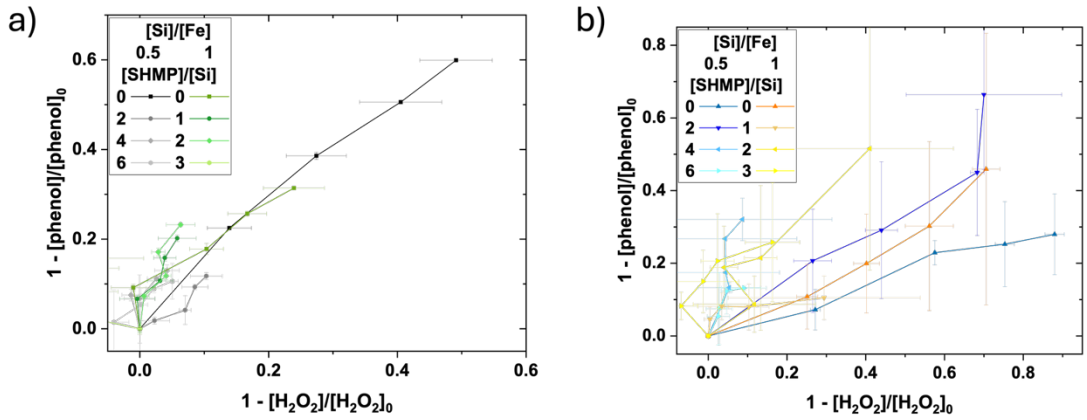


Figure IV-8. Normalized degradation of phenol respective to the normalized degradation of H_2O_2 for different particles derived from (a) Fe(II) and (b) Fe(III) with different [Si]/[Fe] ratios and differing [SHMP]/[Si] ratios. pH values (cf. **Figure SIV-15**) and reaction rates (cf. **Figure SIV-16**) can be found in the supporting information.

When the particles are used as catalysts, two distinct patterns emerge for Fe(II)- and Fe(III)-based materials. (cf. **Figure IV-8**)

Particles derived from Fe(II) with added SHMP show decreased H_2O_2 decomposition over the 8 h reaction time compared to the samples without the addition of SHMP. The degradation of phenol is also reduced, but the trend indicates that the efficient utilization of the oxidative species increases with increased [SHMP]/[Si]. (cf. **Figure IV-8a**) Nevertheless, the reaction proceeds significantly slower overall, as all reaction rates are reduced for particles derived from syntheses with added SHMP. (cf. **Figure SIV-16a**) The only sample that deviates from this trend is the one with [Si]/[Fe] = 0.5 and [SHMP]/[Si] = 2, as it indicates slower kinetics and poorer utilization of the oxidative species.

The trends for particles derived from Fe(III) with added SHMP are similar, but there are certain differences. First, less H_2O_2 is decomposed over the 8 h reaction time compared to the samples without SHMP addition during synthesis. However, in this case, the degradation of phenol is not impaired to the same extent as before for all samples containing added SHMP. For both [Si]/[Fe] = 0.5 and 1, the [SHMP]/[Si] = 2 resulted in higher phenol degradation than the respective reference samples with [SHMP]/[Si] = 0. (cf. **Figure IV-8b**) For higher [SHMP]/[Si] ratios, a similar trend is observed as before, indicating more effective utilization of oxidative species at slower reaction rates. (cf. **Figure SIV-16b**)

4.4.4.4 Discussion

The catalytic performance of the synthesized iron oxide/silica materials is governed by a delicate balance between the accessibility of active iron sites and the stabilization of reactive oxygen species within the silica matrix. This balance can be systematically tuned via synthesis parameters that alter the silica shell, including variation of the [Si]/[Fe] ratio, TEOS hydrolysis time, SHMP addition, and post-synthetic silica removal.

Among all investigated parameters, the [Si]/[Fe] ratio proved to be the most influential for both synthesis and catalytic performance. Increasing silica content improves colloidal stability and results in smaller secondary particle clusters. (see **Chapter III**) At the same time, it results in increased shell thickness and presumably decreased shell permeability, thereby limiting access of reactants to the surface of the cores. Consequently, both hydrogen peroxide decomposition and phenol degradation decreased with increasing [Si]/[Fe] ratio. Similar effects have been reported for silica-supported iron oxide catalysts [1,17,23,24]. However, the underlying mechanism responsible for the enhanced oxidant utilization remains debated, and several explanations have been proposed in the literature [1,17,23,24].

The influence of the hydrolysis time and SHMP highlights the importance of the silica shell. Extended hydrolysis times increased H_2O_2 consumption and iron leaching, whereas reducing the effective ROS utilization for phenol degradation. The particle size remained virtually unchanged, which emphasizes the importance of shell density and permeability.

Longer hydrolysis results in bigger silica clusters prior to synthesis, which results in a less uniform silica network. The silica shell is then not able to restrict mass transport and iron dissolution. This interpretation is consistent with the observed increase in iron leaching and pH decline for samples prepared with extended hydrolysis times.

The addition of SHMP influenced both particle formation and catalytic performance. SHMP is known to strongly interact with multivalent metal ions and can modify nucleation, particle growth, and aggregation processes through complex formation and electrostatic stabilization [49,50]. Because phosphate-based ligands generally exhibit stronger complexation towards Fe(III) than Fe(II), the structural effects of SHMP are expected to be more pronounced for Fe(III)-derived systems [51–53]. The observed reduction in peroxide decomposition, combined with comparatively preserved phenol degradation, suggests that SHMP-derived structural changes increase the efficiency of ROS utilization rather than the absolute rate of ROS generation.

Further evidence for the existence of an optimal silica shell architecture is provided by the HF etching experiments. Moderate removal of silica significantly enhanced catalytic activity, while excessive silica removal resulted in increased aggregation, enhanced iron leaching, and lower catalytic efficiency. These findings demonstrate that neither complete encapsulation nor complete exposure of the iron oxide phase is favorable. Similar relationships between catalyst confinement, ROS stabilization, and oxidant efficiency have been discussed for other heterogeneous Fenton systems [1,13,15].

The observed catalytic behavior cannot be explained solely by particle size or surface area. Although changes in synthesis conditions strongly affected both parameters, catalytic activity did not correlate directly with either quantity. Likewise, Fe(III)-derived materials consistently outperformed Fe(II)-derived materials despite not always exhibiting larger BET surface areas. This suggests that the accessibility, distribution, and redox properties of surface iron sites are more important than geometrical surface area alone [14,15]. Similar observations have frequently been reported for amorphous iron oxides, where structural disorder and surface chemistry often dominate catalytic performance over crystallinity or specific surface area [1,13–15,48].

The catalytic activity obtained under near-neutral conditions is particularly noteworthy, as conventional Fenton chemistry is typically most effective at pH values around 3–4 [1,8,10,11]. Although a pronounced acceleration of the reaction was observed once the pH dropped below approximately 4–5, substantial phenol conversion was already achieved at significantly higher pH values. This behavior highlights the potential of silica-supported iron oxide materials for heterogeneous Fenton-like applications under environmentally relevant conditions.

4.5 Conclusion

Iron oxide/silica core–shell nanoparticles synthesized via the presented one-pot coprecipitation route were successfully applied as heterogeneous Fenton-like catalysts under circumneutral conditions. Despite the simplicity of the synthesis, the obtained materials exhibited catalytic performances comparable to or exceeding those reported for more elaborate multistep silica-supported iron oxide systems.

The catalytic behavior was primarily governed by the structure of the silica shell. Increasing silica content improved colloidal stability and reduced particle aggregation, but simultaneously decreased the accessibility of reactive iron sites. As a consequence, both hydrogen peroxide decomposition and phenol degradation decreased with increasing [Si]/[Fe] ratio. Nevertheless, the silica shell proved essential for efficient oxidant utilization. Compared to the reference hematite, the silica-containing materials achieved higher phenol degradation while consuming substantially less hydrogen peroxide, indicating a more selective utilization of reactive oxygen species.

The comparison between Fe(II)- and Fe(III)-derived materials revealed that catalytic performance cannot be explained by surface area alone. Although Fe(II)-derived particles frequently exhibited larger BET surface areas, Fe(III)-derived particles consistently showed superior catalytic activity. This finding suggests that the accessibility, distribution, and redox properties of surface iron sites are more important than the geometrical surface area itself.

Additional modifications of the silica shell further confirmed its central role in catalyst performance. Controlled partial removal of silica by HF treatment significantly enhanced catalytic activity, demonstrating that an optimal balance between shell permeability and ROS stabilization exists. Similarly, variations in TEOS hydrolysis time and SHMP addition altered shell structure and particle formation, thereby affecting both catalytic activity and oxidant utilization efficiency.

Iron leaching remained below 0.5 % of the total iron content under most reaction conditions, indicating that heterogeneous reaction pathways dominate the observed catalytic behavior. However, pronounced pH decreases were accompanied by increased iron dissolution and deviations from pseudo-first-order kinetics, suggesting a partial transition toward homogeneous Fenton chemistry under these conditions.

Overall, the results demonstrate that the presented one-pot synthesis provides a scalable and versatile route toward highly active silica-supported iron oxide catalysts. The catalytic performance is determined by a delicate balance between iron-site accessibility, colloidal

stabilization, and stabilization of surface-associated oxidizing species. These findings provide important design principles for the development of heterogeneous Fenton catalysts operating at circumneutral pH values.

The transfer of these catalysts to more complex water matrices and continuous-flow systems will be essential to evaluate their practical applicability under environmentally relevant conditions. In such systems, the influence of competing inorganic and organic constituents on both catalytic activity and oxidant efficiency should be systematically investigated. Beyond application-oriented testing, future studies should also address the scalability of the one-pot synthesis route and the long-term stability of the materials under technically relevant operating conditions.

4.6 References

[1] Ioffe M, Kundu S, Perez-Lapid N, Radian A. Heterogeneous Fenton catalyst based on clay decorated with nano-sized amorphous iron oxides prevents oxidant scavenging through surface complexation. Chemical Engineering Journal 2022;433:134609. https://doi.org/10.1016/j.cej.2022.134609.

[2] Pereira MC, Oliveira LCA, Murad E. Iron oxide catalysts: Fenton and Fentonlike reactions – a review. Clay Miner 2012;47:285–302. https://doi.org/10.1180/claymin.2012.047.3.01.

[3] Botas JA, Melero JA, Martínez F, Pariente MI. Assessment of Fe2O3/SiO2 catalysts for the continuous treatment of phenol aqueous solutions in a fixed bed reactor. Catal Today 2010;149:334–40. https://doi.org/10.1016/j.cattod.2009.06.014.

[4] Andrade AL, Souza DM, Pereira MC, Fabris JD, Domingues RZ. Catalytic effect of magnetic nanoparticles over the h 20 2 decomposition reaction. J Nanosci Nanotechnol 2009;9:3695–9. https://doi.org/10.1166/jnn.2009.NS53.

[5] Fenton HJH. Oxidation of tartaric acid in presence of iron. Journal of the Chemical Society, Transactions 1894;65:899–910. https://doi.org/10.1039/CT8946500899.

[6] Haber F, Weiss J, A PRSL. The catalytic decomposition of hydrogen peroxide by iron salts. Proc R Soc Lond A Math Phys Sci 1934;147:332–51. https://doi.org/10.1098/rspa.1934.0221.

[7] Weiss J. The Free Radical Mechanism in the Reactions of Hydrogen peroxide. Advances in Catalysis 1952;4:343–65. https://doi.org/10.1016/S0360-0564(08)60618-5.

[8] Lin SS, Gurol MD. Catalytic decomposition of hydrogen peroxide on iron oxide: Kinetics, mechanism, and implications. Environ Sci Technol 1998;32:1417–23. https://doi.org/10.1021/es970648k.

[9] Watts RJ, Udell MD, Monsen RM. Use of iron minerals in optimizing the peroxide treatment of contaminated soils. Water Environment Research 1993;65:839–44. https://doi.org/10.2175/wer.65.7.5.

[10] Ravikumar JX, Gurol MD. Chemical Oxidation of Chlorinated Organics by Hydrogen Peroxide in the Presence of Sand. Environ Sci Technol 1994;28:394–400. https://doi.org/10.1021/es00052a009.

[11] Jung YS, Lim WT, Park JY, Kim YH. Effect of pH on Fenton and Fenton-like oxidation. Environ Technol 2009;30:183–90. https://doi.org/10.1080/09593330802468848.

[12] Costa RCC, Moura FCC, Ardisson JD, Fabris JD, Lago RM. Highly active heterogeneous Fenton-like systems based on Fe0/Fe3O4 composites prepared by controlled reduction of iron oxides. Appl Catal B 2008;83:131–9. https://doi.org/10.1016/j.apcatb.2008.01.039.

[13] Prucek R, Hermanek M, Zbořil R. An effect of iron(III) oxides crystallinity on their catalytic efficiency and applicability in phenol degradation-A competition between homogeneous and heterogeneous catalysis. Appl Catal A Gen 2009;366:325–32. https://doi.org/10.1016/j.apcata.2009.07.019.

[14] Gregor C, Hermanek M, Jancik D, Pechousek J, Filip J, Hrbac J, et al. The effect of surface area and crystal structure on the catalytic efficiency of Iron(III) oxide nanoparticles in hydrogen peroxide decomposition. Eur J Inorg Chem 2010:2343–51. https://doi.org/10.1002/ejic.200901066.

[15] Hermanek M, Zboril R, Medrik I, Pechousek J, Gregor C. Catalytic efficiency of iron(III) oxides in decomposition of hydrogen peroxide: Competition between the surface area and crystallinity of nanoparticles. J Am Chem Soc 2007;129:10929–36. https://doi.org/10.1021/ja072918x.

[16] Waite TD, Chen Y, Miller CJ. Heterogeneous Fenton chemistry revisited: Mechanistic insights from ferrihydrite-mediated oxidation of formate and oxalate. Environ Sci Technol 2021;55:14414–25. https://doi.org/10.1021/acs.est.1c00284.

[17] Pham AL-T, Lee C, Doyle FM, Sedlak DL. A Silica-Supported Iron Oxide Catalyst Capable of Activating Hydrogen Peroxide at Neutral pH Values. Environ Sci Technol 2009;43:8930–5. https://doi.org/10.1021/es902296k.

[18] Chou S, Huang C. Application of a supported iron oxyhydroxide catalyst in oxidation of benzoic acid by hydrogen peroxide. Chemosphere 1999;38:2719–31. https://doi.org/10.1016/S0045-6535(98)00474-3.

[19] Ono Y, Matsumura T, Kitajima N, Fukuzumi SI. Formation of superoxide ion during the decomposition of hydrogen peroxide on supported metals. Journal of Physical Chemistry 1977;81:1307–11. https://doi.org/10.1021/j100528a018.

[20] Abbot J, Brown DG. Kinetics of Iron-catalyzed decomposition of hydrogen peroxide in alkaline solution. Int J Chem Kinet 1990;22:963–74. https://doi.org/10.1002/kin.550220907.

[21] Miller CM, Valentine RL. Mechanistic studies of surface catalyzed H2O2 decomposition and contaminant degradation in the presence of sand. Water Res 1999;33:2805–16. https://doi.org/10.1016/S0043-1354(98)00500-4.

[22] Giwa ARA, Bello IA, Olabintan AB, Bello OS, Saleh TA. Kinetic and thermodynamic studies of fenton oxidative decolorization of methylene blue. Heliyon 2020;6:4–10. https://doi.org/10.1016/j.heliyon.2020.e04454.

[23] Liu Z, Zhang Y, Lee J, Xing L. A review of application mechanism and research progress of Fe/montmorillonite-based catalysts in heterogeneous Fenton reactions. J Environ Chem Eng 2024;12. https://doi.org/10.1016/j.jece.2024.112152.

[24] Farhadian N, Liu S, Asadi A, Shahlaei M, Moradi S. Enhanced heterogeneous Fenton oxidation of organic pollutant via Fe-containing mesoporous silica composites: A review. J Mol Liq 2021;321. https://doi.org/10.1016/j.molliq.2020.114896.

[25] Lim H, Lee J, Jin S, Kim J, Yoon J, Hyeon T. Highly active heterogeneous Fenton catalyst using iron oxide nanoparticles immobilized in alumina coated mesoporous silica. Chemical Communications 2006:463–5. https://doi.org/10.1039/b513517f.

[26] He J, Yang X, Men B, Wang D. Interfacial mechanisms of heterogeneous Fenton reactions catalyzed by iron-based materials: A review. J Environ Sci (China) 2016;39:97–109. https://doi.org/10.1016/j.jes.2015.12.003.

[27] Crowther N, Larachi F. Iron-containing silicalites for phenol catalytic wet peroxidation. Appl Catal B 2003;46:293–305. https://doi.org/10.1016/S0926-3373(03)00224-8.

[28] Bañuelos JL, Borguet E, Brown GE, Cygan RT, DeYoreo JJ, Dove PM, et al. Oxide– and Silicate–Water Interfaces and Their Roles in Technology and the Environment. Chem Rev 2023;123:6413–544. https://doi.org/10.1021/acs.chemrev.2c00130.

[29] Lee J, Weon S, Lee SSS, Yun ET, Chung MW, Kim C, et al. Microwave-enhanced catalytic degradation of organic compounds with silica-coated iron oxide nanocrystals via fenton-like reaction pathway. NPJ Clean Water 2025;8. https://doi.org/10.1038/s41545-025-00449-3.

[30] Funkner D, Frank T, Kohlmann N, Zahnweh D, Rieder J, Kienle L, et al. Functional nanoparticles from chemically coupled precipitation processes. Mater Today Chem 2023;29:101438. https://doi.org/10.1016/j.mtchem.2023.101438.

[31] Rödig B, Funkner D, Frank T, Schürmann U, Rieder J, Kienle L, et al. Nanodots of Transition Metal Sulfides, Carbonates, and Oxides Obtained Through Spontaneous Co-Precipitation with Silica. Nanomaterials 2024;14:1–15. https://doi.org/10.3390/nano14242054.

[32] Abdullah JAA, Jiménez-Rosado M, Guerrero A, Romero A. Effect of Calcination Temperature and Time on the Synthesis of Iron Oxide Nanoparticles: Green vs. Chemical Method. Materials 2023;16. https://doi.org/10.3390/ma16051798.

[33] El-Bellihi AA. Kinetics of thermal decomposition of iron carbonate. Egypt J Chem 2010;53:871–84. https://doi.org/10.21608/ejchem.2010.1268.

[34] Sullivan PJ, Yelton JL, Reddy KJ. Iron sulfide oxidation and the chemistry of acid generation. Environmental Geology and Water Sciences 1988;11:289–95. https://doi.org/10.1007/BF02574818.

[35] Schwertmann U, Cornell RM. Iron Oxides in the Laboratary. 2nd Editio. Weinheim, Germany: Wiley-VCH Verlag GmbH; 2000. https://doi.org/10.1002/9783527613229.

[36] Eisenberg GM. Colorimetric Determination of Hydrogen Peroxide. Industrial and Engineering Chemistry - Analytical Edition 1943;15:327–8. https://doi.org/10.1021/i560117a011.

[37] Harvey AE, Smart JA, Amis ES. Simultaneous Spectrophotometric Determination of Iron(ll) and Total Iron with 1,10-Phenanthroline. Anal Chem 1955;27:26–9. https://doi.org/10.1021/ac60097a009.

[38] Koppel DE. Analysis of macromolecular polydispersity in intensity correlation spectroscopy: The method of cumulants. J Chem Phys 1972;57:4814–20. https://doi.org/10.1063/1.1678153.

[39] Frisken BJ. Revisiting the method of cumulants for the analysis of dynamic light-scattering data. Appl Opt 2001;40:4087. https://doi.org/10.1364/AO.40.004087.

[40] Provencher SW. Contin: A general purpose constrainded regularization program for inverting noisy linear algebraic and integral equations. Comput Phys Commun 1984;35:C-818-C–819. https://doi.org/10.1016/S0010-4655(84)82935-5.

[41] Provencher SW. A constrained regularization method for inverting data represented by linear algebraic or integral equations. Comput Phys Commun 1982;27:213–27. https://doi.org/10.1016/0010-4655(82)90173-4.

[42] Machala L, Zboril R, Gedanken A. Amorphous Iron(III) Oxide - A Review. J Phys Chem B 2007;111:4003–18. https://doi.org/10.1021/jp064992s.

[43] De Villiers JPR, Lu L. XRD analysis and evaluation of iron ores and sinters. Iron Ore: Mineralogy, Processing and Environmental Sustainability 2015:85–100. https://doi.org/10.1016/B978-1-78242-156-6.00003-4.

[44] Tartaj P, Tartaj J. Preparation, characterization and sintering behavior of spherical iron oxide doped alumina particles. Acta Mater 2002;50:5–12. https://doi.org/10.1016/S1359-6454(01)00336-6.

[45] MacHala L, Tuček J, Zbořil R. Polymorphous transformations of nanometric iron(III) oxide: A review. Chemistry of Materials 2011;23:3255–72. https://doi.org/10.1021/cm200397g.

[46] Guo L, Chen F, Fan X, Cai W, Zhang J. S-doped α-Fe2O3 as a highly active heterogeneous Fenton-like catalyst towards the degradation of acid orange 7 and phenol. Appl Catal B 2010;96:162–8. https://doi.org/10.1016/j.apcatb.2010.02.015.

[47] Son S, Hyun SP, Charlet L, Kwon KD. Thermodynamic stability reversal of iron sulfides at the nanoscale: Insights into the iron sulfide formation in low-temperature aqueous solution. Geochim Cosmochim Acta 2022;338:220–8. https://doi.org/10.1016/j.gca.2022.10.021.

[48] Coelho J V., Guedes MS, Prado RG, Tronto J, Ardisson JD, Pereira MC, et al. Effect of iron precursor on the fenton-like activity of Fe2O3/mesoporous silica catalysts prepared under mild conditions. Appl Catal B 2014;144:792–9. https://doi.org/10.1016/j.apcatb.2013.08.022.

[49] Torresan MF, Parra-Florez L, Sorbello C, Azcárate JC, Etchenique R, Wolosiuk A. Sodium Hexametaphosphate: An Inexpensive Inorganic Polyelectrolyte “Primer” For Upconverting Nanoparticles/Mesoporous Silica Core-Shell Synthesis. ChemistrySelect 2020;5:5210–6. https://doi.org/10.1002/slct.202000287.

[50] Lu J, Sun M, Yuan Z, Qi S, Tong Z, Li L, et al. Innovative insight for sodium hexametaphosphate interaction with serpentine. Colloids Surf A Physicochem Eng Asp 2019;560:35–41. https://doi.org/10.1016/j.colsurfa.2018.09.076.

[51] Nambafu GS, Hollas AM, Rice PS, Weller JM, Boglaienko D, Reed DM, et al. Strategically Modified Ligand Incorporating Mixed Phosphonate and Carboxylate Groups to Enhance Performance in All-Iron Redox Flow Batteries. Adv Energy Mater 2025;15. https://doi.org/10.1002/aenm.202403149.

[52] Voegelin A, Kaegi R, Frommer J, Vantelon D, Hug SJ. Effect of phosphate, silicate, and Ca on Fe(III)-precipitates formed in aerated Fe(II)- and As(III)-containing water studied by X-ray absorption spectroscopy. Geochim Cosmochim Acta 2010;74:164–86. https://doi.org/10.1016/j.gca.2009.09.020.

[53] Veiga N, Torres J, Cerdá F, González G, Gómez K, Mansell D, et al. Redox and structural aspects on iron inositol 1,2,3-trisphosphate interaction: An experimental and computational approach. J Mol Struct 2011;994:343–9. https://doi.org/10.1016/j.molstruc.2011.03.047.

[54] Hollemann AF, Wiberg E. Lehrbuch der Anorganischen Chemie. 103rd ed. New York, NY: Walter de Gruyter & Co.; 2017.

[55] Lide DR. CRC Handbook of Chemistry and Physics. Boca Raton, FL, USA: 2005.

[56] Kolthoff IM. The solubilities and solubility products of metallic sulfides in water. Journal of Physical Chemistry 1931;35:2711–21. https://doi.org/10.1021/j150327a019.

4.7 Supporting Information

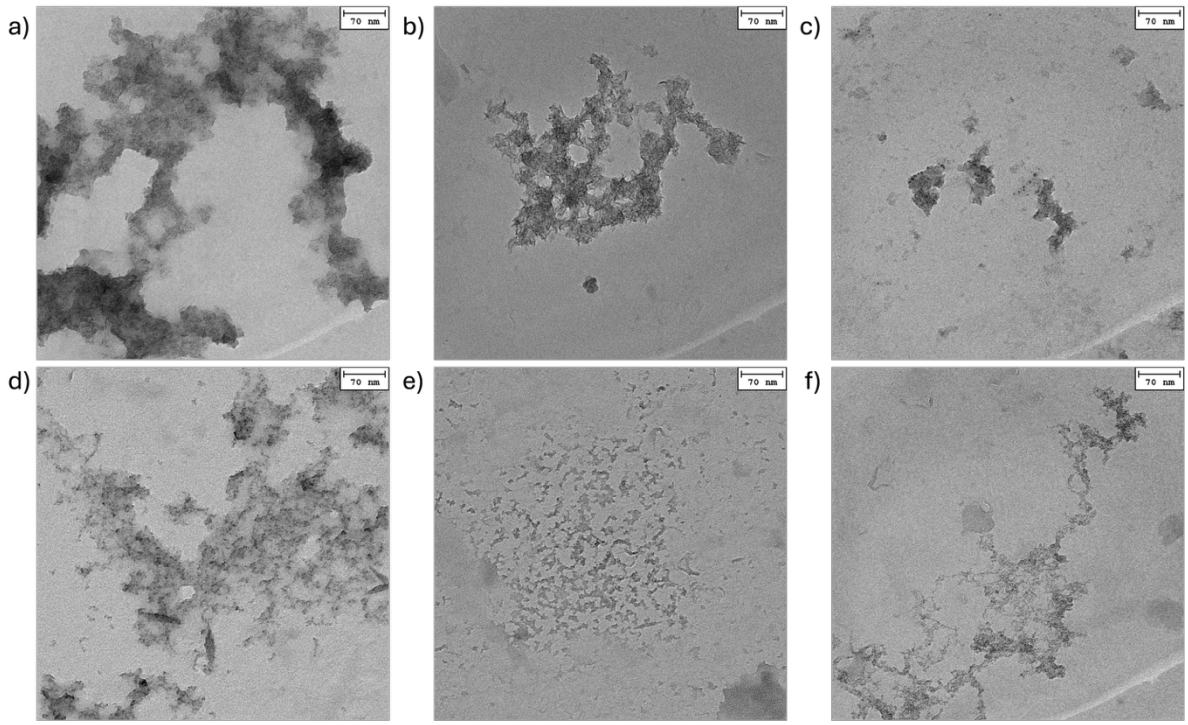


Figure SIV-1. TEM micrographs of various iron oxides (a-c) Fe(II) and (d-f) Fe(III) with increasing [Si]/[Fe] ratio from left to right (a&d) 0.5, (b&e) 1, and (c&f) 2. The scale bar corresponds to 70 nm.

Table SIV-1. Hydrodynamic radii (r_H) derived from DLS measurements of iron oxide particles derived from Fe(II) and Fe(III), respectively at different [Si]/[Fe] ratios. The pH value for synthesis was 11.

[Si]/[Fe]	**Fe(II)**		**Fe(III)**	
	size	**PD.I.**	**size**	**PD.I.**
0.5	196.74 ± 111.08	0.319	83.82 ± 48.36	0.333
1	113.86 ± 61.93	0.296	83.03 ± 49.68	0.358
2	68.09 ± 33.08	0.236	74.38 ± 45.2	0.369

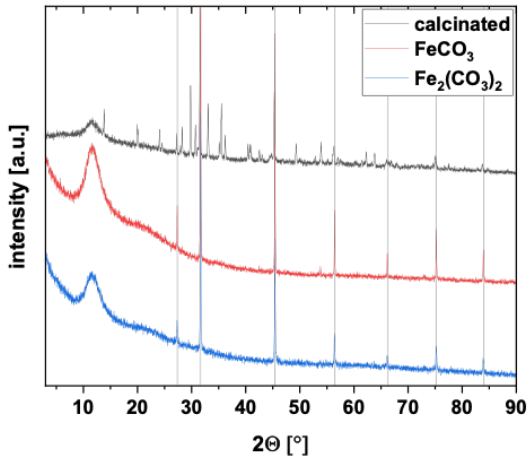


Figure SIV-2. XRD spectra of iron carbonate derived from Fe(II) and Fe(III), respectively. The vertical lines indicate the crystal structure of the synthesis residue NaCl.

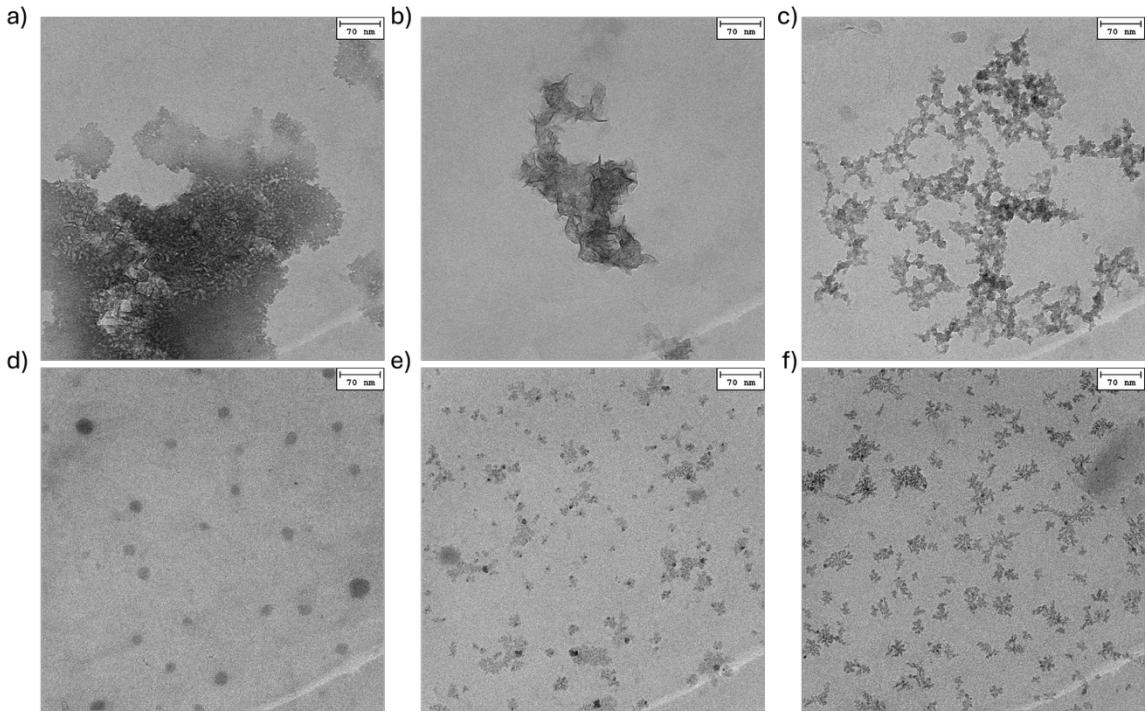


Figure SIV-3. TEM micrograph of FeCO3 and FeO 2p5 und 5 und 5 Fe(III)

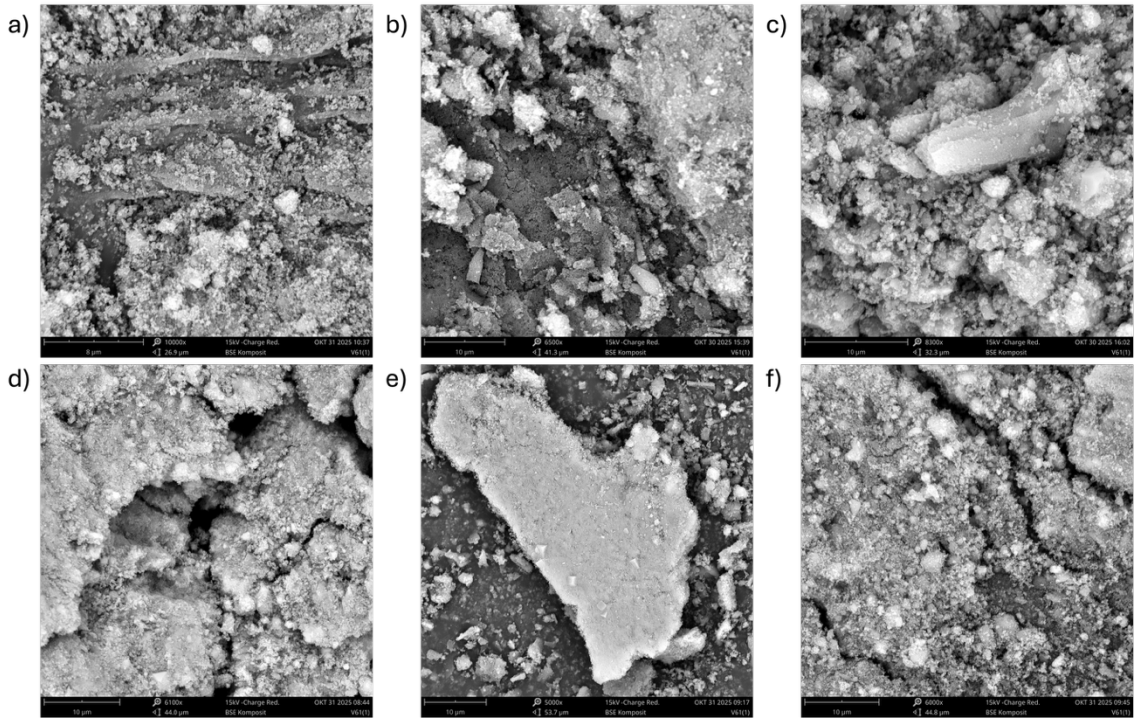


Figure SIV-4. SEM micrographs of various iron oxides (a-c) Fe(II) and (d-f) Fe(III) with increasing [Si]/[Fe] ratio from left to right (a&d) 0.5, (b&e) 1, and (c&f) 2. The scale bar corresponds to (a) 8 µm and (b-f) 10 µm, respectively.

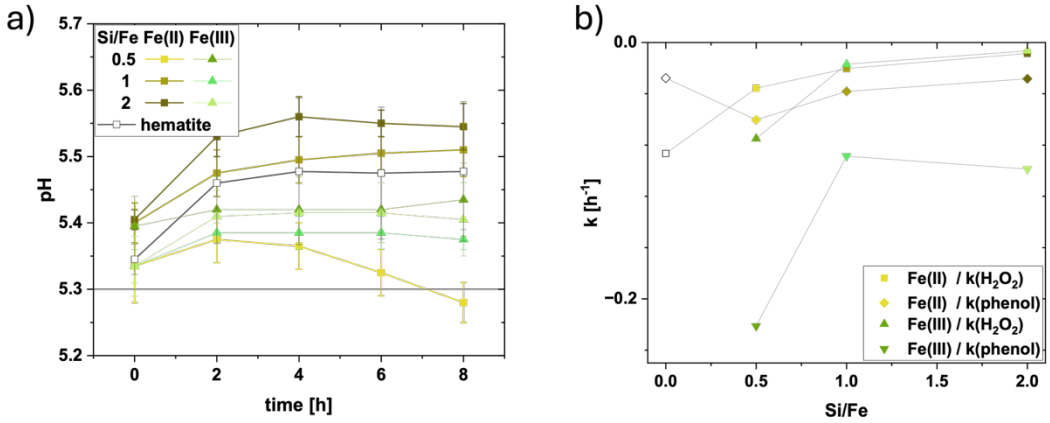


Figure SIV-5. (a) pH values of the reaction solutions in the 8 h time period. (b) First order reaction rates of both, H_2O_2 and phenol degradation, determined from linear fits in **Figure IV-4**.

Table SIV-2. Theoretical [Si]/[Fe] ratio and calculated mean values [Si]/[Fe] derived from EDX measurements from multiple SEM pictures as shown in **Figure SIV-4**.

$[Si]/[Fe]_{theo}$	$[Si]/[Fe]^{(II)}_{EDX}$	$[Si]/[Fe]^{(III)}_{EDX}$
0.5	0.35 ± 0.03	0.30 ± 0.15
1	0.61 ± 0.07	0.69 ± 0.12
2	1.06 ± 0.31	1.16 ± 0.09

Table SIV-3. Calculation of the critical nucleation barrier ΔG^* and the used parameters for the different particles. K_{sp} and ρ values were taken from [54–56]. The concentration used for calculation was 5 mM.

Particle	K_{sp} [mol^2/L^2]	ln(S)	v_M / N_A [10^{-29} m^3]	r^* [nm]	ΔG^* [10^{-20} J]	$\Delta G^* / k_BT$
FeS	4.90*10^{-18}	29.26	3.03	0.10	0.85	2.06
$FeCO_3$	3.50*10-11	13.48	4.95	0.36	10.7	25.99
Fe_2S_3	1.40*10-88	191.69	8.06	0.04	0.14	0.34
$Fe_2(CO_3)_3$	2.79*10-39	78.18	0.13	0.16	2.01	4.90

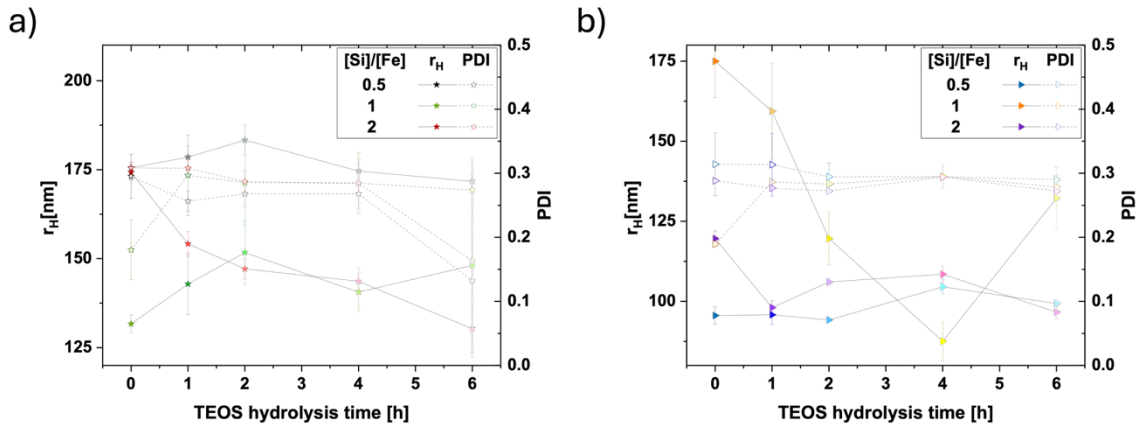


Figure SIV-6. Hydrodynamic radius (r_H) of particles derived from (a) Fe(II) and (b) Fe(III) with varying [Si]/[Fe] ratios and increasing TEOS hydrolysis time before the synthesis.

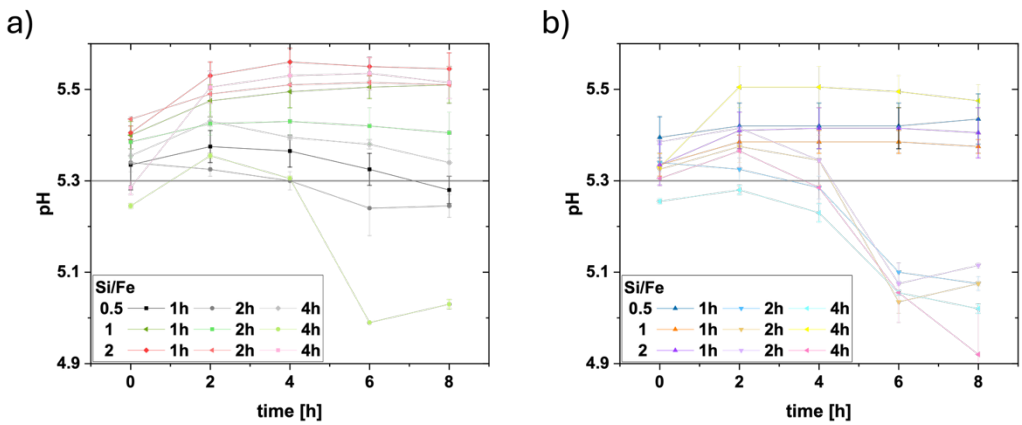


Figure SIV-7. pH values over 8 h reaction time for samples derived from (a) Fe(II) and (b) Fe(III) with varying [Si]/[Fe] ratios and increasing TEOS hydrolysis time before the synthesis. The degradation of phenol/H_2O_2 is shown in **Figure IV-6**.

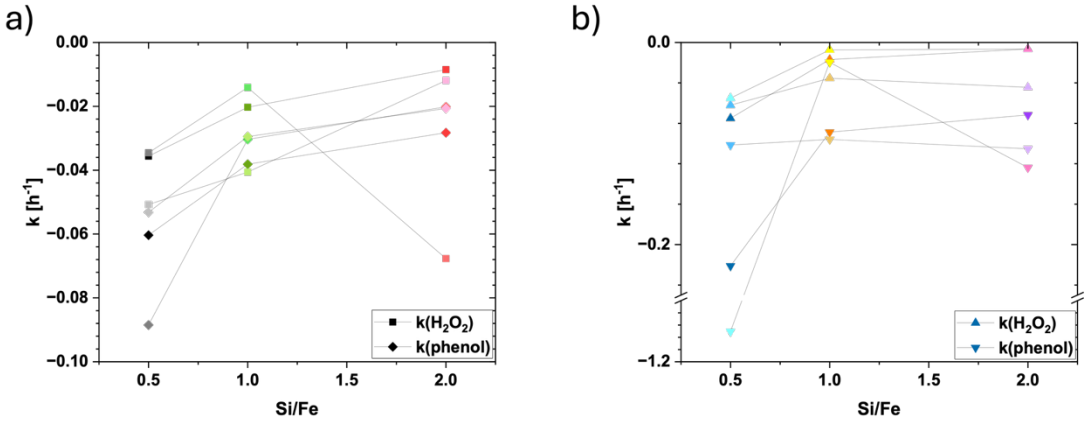


Figure SIV-8. First order reaction rates of both, H_2O_2 and phenol degradation, determined by linear fits of the normalized reaction profile for (a) Fe(II) and (b) Fe(III) derived materials. Samples deviated from linear behavior (cf. **Figure SIV-10**), were only fitted in the linear region (< 4h).

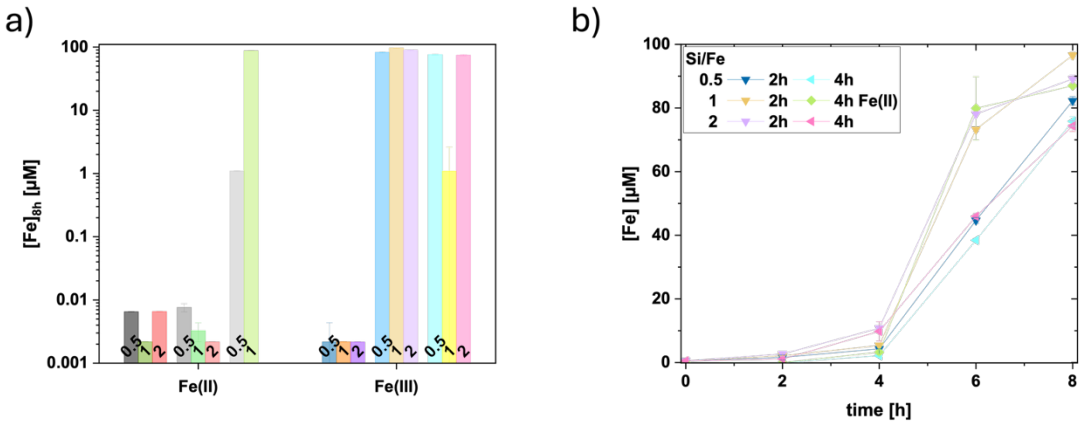


Figure SIV-9. (a) Leached iron concetration after 8 h of reaction time for samples derived from Fe(II) and Fe(III) with varying [Si]/[Fe] ratios and increasing TEOS hydrolysis time before the synthesis. (b) Visualization of the dissolution over the 8 h reaction for selected samples.

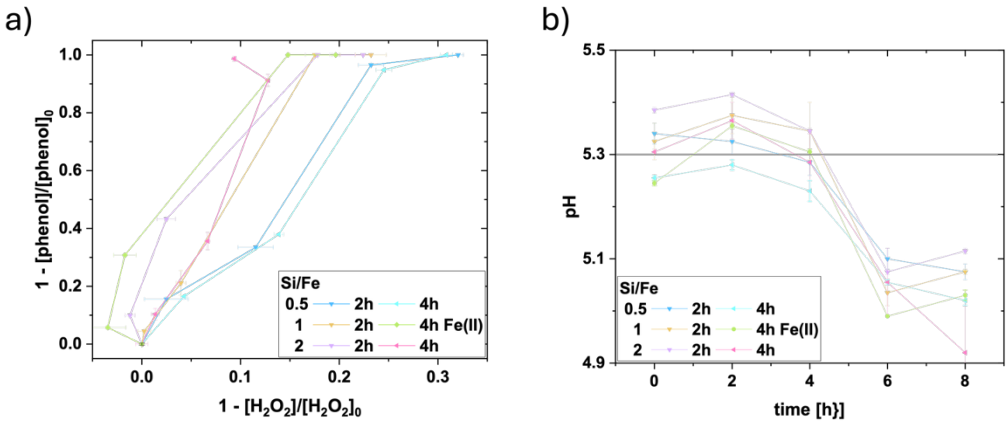


Figure SIV-10. (a) Normalized phenol degradation over normalized H_2O_2 degradation for selected samples. (b) pH over 8 h reaction time for selected samples.

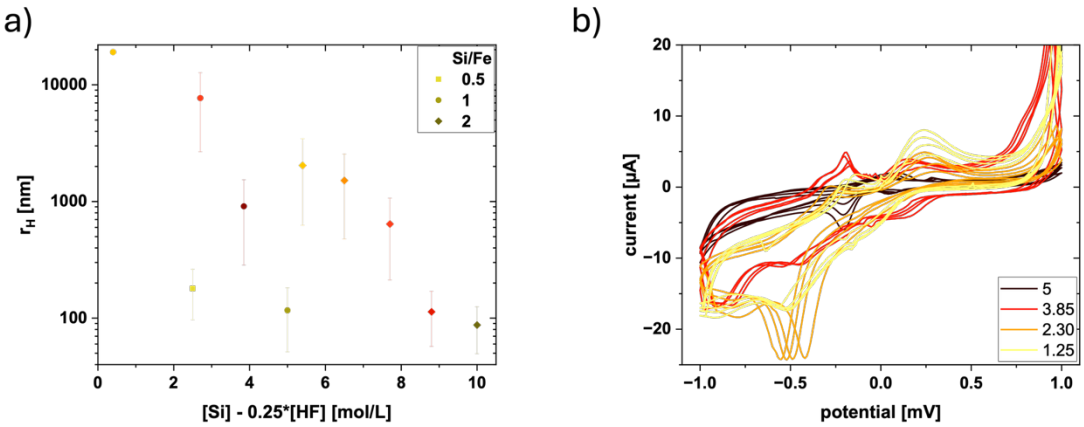


Figure SIV-11. (a) Hydrodynamic radius (r_H) of particles derived from FeS at pH 10 with differing [Si]/[Fe] ratios of 0.5, 1, and 2. The etched particles show significant size increase, which can be directly backtracked to the increased aggregation of

these samples. (b) Cyclic voltammograms of particles derived from FeS at pH 10 with [Si]/[Fe] = 1. The same points are shown, which are used in **Figure IV-7a**.

Two effects contribute to the E_p and I_p shifts visible in the CV measurements. First, the reduced silica shell allows better electrochemical access to the active surface resulting in an increase in the peak current for a decrease in the silica concentreation / thickness / density. Secondly, the shift in the peak potential to more negative values comes due to aggregation effects on the electrode and thus higher overpotentials necessary to induce the electrochemical reaction. This also results in decreasing peak currents from the first to the last cycle for one sample.

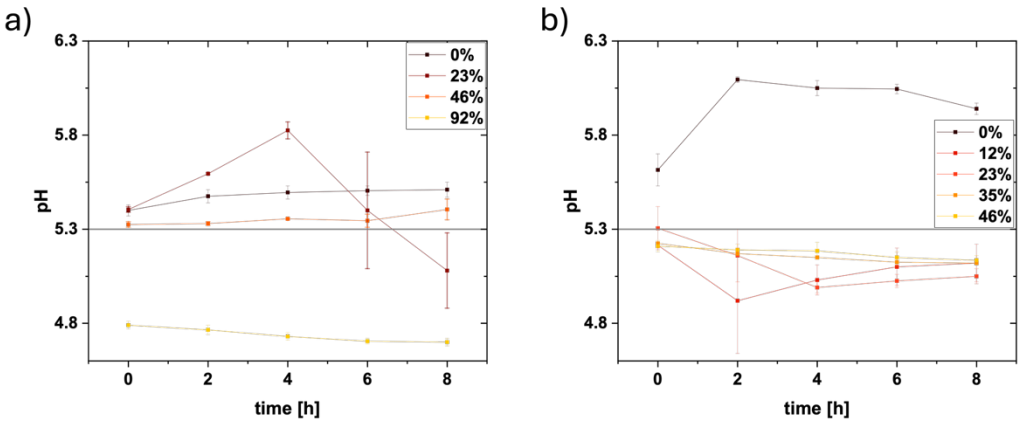


Figure SIV-12. pH values over 8 h of reaction time for the samples with etched silica shell. The degradation of phenol/H_2O_2 is shown in **Figure IV-7**. Samples derived from syntheses with (a) [Si]/[Fe] = 1 and (b) [Si]/[Fe] = 2 before subsequent etching with HF.

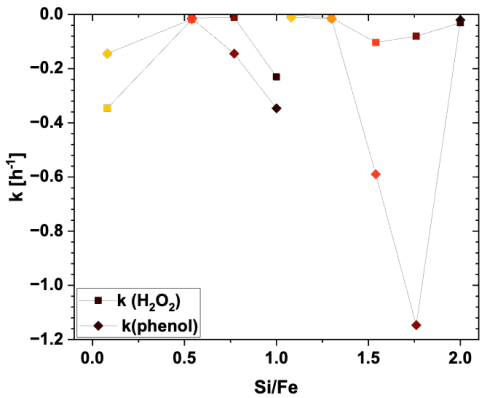


Figure SIV-13. First order reaction rates of both, H_2O_2 and phenol degradation, determined by linear fits of the normalized reaction profiles.

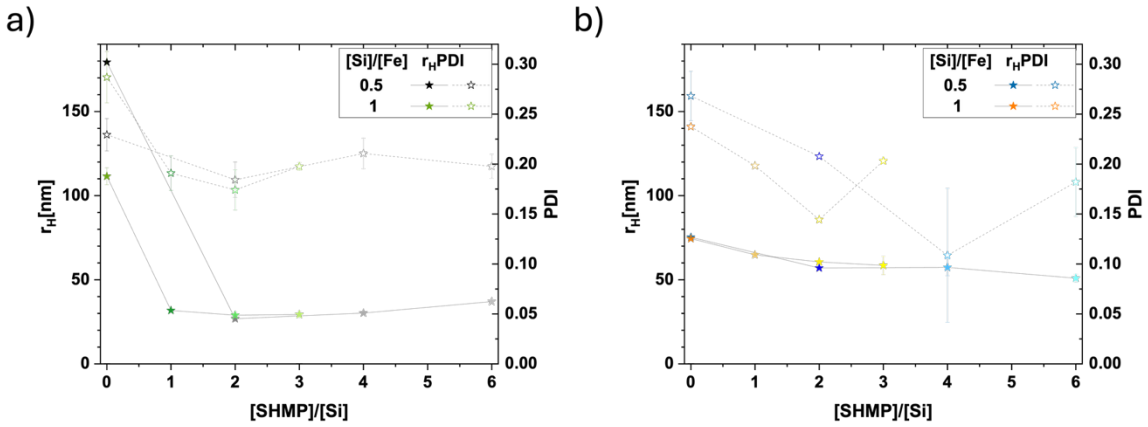


Figure SIV-14. Hydrodynamic radius (r_H) of particles derived from Fe(II) and Fe(III) with varying [SHMP]/[Si] ratios. (a) Fe(II) and (b) Fe(III).

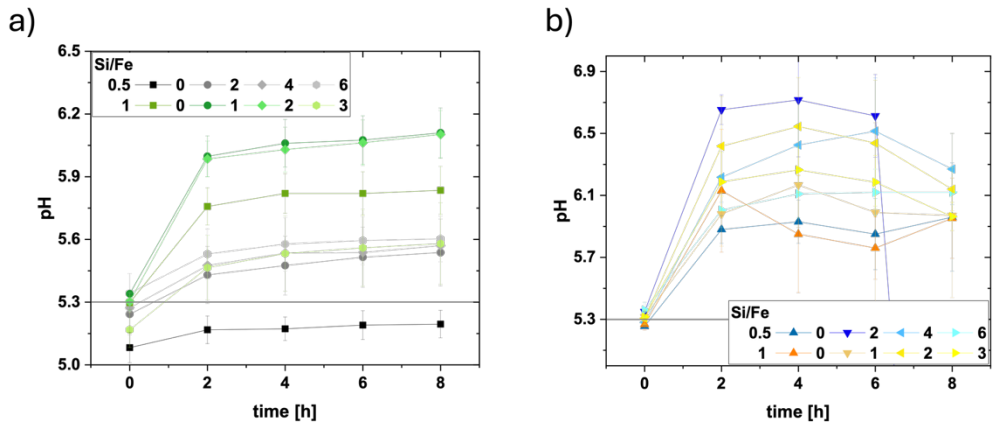


Figure SIV-15. pH values over 8 h reaction time for particles derived from (a) Fe(II) and (b) Fe(III) with varying [SHMP]/[Si] ratios. The degradation of phenol/H_2O_2 is shown in **Figure IV-8**.

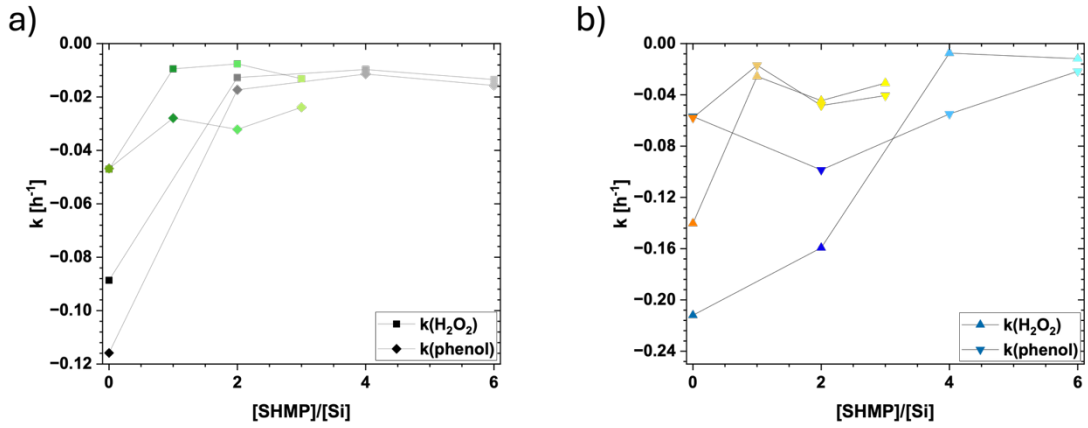


Figure SIV-16. First order reaction rates of both, H_2O_2 and phenol degradation, determined by linear fits of the normalized reaction profile for (a) Fe(II) and (b) Fe(III) derived materials.

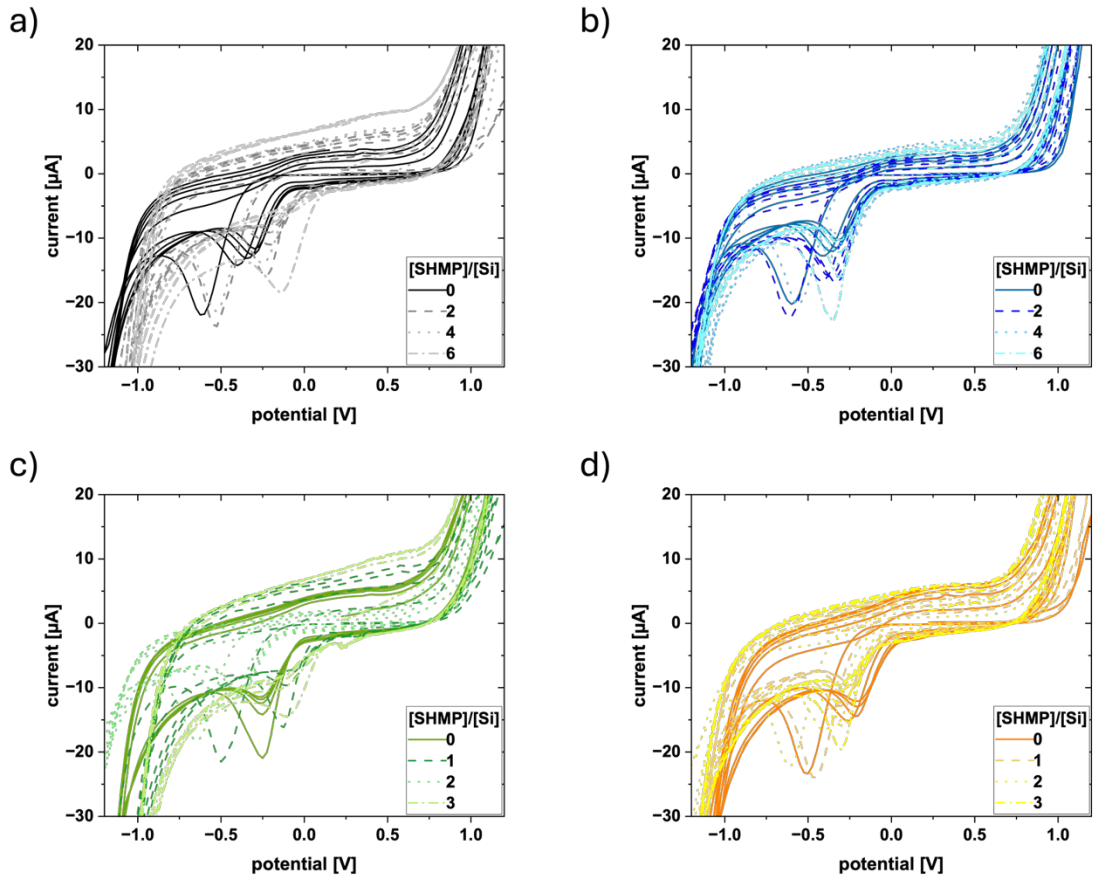


Figure SIV-17. Cyclic voltamogramms for particles derived from (a, c) Fe(II) and (b, d) Fe(III) with varying [SHMP]/[Si] ratios.

Chapter V. Influence of Complex Precursors on the Coprecipitation of Transition Metal Sulfides and Silica

5.1 Abstract

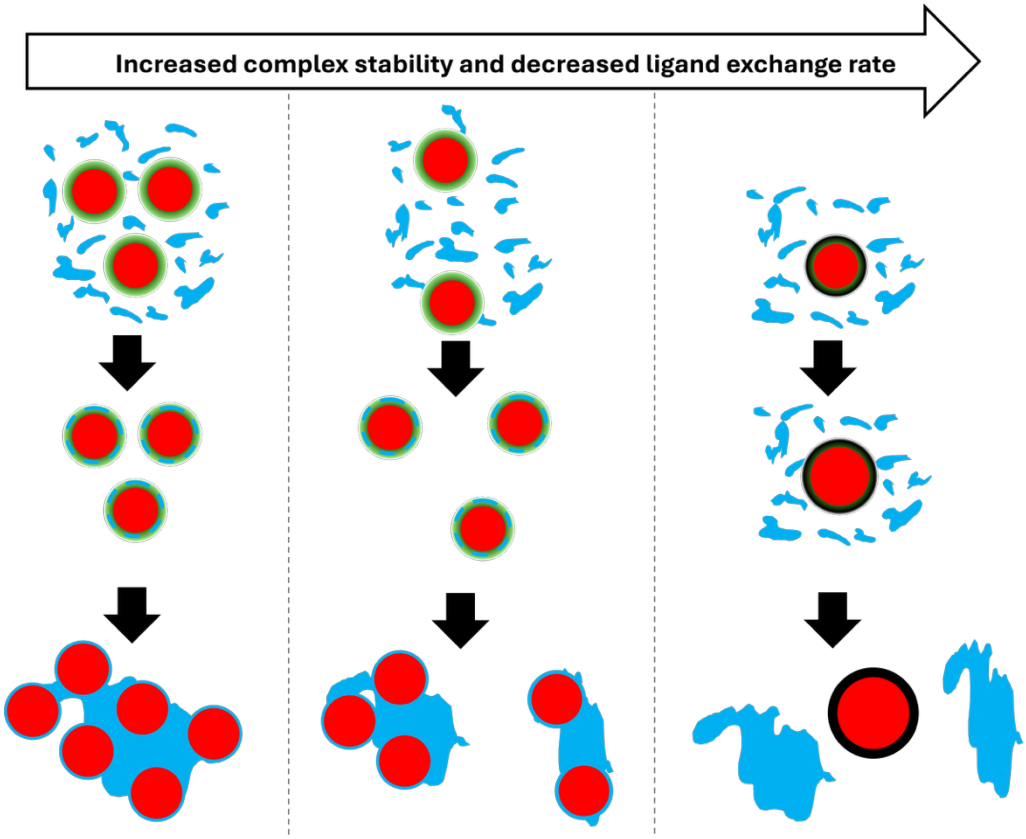


Figure V-1. Graphical Abstract: The combination of two aqueous solutions results in spontaneous coprecipitation of transition metal sulfides (red) in a silica matrix (blue) as shown in **Chapter III**. The formation of transition metal complexes prior to combination alters the precipitation process. With increasing complex stability, the number of nuclei (red), and with decreasing ligand exchange rate, the amount of growth prior to capture can be controlled. Ultimately, ligands with high surface affinity can hinder the silica condensation on the nucleus surface (black rim).

The limitation/control of diffusion and nucleation are powerful tools to create nanoparticles and control their size, uniformity, and polydispersity (**Chapter I**). In this part, metal complexes with differing ligands, such as EDTA, NTA, TETA, PAA, L-His, and L-Cys, were investigated as precursors for the synthesis of transition metal sulfide nanoparticles under biomimetic aqueous conditions. By systematically varying ligand systems, precursor compositions, and

alloying conditions, insights into the competing processes governing particle formation are obtained. The results demonstrate that precursor-controlled synthesis provides a versatile route for tailoring nanoparticle formation pathways and establishes a mechanistic framework for the rational design of biomimetic semiconductor nanomaterials. Detailed investigation of the CdS system provided mechanistic insight into how complex stability and ligand-mediated surface interactions influence nucleation, growth, and particle aggregation. The findings indicate that precursor design offers an additional level of control over the coprecipitation process introduced in **Chapter III** and establish a framework for understanding complex-mediated nanoparticle formation in aqueous systems.

Contributions to experimental work:

- Bastian Rödig: Conceptualization, Experimental Work, Data Evaluation
- Ulrich Schürmann: Experimental Work, Data Evaluation

5.2 Introduction

Information about the coupled coprecipitation of transition metal sulfides and silica can be found in **Chapter III**.

5.2.1 Nanoparticles Formation Utilizing Complexation

The presence of weak chelating agents, such as citrate, tartrate, or ammonia, have shown to influence the hydroxide/sulfide precipitation of heavy metals. While the displacement of the chemical equilibria is only marginal, the size and size distribution of the precipitate is reduced for both, hydroxide and sulfide [2]. Similar effects on the precipitation have also been observed by addition of amino acids such as cysteine [3–5] and histidine [6–8], or polyelectrolytes such as polyacrylic acid [9,10]. Also, the use of more typical chelating ligands such as ethylenediaminetetraacetic acid (EDTA) [11,12], or nitrilotriacetic acid (NTA) [6] have shown size reduction effects on precipitates.

The size decrease of the formed precipitate arises from the chelating agent which can perform several functions, such as acting as a capping agent/growth inhibitor [4–8,12], serving as the anion source through decomposition [3,13,14], functioning as a structure-forming agent [6,9,10,15,16], or acting as a surface-stabilizing agent [3–6,8,10,17]. The relative contribution of these mechanisms depends strongly on the specific ligand and reaction conditions and often cannot be separated.

In addition, the ligands also influence the kinetics of precipitation. Especially, EDTA was found to be a powerful kinetic inhibitor for copper (II) sulfide precipitation even in highly supersaturated solutions. The precipitation rate only increases with increasing copper concentration and decreases with increasing EDTA/Cu ratio making the complex the kinetically active species [12].

Related effects arise in the synthesis of CdS bionanocrystals using cysteine (Cys) [5] or ZnS bionanocrystals using histidine (His) [7] as nucleating agent. In both cases fluorescent, photo catalytically active quantum dots (QDs) with pH dependent photoluminescence (PL) spectra (due to missing surface passivation) can be created. The size in both cases can be influenced by variation of the sulfide concentration rather than the ligand concentration [5,7].

In precipitation experiments with excess ligand concentrations (CdS in His rich media, CuS/ZnS in Cys rich media), the size and therefore PL spectra are highly dependent on the ligand concentration instead [4,8,17].

For the universally applicable kinetics [18] for 1:1 (**Eqn V-1**) and 1:2 (**Eqn V-2**) complexes, the formation of the complex and the equilibrium constant K can be written as:

$$M^a + L^b \rightleftharpoons ML^{a+b} \quad ; \quad K_1 = \frac{[ML^{a+b}]}{[M^a][L^b]} \tag{V-1}$$

$$ML^{a+b} + L^b \rightleftharpoons ML_2^{a+2b} \quad ; \quad K_2 = \frac{[ML_2^{a+2b}]}{[ML^{a+b}][L^b]} \tag{V-2}$$

with $[M^a]$ the free cation (M^a) concentration, $[L^b]$ the free ligand (L^b) concentration, and $[ML^{a+b}]$ and $[ML_2^{a+b}]$ the concentration of the complex. The resulting complex stability β, in literature often given as $\log_{10}\beta$, can be calculated from the equilibrium constants and is related to the reaction rates:

$$\beta_n = \prod_{k=1}^{n} K_n = \prod_{k=1}^{n} \frac{k_{on,i}}{k_{off,i}} \tag{V-3}$$

With the reaction rates of the complex formation k_{on} and the reaction rate of the complex dissociation k_{off}. The change over time of the concentration of free metal cation in solution and the total metal and ligand concentrations are then given by:

$$\frac{d[M]}{dt} = k_{off}[ML] - k_{on}[M][L] \tag{V-4}$$

$$[M]_{tot} = \frac{[M]}{1 + \beta_1[L] + \beta_2[L]^2} \tag{V-5}$$

$$[L]_{tot} = [L] + [M](\beta_1[L] + 2\beta_2[L]^2) \tag{V-6}$$

In precipitation experiments, the initial free metal concentration and therefore the degree of supersaturation (see **Chapter I**) is only dependent on the total concentration of both metal M and ligand L as well as the complex stability β.

In the coupled coprecipitation process, nucleation of metal sulfides releases protons, causing a local pH decrease that triggers silica condensation at the surface of the nuclei. The resulting primary particles are immediately embedded into the forming silica network, and the final secondary clusters arise from the spatial distribution and number of these nuclei. Therefore, it

is hypothesized that ligands influence the resulting nanostructures through modulation of nuclei density / number of nuclei and surface accessibility.

5.2.2 Complexes Used for Nanoparticle Formation

Ethylenediaminetetraacetic acid (EDTA) (cf. **Figure V-2a**) is a commonly used potentially hexadentate chelating ligand, complexing almost any transition metal (TM) in a 1:1 ratio. The fully deprotonated ligand typically adopts an octahedral coordination geometry, in which EDTA can occupy all the vertices; if deprotonation is incomplete, water usually occupies the remaining coordination sites [19,20].

Nitrilotriacetic acid (NTA) (cf. **Figure V-2b**), another commonly used chelating ligand, also typically forms complexes with transition metals in a 1:1 ratio. In its fully deprotonated state, the ligand usually binds in a tetradentate coordination geometry even for highly distorted ligand fields (e.g. Cu(II)). The remaining coordination sites are usually occupied by water [19–21].

Tetraethylenetetraamine (TETA) (cf. **Figure V-2c**) is a linear polyamine which can form transition metal complexes as tetradentate ligand in a 1:1 ratio. Due to its flexibility the coordination sphere is not as strictly limited as for EDTA/NTA. While TETA is able to form octahedral complexes with two water molecules in cis configuration for most transition metals, in the case of highly distorted ligand fields (e.g. Cu(II)), TETA occupies coordination sites in one plane with trans water coordination in elongated axial position [22].

Polyacrylic acid (PAA) (cf. **Figure V-2d**) is a linear polymer containing multiple carboxylate groups capable of complexing transition metal cations. At high PAA dissociation α ($\alpha > 0.2$, $pH > 5$), cations are bound bidentate, while at lower α ($\alpha < 0.2$, $pH < 5$) monodentate ligand complexes become more appreciable [23–25]. For more information about the behavior of PAA in the presence of transition metal cations at intermediate / elevated pH values, see **Chapter VI**.

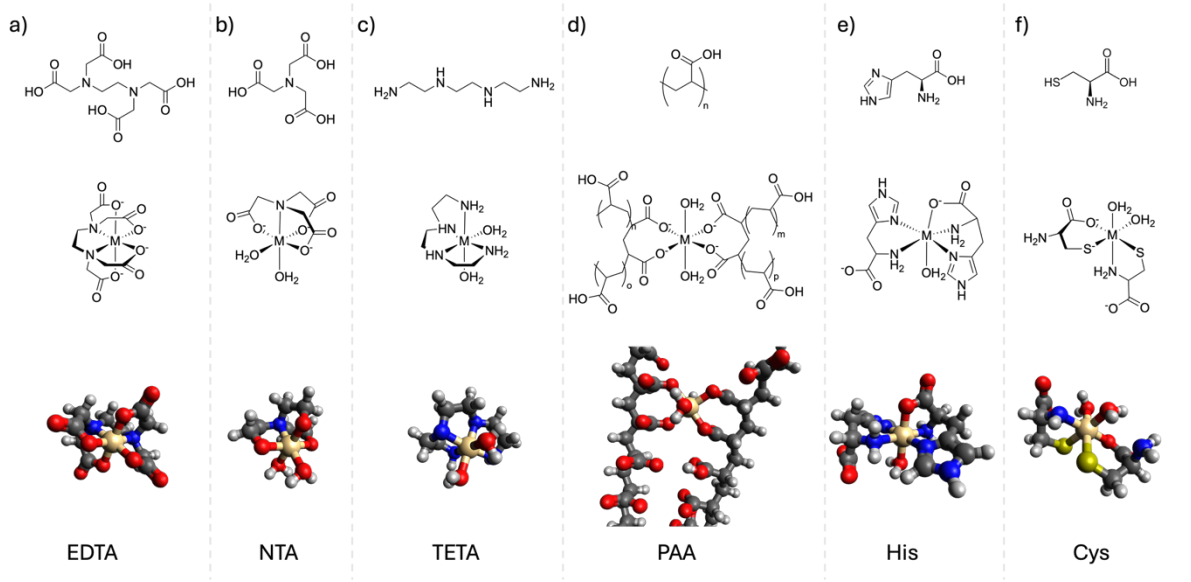


Figure V-2. Visualization of used complexes from top to bottom: valence structural formula of the ligands (neutral charge), Natta projection of formed octahedral complex with ligand charges corresponding to a pH value of 11, and the three-dimensional shape as balls and stick model. For polyacrylic acid (PAA), one complex center is shown exemplary even though multiple centers may occur along one chain. For Cysteine (f) both bidentate complexation modes with the sidechain and the carboxylate/the amino group are shown (S,O and S,N). Note that the metal center/complex is shown without charges. For the typically used charge in the experiments (2+) the charged complexes from left to right are: $[M(EDTA)(H_2O)_2]^{2-}$, $[M(NTA)(H_2O)_2]^{-}$, $[M(TETA)(H_2O)_2]^{2+}$, $[M(AA)_4(H_2O)_2]^{2-}$, $[M(His)_2(H_2O)]^{0}$, $[M(Cys)_2(H_2O)_2]^{2-}$.

All natural amino acids can form complexes with transition metal cations in various ratios (1:1, 1:2, 1:3, 1:4, and even sometimes 1:6) with differing thermodynamic stability understandable by the HSAB concept. However, at elevated pH values and in the lower ratios, only a few are stable against hydroxide precipitation [26]. The coordination geometry is typically octahedral, usually binding the AS bidentate (O,N) or sometimes even tridentate (O,N, and sidechain). At high protonation, typical glycin-like (N, O) coordination occurs, while at elevated pH the side chain is more likely to complex the metal [27]. For simple complexes, depending on the ligand, both octahedral and tetragonal complexes can be formed depending on the ligand field of the respective cation [26].

L-Histidin (His) (cf. **Figure V-2e**) can complex various transition metals in a 1:2 ratio, typically in an octahedral geometry [28,29]. For highly distorted ligand fields (e.g. Cu(II)) the ligand is able to bind tridentate (N, N, O) with the nitrogen sites in equatorial and the carboxylates in axial position [30,31]. For other cations, His usually binds bidentate (N, N) in equatorial position with potentially one axial bound carboxylate, while the remaining coordination site is occupied by water [31–33]. Mixed ligand complexes of D-His and L-His have shown to be favored over LL/DD complexes due to less steric hindrance in the coordination sphere [34].

L-Cysteine (Cys) (cf. **Figure V-2f**) can complex various transition metals in a 1:2 ratio in octahedral geometry [35,36]. The bidentate ligand typically binds with the thiolate and depending on the hardness of the cation with O or N. The two remaining cis coordination sites are typically occupied by water molecules [37]. The thiolate can also act as bridging ligand forming polynuclear complexes, especially at excess Cys concentrations or in the solid state resulting in distorted tetragonal geometry (MS_4) [26,35,38–40].

Also possible is the formation of mixed ligand complexes in a 1:2 ratio, especially for variations of amino acids forming complexes with enhanced/decreased complex stability compared to the complexes with identical ligands [41]. In Cys/His mixed ligand complexes in 1:2 ratio, the ligands are typically bound bidentate in octahedral geometry. At elevated pH values again coordination with the sidechain is favored [27,42–47].

5.3 Experimental

5.3.1 Materials

The following substances were used as received without further purification: 28% ammonium hydroxide solution (NH_3 in H_2O, Merck, ≥99.99 %), cadmium nitrate tetrahydrate ($CdNO_3$; Sigma-Aldrich, 99.997 %), cobalt nitrate hexahydrate ($CoNO_3 \cdot 6H_2O$; Merck, p.A.), copper nitrate trihydrate ($CuNO_3 \cdot 3H_2O$; Fluka, p.A.), ethylenediaminetetraacetic acid ($C_{10}H_{16}N_2O_8$, EDTA, TCI, ≥98 %), glycine ($C_2H_5NO_2$, Sigma-Aldrich, ≥98 %), hydrochloric acid (32 % HCl in water; Sigma-Aldrich, analytical grade), iron nitrate nonahydrate ($Fe_2(NO_3)_3 \cdot 9H_2O$, Merck, p.A.), L-alanine ($C_3H_7NO_2$, Sigma-Aldrich, ≥98 %), L-arginine ($C_6H_{14}N_4O_2$, Sigma-Aldrich, p.A.), L-cysteine ($C_3H_7NO_2S$, Sigma-Aldrich, ≥98 %), L-histidine ($C_6H_9N_3O_2$, TCI, ≥99 %), L-lysine ($C_6H_{14}N_2O_2$, Sigma-Aldrich, ≥98 %), L-tyrosine ($C_9H_{11}NO_3$, Sigma-Aldrich, ≥98 %), manganese nitrate hydrate ($MnNO_3 \cdot H_2O$; Sigma-Aldrich, ≥98 %), nickel nitrate hexahydrate ($NiNO_3 \cdot 6H_2O$; Merck, p.A.), nitrilotriacetic acid ($C_6H_9NO_6$, Merck, ≥98 %), polyacrylic acid sodium salt (PAANa, Mw ~2.1k, Sigma-Aldrich), polyacrylic acid sodium salt solution (PAANa, Mw ~8k, Sigma-Aldrich, 45wt% in water), polyacrylic acid solution (PAA, Mw ~100k, Sigma-Aldrich, 35wt% in water), sodium sulfide trihydrate ($Na_2S \cdot 3H_2O$; VWR International, analytical grade), tetraethylorthosilicate (TEOS; Sigma-Aldrich, 98 %), sodium chloride (NaCl; Carl Roth, ≥99.8 %), sodium hydroxide (NaOH; Sigma-Aldrich, ≥98 %), triethylenetetramine (TETA, Sigma-Aldrich, mixture of isomers ≥98 %), and zinc nitrate hexahydrate ($ZnNO_3$; Sigma-Aldrich, ≥98 %). All solutions and dilutions were prepared using water taken from a Millipore system.

5.3.2 Apparatus

5.3.2.1 Synthesis of Nanoparticles:

The synthesis was analogous to the synthesis described in **Chapter III**. For the preparation of the metal ion containing solution the ligands were added and the pH was set to 11 to ensure complexation and check complex stability. The molar ratios used were: 1:1 (EDTA, NTA, TETA), 1:2 (Cys, His), and 1:3 (Cys, His).

Immediately after mixing, colored suspensions of more or less finely dispersed precipitates were obtained in all cases except for solutions derived from cysteine complexes. After a stirring time of 24h, the formed particles were separated from dissolved salt (mainly NaCl) by

centrifugation in a Sigma 3-18KS centrifuge at 4700 rpm (4248 g) for 5 min at room temperature. If separation was not possible under these conditions, ultracentrifuge filters with a molecular weight cutoff (MWCO) of 3 kDa were used at 2200 rpm (2000 g). The sedimented material was washed three times with water to further remove any residues. Finally, the purified particles were re-dispersed in water using an ultrasonic processor (Hielscher UP200Ht).

5.3.2.1.1 pH Variation

For pH variation during synthesis, the complex solution was either set to pH 11 or 12 before the combination with the silica solution. The silica solution was also set to the respective pH value before the combination and after the hydrolysis time.

5.3.2.1.2 Variation of Sulfide Concentration

Cadmium cysteinate solution is prepared as before. To the silica containing (10, 20, and 30 mM) solution different amounts (10, 15, and 20 mM) of sodium sulfide is added and the pH is set to 11 before combination.

5.3.2.1.3 Mixed Complexes

1 equiv. cysteine and 2 equiv. amino acid (Ala, Arg, Gly, His, Lys, Tyr) are mixed with 1 equiv. cadmium and the pH is set to 11 to obtain the cadmium complex solution.

5.3.2.1.4 ZnxCdx-1S from Cys / His Complexes

Complex solutions (2:1) of Cd or Zn with histidine and with cysteine are created and set to pH 11. The desired amount of Zn and Cd complex solution are mixed prior to synthesis and then combined with the respective amount of silica and sulfide containing solution.

5.3.3 Methods

5.3.3.1 Dynamic Light Scattering (DLS)

Preparation and measurement procedure were performed as described in **Chapter III**. Average hydrodynamic diameters of the scattering species were extracted via a second-order cumulant analysis [48] and the CONTIN algorithm [49,50]. As many of the studied systems showed

rather high polydispersity, the derived apparent sizes should be considered as rough estimates of the dimensions of nanostructures occurring in solution.

5.3.3.2 Transmission Electron Microscopy (TEM)

Preparation on carbon film copper grids analogous to the procedure described in **Chapter III**. TEM studies and electron diffraction patterns were carried out on a Tecnai F30 G2 STwin from FEI (300 kV) equipped with an EDX detector (Si/Li, EDAX). ADF-STEM micrographs and EDX elemental mapping were conducted on a probe Cs-corrected JEM-ARM200F NEOARM from JEOL (200 kV) equipped with two front and entry side positioned silicon drift EDX (100 mm^2 area each) detectors.

5.3.3.3 Scanning Electron Microscopy / Energy Disperse X-ray Spectroscopy

Field emission scanning electron microscopy (SEM) images were recorded on a Phenom Pro X scanning electron microscope (FEI Company, Hillsboro, OR, US) equipped with an EDX and a backscattering detector. Lyophilized samples were prepared on a sample holder (d = 12.7 mm, aluminum and double-sided adhesive carbon tab) and sputtered with Au/Pd for 30 s (2.45 kV, 22 mA) under an Argon atmosphere using a Polaron E 510 Series II Sputter Coater (Polaron Instruments, London, UK).
Additional electron micrographs (TEM/SEM) and tables containing the EDX data can be found in the online repository.

5.3.3.4 Fluorescence

Fluorescence spectra were recorded using a Cary Eclipse Fluorescence spectrometer from Agilent Technologies (Santa Clara, CA, USA). The temperature was held constant at 25°C. Because of the multi-sample holder, reference and sample can be measured simultaneously. The NPs were suspended in water or PBS to obtain the sample, and the reference is the corresponding solvent. 3 mL of these suspensions and the respective references were inserted into a quartz glass fluorescence cuvette with a 10 mm path length. To obtain the relevant range of the spectrum, multiple measurements were performed. The excitation filter and the emission filter were adjusted after each measurement to the maximum of the opposite spectrum until the value remained constant. Then, the final excitation and emission spectrum can be measured.

To estimate the proportion of defect-induced emission, the photoluminescence (PL) spectra were deconvoluted using a bimodal model consisting of a Gaussian component and a log-normal component. The Gaussian component was attributed to emission near the band edge, while the asymmetric component described by the log-normal function was attributed to the long-wavelength region of defect-induced (trap state) emission, which is consistent with previous reports on CdS- and ZnS-based quantum dots [51–55]. The fraction of defect-related emission (DE) was then calculated from the integrated area of the defect-related contribution ($\int I_D(\lambda)d\lambda$) relative to the total emission ($\int I_{BE}(\lambda)d\lambda + \int I_D(\lambda)d\lambda$):

$$f_D = \frac{\int I_D(\lambda)d\lambda}{\int I_{BE}(\lambda)d\lambda + \int I_D(\lambda)d\lambda} \quad \text{(V-7)}$$

5.3.3.5 Data Availability

Additional data, including SAED indexing tables, EDX, fit parameters, and associated scripts, are available in the online repository (Novel nanoparticle synthesis in self-organizing water–based systems - online repository, 10.5283/epub.80300). Representative data and fits are shown in the SI.

5.4 Results and Discussion

5.4.1 Cation and Ligand Screening in the Coupled Coprecipitation Process

5.4.1.1 Overview of the Investigated Transition Metal Cations

To evaluate the influence of complex precursor agents as a transition metal source for the coupled precipitation reaction (see **Chapter III**), various transition metals were complexed with various ligands and then precipitated in the presence of silica ([Si]/[M] = 2).

To investigate the overall structure (secondary clusters) and size, TEM/SEM/EDX and DLS measurements were conducted. To obtain additional information about the primary particles, fluorescence measurements were conducted. Averages of hydrodynamic radii derived from multiple DLS measurements are shown in **Figure V-3**, visualizing the overall size trends, while the more detailed CONTIN [49,50] derived size distributions can be found in **Figure SV-1**.

Additional experiments have been conducted for manganese (data not shown), but due to the instability of the complexes at elevated pH values (~11) against oxidation [56,57] manganese dioxide precipitates make the coupling and sulfide precipitation unfeasible.

For the purposes of this analysis, the cations are divided into two groups: the cations that are relatively soft ($Cd^{2+} < Zn^{2+} \approx Cu^{2+}$) (cf. **Figure V-3a**) according to the HSAB concept [58], and the cations that are somewhat harder ($Ni^{2+} < Co^{2+} < Fe^{2+}$) (cf. **Figure V-3b**).

For the softer cations (Cu, Zn, Cd) two distinct trends emerge. First, a size reduction, compared to the reference particles (synthesis without prior complexation of the cations), occurs for all particles derived from complexes of either cation with the amino acids (Cys, His) as ligands. Second, a size increase compared to the reference arises for all particles derived from other Cu complexes. For Zn, the complexes of PAA and EDTA result in a slight size decrease, while the complexes of NTA and TETA both lead to a size increase. For Cd all other complexes result in a size increase. (cf. **Figure V-3a**)

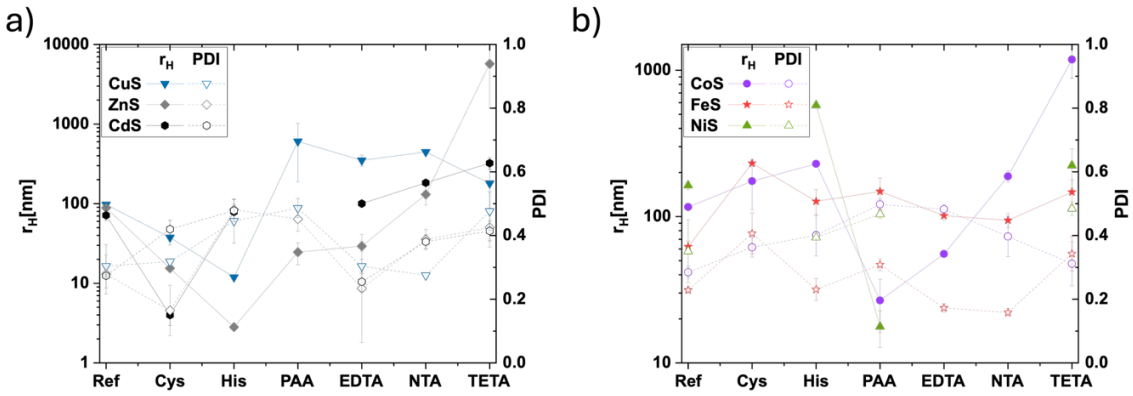


Figure V-3. Hydrodynamic radius and polydispersity index (PDI) for (a) copper, zinc, and cadmium sulfides and (b) cobalt, iron, and nickel sulfides, derived from various complexes, as shown in **Figure V-2**. Shown values are averages of multiple measurements to highlight trends. The more detailed size distributions derived from CONTN analysis can be found in **Figure SV-1**. Missing values indicate highly aggregating samples that cannot be measured reproducibly (Cd–PAA, Ni–Cys, Ni–EDTA, Ni–NTA).

For the harder cations (Co, Fe, Ni), two trends also stand out. First, a size increase relative to the reference occurs for all particles derived from Fe complexes, most likely attributable to oxidation to Fe(III) by atmospheric oxygen at elevated pH [59] and to early hydroxide precipitation [59]. Therefore, similar to the manganese complexes, the iron complexes were not further investigated. Second, a size decrease relative to the reference occurs only for particles derived from complexes with PAA as the ligand and from the CoEDTA complex. For Ni, a majority of the samples aggregated/sedimented heavily/quickly, making DLS measurements unreproducible. (cf. **Figure V-3b**)

TETA stands out as a ligand, as it is the only one exclusively binding via amino groups. The pairing (Cu/Fe, Zn/Co, Cd/Ni) of the cations based on their stability constants [60] is reflected in the resulting particle size. Combined with the rather open complex geometry (cf. **Figure V-2c**) and the possibly fast ligand exchange [61], it stands to reason that the use of TETA as a ligand in a 1:1 complex and at stoichiometric concentrations does not reduce the size of secondary clusters. Instead, TETA may release metal ions sufficiently rapidly to generate a comparatively high nuclei density. Therefore, fusion of secondary clusters is likely promoted by the comparatively high nuclei density resulting from the rapid release of metal ions. Additional contributions from electrostatic interactions between partially protonated TETA and negatively charged silicate species that promote aggregation cannot be excluded.

EDTA and NTA primarily influence the coupled precipitation process by modulating the concentration of kinetically available metal ions. Consequently, the resulting nucleation

behavior is determined by the interplay between complex stability, ligand exchange kinetics, and respective sulfide solubility.

In the case of EDTA complexes, the comparatively high complex stabilities [21] and slow ligand exchange rates [62] reduce the concentration of available metal ions and delay the establishment of supersaturation. The influence on the coprecipitation depends on the solubility of the respective sulfide. In the case of CuS, the low solubility product [63] nevertheless allows for rapid nucleation and partial coupling to silica condensation. (cf. **Figure SV-1**, EDX) The higher solubility of NiS [63] leads to lower supersaturation, thereby suppressing the formation of secondary clusters. (cf. **Figure SV-1**, EDX) Zn and Co represent intermediate cases, where nucleation remains sufficiently fast for successful coprecipitation but is slowed to the point that the effective nucleation density, and consequently the fusion of secondary clusters, is reduced. CdEDTA exhibits the weakest influence on secondary cluster size, which is consistent with its comparatively rapid ligand exchange [62] and low sulfide solubility [63]. (cf. **Figure SV-1**, EDX)

Compared with EDTA, NTA forms less stable complexes [18,21,64] and exhibits significantly faster ligand exchange kinetics [65]. As a result, supersaturation is reached more quickly, and the effect on the nuclei density is considerably reduced. Consequently, NTA has a smaller effect on the size of the secondary clusters. Only in the case of NiS does the combined effect of complex formation [66,67] and comparatively high sulfide solubility [63] remain strong enough to inhibit the formation of typical silica-containing secondary structures. (cf. **Figure SV-1**, EDX)

EDTA had previously been used as a kinetic inhibitor in sulfide precipitation systems at ligand-to-metal ratios of 1 or higher [12]. In the present coprecipitation system, however, the observed effects are more consistent with a modulation of supersaturation and nucleation density than with a direct inhibition of particle growth. Once silica deposition has begun, the growth of the primary particles is rapidly halted by encapsulation; the significance of subsequent growth inhibition by EDTA is limited [18,56].

PAA complexes differ from EDTA or NTA complexes in being significantly less stable [23–25], and the polymer induces steric and electrostatic effects [68,69]. For Cu, Zn, and Cd, high supersaturation, combined with low sulfide solubility, dominates precipitation behavior and largely masks the polymers influence. In contrast, CoS and NiS exhibit higher sulfide solubilities [63] and thus lower achievable supersaturations. Under these conditions, the modulation caused by PAA becomes clearly apparent, and a reduction in the size of the secondary clusters can be observed.

The observed behavior can be explained without invoking significant PAA-induced surface passivation. Its influence is therefore likely exerted primarily through the modulation of local ion availability [70] and through steric interactions between growing clusters [71]. The observed size reduction in CoS and NiS is consistent with these effects becoming relevant when nucleation is not dominated by extremely high supersaturation [63]. Increasing the molecular weight of the polymer could further enhance this behavior by increasing steric hindrance and slowing the release of metal ions [10,72–74].

5.4.1.2 Size Capping by Surface Chemistry

For complexes with His or Cys as ligands, a difference during precipitation was already observable. While almost an immediate color change after the sulfide addition (slight delay for EDTA complexes) was visible for all other complexes, the precipitation from complexes of Cys / His showed a rather slow color change. (cf. **Figure SV-2**)

TEM micrographs of CuS (cf. **Figure V-4a-**b) and CoS (cf. **Figure V-4d-e**) derived from Cys and His complexes, respectively, reveal the formation of particles in the range of few nanometers highly aggregated on the grid. For CuS the particles are of around 2.5 ± 1.5 nm in radius (cf. **Figure V-4c**), while for CoS the resulting particles are of around 2.1 ± 1.5 nm in radius (cf. **Figure V-4f**). The particles also show clearly visible lattice fringes indicative of a crystalline nature in the HRTEM micrographs (cf. **Figure SV-4 a**nd **Figure SV-7**). Derived from SAED (cf. **Figure SV-5 a**nd **Figure SV-8**), crystals of the covellite structure are detected for CuS and crystals of the NiAs structure are detected for CoS. Due to their partially amorphous nature, the reflexes are broadened or deviate slightly from the reference. The combination of the elemental compositions derived from EDX measurements of both TEM and SEM, and the visual appearance reveals an incomplete coupling of precipitation and silica condensation. (cf. online repository)

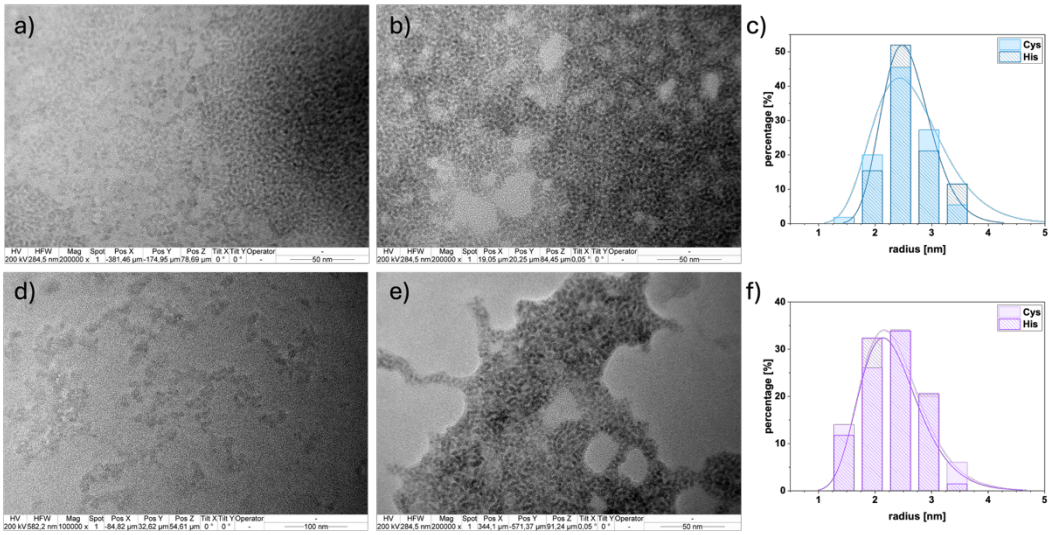


Figure V-4. HRTEM micrographs of CuS derived from (a) cysteine complex, (b) histidine complex, and CoS derived from (d) cysteine complex, and (e) histidine complex. The scale bar corresponds to 50 nm for (a), (b), and (e) and to 100 nm for (d), equivalent to a magnification of 20000x and 10000x, respectively. The size distributions for (c) CuS and (f) CoS are derived from size measurements in the TEM micrographs (n > 50). Further SEM/TEM micrographs can be found in **Figure SV-3 a**nd **Figure SV-4 f**or CuS and in **Figure SV-6 a**nd **Figure SV-7 f**or CoS. Diffraction patterns and the respective radial averages can be found in **Figure SV-5 f**or CuS and in **Figure SV-8 f**or CoS.

TEM micrographs of CdS (cf. **Figure V-5a-**b) and ZnS (cf. **Figure V-5d-**e) derived from Cys and His complexes respectively reveal the formation of particles in the range of a few nanometers, slightly aggregated, on the grid. For CdS the particles are of around 2.1 ± 2 nm in radius (cf. **Figure V-5c**), while for ZnS the resulting particles are slightly narrower in distribution of around 2.1 ± 1 nm in radius (cf. **Figure V-5f**). The particles also show clearly visible diffraction lines indicative of a crystalline nature in the HRTEM micrographs (cf. **Figure SV-10**, **Figure SV-12**, and **Figure SV-14**). Derived from SAED (cf. **Figure SV-11**, **Figure SV-13**, and **Figure SV-15**), crystals of the cubic zinc blende structure are detected for both ZnS (deviating from the reported hexagonal ZnS with QD size of 4.2 nm [7]) and CdS. Due to their partially amorphous nature and, in some cases, additionally due to the amorphous silica, the reflexes are broadened and can deviate slightly from the reference.

Combination of the elemental compositions derived from EDX measurements of both TEM and SEM and the visual appearance reveals an incomplete coupling of precipitation and silica condensation. (cf. online repository) The only sample also containing silica matrices with included QDs is ZnS derived from His complexes. (cf. **Figure V-5e**)

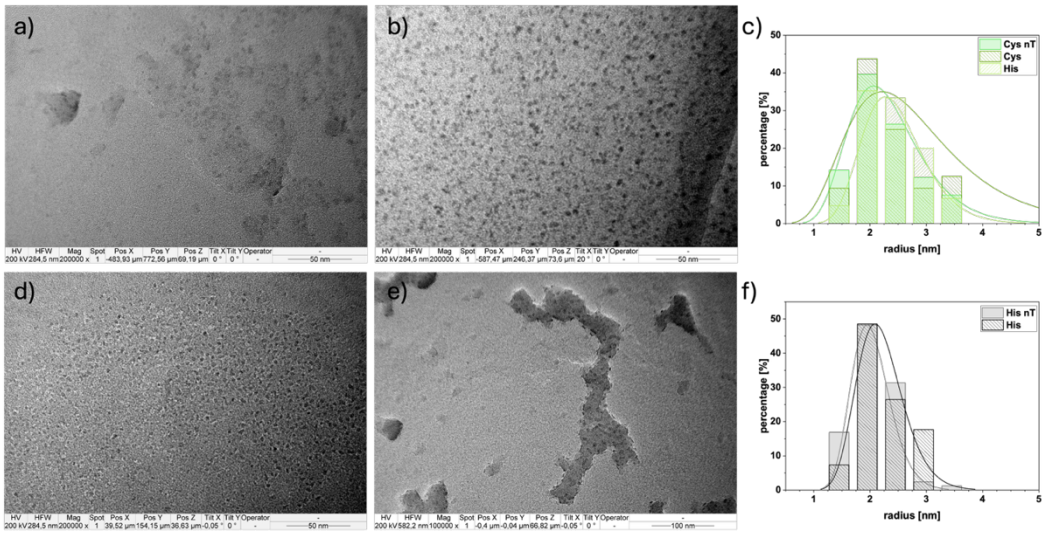


Figure V-5. HRTEM micrographs of CdS derived from (a) cysteine complex, (b) histidine complex, and ZnS derived from (d) cysteine complex, and (e) histidine complex. The scale bar corresponds to 50 nm for (a), (b), and (d) and to 100 nm for (e), equivalent to a magnification of 20000x and 10000x, respectively. The size distributions for (c) CdS and (f) ZnS are derived from size measurements in the TEM micrographs (n > 50). Further SEM/TEM micrographs can be found in **Figure SV-9 a**nd **Figure SV-10** for CdS, **Figure SV-12** and **Figure SV-6 f**or ZnS, and **Figure SV-14** for CdS/ZnS from a reference synthesis [5,7] without silica. Diffraction patterns and the respective radial averages can be found in **Figure SV-11** for CdS, in **Figure SV-13** for ZnS, and in **Figure SV-15** for the reference samples.

Syntheses of CuS [3,4], CoS [6], ZnS [4,75], and CdS [8,17] nanoparticles from cysteine and histidine complexes, as reported in the literature, rely on a large excess of ligand. In these cases, the large excess of ligand promotes persistent surface coverage during particle formation and thereby achieves growth control. In the present system, however, stoichiometric metal-ligand ratios are used.

Despite the absence of a large ligand excess, the resulting particles closely resemble quantum dots of CdS [5] and ZnS [7] from stoichiometric Cys and His complexes, respectively. (cf. **Figure SV-10** and **Figure SV-12**) This suggests that nanoparticle formation can already be achieved through precursor complexation, without the need of extensive ligand excess.

Cysteine is able to bind strongly to metal sulfide surfaces via thiolate coordination [76,77] and can limit further particle growth by suppressing monomer addition. The experimental observations are consistent with strong surface association of cysteine hindering efficient coupling between sulfide precipitation and silica condensation. Histidine appears to impair surface accessibility to a lesser extent, allowing silica deposition to occur at least in part of the system. (cf. **Figure V-5e**) Both amino acids form comparatively stable complexes [26,28,60], which reduces the initial supersaturation and therefore the nuclei density, but differ significantly in ligand exchange rates [78,79]. Therefore, the impact of surface passivation on growth and

the efficient occupation of the surface, hindering silica condensation, is becoming more important for cysteine.

Without further optimization, the coupling between sulfide precipitation and silica condensation remains incomplete. Although nanoparticle formation is clearly achieved, the local acidification appears insufficient to produce efficient silica encapsulation under the present conditions. These observations indicate that, unlike TETA, EDTA, NTA, and PAA, cysteine and histidine affect not only the supersaturation and nucleation but also the surface chemistry of the growing sulfide particles. Nevertheless, the concept of nanoparticle formation from stoichiometric complexes (without the size capping by coprecipitation) can be extended beyond CdS/ZnS to CuS/CoS.

5.4.1.3 Change in Primary Particles – CdS

While the previous section primarily discussed the formation of secondary clusters, the fluorescence properties of the resulting CdS particles provide additional information about the process of primary particle formation.

Fluorescence spectra of CdS derived from complexes with differing ligands precipitated at pH 11 and 12 can be divided into two groups. The first group, containing particles derived from EDTA, NTA, and PAA complexes (cf. **Figure V-6a**), shows no fluorescence behavior varying from that of particles derived from the reference synthesis. The absence of the fluorescence characteristic of QDs suggests either particle sizes outside the range of strong quantum confinement [80–82] or efficient non-radiative relaxation pathways [53,82].

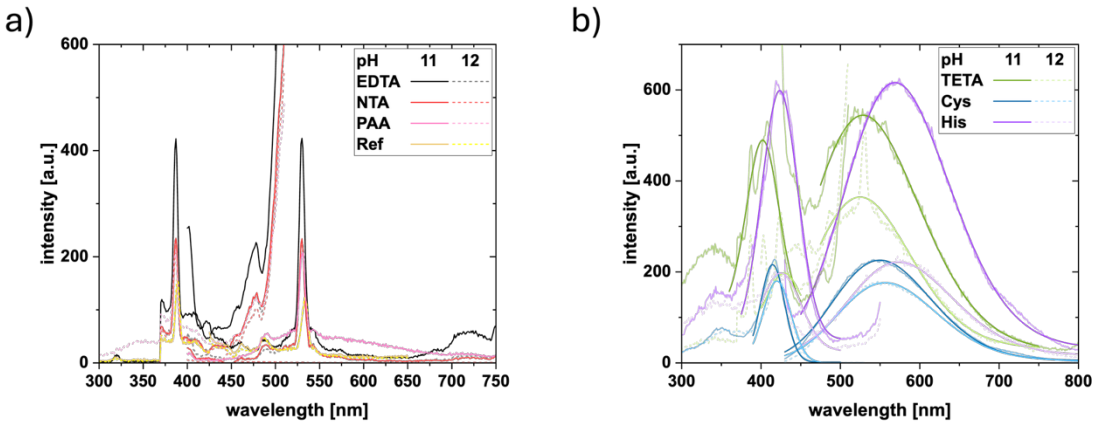


Figure V-6. Fluorescence spectra of CdS samples derived from different complexes synthesized at pH values of 11 and 12. Samples in (a) derived from EDTA and NTA complexes are directly compared to a reference (see **Chapter III**) (λ_{exc} = 387 nm, λ_{em} = 530 nm). Samples in (b) are derived from TETA, cysteine, and histidine complexes (λ_{exc} = 407 nm, 418 nm, and 420 nm, λ_{em} = 530 nm, 545 nm, and 570 nm).

The second group, containing CdS particles derived from TETA, Cys, and His complexes (cf. **Figure V-6b**), shows clear fluorescence behavior with rather broad excitation and emission. Especially the emission spectra with FWHM > 150 nm indicate not only bandgap emission but also a significant contribution by defect-related emission (DE) [51]. The peak excitation and emission do not change significantly either by increasing the pH or by variation of the ligand before to precipitation. (cf. **Figure V-7a**) Also, the shape of the PL curve, with an extended tail emission, does not change when comparing particles derived from TETA/His complexes with those derived from Cys complexes. Even though the particles differ structurally, since those derived from Cys do not have a silica shell.

No clear trend is evident in the PL intensities either. Since particles derived from TETA exhibit higher aggregation, this deviation is not particularly surprising. For Cys and His, however, a higher pH value decreases the PL intensity, most likely due to increased concentration of precipitate exceeding the size limit for fluorescence. A higher pH is expected to increase the fraction of S^{2-} and, therefore, the supersaturation, while simultaneously decreasing the degree of coupling to silica condensation [63]. (cf. **Figure V-7a**)

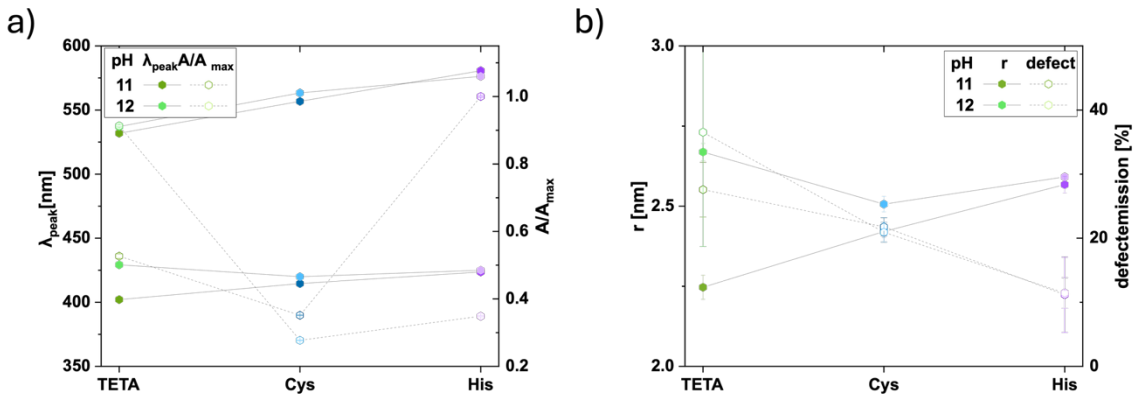


Figure V-7. (a) Emission and excitation peak of fitted fluorescence spectra (cf. **Figure V-6b**) and relative area of the emission for samples derived from complexes with TETA, cysteine, or histidine at pH of 11 or 12. (b) QD radius derived from calculation using the Brus equation and DE determined by fitting the emission tail of the transformed emission spectra (cf. **Figure SV-17**) for samples derived from complexes with TETA, cysteine, or histidine at pH of 11 or 12.

Evaluation of the fraction of DE reveals a reduction of deep trap states for His-derived particles compared to the other complexes, most likely due to better surface passivation by the coupled precipitation. The Cys-derived particles surface is only occupied by remaining Cys molecules, and TETA is most likely not covering the surface of the formed particles at all. Additionally, the TETA complex is already susceptible to hydroxide precipitation at a pH value of 12, while the other complexes remain stable. The size of around 2.5 nm calculated from PL using the

Brus equation is in agreement with the values determined by measurements in the TEM micrographs (cf. **Figure V-5c**).

The collected data suggest that the influence of ligands on the coprecipitation process cannot be described solely by complex stability. Instead, there appear to be two mechanistically distinct regions. Complex stability primarily determines the formation of supersaturation and thus the nucleation density. The kinetics of ligand exchange and surface passivation dominate during particle growth and in the coupling of sulfide precipitation to silica condensation.

5.4.2 Variation of Synthesis Parameters – Mixed Ligand Complexes - Enabling Coprecipitation for Particles Derived from $CdCys_2$?

5.4.2.1 Variation of the Sulfide Concentration

To further investigate if the enhanced fluorescence ability of CdS derived from Cys complexes can be preserved in a coprecipitation with silica, different variations of the standard synthesis were made. First, the sulfide and silica concentrations during synthesis were varied to accelerate CdS precipitation, thereby possibly coupling CdS precipitation with silica condensation. If the failure of coprecipitation is primarily due to mismatched reaction kinetics, an increase in the CdS precipitation rate is likely to promote the coupling. Overall, two distinct trends regarding the size of formed particles are visible. (cf. **Figure V-8**) First, the average hydrodynamic radius increases for increased [S]/[Cd] ratios, while the polydispersity index decreases. Second, the size decreases with increasing silica concentration at constant [S]/[Cd] ratios. The latter could be an indication of size restriction by capturing of the QDs.

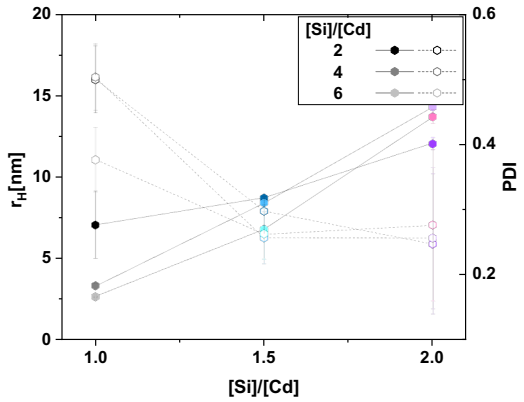


Figure V-8. Hydrodynamic radius and polydispersity index (PDI) for CdS derived from cysteine complex at different silica and sulfide concentrations. Shown values are averages of multiple measurements to highlight trends. Correlation functions and the more detailed size distributions derived from CONTN analysis can be found in **Figure SV-18**.

The more detailed size distribution also suggests two fractions at [S]/[Cd] = 1 with the larger fraction disappearing at [S]/[Cd] > 1. The smaller fraction presumably may correspond to the QDs directly, derived from an uncoupled synthesis, while the larger fraction consists predominantly of uncontrolled polycondensed silica. The vanishing of the larger fraction could be interpreted as the first indication of successful coupling, or it may be due to stronger

scattering signals resulting from the size increase of the smaller particle fraction ($I \propto r^6$). Therefore, DLS alone does not allow an unambiguous assessment of successful coprecipitation. Additional TEM and SEM/EDX micrographs confirm the absence of silica on the surfaces of the formed particles. (online repository) Surface passivation by cysteine appears to be sufficiently persistent to suppress silica coating and, more generally, the formation of secondary clusters even at elevated [S]/[Cd] ratios in this simple one-pot approach.

Fluorescence measurements of the particles indicate no shifts with varying silica concentration, whereas an increase in sulfide concentration results in a redshift accompanied by a significant decrease in intensity. (cf. **Figure V-9a**) Again, a broad PL peak is formed (FWHM > 140 nm), indicating that DEs account for a large proportion of total emissions, as seen before. (cf. **Figure SV-19**)

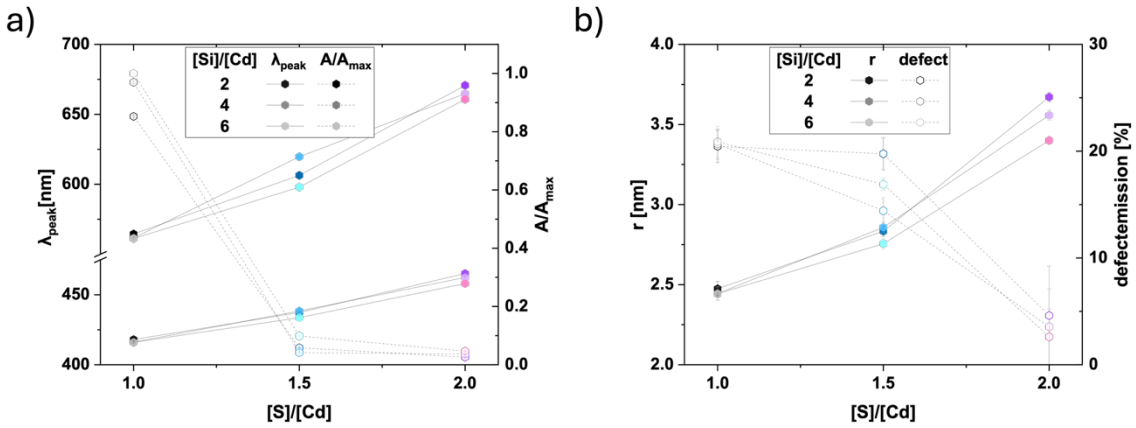


Figure V-9. (a) Emission and excitation peak of fitted fluorescence spectra (cf. **Figure SV-19a**) and relative area of the emission for samples derived from complexes with cysteine at a pH value of 11 and varying silica content and increasing sulfide concentration during synthesis. (b) QD radius derived from calculation using the Brus equation and DE determined by fitting the emission tail of the transformed emission spectra (cf. **Figure SV-19b**) for samples derived from complexes with cysteine at a pH value of 11 and varying silica content and increasing sulfide concentration during synthesis.

Evaluation of the formed sizes using the Brus equation indicates an overall increase in size with increasing sulfide concentration, from around 2.5 nm to around 3.5 nm. (cf. **Figure V-9b**) This is consistent with previously reported values in similar systems [5] and the sizes determined by DLS measurements ($r_H > r$). The proportion of DE at the PL peak decreases with increasing sulfide concentration. (cf. **Figure V-9b**) Combined with the decreasing PL intensities, a stronger non-radiative band-edge decay is indicated [51,53].

The decrease in PL intensity cannot be attributed directly / solely to the particle concentration. As the optical properties of the particles change with increasing sulfide concentration, fluctuations in the radiative and non-radiative recombination pathways are likely to contribute. According to LaMer, increasing supersaturation should create more nuclei and, therefore, a smaller final particle size [83]. However, the opposite is observable in the experiments. Nucleation does not, therefore, determine the particle size alone. Instead, particle growth appears to be controlled by cysteine-mediated surface passivation. At low sulfide concentrations, the thiolate groups efficiently stabilize the particle surface and restrict further growth. Increasing sulfide concentrations progressively favor Cd–S bond formation and thereby reduce the relative influence of thiolate coordination. Consequently, existing nuclei can grow more extensively, resulting in larger and optically more homogeneous (lower trap-dominated emission) quantum dots [5,84,85].

Although increasing the sulfide concentration alters the nucleation and growth behavior, no evidence for successful silica coating is obtained. The failed coprecipitation of the homocysteine complexes cannot be explained solely by slow CdS formation kinetics. Instead, the results indicate that persistent cysteine-mediated surface passivation suppresses the interaction between the CdS surface and hydrolyzed silica even under conditions that favor rapid CdS precipitation [86–88].

5.4.2.2 Mixed Ligand Complexes – $CdCys_1AS_2$

Another approach to weaken the strong growth inhibition of homocysteine complexes, thereby enabling coprecipitation with silica while preserving the formation of quantum-confined CdS particles, was to form mixed-ligand complexes. As discussed before, particle formation is governed by two factors: the free cadmium concentration controls nucleation, while the surface passivation affects growth and coupling to silica condensation. By partially replacing cysteine with other amino acids, both effects can be potentially adjusted independently. The added amino acids (cf. **Figure V-10**) can be divided into three groups based on the functionalization of their side chains. Specifically, there are those with no functional group in the side chain (Ala and Gly), those with an amino group (Arg and Lys), and those with an aromatic side chain (Tyr and His).

Differences are already noticeable during complex formation, particularly when the pH is raised to 11. While the solutions remained clear for the amino acids with aromatic side chains, all other samples began to show slight turbidity. The onset of turbidity is consistent with partial

hydroxide formation and therefore suggests an increased availability of free cadmium compared to homocysteine complexes. Consequently, the mixed-ligand complexes formed with Ala, Gly, Arg, and Lys appear less stable under alkaline conditions. However, no flocs or separable precipitate form. After the addition of sulfide, the samples become clear/opalescent and turn yellowish (CdS formation).

The precipitated secondary clusters are all in the same size range (~60 nm), bigger than particles for homocysteine complexes (no secondary clusters) and smaller than for reference reactions. (cf. **Figure V-10** and **Figure V-3**) Particles derived from the complex with added histidine differ significantly, as two fractions are visible in the size distribution (cf. **Figure SV-20**), similar to what was previously observed in the homocysteine complex. The bigger fraction is in the same size range as the other samples, while the smaller fraction is in the range of 1-10 nm, corresponding to the primary particles without a silica shell. The separation into two fractions also explains the increased PDI.

The size trends suggest that partial coprecipitation between the CdS precipitation and the silica condensation becomes possible once the strong surface passivation of pure cysteine complexes is weakened. Thus, the introduction of a second ligand appears to shift the system from growth-controlled formation of isolated quantum dots toward partial coprecipitation.

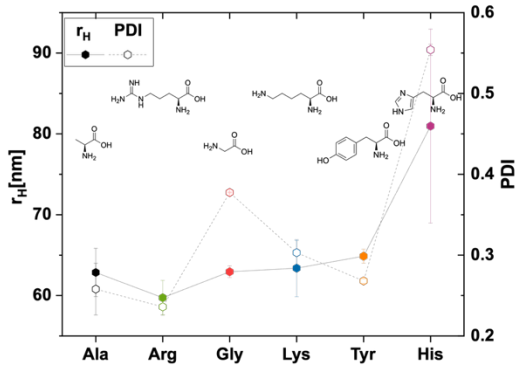


Figure V-10. Hydrodynamic radius and polydispersity index (PDI) for CdS derived from cadmium complexes containing mixed ligands of cysteine and other amino acids. Shown values are averages of multiple measurements to highlight trends. Correlation functions and the more detailed size distributions derived from CONTIN analysis can be found in **Figure SV-20**. Structural formulas of the amino acids used, from left to right: L-alanine, L-arginine, glycine, L-lysine, L-tyrosine, and L-histidine.

The elevated PDI values for the samples derived from glycine or lysine indicate a broader size distribution. Since no distinct second fraction is detectable in the CONTIN analysis (cf.

Figure SV-20b), the broadening most likely reflects increased heterogeneity rather than the formation of an additional particle population, presumably a direct result of the preceding hydroxide formation [89,90].

The fluorescence behavior of these samples does not change significantly. (cf. **Figure SV-21a**) The peak excitation and emission remain at the same wavelength, and only the intensity changes. The highest PL signal is observed for His, followed by Arg and Tyr, while Ala, Gly, and Lys result in lower intensity. (cf. **Figure V-11a**) When the calculated size derived from the Brus equation is compared, an almost identical size of around 2.4 nm is observed for all samples. Even the amount of DE does not change significantly. (cf. **Figure V-11b**)

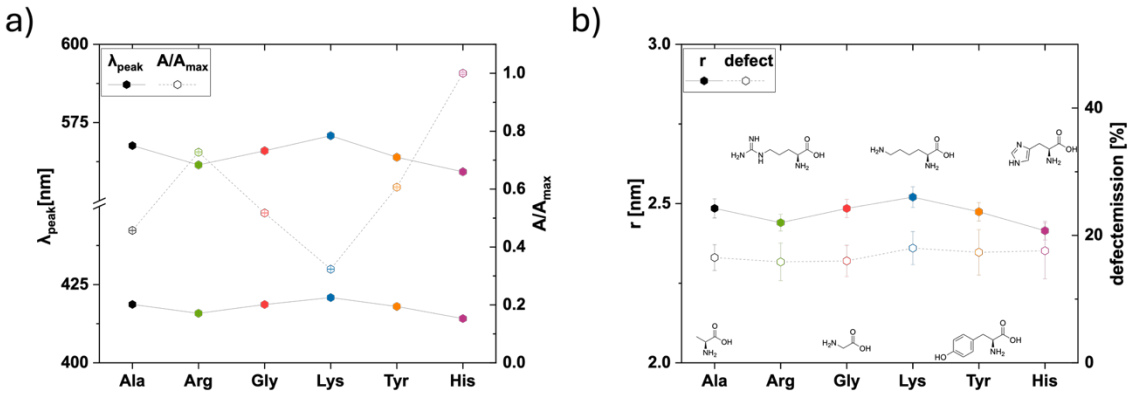


Figure V-11. (a) Emission and excitation peak of fitted fluorescence spectra (cf. **Figure SV-21a**) and relative area of the emission for samples derived from mixed ligand complexes with cysteine and other amino acids in a 1 to 2 ratio. (b) QD radius derived from calculation using the Brus equation and DE determined by fitting the emission tail of the transformed emission spectra (cf. **Figure SV-21b**) for samples derived from mixed ligand complexes with cysteine and other amino acids in a 1 to 2 ratio.

The combined results from DLS and fluorescence suggest that the second amino acid primarily influences precursor speciation and cadmium availability prior to nucleation. Cysteine remains the dominant ligand at the surface of the CdS nanoparticles. This view is supported by the near-identical sizes of the quantum dots, their emission wavelengths, and the DE observed across all ligand combinations investigated. As a result, the effect of the second amino acid on the final QD size appears limited. Meanwhile, cysteine continues to control particle growth via surface passivation once CdS formation begins. This behavior aligns with the mechanistic framework in which complex stability primarily controls supersaturation and nucleation, while surface-bound ligands govern growth and coupling to silica condensation, as outlined previously.

At pH 11, cysteine binds very strongly to cadmium due to the deprotonated thiolate group. Since cysteine and the second amino acid are present in a 1:2 ratio, mixed-ligand complexes are generally favored, because statistically, there is not enough cysteine present to form homocystine complexes. The likelihood of a stable mixed complex is expected to depend strongly on the identity of the second amino acid [27,41–43,45,46,91,92].

To estimate the relative ligand binding affinities and the expected availability of free cadmium ions during precipitation, the stability constants of the corresponding Cd complexes with homogeneous ligands are used as a first approximation [26]:

Tyr <	Arg <	Ala <	Lys ≈	Gly <	His <	Cys
6.08	6.45	7.37	7.80	7.83	9.92	21.71

Using the complex stabilities combined with the results, a few statements can be made:

First, the mixed complexes with the amino acids Gly, Ala, and Lys are unstable to hydroxide formation at pH 11. The homo complex stabilities are in the same range, and all results indicate almost identical particle formation. Only an elevated PDI separates Gly from the others, most likely due to increased hydroxide formation. In all cases, coprecipitation occurs, indicating that cysteine alone no longer fully suppresses silica condensation. Nevertheless, the existing growth inhibition is sufficient to still result in QDs. The added amino acid modulates primarily so that cysteine cannot sufficiently passivate the nuclei's surface against silica condensation.

Secondly, even though they have the smallest complex stabilities, mixed complexes with Tyr or Arg show different reactions. The complexes are more stable to hydroxide formation, as no or only a mild turbidity increase during complex formation is observed. Another interpretation would be the surface activity of both ligands size capping formed hydroxide and enabling colloidal stability thus just appear stable [93,94]. In both cases, the result is the same. The observations suggest a rapid nucleation with subsequent capture by the formation of the silica matrix. The cysteine ligands may induce growth inhibition before capture occurs, still resulting in primary QDs.

Lastly, the two particle fractions derived from a cysteine-histidine mixed complex suggest two-step particle formation. One fraction undergoes successful coprecipitation, resulting in secondary clusters of around 80 nm. The possibly uncontrolled release of ligand during the initial precipitation (nucleation burst) could result in excess ligand concentration compared to free cadmium. The second fraction resembles the uncoupled homocysteine system and may originate from continued CdS nucleation and growth after the initial coprecipitation

[8,17,95,96]. Although the available data do not definitely prove a sequential two-step mechanism, the observations are consistent with such a scenario.

Overall, the mixed-ligand strategy succeeds in restoring the partial coupling between CdS precipitation and silica condensation. At the same time, the growth-inhibiting effect of cysteine can be maintained. However, the type of the second amino acid has only a minor influence on the size and optical properties of the resulting primary particle (QD). The main effect, therefore, appears to lie more in modulating the stability of the precursors and the number of nuclei formed. The growth of the QDs remains largely governed by cysteine-mediated surface passivation and silica capturing. To achieve a shift in wavelength or particle size, experiments should be conducted with varying ligand ratios.

5.4.2.3 Mixed Ligand Complexes - $CdCys_xHis_{2-x}$

Mixed ligand complexes of cadmium with varying ratios of Cys and His as ligands were used for the CdS precipitation in the presence of silica in varying concentrations. No clear size trend can be observed for either the investigated silica concentration or the ligand ratio variation. Instead, the CONTIN-derived size distributions indicate formation of two distinct size fractions of small particles of a few nanometers (1-10 nm) and possibly secondary aggregates (50-1000 nm). (cf. **Figure SV-22**) For the samples with higher silica concentration ([Si]/[Cd] = 6), the smaller fraction is more expressed (e.g., higher unweighted intensity) than the bigger fraction. When the intensity of the fraction distributions is compared directly, one single trend is visible. A higher [Cys]/[His] ratio favors the formation of the smaller fraction, causing the intensity of the other fraction to decrease as the ratio increases gradually.

The change in silica concentration has little to no effect on the fluorescence behavior of the particles. Both the intensity and the excitation emission peaks are almost identical, indicating no enhanced shell formation at increased [Si]/[Cd].

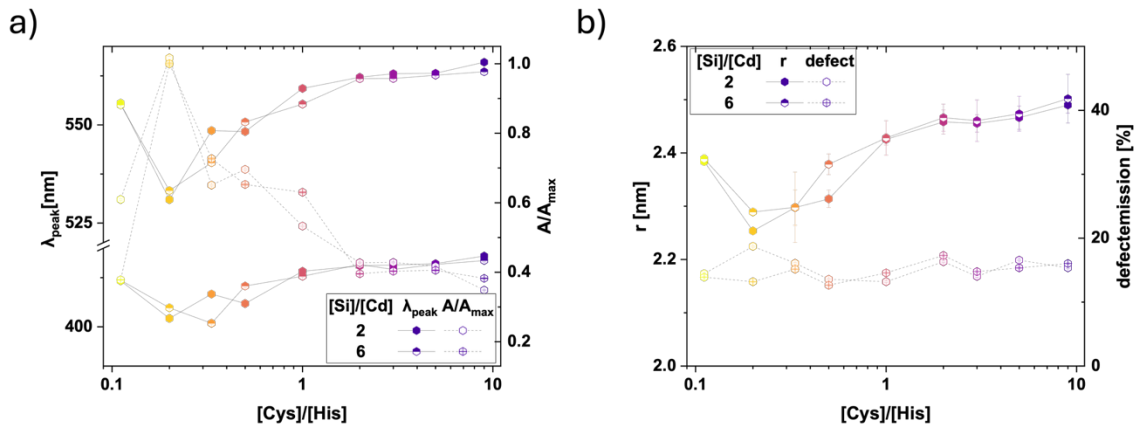


Figure V-12. (a) Emission and excitation peak of fitted fluorescence spectra (cf. **Figure SV-23**) and relative area of the emission for samples derived from mixed ligand complexes with cysteine and histidine in varying [Cys]/[His] ratios. (b) QD radius derived from calculation using the Brus equation and DE determined by fitting the emission tail of the transformed emission spectra (cf. **Figure SV-24**) for samples derived from mixed ligand complexes with cysteine and histidine in varying [Cys]/[His] ratios.

NMR measurements confirm the inclusion of His into complexes at [Cys]/[His] < 1, while for higher ratios, the peak position remains constant. A similar trend is visible in the fluorescence behavior. (cf. **Figure V-12a**)

The PL intensity decreases while the excitation and emission peaks approach the behavior of particles derived from homo Cys complexes. At [Cys]/[His] = 0.2, a maximum in PL intensity and a negative shift of both excitation and emission are observable. The observed size minimum at this ratio (cf. **Figure V-12b**) suggests synergistic effects of the mixed ligands on complex stability and increased growth inhibition. The mixed ligand seems to alter the balance between free cadmium availability and surface passivation more than either ligand alone. Interestingly, the strongest effect is observed at neither extreme composition. This may indicate that the interaction between the ligands is non-linear [27,41,46,92].

The amount of defect-induced emission does not change over the observed [Cys]/[His] ratios, indicating similar surface chemistry/ligand coverage.

Overall, the previously discussed mechanism becomes apparent once again, as the observed trends are consistent with stronger surface passivation of cysteine than of histidine [29,86]. The existence of two particle populations indicates that the system does not evolve into a single dominant growth regime [97–99]. Instead, the decreasing contribution of the larger fraction with increasing [Cys]/[His] ratio suggests that this fraction is increasingly suppressed. This corresponds to increased surface passivation governed by the increased amount of cysteine. At low [Cys]/[His] ratios, insufficient cysteine availability enables the silica condensation on the

nuclei surface [88], leading to the pronounced secondary cluster formation. With increasing [Cys]/[His] ratio, surface passivation becomes more effective [84,86] already during early growth stages, suppressing secondary cluster formation. Above a [Cys]/[His] ratio of approximately 1, the system becomes increasingly Cys-dominated, which is consistent with the observed reduction of His incorporation and the disappearance of distinct secondary populations [100].

Varying the [Cys]/[His] ratio only moderately affects the optical properties and size of the resulting quantum dots. Although a size minimum is observed at [Cys]/[His] = 0.2, no systematic size trend emerges over the investigated composition range. Further, changing the ligand ratio does not lead to a clear increase of silica incorporation. Thus, modifying the [Cys]/[His] ratio alone does not provide a reliable route towards independent control of quantum dot size and coprecipitation behavior.

5.4.2.4 Size Exclusion

An approach was made using ultra-centrifuge filters of differing molecular cutoff (MWCO) membranes to separate different fractions of formed particles. Therefore, 30 kDa and 10 kDa membranes were used, corresponding to pore sizes of approximately 4.8 nm and 2.7 nm, respectively [101,102]. All samples show two distinct size distributions of a smaller fraction around the size of the QDs and a bigger around 100 nm in size. (cf. **Figure SV-25b**) The big fraction is a result of the uncoupled coprecipitation. Filtration can confirm that the bimodal DLS distribution corresponds to separable physical populations rather than measurement artifacts. When only the smaller fraction is considered, a size trend matching the expectations is emerging (ref < 10kDa < 30kDa), consistent with the expected size-selective retention of QDs.

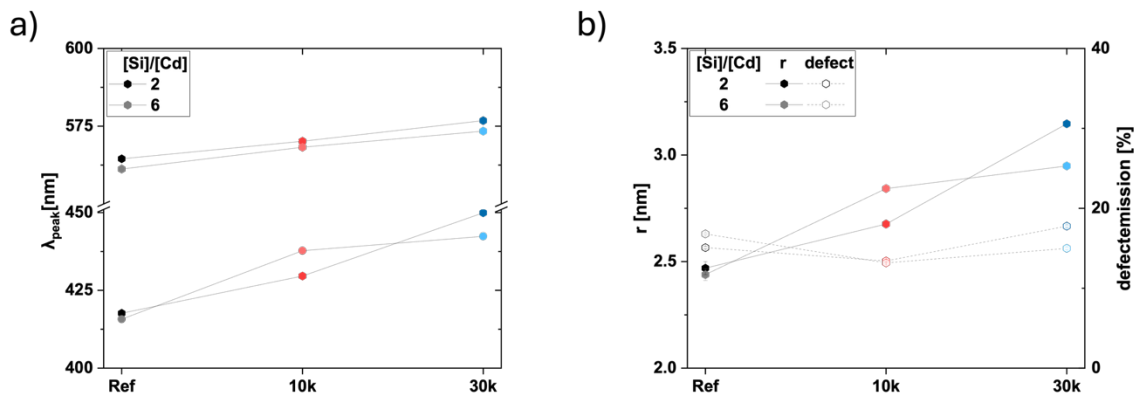


Figure V-13. (a) Emission and excitation peak of fitted fluorescence spectra (cf. **Figure SV-26a**) for samples derived from cysteine complexes with subsequent size exclusion by filtration with 30k and 10k MWCO ultracentrifuge filters. (b) QD radius derived from calculation using the Brus equation and DE determined by fitting the emission tail of the transformed emission spectra (cf. **Figure SV-26b**).

When the fluorescence behavior of these particles is studied (cf. **Figure SV-26**), a few trends are visible. Again, the elevated silica concentration during synthesis has no significant effect on emission/excitation behavior or the surface passivation. (cf. **Figure V-13b**) Combined with the EDX measurements, the decoupling of coprecipitation is visible. (cf. online repository) Nevertheless, a separation of different size fractions is possible. The filtrates show blue-shifted emission/excitation when filtered using smaller pores. This is directly visible in the evaluated size of around 3 nm for the 30 kDa filtered particles, 2.7 nm for the 10k Da filtered particles, and 2.5 nm for the filtrate at the end. (cf. **Figure V-13b**)

Overall, the separated fractions do not show detectable differences in chemical composition. Nevertheless, they can be efficiently separated by particle size, confirming that the observed bimodal distribution reflects physically distinct populations rather than compositional variation. Despite their different sizes, no evidence for significant compositional differences between the fractions was found.

These findings further support the strong surface affinity of cysteine, which effectively dominates particle surface chemistry and suppresses efficient silica-mediated coupling, particularly under cysteine-rich conditions.

5.4.3 Tuning of the Bandgap – From CdS to $Zn_xCd_{1-x}S$

Another approach to adjust the bandgap of binary nanocrystals, other than by adjusting their size, is alloying nanocrystals with a semiconductor that has a larger bandgap [103–105].

Therefore, the synthesis of $Zn_xCd_{x-1}S$ in varying compositions using differing complexes as precursors is compared to coprecipitated particles as in ref [106].

When the size of the formed particles derived from DLS is compared, a few trends arise. (cf. **Figure SV-27**) First, the size distributions for particles derived from cysteine complexes and from mixtures of $CdCys_2$ and $ZnHis_2$ complexes indicate one fraction of a few nanometers corresponding to the primary QDs and a second fraction of around 100 nm. The size distribution for particles derived from histidine complexes is around 100 nm with no second fraction at smaller hydrodynamic radii. Second, a trend for increasing size with increasing molar fraction of zinc is observable for the cysteine complexes, while for the histidine complexes, this trend is inverse. For the mixtures of both, no such trend is observable. The size distribution of reference samples, mainly secondary clusters (see **Chapter III**), gradually decreases from around 100 nm to around 70 nm with increasing zinc content [106,107].

The size of the primary QDs, on the other hand, can be evaluated by TEM and fluorescence measurements. The TEM and EDX results confirm the limited coupling of the sulfide precipitation and the silica polycondensation. (cf. **Figure V-14a**, d) The lattice fringes confirm crystallinity for both the reference and the sample derived of mixed complexes. (cf. **Figure V-14b**, e) Since both CdS and ZnS can crystallize in the same crystal structures, mixed crystals of both form in the hexagonal wurtzite structure. (cf. **Figure SV-29**)

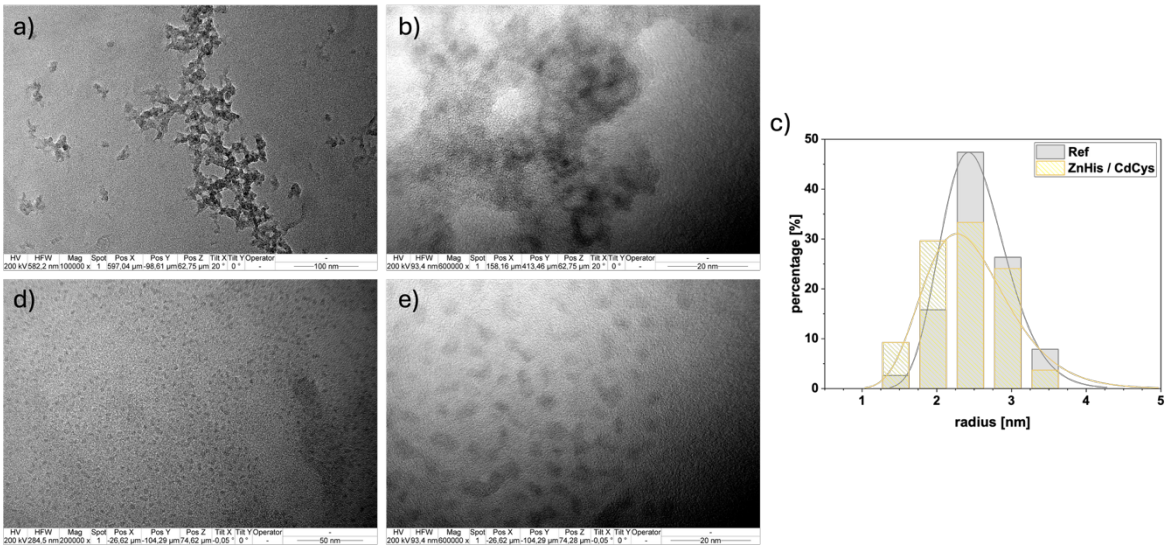


Figure V-14. HRTEM micrographs of (a), (b) ZnCdS (x = 0.8) derived from reference synthesis without complexation and (d), (e) ZnCdS (x = 0.8) derived from a cadmium cysteine complex and a zinc histidine complex. The scale bar corresponds to 100 nm for (a), to 50 nm for (d), and to 20 nm for (b) and (e), equivalent to a magnification of 10000x, 20000x and 60000x, respectively. (c) The size distributions for (a) and (d) are derived from size measurements in the TEM micrographs (n > 50). Diffraction patterns and the respective radial averages can be found in **Figure SV-29**.

Size measurements of the TEM micrographs reveal slightly bigger particles with a narrower size distribution for the reference particles than for the particles derived from mixed complexes. (cf. **Figure V-14c**)

Observable for all samples is a decrease in excitation/emission wavelength with increasing zinc content. (cf. **Figure V-15a**) All samples derived from complexes show almost identical excitation and emission wavelengths for x(Zn) < 0.5. For the reference sample, the excitation wavelength increases, while the PL intensity declines drastically [106,107]. Second, the mixed complexes exhibit higher excitation/emission wavelengths than the other complex-derived samples, especially at x(Zn) < 0.5.

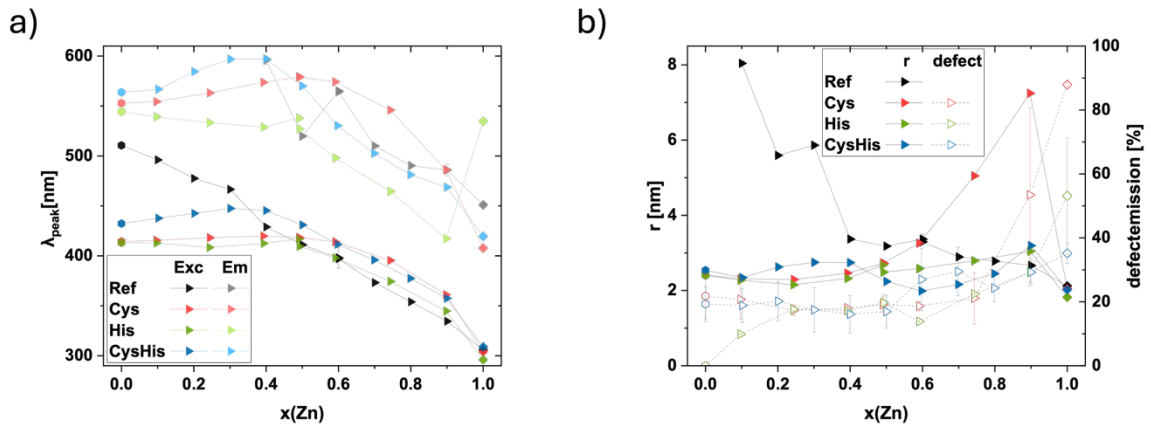


Figure V-15. (a) Emission and excitation peak of fitted fluorescence spectra (cf. **Figure SV-28a**, c, and e) for samples derived mixtures of zinc and cadmium His/Cys complexes in varying concentrations (b) QD radius derived from calculation using the Brus equation and DE determined by fitting the emission tail of the transformed emission spectra (cf. **Figure SV-28b**, d, and f).

The amount of DE does not significantly change over a wide range of variations (0.2 < x(Zn) < 0.8). (cf. **Figure V-15b**) For high zinc contents, the fraction of DE increases significantly, which is a known phenomenon for ZnS fluorescence in general [53,85].

The reference samples show a clear trend of QD size reduction with increasing zinc content, while the samples derived from cysteine complexes increase in QD size until x(Zn) = 0.9. ZnS derived from cysteine complexes alone is then again reduced to around 2 nm in size. Samples derived from histidine complexes and from mixed complexes show no clear size trend and fluctuate around 2.5 nm radius. In this way, $Zn_xCd_{1-x}S$ alloys can be produced with properties comparable to those obtained using more complex synthesis strategies [103–105,108–112]. Such materials are already widely used as photocatalysts [108,109] and for bioimaging

purposes [113]. (Optimization attempts towards such applications can be found in the online repository)

Overall, the results consistently suggest that alloy composition and ligand-controlled growth cannot be considered to be independent parameters. While increasing zinc content systematically modifies the optical properties through bandgap engineering, particle formation remains strongly influenced by precursor chemistry. In all systems, cysteine-rich precursors favor the formation of clearly defined QDs, whilst the histidine system allows the additional formation of secondary clusters. Consequently, ligand-controlled nucleation and growth processes determine not only the particle size distribution, but also the extent to which compositional tuning can be translated into predictable optical behavior.

5.5 Conclusion

In this work the extent to which metal ligand precursor complexes can be used to control the coprecipitation process of TM sulfides and silica was investigated. Particular focus was placed on understanding, how precursor chemistry affects nucleation, growth, optical properties, and the incorporation of the primary QDs into silica.

The findings demonstrate that distinct yet interconnected processes govern particle formation. Complex stability primarily regulates the free metal ion concentration, thereby influencing nucleation behavior, whereas growth and coupling to silica condensation are mainly determined by ligand-mediated surface passivation. The interaction between these factors ultimately dictates the size distribution of both primary quantum dots and secondary clusters.

Among the ligands investigated, cysteine exerted the most pronounced effect on particle formation. Its high affinity for transition metals and nanoparticle (sulfide) surfaces effectively mediates particle growth and stabilizes particles within the quantum dot size range. However, this strong surface passivation inhibits interaction with hydrolyzed silica species, thereby limiting successful coprecipitation.

The incorporation of a second amino acid as a ligand partially diminished the dominant effect of cysteine and improved the coupling efficiency during coprecipitation. Despite notable differences in precursor stability, the size and optical properties of the resulting quantum dots remained largely consistent. These observations suggest that the secondary ligand primarily affects nucleation via precursor speciation, while growth continues to be governed by cysteine-mediated surface passivation.

Size-selective ultrafiltration confirmed that the observed bimodal size distributions correspond to physically distinct particle populations. Despite differences in size, no significant compositional variations were detected.

Alloying CdS with ZnS was found to be an effective approach for tuning optical properties. Increasing zinc content resulted in the anticipated blue shift, confirming successful bandgap modification via alloy formation. However, ligand chemistry continued to exert a substantial influence on nucleation and growth behavior, consistent with the trends observed in this study.

Overall, the results demonstrate that precursor chemistry is a highly effective strategy for controlling particle formation during coprecipitation. Variations in ligand composition, complex stability, and surface passivation exert a greater influence on particle growth, aggregation, and silica coupling than changes in nominal synthesis parameters alone (cf.

Chapter III). Therefore, the successful design of nanomaterials using this approach necessitates the simultaneous consideration of both precursor speciation and surface chemistry. The findings for mixed ligand systems indicate that combining ligands with varying coordination strengths offers an effective method for modifying precursor stability while maintaining control over particle growth. Future research should systematically expand the range of mixed ligand combinations to identify pairs that enable independent adjustment of nucleation behavior and surface passivation. Such systems may offer greater flexibility in controlling particle formation compared to single-ligand approaches.

Beyond ligand identity, total ligand concentration represents a potentially significant yet only partially explored parameter. Although this study primarily addressed ligand composition and complex stoichiometry, systematic variation of absolute ligand concentration may enable independent control over both precursor stability and surface coverage. Such investigations could yield further insights into the interplay among nucleation, growth inhibition, and aggregation processes identified in this work.

The proposed formation mechanisms are primarily derived from ex situ characterization. Time-resolved studies employing techniques such as in situ dynamic light scattering (DLS) or small-angle X-ray scattering (SAXS) could provide direct insights into nucleation, growth, and aggregation processes, thereby aiding in the validation of the mechanistic model presented in this study.

In a broader context, the results demonstrate that precursor chemistry serves as a powerful tool for directing semiconductor nanoparticle formation under mild aqueous conditions. Future research should focus on establishing predictive relationships among complex stability, ligand-exchange dynamics, and particle growth behavior. This approach could ultimately facilitate the rational design of biomimetic synthesis routes for semiconductor nanomaterials with tailored structural and optical properties.

5.6 References

[1] Rödig B, Funkner D, Frank T, Schürmann U, Rieder J, Kienle L, et al. Nanodots of Transition Metal Sulfides, Carbonates, and Oxides Obtained Through Spontaneous Co-Precipitation with Silica. Nanomaterials 2024;14:1–15. https://doi.org/10.3390/nano14242054.

[2] Ku Y, Peters RW. The effect of weak chelating agents on the removal of heavy metals by precipitation processes. Environmental Progress 1986;5:147–53. https://doi.org/10.1002/ep.670050307.

[3] Saona LA, Campo-Giraldo JL, Anziani-Ostuni G, Órdenes-Aenishanslins N, Venegas FA, Giordana MF, et al. Cysteine-Mediated Green Synthesis of Copper Sulphide Nanoparticles: Biocompatibility Studies and Characterization as Counter Electrodes. Nanomaterials 2022;12:3194. https://doi.org/10.3390/nano12183194.

[4] Zhilenko MP, Lupandina K V., Ehrlich H V., Lisichkin G V. Preparation of copper and zinc sulfide nanoparticles and their modification with cysteine. Russian Chemical Bulletin 2010;59:1307–11. https://doi.org/10.1007/s11172-010-0239-4.

[5] Bae W, Abdullah R, Mehra RK. Cysteine-mediated synthesis of CdS bionanocrystallites. Chemosphere 1998;37:363–85. https://doi.org/10.1016/S0045-6535(98)00051-4.

[6] Liu X, Du Y, Wang S, Huang Y, Tian Y, García-Lojo D, et al. Histidine-Mediated Synthesis of Chiral Cobalt Oxide Nanoparticles for Enantiomeric Discrimination and Quantification. Small 2023;19:1–9. https://doi.org/10.1002/smll.202205187.

[7] Kho R, Nguyen L, Torres-Martínez CL, Mehra RK. Zinc–Histidine as Nucleation Centers for Growth of ZnS Nanocrystals. Biochem Biophys Res Commun 2000;272:29–35. https://doi.org/10.1006/bbrc.2000.2712.

[8] Yadav RS, Mishra P, Mishra R, Kumar M, Pandey AC. Growth mechanism and optical property of CdS nanoparticles synthesized using amino-acid histidine as chelating agent under sonochemical process. Ultrason Sonochem 2010;17:116–22. https://doi.org/10.1016/j.ultsonch.2009.04.011.

[9] Ma Y, Qi L, Ma J, Cheng H, Shen W. Synthesis of Submicrometer-Sized CdS Hollow Spheres in Aqueous Solutions of a Triblock Copolymer. Langmuir 2003;19:9079–85. https://doi.org/10.1021/la034994t.

[10] Celebi S, Erdamar AK, Sennaroglu A, Kurt A, Acar HY. Synthesis and Characterization of Poly(acrylic acid) Stabilized Cadmium Sulfide Quantum Dots. J Phys Chem B 2007;111:12668–75. https://doi.org/10.1021/jp0739420.

[11] Lewis AE. Review of metal sulphide precipitation. Hydrometallurgy 2010;104:222–34. https://doi.org/10.1016/j.hydromet.2010.06.010.

[12] Helz GR, Horzempa LM. EDTA as a kinetic inhibitor of copper(II) sulfide precipitation. Water Res 1983;17:167–72. https://doi.org/10.1016/0043-1354(83)90097-0.

[13] Hu J, Ren L, Guo Y, Liang H, Cao A, Wan L, et al. Mass Production and High Photocatalytic Activity of ZnS Nanoporous Nanoparticles. Angewandte Chemie 2005;117:1295–9. https://doi.org/10.1002/ange.200462057.

[14] Kavitha T, Haider S, Kamal T, Ul-Islam M. Thermal decomposition of metal complex precursor as route to the synthesis of Co3O4 nanoparticles: Antibacterial activity and mechanism. J Alloys Compd 2017;704:296–302. https://doi.org/10.1016/j.jallcom.2017.01.306.

[15] Kaur R, Mehta SK. Self aggregating metal surfactant complexes: Precursors for nanostructures. Coord Chem Rev 2014;262:37–54. https://doi.org/10.1016/j.ccr.2013.12.014.

[16] Mourdikoudis S, Liz-Marzán LM. Oleylamine in Nanoparticle Synthesis. Chemistry of Materials 2013;25:1465–76. https://doi.org/10.1021/cm4000476.

[17] Chanu TI, Negi DPS. Synthesis of histidine-stabilized cadmium sulfide quantum dots: Study of their fluorescence behavior in the presence of adenine and guanine. Chem Phys Lett 2010;491:75–9. https://doi.org/10.1016/j.cplett.2010.03.068.

[18] Wilkins RG. Kinetics and Mechanism of Reactions of Transition Metal Complexes. Wiley; 1991. https://doi.org/10.1002/3527600825.

[19] Owens G, Ferguson VK, McLaughlin MJ, Singleton I, Reid RJ, Smith FA. Determination of NTA and EDTA and Speciation of Their Metal Complexes in Aqueous Solution by Capillary Electrophoresis. Environ Sci Technol 2000;34:885–91. https://doi.org/10.1021/es990309m.

[20] Bürgisser CS, Stone AT. Determination of EDTA, NTA, and Other Amino Carboxylic Acids and Their Co(II) and Co(III) Complexes by Capillary Electrophoresis. Environ Sci Technol 1997;31:2656–64. https://doi.org/10.1021/es970080f.

[21] Anderegg G. Critical survey of stability constants of NTA complexes. Pure and Applied Chemistry 1982;54:2693–758. https://doi.org/10.1351/pac198254122693.

[22] Li Z, Chang P-H, Jiang W-T. Mechanisms of Cu2+, triethylenetetramine (TETA), and Cu-TETA sorption on rectorite and its use for metal removal via metal-TETA complexation. J Hazard Mater 2019;373:187–96. https://doi.org/10.1016/j.jhazmat.2019.03.085.

[23] Miyajima T, Mori M, Ishiguro S, Chung KH, Moon CH. On the Complexation of Cd(II) Ions with Polyacrylic Acid. J Colloid Interface Sci 1996;184:279–88. https://doi.org/10.1006/jcis.1996.0621.

[24] Anspach WM, Marinsky JA. Complexing of nickel(II) and cobalt(II) by a polymethacrylic acid gel and its linear polyelectrolyte analog. J Phys Chem 1975;79:433–9. https://doi.org/10.1021/j100572a008.

[25] Travers C, Marinsky JA. The complexeng of Ca(II), Co(II), and Zn(II) by polymethacrylic and polyacrylic acid. Journal of Polymer Science: Polymer Symposia 1974;47:285–97. https://doi.org/10.1002/polc.5070470134.

[26] Sóvágó I, Várnagy K. Cadmium(II) Complexes of Amino Acids and Peptides. Met. Ions Life Sci., vol. 11, 2013, p. 275–302. https://doi.org/10.1007/978-94-007-5179-8_9.

[27] Pyreu D, Gridchin S. Mixed-Ligand Nickel(II) Complexes with Histidine and Cysteine in Aqueous Solution: Thermodynamic Approach. J Solution Chem 2024;53:372–85. https://doi.org/10.1007/s10953-023-01337-5.

[28] Leberman R, Rabin BR. Metal complexes of histidine. Transactions of the Faraday Society 1959;55:1660. https://doi.org/10.1039/tf9595501660.

[29] Gockel P, Vahrenkamp H, Zuberbühler AD. Zinc Complexes of Cysteine, Histidine, and Derivatives Thereof: Potentiometric determination of their compositions and stabilities. Helv Chim Acta 1993;76:511–20. https://doi.org/10.1002/hlca.19930760133.

[30] Mesu JG, Visser T, Soulimani F, van Faassen EE, de Peinder P, Beale AM, et al. New Insights into the Coordination Chemistry and Molecular Structure of Copper(II) Histidine Complexes in Aqueous Solutions. Inorg Chem 2006;45:1960–71. https://doi.org/10.1021/ic051305n.

[31] Hübner M, Hauer I, Muller C, Rusu D, Botond K, David L. Spectroscopic Studies of Copper (II) Complexes With Some Amino Acid As Ligand. Annals of the West University of Timisoara Physic Series 2011;LV:77–85.

[32] Deschamps P, Kulkarni PP, Gautam-Basak M, Sarkar B. The saga of copper(II)–l-histidine. Coord Chem Rev 2005;249:895–909. https://doi.org/10.1016/j.ccr.2004.09.013.

[33] Gorboletova GG, Metlin AA, Bychkova SA. Thermodynamics of the Formation of Complexes of Nickel(II), Triglycine, and L-Histidine in Aqueous Solutions. Russian Journal of Physical Chemistry A 2018;92:1715–9. https://doi.org/10.1134/S003602441809008X.

[34] Morris PJ, Bruce Martin R. Stereoselective formation of cobalt(II), nickel(II) and zinc(II) chelates of histidine. Journal of Inorganic and Nuclear Chemistry 1970;32:2891–7. https://doi.org/10.1016/0022-1902(70)80352-9.

[35] Jalilehvand F, Mah V, Leung BO, Mink J, Bernard GM, Hajba L. Cadmium(II) Cysteine Complexes in the Solid State: A Multispectroscopic Study. Inorg Chem 2009;48:4219–30. https://doi.org/10.1021/ic900145n.

[36] Ramani S, Raspor B, Arbneshi T. Electrochemical Study of Cadmium (II) Complexation with Cysteine. Am J Analyt Chem 2013;04:577–83. https://doi.org/10.4236/ajac.2013.410068.

[37] McAuliffe CA, Murray SG. Metal complexes of sulphur-containing amino acids. Inorganica Chimica Acta Reviews 1972;6:103–21. https://doi.org/10.1016/0073-8085(72)80013-5.

[38] Dokken KM, Parsons JG, McClure J, Gardea-Torresdey JL. Synthesis and structural analysis of copper(II) cysteine complexes. Inorganica Chim Acta 2009;362:395–401. https://doi.org/10.1016/j.ica.2008.04.037.

[39] Jalilehvand F, Leung BO, Mah V. Cadmium(II) Complex Formation with Cysteine and Penicillamine. Inorg Chem 2009;48:5758–71. https://doi.org/10.1021/ic802278r.

[40] Barrie PJ, Gyani A, Motevalli M, O'Brien P. Solid-state cadmium-113 NMR studies on cadmium complexes with glycine, L-alanine, and L-cysteine. Inorg Chem 1993;32:3862–7. https://doi.org/10.1021/ic00070a016.

[41] Mlakar M, Pavković S, Tumir L, Vukosav P, Gašparović B. Electrochemical Characterization of Biochemically Active Cu(II) Mixed Ligand Complex with Histidine and Cysteine. Electroanalysis 2017;29:392–7. https://doi.org/10.1002/elan.201600253.

[42] Karaseva YE, Pyreu DF. Mixed-Ligand Complexation of Nickel(II) and Zinc Cations with Histidine, Lysine, and Arginine in Aqueous Solutions. Russian Journal of Physical Chemistry A 2025;99:1794–800. https://doi.org/10.1134/S0036024425701201.

[43] Kiseleva I, Pyreu D, Krivonogikh T, Bazanova M, Hochenkova T, Kozlovskii E. Thermodynamic study of mixed-ligand complex formation of copper(II) and nickel(II) nitrilotriacetates with amino acids in solution. I. Polyhedron 2013;51:10–7. https://doi.org/10.1016/j.poly.2012.12.010.

[44] Pyreu D, Bedenko J. Thermodynamics of Ternary Complex Formation of Copper(II) and Nickel Iminodiacetates with Histidine in Solution. J Solution Chem 2017;46:633–42. https://doi.org/10.1007/s10953-017-0596-9.

[45] Pyréu D, Gridchin S. Thermodynamics of Mixed Ligand Complex Formation of Copper(II) and Nickel Ions with Glycine and Histidine in Solution. J Solution Chem 2020;49:239–53. https://doi.org/10.1007/s10953-020-00957-5.

[46] Reddy PR, Radhika M, Manjula P. Synthesis and characterization of mixed ligand complexes of Zn(II) and Co(II) with amino acids: Relevance to zinc binding sites in zinc fingers. Journal of Chemical Sciences 2005;117:239–46. https://doi.org/10.1007/BF02709293.

[47] Agarwal RP, Perrin DD. Stability constants of complexes of zinc and cobalt(II) ions with some histidine-containing peptides. Journal of the Chemical Society, Dalton Transactions 1975:1045. https://doi.org/10.1039/dt9750001045.

[48] Frisken BJ. Revisiting the method of cumulants for the analysis of dynamic light-scattering data. Appl Opt 2001;40:4087. https://doi.org/10.1364/AO.40.004087.

[49] Provencher SW. A constrained regularization method for inverting data represented by linear algebraic or integral equations. Comput Phys Commun 1982;27:213–27. https://doi.org/10.1016/0010-4655(82)90173-4.

[50] Provencher SW. Contin: A general purpose constrainded regularization program for inverting noisy linear algebraic and integral equations. Comput Phys Commun 1984;35:C-818-C–819. https://doi.org/10.1016/S0010-4655(84)82935-5.

[51] Hinterding SOM, Salzmann BBV, Vonk SJW, Vanmaekelbergh D, Weckhuysen BM, Hutter EM, et al. Single Trap States in Single CdSe Nanoplatelets. ACS Nano 2021;15:7216–25. https://doi.org/10.1021/acsnano.1c00481.

[52] Bera D, Qian L, Tseng TK, Holloway PH. Quantum dots and their multimodal applications: A review. Materials 2010;3:2260–345. https://doi.org/10.3390/ma3042260.

[53] Babentsov V, Sizov F. Defects in quantum dots of IIB-VI semiconductors. Opto-Electronics Review 2008;16:208–25. https://doi.org/10.2478/s11772-008-0025-0.

[54] Oliva AI, Solís-Canto O, Castro-Rodríguez R, Quintana P. Formation of the band gap of CdS thin films growth by different techniques. Modern Physics Letters B, vol. 15, 2001, p. 671–4. https://doi.org/10.1142/S0217984901002269.

[55] Lee GJ, Lee Y, Lim H, Cheong H, Kil B-H, Han S-H. Photoluminescence and Nonlinear Optical Properties of Semiconductor Nanocomposites Consisting of ZnO Nanorods and CdS Nanodots. Journal of the Korean Physical Society 2011;58:1290–4. https://doi.org/10.3938/jkps.58.1290.

[56] Norvell WA, Lindsay WL. Reactions of EDTA Complexes of Fe, Zn, Mn, and Cu with Soils. Soil Science Society of America Journal 1969;33:86–91. https://doi.org/10.2136/sssaj1969.03615995003300010024x.

[57] Morgan JJ. Kinetics of reaction between O2 and Mn(II) species in aqueous solutions. Geochim Cosmochim Acta 2005;69:35–48. https://doi.org/10.1016/j.gca.2004.06.013.

[58] Atkins PW. Shriver & Atkins' inorganic chemistry. Oxford University Press; 2010.

[59] Hollemann AF, Wiberg E. Lehrbuch der Anorganischen Chemie. 103rd ed. New York, NY: Walter de Gruyter & Co.; 2017.

[60] Martell AE, Editors RMS. Critical Stability Constants Volume 5. Biochem Educ 1983;11:77. https://doi.org/10.1016/0307-4412(83)90054-7.

[61] Chaves S, Delgado R, Da Silva JJRF. The stability of the metal complexes of cyclic tetra-aza tetra-acetic acids. Talanta 1992;39:249–54. https://doi.org/10.1016/0039-9140(92)80028-C.

[62] Van Leeuwen HP, Town RM. Outer-sphere and inner-sphere ligand protonation in metal complexation kinetics: The lability of EDTA complexes. Environ Sci Technol 2009;43:88–93. https://doi.org/10.1021/es802185h.

[63] Kolthoff IM. The solubilities and solubility products of metallic sulfides in water. Journal of Physical Chemistry 1931;35:2711–21. https://doi.org/10.1021/j150327a019.

[64] Sagresti L, Benedetti L, Merz KM, Brancato G. Simulating Metal Complex Formation and Ligand Exchange: Unraveling the Interplay between Entropy, Kinetics, and Mechanisms on the Chelate Effect. J Chem Theory Comput 2025;21:8950–62. https://doi.org/10.1021/acs.jctc.5c01079.

[65] Mentasti E. Metal-exchange reactions between cobalt(II) and lead(II) complexes of nitrilotriacetic acid and copper(II). Journal of the Chemical Society, Dalton Transactions 1982:721. https://doi.org/10.1039/dt9820000721.

[66] Kodama M, Hagiya K. Kinetics of Multidentate Ligand Substitution Reactions. XV. Substitution Reactions of 1,2-Cyclohexanediamine-N,N,N′,N′-tetraacetic Acid (CyDTA) with Zinc(II) Iminodiacetate (IDA), N-(2-Hydroxyethyl)iminodiacetate (HIDA), and Nitrilotriacetate (NTA) Complexes and Those with Cobalt(II)-IDA, -HIDA, NTA, -N-(2-Hydroxyethyl)ethylenediamine (EtEN), and Diethylenetriamine (Dien) Complexes. Bull Chem Soc Jpn 1973;46:3151–4. https://doi.org/10.1246/bcsj.46.3151.

[67] Kodama M. Kinetics of Multidentate Ligand-substitution Reactions. XVIII. Substitution Reactions of Triethylenetetraaminehexaacetate (TTHA) with Nickel(II)–Dien, –EDMA,

and –NTA Complexes. Bull Chem Soc Jpn 1975;48:2813–5. https://doi.org/10.1246/bcsj.48.2813.

[68] Rufier C, Reufer M, Dietsch H, Schurtenberger P. Single step hybrid coating process to enhance the electrosteric stabilization of inorganic particles. Langmuir 2011;27:6622–7. https://doi.org/10.1021/la200525u.

[69] Tsukruk V V., Bliznyuk VN, Visser D, Campbell AL, Bunning TJ, Adams WW. Electrostatic Deposition of Polyionic Monolayers on Charged Surfaces. Macromolecules 1997;30:6615–25. https://doi.org/10.1021/ma961897g.

[70] Roma-Luciow R, Sarraf L, Morcellet M. Complexes of poly(acrylic acid) with some divalent, trivalent and tetravalent metal ions. Eur Polym J 2001;37:1741–5. https://doi.org/10.1016/S0014-3057(01)00066-0.

[71] Larson-Smith K, Pozzo DC. Scalable synthesis of self-assembling nanoparticle clusters based on controlled steric interactions. Soft Matter 2011;7:5339–47. https://doi.org/10.1039/c0sm01497d.

[72] Rödig B, Denk P, Schürmann U, Kellermeier M, Kunz W. Nanoparticle formation utilizing simple polyacrylic acid-cation coacervates as template. RSC Adv 2026;16:8633–40. https://doi.org/10.1039/D6RA00330C.

[73] Boisvert J-P, Malgat A, Pochard I, Daneault C. Influence of the counter-ion on the effective charge of polyacrylic acid in dilute condition. Polymer (Guildf) 2002;43:141–8. https://doi.org/10.1016/S0032-3861(01)00603-6.

[74] Charman WN, Christy DP, Geunin EP, Monkhouse DC. Interaction between calcium, a model divalent cation, and a range of poly (Acrylic Acid) resins as a function of solution pH. Drug Dev Ind Pharm 1991;17:271–80. https://doi.org/10.3109/03639049109043824.

[75] Lau BLT, Hsu-Kim H. Precipitation and growth of zinc sulfide nanoparticles in the presence of thiol-containing natural organic ligands. Environ Sci Technol 2008;42:7236–41. https://doi.org/10.1021/es801360b.

[76] Protter CR, Bjorklund JL, Mason SE, Hamers RJ. Selective Adsorption of Thiol-Containing Molecules on Copper Sulfide Surfaces via Molecule-Surface Disulfide Bridges. Journal of Physical Chemistry C 2025;129:1976–87. https://doi.org/10.1021/acs.jpcc.4c06463.

[77] Suzuki T, Yano T aki, Hara M, Ebisuzaki T. Cysteine and cystine adsorption on FeS2(100). Surf Sci 2018;674:6–12. https://doi.org/10.1016/j.susc.2018.03.011.

[78] Helfferich F. Ligand Exchange. I. Equilibria. J Am Chem Soc 1962;84:3237–42. https://doi.org/10.1021/ja00876a003.

[79] Pearson RG, Anderson MM. Exchange Rates of Ligands in Complex Ions. Angewandte Chemie International Edition in English 1965;4:281–7. https://doi.org/10.1002/anie.196502811.

[80] Brus L. Electronic wave functions in semiconductor clusters: Experiment and theory. Journal of Physical Chemistry 1986;90:2555–60. https://doi.org/10.1021/j100403a003.

[81] Brus LE. Electron-electron and electron-hole interactions in small semiconductor crystallites: The size dependence of the lowest excited electronic state. J Chem Phys 1984;80:4403–9. https://doi.org/10.1063/1.447218.

[82] Rossetti R, Ellison JL, Gibson JM, Brus LE. Size effects in the excited electronic states of small colloidal CdS crystallites. J Chem Phys 1984;80:4464–9. https://doi.org/10.1063/1.447228.

[83] LaMer VK, Dinegar RH. Theory, Production and Mechanism of Formation of Monodispersed Hydrosols. J Am Chem Soc 1950;72:4847–54. https://doi.org/10.1021/ja01167a001.

[84] Sandmann A, Kompch A, Mackert V, Liebscher CH, Winterer M. Interaction of L-cysteine with zno: Structure, surface chemistry, and optical properties. Langmuir 2015;31:5701–11. https://doi.org/10.1021/la504968m.

[85] Tiwari A, Dhoble SJ, Kher RS. Influence of thiol capping on the photoluminescence properties of L-cysteine-, mercaptoethanol- and mercaptopropionic acid-capped ZnS nanoparticles. Luminescence 2015;30:1148–52. https://doi.org/10.1002/bio.2877.

[86] Song H, Yang J, Lim SG, Lee J, Jeong WH, Choi H, et al. On the surface passivating principle of functional thiol towards efficient and stable perovskite nanocrystal solar cells. Chemical Engineering Journal 2023;454. https://doi.org/10.1016/j.cej.2022.140224.

[87] Yang P, Ando M, Murase N. Highly luminescent CdSe/CdxZn1-xS quantum dots coated with thickness-controlled SiO2 shell through silanization. Langmuir 2011;27:9535–40. https://doi.org/10.1021/la201213c.

[88] Rosen JE, Gu FX. Surface functionalization of silica nanoparticles with cysteine: A low-fouling zwitterionic surface. Langmuir 2011;27:10507–13. https://doi.org/10.1021/la201940r.

[89] Fan C, Chen J, Chen Y, Ji J, Teng HH. Relationship between solubility and solubility product: The roles of crystal sizes and crystallographic directions. Geochim Cosmochim Acta 2006;70:3820–9. https://doi.org/10.1016/j.gca.2006.06.011.

[90] Hidmi L, Edwards M. Role of temperature and pH in Cu(OH)2 solubility. Environ Sci Technol 1999;33:2607–10. https://doi.org/10.1021/es981121q.

[91] Nikitina MG, Pyreu DF. Thermodynamics of Mixed-Ligand Nickel(II) Complex Formation with Ornithine and Histidine in Aqueous Solutions. Russian Journal of Inorganic Chemistry 2021;66:1569–76. https://doi.org/10.1134/S0036023621100120.

[92] Matsui H, Ohtaki H. A Potentiometric Study on Mixed Ligand Cadmium(II) Complexes with 2-Amino Carboxylic Acids. Bull Chem Soc Jpn 1982;55:461–5. https://doi.org/10.1246/bcsj.55.461.

[93] Haldar D. Amino Acids and Peptides in Colloidal Nanoparticle Synthesis. Reducing Agents in Colloidal Nanoparticle Synthesis, The Royal Society of Chemistry; 2021, p. 184–218. https://doi.org/10.1039/9781839163623-00184.

[94] Tagawa M, Inoue T, Ogi N, Nakagaki M. Steric stabilization of iron (III) hydroxide sols by various amino acids. Colloid Polym Sci 1985;263:406–12. https://doi.org/10.1007/BF01410389.

[95] Gondikas AP, Masion A, Auffan M, Lau BLT, Hsu-Kim H. Early-stage precipitation kinetics of zinc sulfide nanoclusters forming in the presence of cysteine. Chem Geol 2012;329:10–7. https://doi.org/10.1016/j.chemgeo.2011.06.009.

[96] Bae W, Mehra RK. Cysteine-capped ZnS nanocrystallites: Preparation and characterization. J Inorg Biochem 1998;70:125–35. https://doi.org/10.1016/S0162-0134(98)10008-9.

[97] Jamting AK, Cullen J, Coleman VA, Lawn M, Herrmann J, Miles J, et al. Systematic study of bimodal suspensions of latex nanoparticles using dynamic light scattering. Advanced Powder Technology 2011;22:290–3. https://doi.org/10.1016/j.apt.2011.03.009.

[98] Zhu X, Shen J, Song L. Accurate retrieval of bimodal particle size distribution in dynamic light scattering. IEEE Photonics Technology Letters 2016;28:311–4. https://doi.org/10.1109/LPT.2015.2495271.

[99] Litmanovich EA, Ivleva EM. The problem of bimodal distributions in dynamic light scattering: Theory and experiment. Polymer Science - Series A 2010;52:671–8. https://doi.org/10.1134/S0965545X10060143.

[100] Koole R, Schapotschnikow P, de Mello Donegá C, Vlugt TJH, Meijerink A. Time-dependent photoluminescence spectroscopy as a tool to measure the ligand exchange kinetics on a quantum dot surface. ACS Nano 2008;2:1703–14. https://doi.org/10.1021/nn8003247.

[101] Imbrogno A, Calvo JI, Breida M, Schwaiger R, Schäfer AI. Molecular weight cut off (MWCO) determination in ultra- and nanofiltration: Review of methods and implications on organic matter removal. Sep Purif Technol 2025;354. https://doi.org/10.1016/j.seppur.2024.128612.

[102] Mahdavi H, Kamyabi A, Shahalizade T, Asadollahi Taheri H. Preparation of highly flexible cellulose acetate membranes modified by hyperbranched poly(amine ester)-epoxidized soybean oil and evaluation of its filtration properties. Cellulose 2017;24:5389–402. https://doi.org/10.1007/s10570-017-1526-0.

[103] Alehdaghi H, Marandi M, Molaei M, Irajizad A, Taghavinia N. Facile synthesis of gradient alloyed ZnxCd1-xS nanocrystals using a microwave-assisted method. J Alloys Compd 2014;586:380–4. https://doi.org/10.1016/j.jallcom.2013.09.190.

[104] Algarni H, Bouarissa N, Khan MA, Al-Hagan OA, Alhuwaymel TF. Optical constants and exciton properties of ZnxCd1-xS. Optik (Stuttg) 2019;193. https://doi.org/10.1016/j.ijleo.2019.163022.

[105] Huang D, Wen M, Zhou C, Li Z, Cheng M, Chen S, et al. ZnxCd1-xS based materials for photocatalytic hydrogen evolution, pollutants degradation and carbon dioxide reduction. Appl Catal B 2020;267. https://doi.org/10.1016/j.apcatb.2020.118651.

[106] Funkner D, Frank T, Kohlmann N, Zahnweh D, Rieder J, Kienle L, et al. Functional nanoparticles from chemically coupled precipitation processes. Mater Today Chem 2023;29. https://doi.org/10.1016/j.mtchem.2023.101438.

[107] Rödig B. Silicate structures - spontaneous formation in structured media and application. Master Thesis. University of Regensburg, 2022.

[108] Liu Y, Zheng X, Yang Y, Song Y, Yang Y, Li J, et al. Recent Advances in the Hydrogen Evolution Reaction of ZnxCd1−xS-Based Photocatalysts. Solar RRL 2022;6:1–12. https://doi.org/10.1002/solr.202101061.

[109] Zheng X, Ge J, Ye L, Yang Y, Wang J, Ren W, et al. The morphological research of ZnxCd1-xS based photocatalysts for energy conversion. J Environ Chem Eng 2024;12:113420. https://doi.org/10.1016/j.jece.2024.113420.

[110] Chen M, Hou W, Chen C, Wang Y, Xu Y. Wavelength-dependent photoactivity of ZnxCd1−xS and ZnCo2O4/ZnxCd1−xS for H2 and H2O2 production. Int J Hydrogen Energy 2022;47:17241–51. https://doi.org/10.1016/j.ijhydene.2022.03.220.

[111] Bouarissa N, Mezrag F, Turki-Kamoun N. Disorder effect upon energy band gaps and carrier effective masses of ZnxCd1−xS. Eur Phys J Plus 2021;136:1–10. https://doi.org/10.1140/epjp/s13360-021-01526-5.

[112] Li A, Pang H, Li P, Zhang N, Chen G, Meng X, et al. Insights into the critical dual-effect of acid treatment on ZnxCd1-xS for enhanced photocatalytic production of syngas under visible light. Appl Catal B 2021;288:1–10. https://doi.org/10.1016/j.apcatb.2021.119976.

[113] Hong L, Cheung TL, Rao N, Ouyang Q, Wang Y, Zeng S, et al. Millifluidic synthesis of cadmium sulfide nanoparticles and their application in bioimaging. RSC Adv 2017;7:36819–32. https://doi.org/10.1039/c7ra05401g.

5.7 Supporting Information

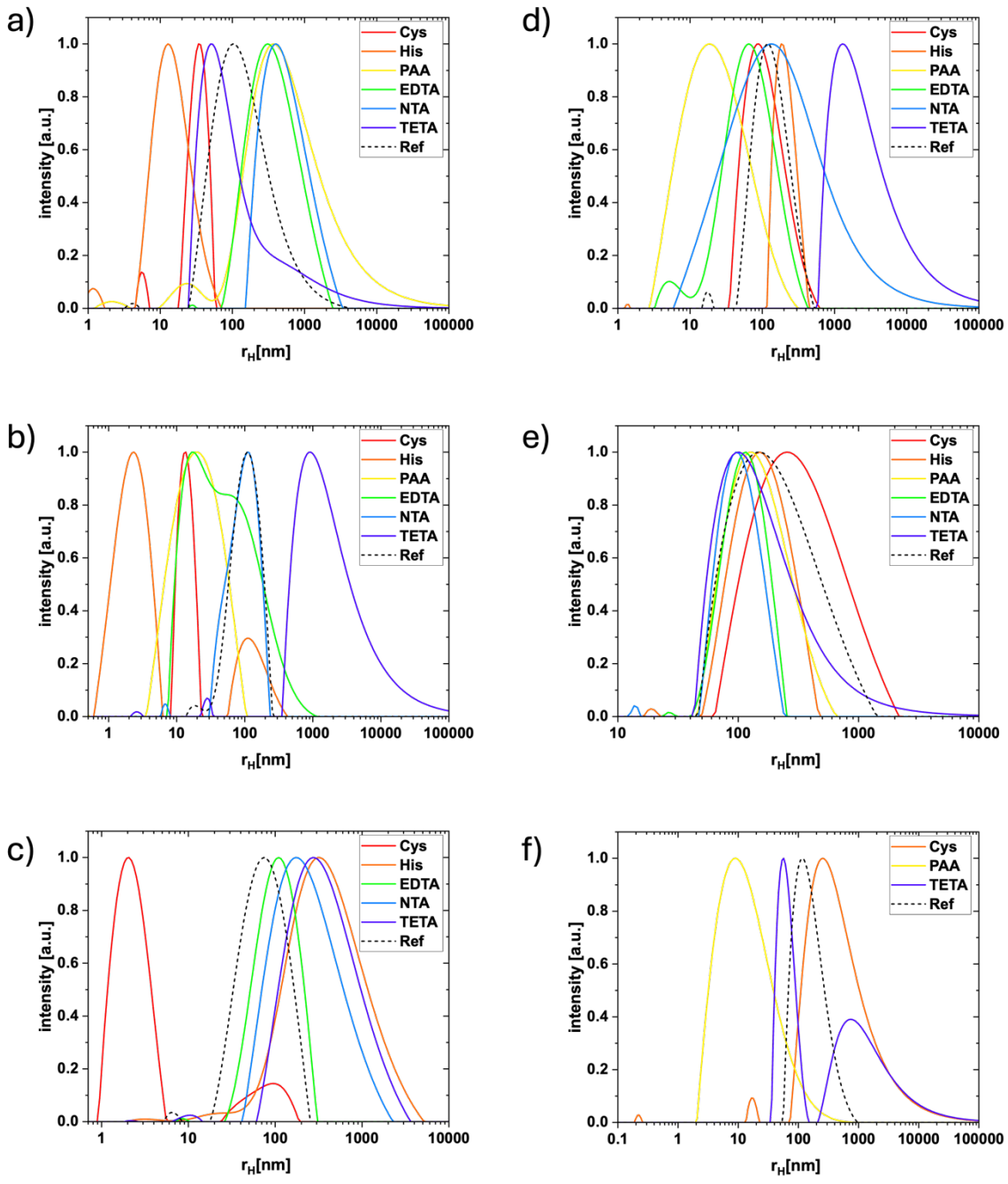


Figure SV-1. Unweighted size distributions derived from DLS measurements of samples of (a) CuS, (b) ZnS, (c) CdS, (d) CoS, (e) FeS, and (f) NiS. derived from attempted coupled coprecipitation from various complexes as shown in **Figure V-2**, using the CONTIN algorithm [50].

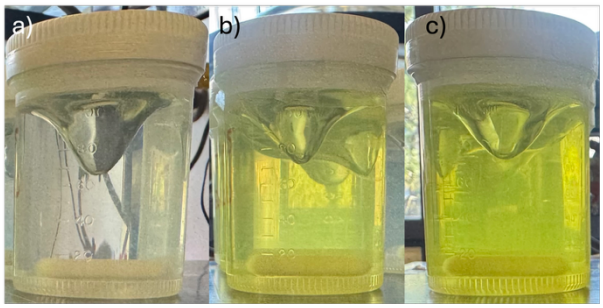


Figure SV-2. Pictures of synthesis mixtures of CdS from cysteine complexes at [Si]/[Cd] = 2 at pH 11 after differing reaction times. (a) 1h, (b) 6h, and (c) 12h.

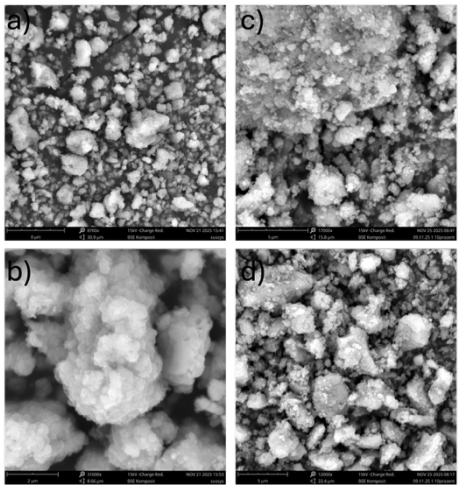


Figure SV-3. SEM micrographs of CuS derived from complexes of (a) and (b) cysteine and (c) and (d) histidine. The scale bars correspond to (a) 8 µm, (b) 2 µm, and (c) and (d) 5 µm.

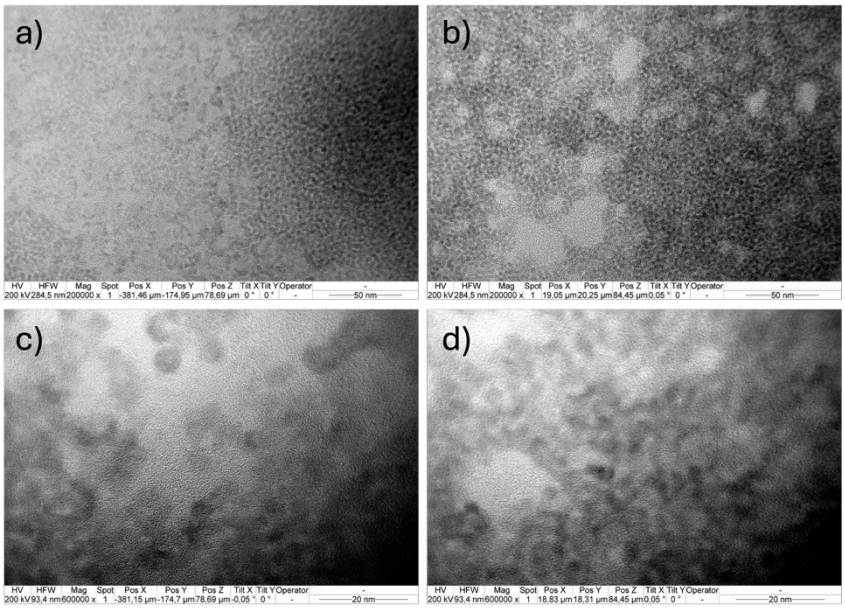


Figure SV-4. HRTEM micrographs of CuS derived from (a), (c) cysteine complex, (b), (d) histidine complex. The scale bar corresponds to 50 nm for (a), (b), and to 20 nm for (c), (d), equivalent to a magnification of 20000x and 60000x, respectively. Size distribution can be found in **Figure V-4c**.

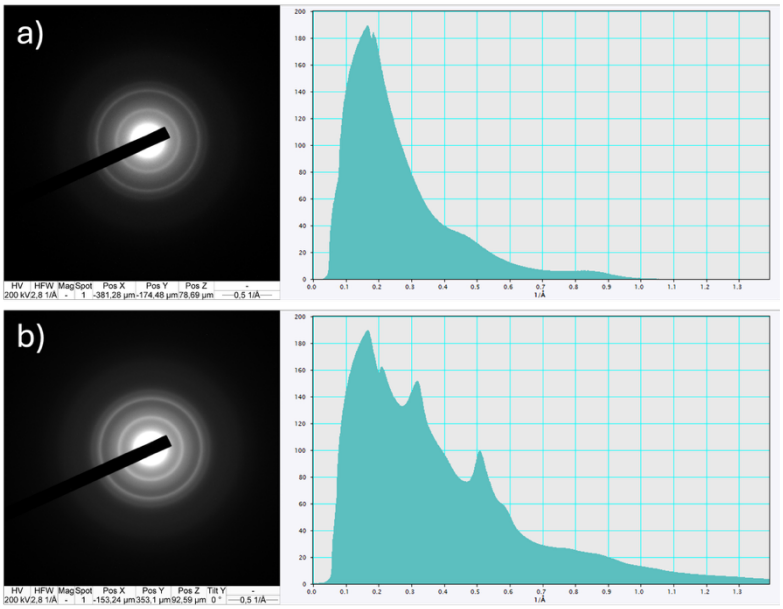


Figure SV-5. HRTEM diffraction pattern and radial average derived from HRTEM micrographs of CuS derived from (a) cysteine complex and (b) histidine complex. The SAED pattern was indexed according to the hexagonal chovellite structure of CuS (space group P63/mmc, COD ID: 1010920). The observed deviations from the reference d-spacings are attributed to the partially amorphous character of the sample.

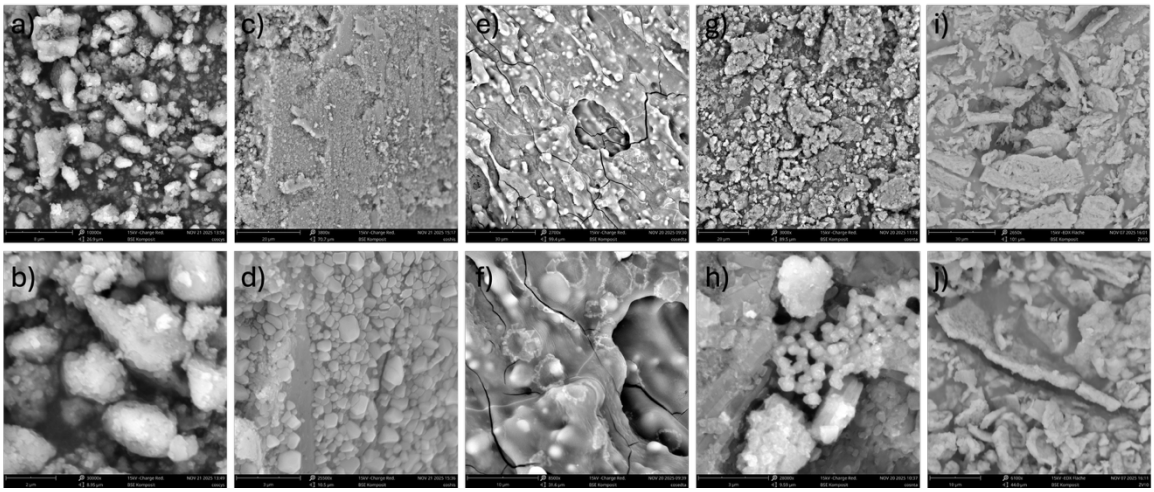


Figure SV-6. SEM micrographs of CoS derived from (a), (b) cysteine complex, (c), (d) histidine complex, (e), (f) EDTA complex, (g), (h) NTA complex, and (i), (j) PAA complex. The scale bars correspond to 30 µm for (e) and (i), 20 µm for (c) and (g), 10µm for (f) and (j), 8 µm for (a), 3 µm for (d) and (h), and 2 µm for (b).

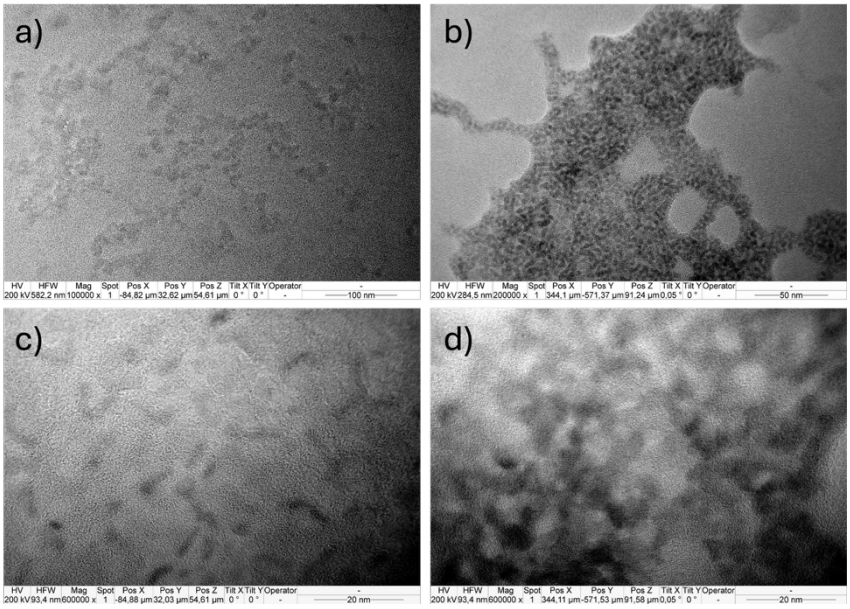


Figure SV-7. HRTEM micrographs of CoS derived from (a), (c) cysteine complex, (b), (d) histidine complex. The scale bar corresponds to 100 nm for (a), 50 nm for (b), and to 20 nm for (c), (d), equivalent to a magnification of 10000x, 20000x, and 60000x, respectively. Size distribution can be found in **Figure V-4f**.

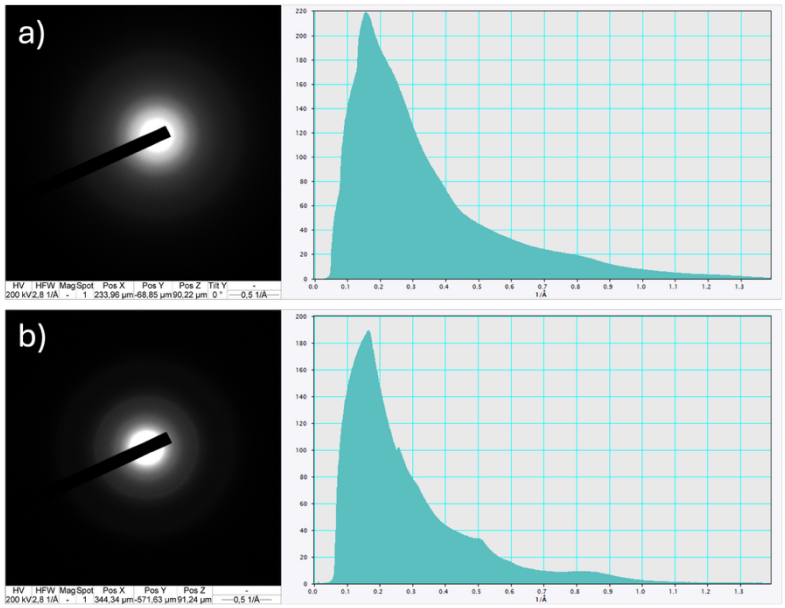


Figure SV-8. HRTEM diffraction pattern and radial average derived from HRTEM micrographs of CoS derived from (a) cysteine complex and (b) histidine complex. The SAED pattern was indexed according to the hexagonal NiAs structure of CoS (space group P63/mmc, ICSD No. 624857). The observed deviations from the reference d-spacings are attributed to the partially amorphous character of the sample.

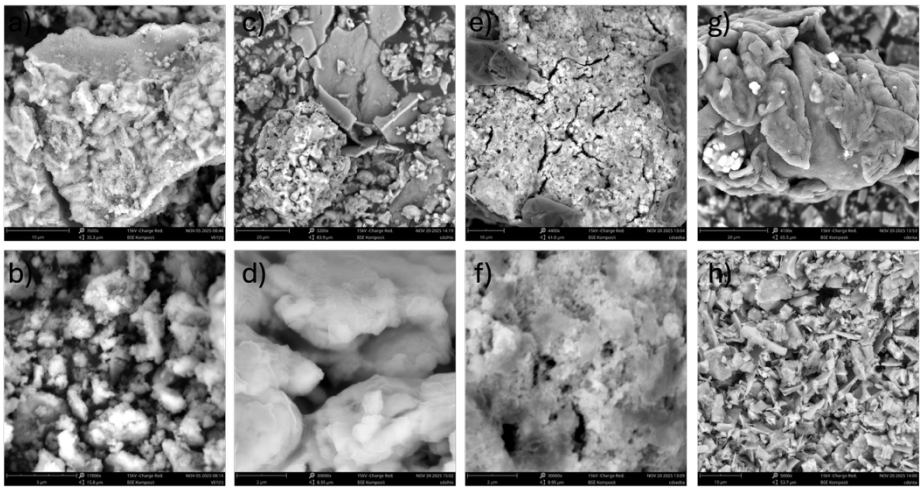


Figure SV-9. SEM micrographs of CoS derived from (a), (b) cysteine complex, (c), (d) histidine complex, (e), (f) EDTA complex, and (g), (h) NTA complex. The scale bars correspond to 20 µm for (c) and (g), 10µm for (a), (e) and (h), 5 µm for (b), and 2 µm for (d) and (f).

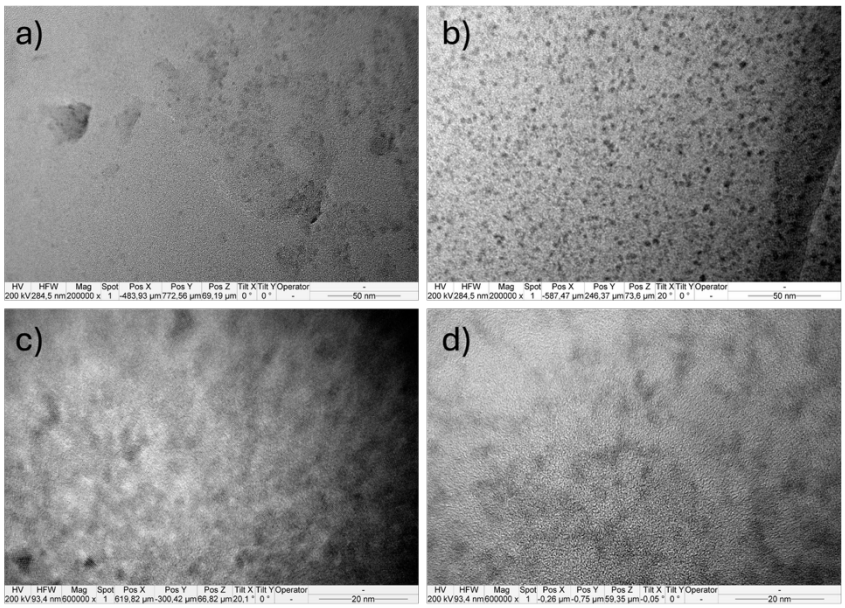


Figure SV-10. HRTEM micrographs of CdS derived from (a), (c) cysteine complex, (b), (d) histidine complex. The scale bar corresponds to 50 nm for (a), (b), and to 20 nm for (c), (d), equivalent to a magnification of 20000x and 60000x, respectively. Size distribution can be found in **Figure V-5c**.

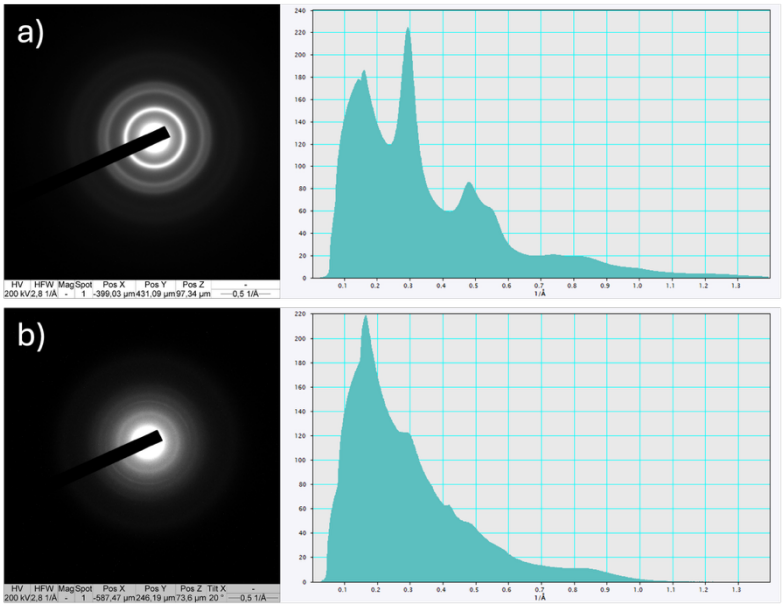


Figure SV-11. HRTEM diffraction pattern and radial average derived from HRTEM micrographs of CdS derived from (a) cysteine complex and (b) histidine complex. The SAED pattern was indexed according to the cubic zinc-blende structure of CdS (space group F43m, ICSD No. 31075). The observed deviations from the reference d-spacings are attributed to the amorphous SiO_2 matrix and the partially amorphous character of the sample.

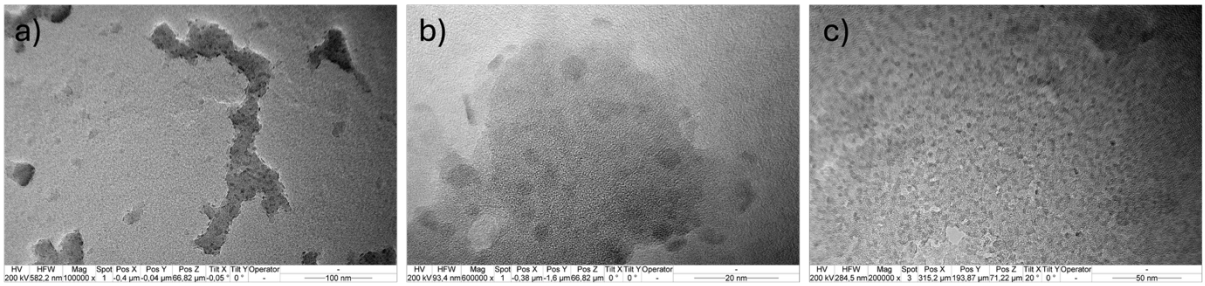


Figure SV-12. HRTEM micrographs of ZnS derived histidine complex. The scale bar corresponds to 100 nm for (a), 50 nm for (c), and to 20 nm for (c), equivalent to a magnification of 10000x, 20000x and 60000x, respectively. Size distribution can be found in **Figure V-5f**.

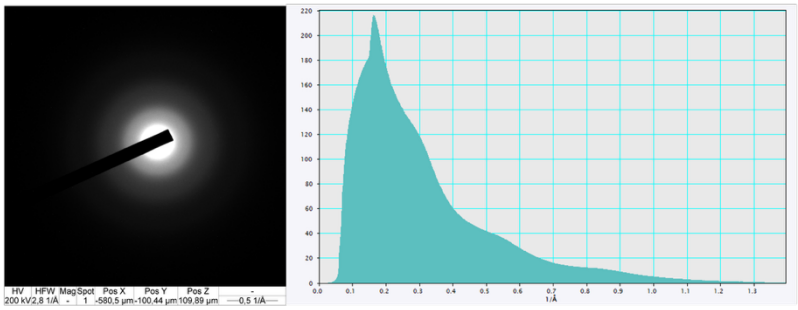


Figure SV-13. HRTEM diffraction pattern and radial average derived from HRTEM micrographs of ZnS derived from histidine complex. The SAED pattern was indexed according to the cubic zinc-blende structure of ZnS (space group F43m, ICSD No. 162754). The observed deviations from the reference d-spacings are attributed to the amorphous SiO_2 matrix and the partially amorphous character of the sample.

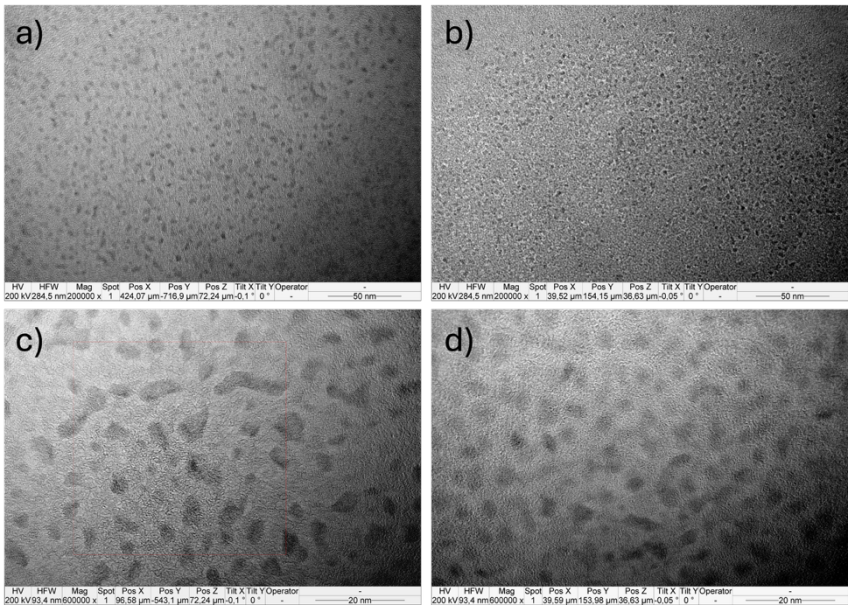


Figure SV-14. HRTEM micrographs of (a), (c) CdS derived from cysteine complex, and (b), (d) ZnS derived from histidine complex (precipitation without silica). The scale bar corresponds to 50 nm for (a), (b), and to 20 nm for (c), (d), equivalent to a magnification of 20000x and 60000x, respectively. Size distribution can be found in **Figure V-5c** and **Figure V-5f**, respectively.

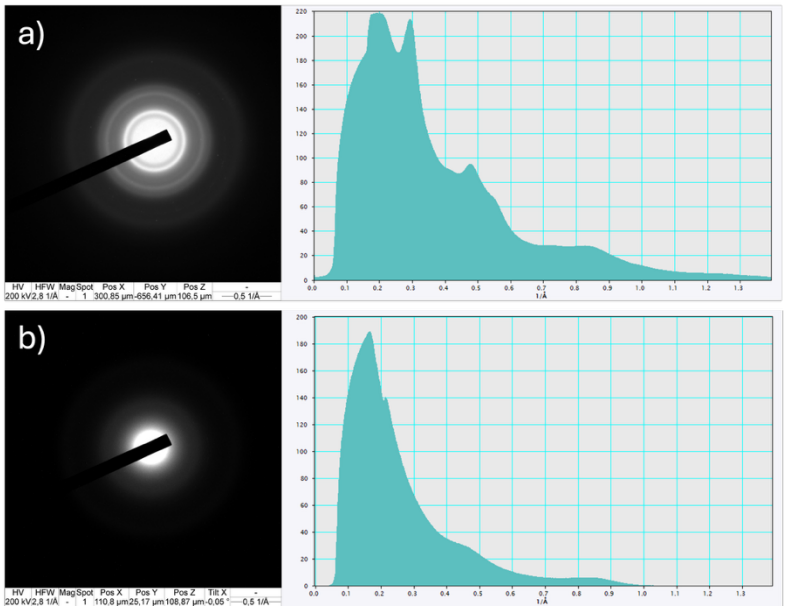


Figure SV-15. HRTEM diffraction pattern and radial average derived from HRTEM micrographs of (a) CdS derived from cysteine complex and (b) ZnS derived from histidine complex in a reference synthesis[5,7]. The SAED pattern was indexed according to the cubic zinc-blende structure of CdS (space group F43m, ICSD No. 31075) and of ZnS (space group F43m, ICSD No. 162754), respectively. The observed deviations from the reference d-spacings are attributed to the amorphous SiO_2 matrix and the partially amorphous character of the sample.

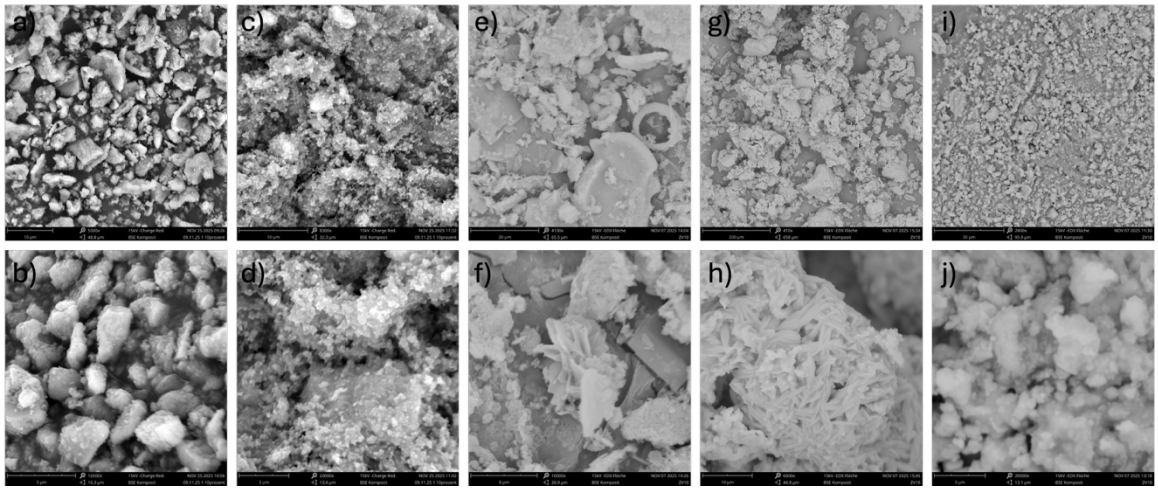


Figure SV-16. SEM micrographs of NiS derived from (a), (b) cysteine complex, (c), (d) histidine complex, (e), (f) EDTA complex, (g), (h) NTA complex, and (i), (j) PAA complex. The scale bars correspond to 200 µm for (g), 30 µm for (i), 20 µm for (e), 10µm for (a), (c) and (h), 8 µm for (f), 5 µm for (b), and 3 µm for (d) and (j).

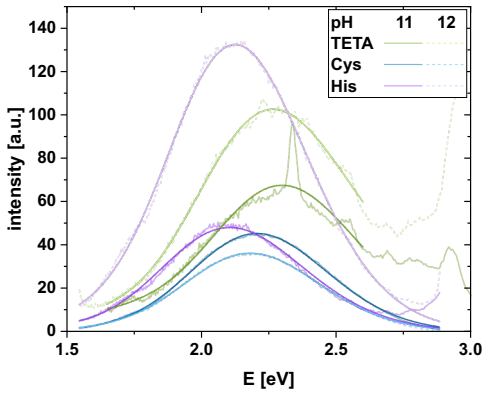


Figure SV-17. Transformed emission spectra and fits for samples derived from TETA, cysteine, and histidine complexes at pH values of 11 and 12. The measured spectra can be found in **Figure V-6b**.

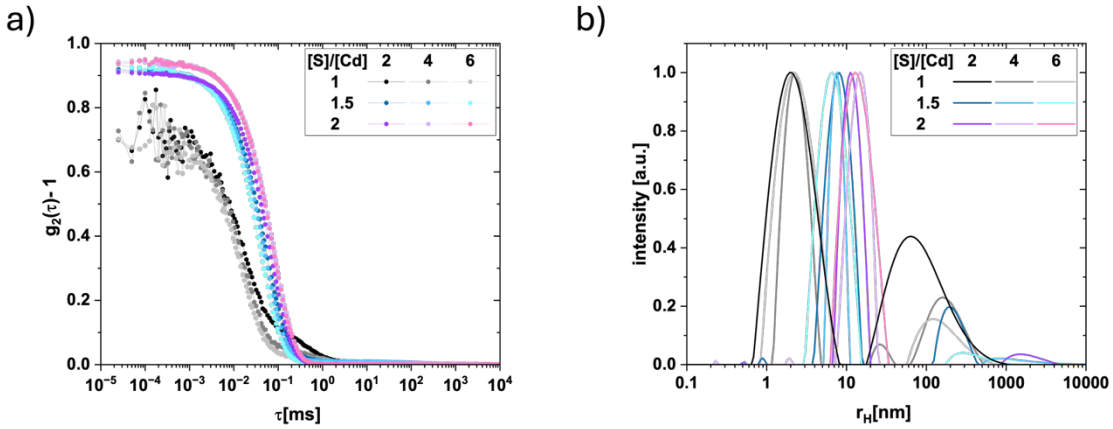


Figure SV-18. (a) DLS measurements for CdS derived from cysteine complex at different silica and sulfide concentrations. (b) Unweighted size distribution derived from DLS measurements shown in (a) using the CONTIN algorithm [50].

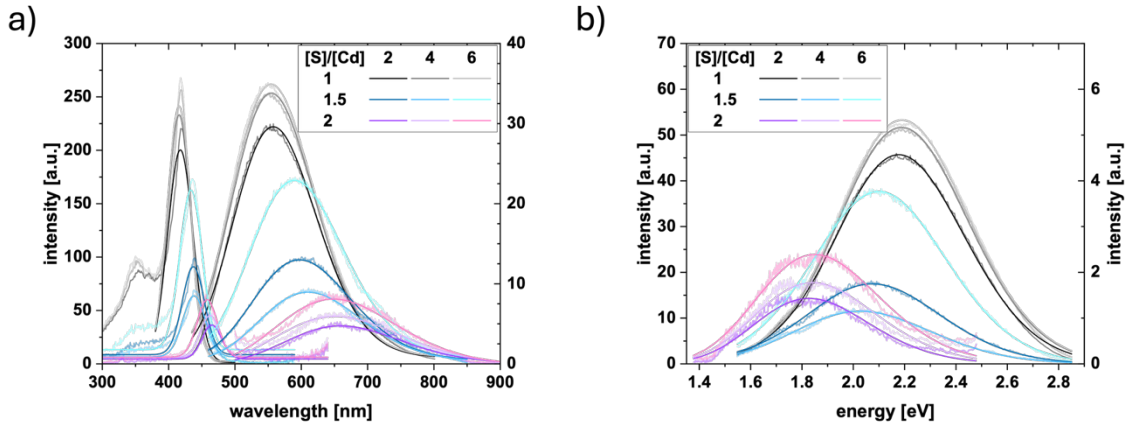


Figure SV-19. (a) Fluorescence spectra of CdS for samples derived from complexes with cysteine at a pH value of 11 and varying silica content and increasing sulfide concentration during synthesis. For the excitation spectra the emission wavelength was set to 545 nm, 610 nm, and 660 nm and for the emission spectra the excitation wavelength of 420 nm, 430 nm, and 440 nm

was used, respectively. (increasing with increasing sulfide concentration) (b) Respective transformed emission spectra and fits. Note that for both, (a) and (b) a second y-axis is used to visualize the spectra of samples with [S]/[Cd] > 1 together with the samples with [S]/[Cd] = 1.

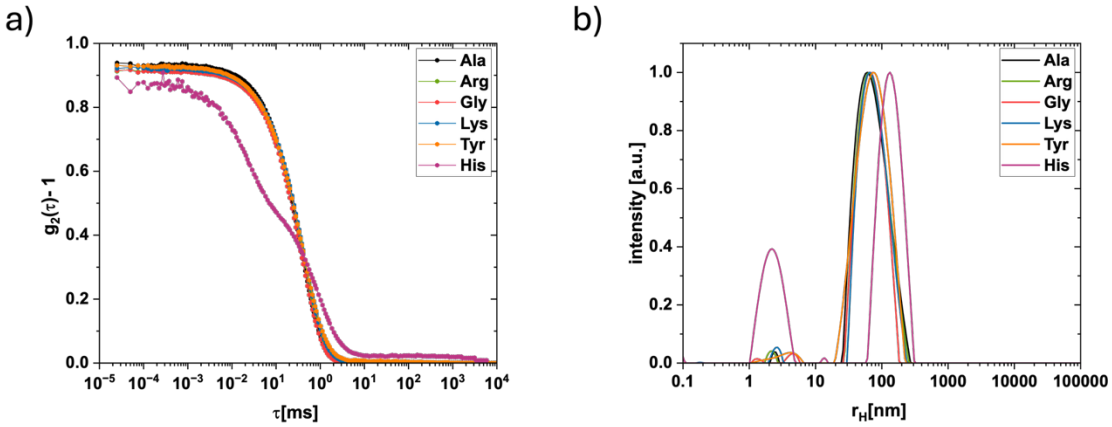


Figure SV-20. (a) DLS measurements for CdS samples derived from mixed ligand complexes with cysteine and other amino acids in a 1 to 1 ratio. (b) Unweighted size distribution derived from DLS measurements shown in (a) using the CONTIN algorithm [50].

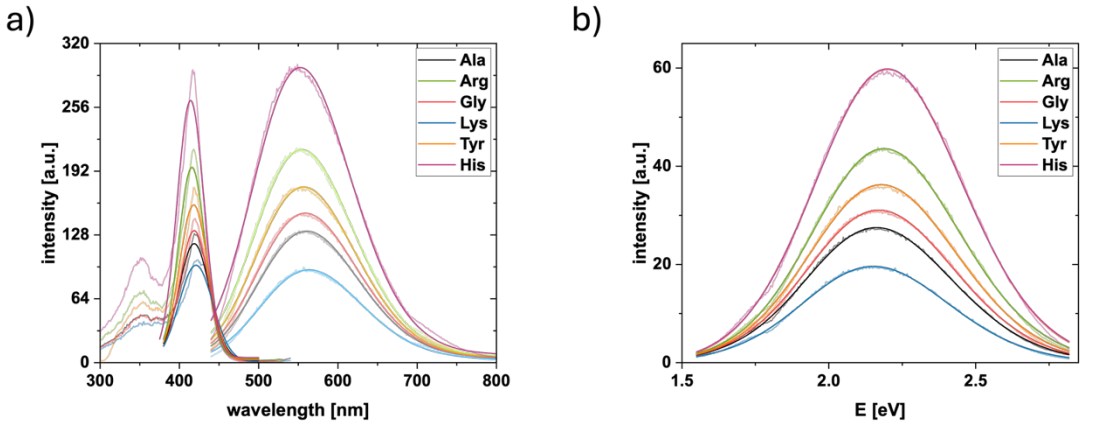


Figure SV-21. (a) Fluorescence (λ_{exc} = 420 nm, λ_{em} = 550 nm) spectra for CdS samples derived from mixed ligand complexes with cysteine and other amino acids in a 1 to 1 ratio. (b) Respective transformed emission spectra and fits.

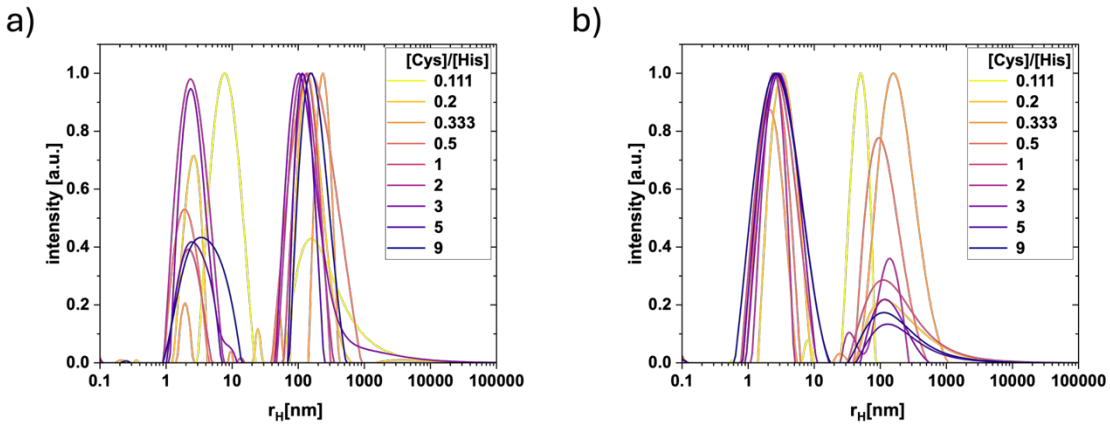


Figure SV-22. Unweighted size distribution derived from DLS measurements for samples derived from mixed ligand complexes with cysteine and histidine in varying [Cys]/[His] ratios, using the CONTIN algorithm [50]. (a) [Si]/[Cd] = 2, (b) [Si]/[Cd] = 6.

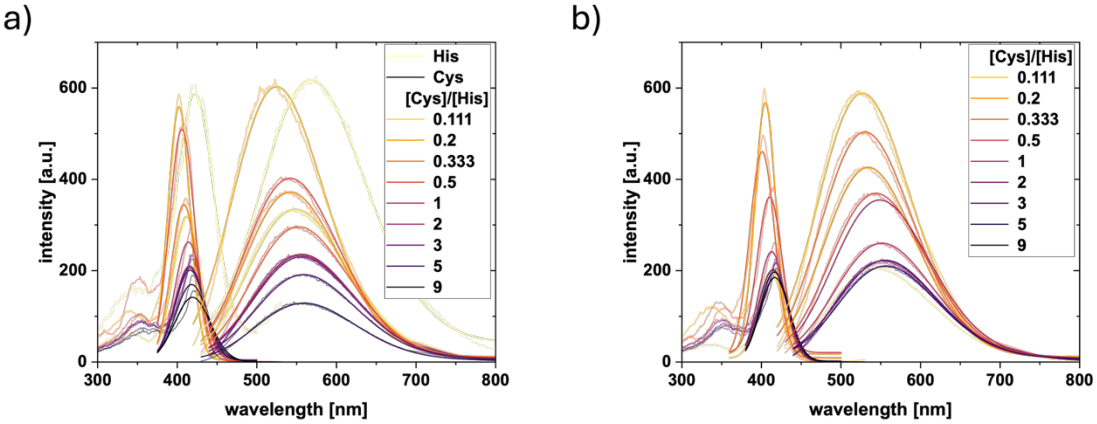


Figure SV-23. Fluorescence spectra for samples derived from mixed ligand complexes with cysteine and histidine in varying [Cys]/[His] ratios. (a) [Si]/[Cd] = 2, (b) [Si]/[Cd] = 6. For the excitation spectra the emission wavelength was set to 550 nm ([Cys]/[His] > 0.5), 540 nm, 535 nm, 520 nm, and 545 nm and for the emission spectra the excitation wavelength of 420 nm ([Cys]/[His] > 0.5), 418 nm, 410 nm, 402 nm, and 415 nm was used. (ordered in decreasing [Cys]/[His] ratio). Also, references are shown in (a) comparable to **Figure V-6b**.

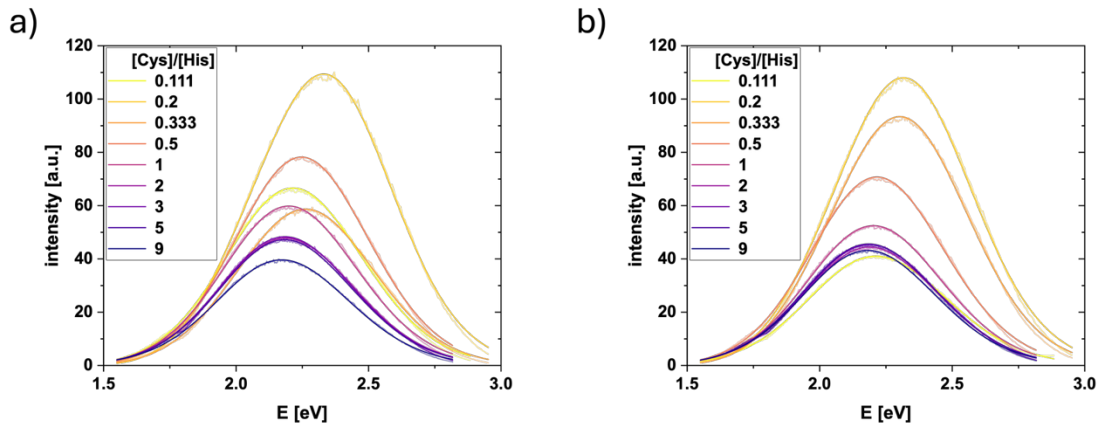


Figure SV-24. Transformed emission spectra and fits for samples derived from mixed ligand complexes with cysteine and histidine in varying [Cys]/[His] ratios. (a) [Si]/[Cd] = 2, (b) [Si]/[Cd] = 6.

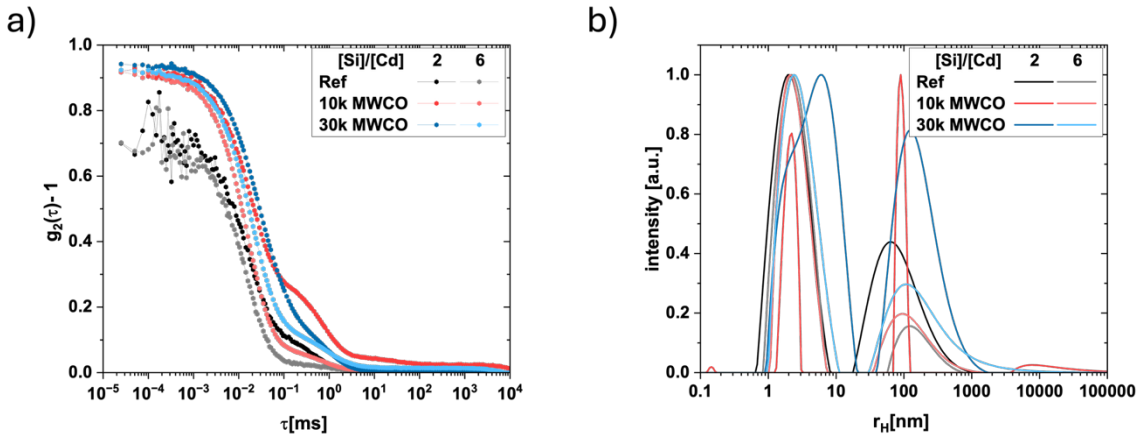


Figure SV-25. (a) DLS measurements for samples derived from cysteine complexes with subsequent size exclusion by filtration with 30k and 10k MWCO ultracentrifuge filters. (b) Unweighted size distribution derived from DLS measurements shown in (a) using the CONTIN algorithm [50].

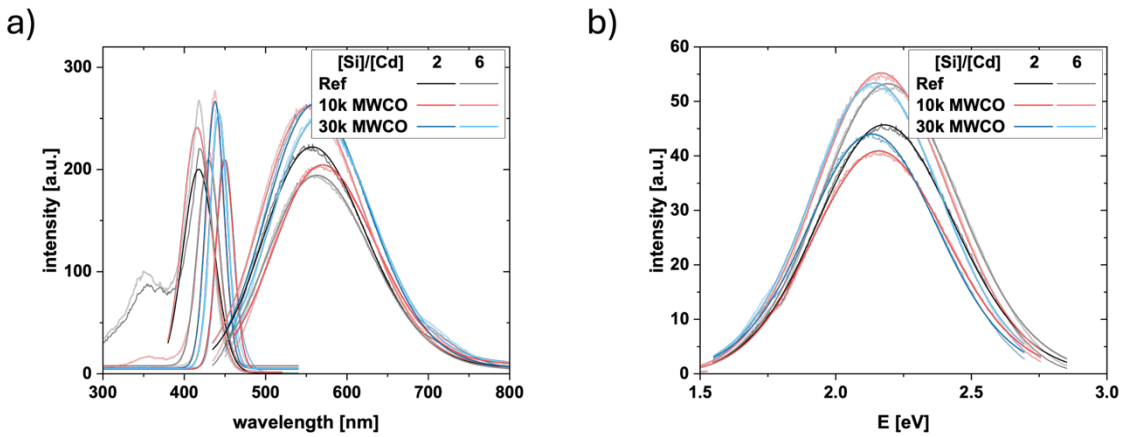


Figure SV-26. (a) Fluorescence (λ_{exc} = 420 nm, λ_{em} = 550 nm) spectra for samples derived from cysteine complexes with subsequent size exclusion by filtration with 30k and 10k MWCO ultracentrifuge filters. (b) Respective transformed emission spectra and fits.

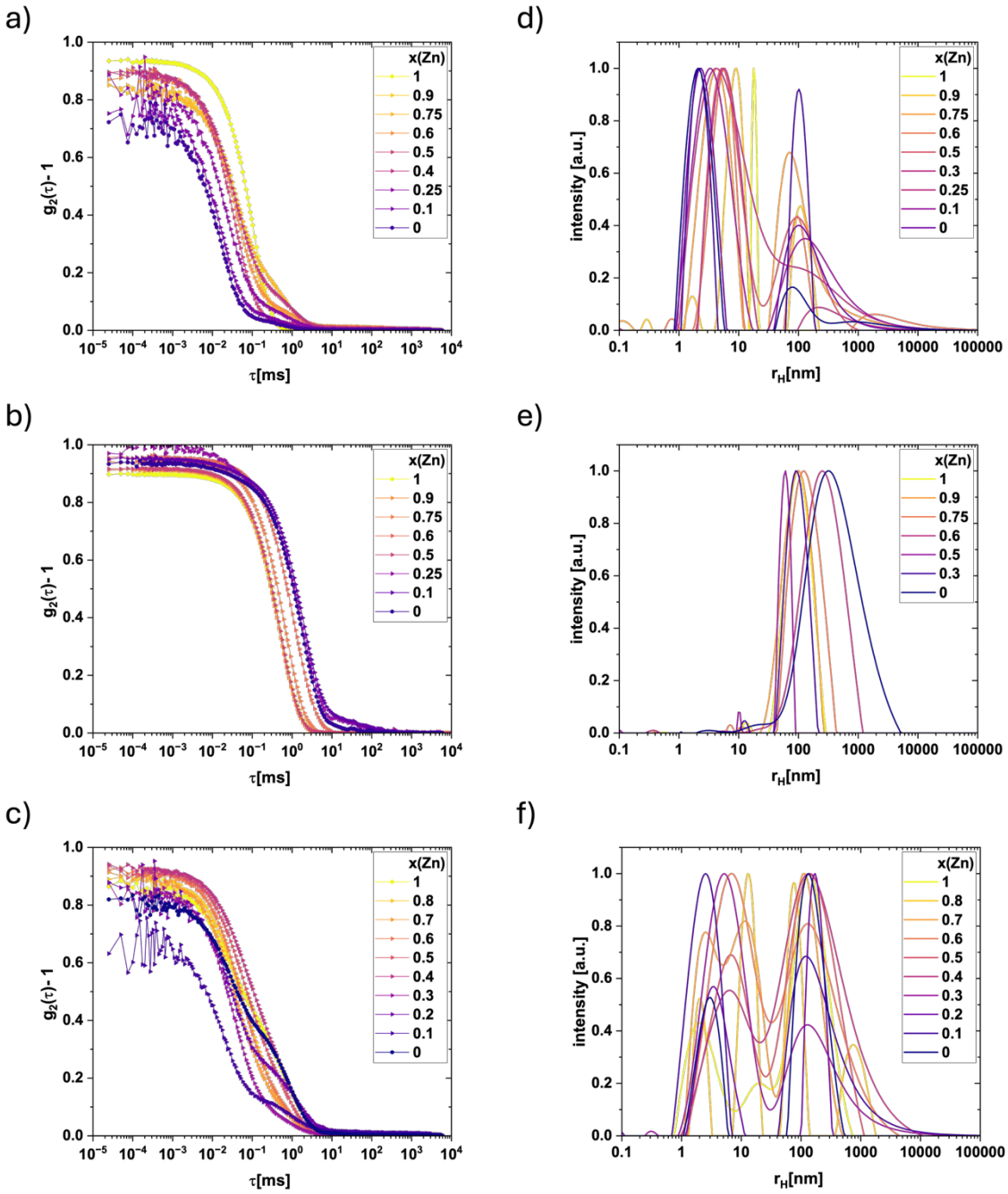


Figure SV-27. DLS measurements for samples derived from (a) cysteine, (b) histidine, and (c) mixed ligand complexes with differing molar fractions of Zn. Respective unweighted size distribution derived from DLS measurements shown in (d), (e), and (f) using the CONTIN algorithm [50].

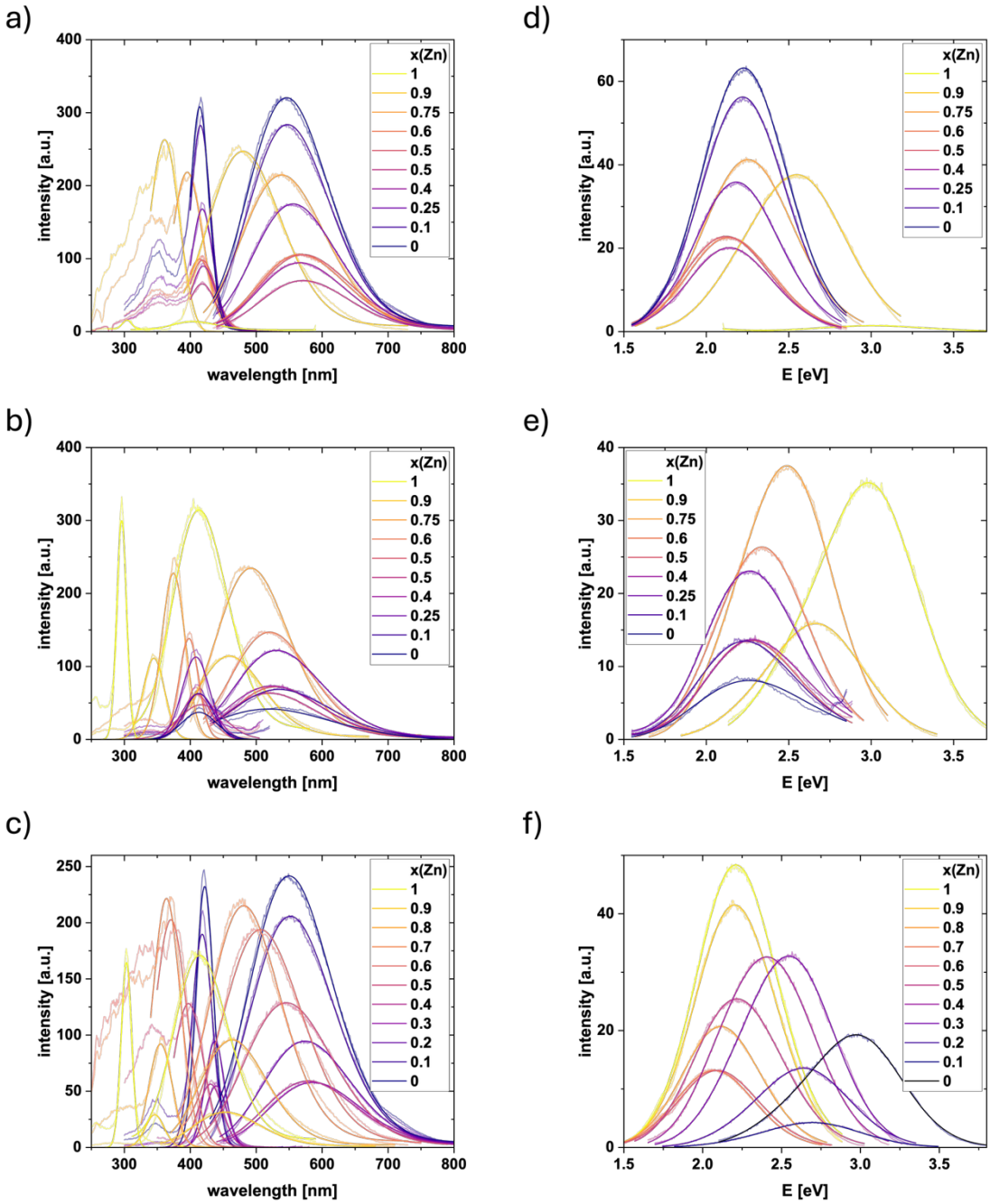


Figure SV-28. Fluorescence spectra for samples derived from (a) cysteine, (b) histidine, and (c) mixed ligand complexes with differing molar fractions of Zn. For the excitation spectra the emission wavelength was set to 550 nm and for the emission spectra the excitation wavelength of 420 nm was used. (d), (e), and (f) Respective transformed emission spectra and fits. The used wavelengths and the respective fit parameters are available in the online repository.

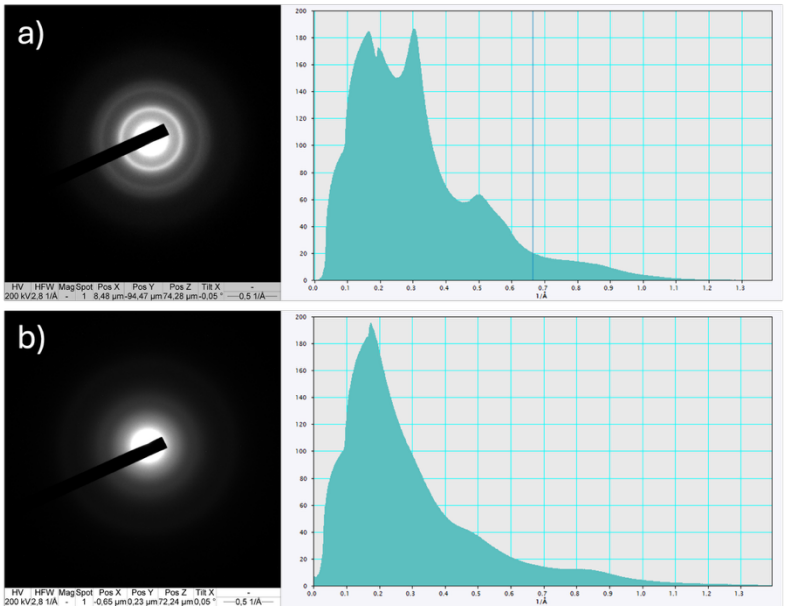


Figure SV-29. HRTEM diffraction pattern and radial average derived from HRTEM micrographs of $Zn_{0.8}Cd_{0.2}S$ derived from (a) cysteine complex and (b) reference reaction without complex precursor. The SAED pattern for (a) was indexed according to the hexagonal wurtzite structure of ZnCdS (space group P63mc, ICSD No. 620387). The SAED pattern ob (b) could not be indexed to a defined crystal structure. The observed deviations from the reference d-spacings are attributed to the partially amorphous character of the sample.

Chapter VI. Nanoparticle Formation Utilizing Simple Polyacrylic Acid-Cation Coacervates as Template

6.1 Abstract

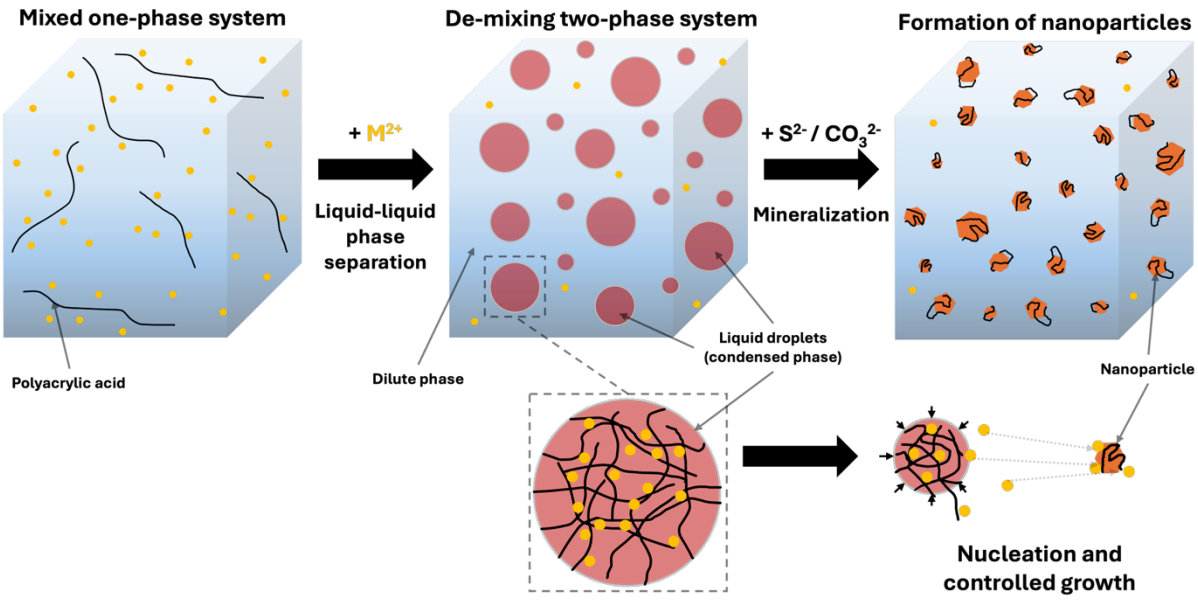


Figure VI-1. Graphical Abstract: Increasing the concentration of divalent cations in a PAA containing solution in the right pH regime results in a liquid-liquid phase separation, called coacervation. The solution separates into a polymer rich (condensed phase) and polymer depleted (dilute phase) phase. Adding sulfide/carbonate anions results in the formation of nanoparticles. The coacervates dissolve, slowly releasing cations, and the polymers stabilize the nanoparticles surfaces.

The liquid-liquid phase separation (coacervation) of simple solutions containing only polyacrylic acid (PAA) and multivalent transition metal (TM) cation can be used as template for nanoparticle formation. It is shown that transition metal carbonate/sulfide/oxide nanoparticles can be prepared by a simple coacervate-mediated process using only PAA, the transition metal chloride, and either sodium carbonate or sulfide. The rather simple approach first demonstrated for calcium carbonate could be extended to the chosen transition metals Co, Mn, Ni, and Cu. Using DLS and UV/vis, the formation and properties of PAA/TM coacervates were studied showing that in a broad pH range, coacervation is possible when a critical cation concentration is reached. Using these findings, mineralization of the coacervates results in defined small nanoparticles that can be easily separated from other bigger residues. Calcination

of carbonate particles results in their respective oxide counterparts. The rather small sizes (5 nm) of the primary particles and their amorphous crystal structure suggest further investigation into their use as catalysts.

Parts of this chapter are published in *RSC Advances* (Rödig, B.; Denk, P.; Schürmann, U.; Kellermeier, M.; Kunz, W. Nanoparticle Formation Utilizing Simple Polyacrylic Acid-Cation Coacervates as Template. RSC Adv. 2026, 16 (10), 8633–8640. https://doi.org/10.1039/D6RA00330C. Figures and text reproduced under the terms of the CC BY 4.0 license). [1]

Contributions to experimental work:

- Bastian Rödig: Conceptualization, Experimental Work, Data Evaluation
- Verena Graf, Anna Mändl, Olga Gebert, Julian Dolina: Experimental work

6.2 Introduction

Research on nanoparticles is at its all-time high due to their role in numerous applications, ranging from catalysis [2] and electronics [3] to energy storage [4], sensors [5], and functional coatings [6,7]. Several techniques have been established for the synthesis of nanoparticles with precise characteristics, such as sol-gel methods [8], hydrothermal [9] and solvothermal techniques [10], and mechanochemical strategies [11], achieving control over their size, composition, structural form (whether crystalline or amorphous), shape, and surface properties. Despite all these achievements, the control over these parameters remains a challenge and the process is often elaborate. In contrast, a rather simple approach for the synthesis of amorphous calcium carbonate (ACC) using coacervates as template is shown by Kaempfe et al [12].

6.2.1 Simple and Complex Coacervation

Coacervation is a special form of phase separation in colloidal systems, especially known for aqueous polyelectrolyte solutions. Coacervation was first mentioned by the Dutch chemists Hendrik Bungenberg de Jong and Hugo Kruyt, who investigated gelatin solutions [13,14]. It is a form of liquid-liquid phase separation, in which a colloidal solution separates in a colloid-rich (coacervate) and colloid-poor (equilibrium) phase. These coacervates form spontaneously throughout the solution and, depending on the density and surface properties, the coacervate phase can remain dispersed in the equilibrium phase or coalesce to form a top or bottom phase [13,15]. Coacervate formation depends on primary properties, such as solubility, molecular weight, charge density, and hydrophobicity of the sol as well as secondary properties primarily affecting the solution such as temperature, pH, salt concentration, and solvent [15]. Changes in these parameters can lead to reduced solubility of the colloid and induce coacervation [13,14]. Coacervation is a complex balance of electrostatics, hydrophobicity, excluded volume, van der Waals, and other contributions to the system's overall stability [16]. Coacervates are typically divided into two classes. While simple coacervates only consist of one colloidal or colloid-forming species at certain environmental conditions, complex coacervates consist of at least two colloidal or colloid-forming, usually polymeric, surface-active compounds [15]. Simple coacervate formation of polyelectrolytes depends on salt or alcohol concentration, or a change in pH or temperature [17]. Generally speaking, a dehydrating agent (solvent, salt, or both) can cause simple coacervation by reducing the interaction between colloid and solvent, resulting in favorable inter-colloid interactions.

6.2.2 Mechanisms of Coacervate Formation of PAA and Divalent Cations

To form the coacervates, the two attractive interactions shown in **Figure VI-2a** are essential. At elevated pH values the carboxylic groups on the PAA chain are deprotonated. The divalent cation can be complexed by the negatively charged carboxylic group and can, this way, bridge two different PAA chains (highlighted in grey). At lower pH values, the carboxylic groups are more protonated. In this state, the formation of hydrogen bonds between different PAA chains is possible (highlighted in green). The pH dependence of the fractional charge f of PAA is given by [18]:

$$pH = pK_a + 4.1f^{\frac{1}{3}} - log\left(\frac{1-f}{f}\right) \qquad \text{(VI-1)}$$

with pK_a as the acid dissociation constant. This interplay of different interactions results in a wide range of pH values, where the simple coacervation of PAA/M^{2+} is possible (c.f. **Figure VI-2b**). The range indicates that a significant portion, around 3/4 of the carboxylic groups have to be protonated for sufficient attraction to form coacervates.

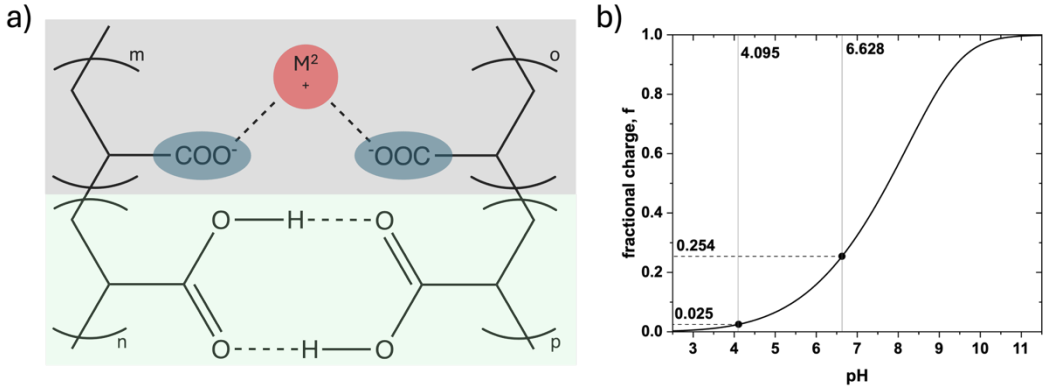


Figure VI-2. a) The two main attractive interactions to form simple PAA/M^{2+} coacervates. Divalent cation (M^{2+}) is complexed by deprotonated carboxylic groups and can bridge between two PAA chains (highlighted gray). Protonated carboxylic groups can form hydrogen bonds between different PAA chains (highlighted green). b) Fractional charge of PAA molecule calculated from **Eqn VI-1** [19]. Reference lines correspond to the highest (6.63) and lowest (4.09) pH values at which coacervation was observed in this work.

While these interactions provide the direct attractive forces responsible for phase separation, they alone do not fully explain the thermodynamic driving force of coacervation. Additionally, the thermodynamics of polyelectrolyte association must be considered. When divalent cations

form complexes with deprotonated carboxylate groups, some of the counter-ions are released into the surrounding solution. This release increases the entropy of the system and thereby promotes phase separation. The resulting coacervate state thus represents a balance between cation-mediated bridging, hydrogen bonding, the conformational entropy of the chains and the entropy of ion release [17,20,21].

6.2.3 Coacervates as Template for Nanoparticle Formation

Coacervates have attracted considerable attention as confined reaction environments. Their high local concentration of functional groups and ions, their increased viscosity and the restricted diffusion transport can significantly alter nucleation and growth processes [22,23]. Scattering experiments and cryo-TEM measurements have shown the hollow, spongelike structure inside the coacervate droplets for various simple and complex coacervates [24]. In previous works, polyacrylic acid (PAA)/Ca^{2+} coacervates were used to produce defined $CaCO_3$ microstructures and nanoparticles [12,25], which is in this work extended to PAA/transition metal cation coacervates and respectively particles of transition metal sulfide/carbonate/oxide. It will be shown that the mineralization of these coacervates results in small particles of around 5 nm, which can be isolated from bigger structures forming in the supernatant.

6.3 Experimental

6.3.1 Materials

Poly(acrylic acid, sodium salt) (PAANa) solution (Mw ≈ 8000, 0,45 wt.% in H_2O, Mw ≈ 2000, 0,45 wt.% in H_2O), Poly(acrylic acid) (PAA) solution (Mw ≈ 100000, 0,35 wt.% in H_2O), Cobalt(II) chloride hexahydrate (purity ≥ 98%), Manganese(II) chloride tetrahydrate (BioReagent grade), Nickel(II) chloride (purity ≥ 98%), Sodium carbonate (purity ≥ 99.5%), 1M HCl solution (for titrations) were purchased from Sigma Aldrich (St. Louis, USA). Copper(II) chloride dihydrate (purity ≥ 99.0%) and Sodium hydrosulfide monohydrate (purity ≥ 90%) were obtained from Honeywell (Charlotte, North Carolina, USA). All chemicals were used without further purification. Ultrapure water from a Millipore purification system (resistivity > 18 MΩ·cm) was used for all systems containing water.

6.3.2 Apparatus

6.3.2.1 Formation of Coacervates and Synthesis of Particles

Aqueous solutions of PAANa were prepared from 1 to 10 wt% at different pH values ranging from 4 to 8.6 (native pH). The pH was adjusted using 1M HCl solution. Aqueous solutions of 0.25 M transition metal chloride were prepared and added dropwise to the PAA solutions under continuous stirring with a magnetic stirrer until the onset of turbidity indicates coacervate formation. Mineralization was achieved by adding the stochiometric ($[M^{2+}] = [CO_3^{2-}/S^{2-}]$) amount of either sodium carbonate or sodium sulfide to the solution immediately after coacervate formation. By centrifugation, the formed particles were separated from the supernatant. After resuspension in water, they were lyophilized to obtain a dry powder. Oxides were formed by calcination of the respective carbonate powder at 600°C for at least 6h.

6.3.3 Methods

6.3.3.1 X-ray diffraction analysis (XRD)

X-ray diffraction analysis was carried out using a STADI-P device from STOE & Cie GmbH (Darmstadt, Germany), with $CuK_{\alpha 1}$ radiation (λ=1.540598Å). The dry samples were ground to form a homogeneous powder and scanned from 2° to 92° in 0.015° steps.

6.3.3.2 Dynamic Light Scattering (DLS)

For dynamic light scattering (DLS) measurements, a CGS-3 Compact Goniometer System from ALV (Langen, Germany), combined with an ALV/LSE-5004 Multiple Tau Digital Correlator and a vertically polarized 22 mW HeNe laser ($\lambda = 632.9$ nm), was used. Measurements were performed at a scattering angle of 90° with a constant temperature of 25°C for 300 s. Using the 2nd order cumulant analysis [26,27] of the ALV-7004 Correlator software, the hydrodynamic radius and size distributions can be calculated from the autocorrelation function. Also, the CONTIN algorithm [28,29] was used to gather information from more noisy measurements. Coacervates were measured immediately after formation (cf. **Figure SVI-3**). Particles were resuspended in water and briefly sonicated with an ultrasonic probe from Hielscher (Germany) before the measurement.

6.3.3.3 Transmission Electron Microscopy (TEM)

The structure and size of the particles were evaluated using transmission electron microscopy (TEM) using a CM-12 transmission electron microscope from FEI/Phillips (Dreieich, Germany) with a tungsten cathode and 120 kV acceleration voltage. Pictures were taken with the digital camera 1kx1k from TVIPS (Gauting, Germany). The images were processed and evaluated with the software EMMenu4. Samples were resuspended in EtOH and prepared on 200 mesh copper grids with a carbon film from PLANO GmbH (Wetzlar, Germany).

6.3.3.4 UV/Vis measurements

UV/vis measurements were carried out at the infinite m nano^{+} UV/vis photo spectrometer from TECAN (Männedorf, Switzerland) using a 96-well plate to determine cation concentration. Therefore, the supernatants of the coacervate samples were measured after a settling time of 24h after full phase separation.

6.3.3.5 Small-angle X-ray Scattering (SAXS)

Extensive in situ SAXS measurements (beamline ID01, Grenoble, France) were conducted to monitor structural changes during coacervate formation and nanoparticle synthesis. Although the data confirmed the investigated processes, the obtained scattering profiles did not reveal additional features that enabled a quantitative structural analysis beyond the information

already provided by DLS, TEM, and XRD. To ensure transparency and reproducibility, the complete SAXS datasets are provided in the accompanying online repository.

6.3.3.6 Data availability

Additional raw data, fit parameters, and associated scripts, are available in the online repository (Novel nanoparticle synthesis in self-organizing water–based systems - online repository, 10.5283/epub.80300). Representative data and fits are shown in the SI.

6.4 Results and Discussion

6.4.1 Coacervate Formation

Figure VI-3a schematically shows the formation of coacervates by the addition of metal chloride solution (MCl_2) to the PAANa solution. The formed coacervate droplets coalesce over time and ultimately, they fuse to form a separate phase. The supernatant is the polymer-depleted phase, whereas the lower phase contains a high amount of PAA^-/M^{2+} coacervates and is therefore highly viscous.

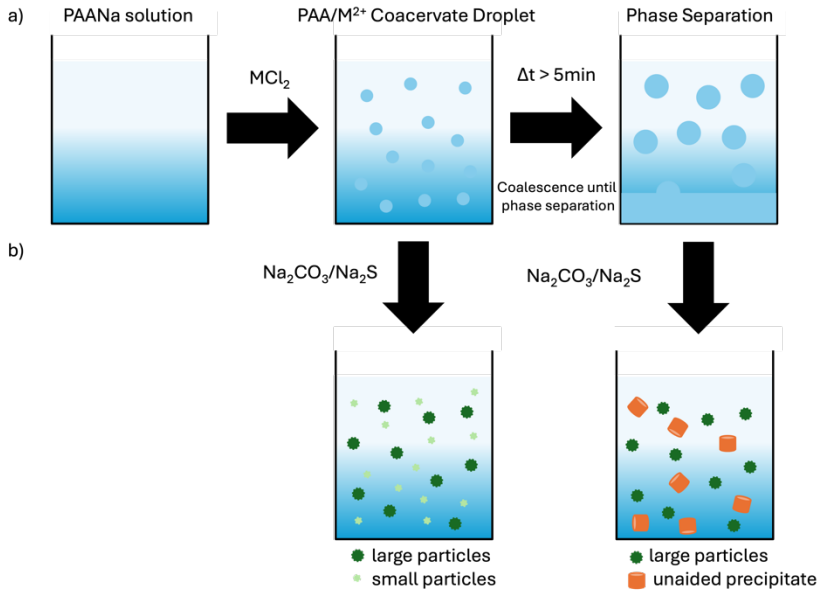


Figure VI-3. Scheme of the simple coacervating system: (a) PAA^-/Co^{2+} coacervate droplets form at concentrations greater than a certain threshold ratio and coalesce over time. (b) Mineralization with Na_2CO_3/Na_2S results in different structures before and after phase separation. (inspired by ref [12])

Once formed, the separated phase cannot be resolubilized again, which also hinders the mineralization in the second step. Shown in **Figure VI-3b** is the mineralization process at different times after the coacervate droplet formation. The simple coacervation formation of divalent cations and PAA is fundamental to the investigation of the mineralization process to form nanoparticles. Therefore, the association of divalent cation and PAA to form coacervate droplets and their phase behavior is studied first and the mineralization of the coacervates is shown afterward. While mostly results with Co^{2+} are shown, additionally Ca^{2+}, Cu^{2+}, Mn^{2+}, and Ni^{2+} were tested. If not stated otherwise, $M_W \approx 8000$ g/mol PAANa was used and the concentration in the final mixtures is 1 wt%.

pH titrations for various divalent cations (c.f. **Figure SVI-1**) have shown that complexed cations do not precipitate as hydroxide. Instead, the coacervates are resolubilized again at a sufficiently high pH, resulting in the formation of a clear solution beyond the pH at which the hydroxide formation of the respective cation begins. This happens not only for cations like Cu^{2+}, which forms soluble hydroxides at elevated pH values, but for all cations tested. So, the upper limit for coacervate formation is not the precipitation of metal hydroxide ($M(OH)_2$), but the dissolution of the coacervates due to inadequate interactions, especially to few formed hydrogen bonds. Nevertheless, the competition of hydroxide formation and PAA/M^{2+} complexation occurs in certain pH ranges depending on the cation, increasingly important for hydroxides with smaller solubility products like Cu^{2+} (c.f. **Figure SVI-2**). The addition of divalent cation to a solution containing PAA in the right pH regime can result in coacervate formation, whereas simple pH titration or the addition of monovalent cations like Na^+ does not (c.f. **Figure SVI-1**).

6.4.2 Coacervate Characterization

At the elevated end of the pH range, DLS measurements of the coacervate droplets, immediately after formation (cf. **Figure SVI-3**), indicate smaller radii than for lower pH values, as visible in **Figure VI-4**. The measurable size of the droplets depends on a balance of different forces. First, due to the higher charges of the PAA chains at higher pH, more cations can be complexed, resulting in more electrostatic attraction inside the coacervate phase and therefore the formed coacervate droplets are more compact. Secondly, at lower pH values, the coalescence is faster, due to fewer surface charges on the coacervate droplets and therefore less electrostatic repulsion between the droplets. Even though the Debye length λ_D (**Figure VI-4a**) remains smaller than 1 nm for the investigated pH values, the small decrease with increased pH shows less screening at lower pH values, which results, combined with fewer charges on the coacervate droplets, in faster coalescence. This is hardly observable for Ni^{2+} and Cu^{2+}, because both induce the formation of PAA/cation flakes at higher pH values indicating a competition of complexation by the carboxylic groups and hydroxide precipitation. This results in a narrower pH range in which coacervation is possible, but which is already characterized by fairly rapid coalescence. The solubility product of the respective hydroxides [30] is lower compared to the other cations tested. Corresponding to the onset of hydroxide formation at this pH value, the required minimal copper concentration of around 24 mM is almost half of the concentration necessary for other cations (c.f. **Figure SVI-2**). Especially for copper, coacervation is only

possible at pH values lower than 4.8, whereas for nickel the respective pH value is around 7, resulting in coacervate formation at pH values below with increasing flocculation with increasing pH. At lower pH values, coacervation is possible until too less carboxylic groups are deprotonated to interact sufficiently with the cations. No coacervation was observed at pH values ≤ 4 or ≥ 7 for all tested cations.

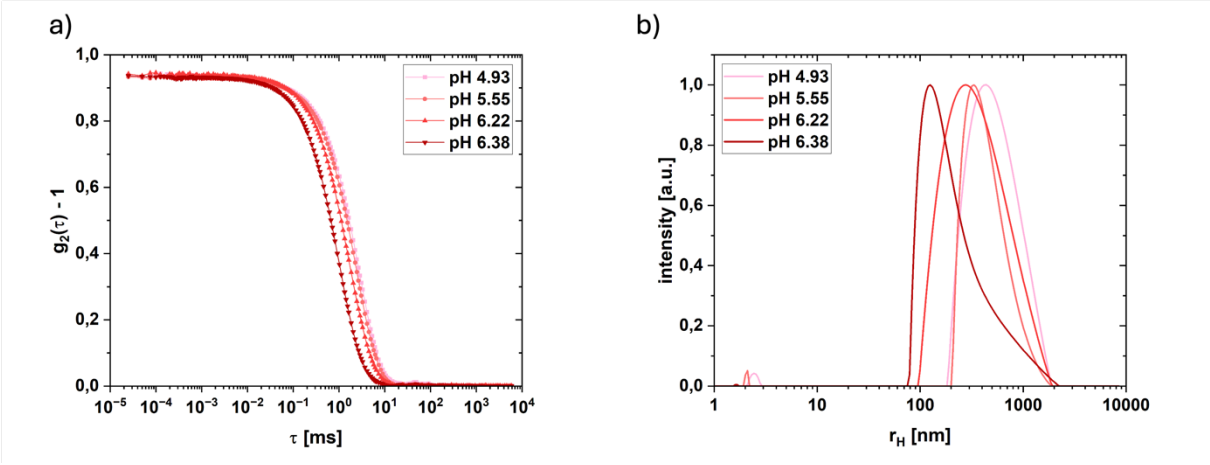


Figure VI-4. (a) DLS correlation function of PAA^{-}/Co^{2+} coacervates formed at different pH values measured at 25°C. Debye length with decreasing pH: 0.488 nm, 0.522 nm, 0.664 nm, 0.739 nm. (b) Unweighted size distribution of PAA^{-}/Co^{2+} coacervates at different pH values, derived from DLS using the CONTIN [28,29] algorithm. Further information on coalescence rates can be found in **Figure SVI-3**.

To form coacervates, a certain threshold concentration of divalent cation [15,31] must be reached. This threshold depends on the PAA concentration, the pH of the solution [19], the chain length of the PAA [19,32,33], and to some degree also on temperature [31]. The optimal chain length for the experiments was found to be at 8000 g/mol. Longer chains needed a longer time to reach the equilibrium and often formed flakes during the addition of the cation, whereas the shorter chain coacervates coalesce faster and also showed a higher threshold concentration (1 wt% of 2000 g/mol PAANa, $c(M^{2+}) \approx 80$ mM, $AA/M^{2+} \approx 0.8$). Whereas the cation species showed minimal influence on the threshold concentration of around 40 mM ($AA/M^{2+} \approx 2.6$) for most of the cations tested, Cu^{2+} behaves differently with a threshold concentration of around 24 mM ($AA/Cu^{2+} \approx 6.6$). The reduced threshold concentration for Cu^{2+} could be due to its higher affinity for carboxylates (according to the Irving-Williams series [34]) and thus stronger interactions. On the other hand, Cu also exhibits a higher affinity for hydroxide formation [35], which would explain the narrower pH range.

Below this concentration, association of divalent cation and PAA occurs, but the total interactions are not yet enough to result in a phase separation. If the concentration is raised beyond this threshold, coacervates form (c.f **Figure SVI-1**). The higher the concentration, the faster the coalescence to a unified phase, depleting the supernatant of the polymer as well as the cation. Visible in **Figure VI-5a** is the increased volume of the separated coacervate phase and the fading color of the supernatant for higher concentrated samples. Visible in **Figure VI-5b** are the Co^{2+} concentrations in the supernatants, as measured by UV/vis spectroscopy, revealing that the fraction of cations actively participating in coacervate formation increases with decreasing acrylic acid (AA)/M^{2+} ratio. From the onset of coacervation around an AA/M^{2+} ratio of 2.6, where only a small fraction of the cations are bound in the coacervate, the fraction of the cations bound in the coacervate increases to around 70% at the highest pH shown. Whereas the onset concentration remains the same for different pH values, the amount of bound cation decreases with decreasing pH. This is a direct result of less deprotonated carboxylic groups on the PAA chains resulting in fewer complexation sites for the cations. A similar trend is visible in **Figure SVI-4a**, where the total organic carbon (TOC) and therefore the PAA remaining in the supernatant solution decreases with increasing pH and increasing cobalt concentration. Overall, the decrease in the PAA content with increasing pH values is only strictly visible after the AA/M^{2+} ratio of 2.6 is undercut. Above, no pH dependence can be seen, but even in the samples where no coacervation is recognizable, only about 90% of the PAA can be detected via TOC measurements. At the highest cation concentration (65 mM) and the highest pH value (5.9) approximately 75 % of the total PAANa in solution is bound in the coacervate phase, which correlates with the amount of removed cation in the supernatant.

The calculation of the actual amount of interacting deprotonated carboxylates, determined using **Eqn VI-1**, and the amount of cation in the coacervates, results in a ratio of 0.45 AA^-/M^{2+} at the onset of coacervation at the highest pH value tested. At even lower ratios (AA/M^{2+} < 1.6), the concentration in the supernatant seems to slightly increase again hinting at an almost complete association of available PAA molecules and precipitation/phase separation as coacervates. Or in other words, the remaining PAA in the supernatant is not sufficient to form further coacervates despite sufficient cobalt concentration.

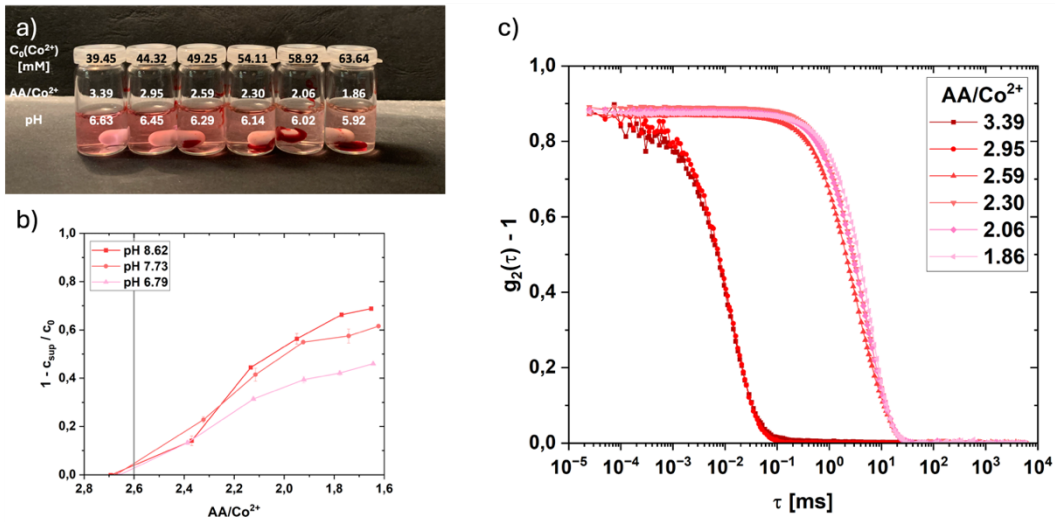


Figure VI-5. (a) Picture of PAA/Co^{2+} solutions with different AA/Co^{2+} ratios after an equilibration time of 24h containing PAA/Co^{2+} coacervates after coalescence. (b) Share of the Co^{2+} concentration in the coacervates of the total concentration at the different AA/Co^{2+} ratios derived from UV/vis measurements of the supernatants after coalescence (equilibration time 24h). (c) DLS correlation functions of PAA/Co^{2+} solutions at the different AA/Co^{2+} ratios (3.4-1.9), measured immediately after coacervate formation, when the coacervates were still finely dispersed as droplets (cf. **Figure SVI-3**).

The onset of coacervation is also visible in **Figure VI-5c**. For cation concentrations below the threshold concentration (≈ 40 mM, AA/Co^{2+} ≈ 2.6), the correlation function only represents dissolved PAA molecules at a size of around 2.2 nm. Above the threshold concentration, the correlation function represents the formed coacervate droplets and is shifted to slightly higher lag times, indicating bigger droplets, for higher cation concentrations. This is a result of faster coalescence and slightly smaller pH values. Whereas the coacervate droplet dispersion near the threshold concentration remains dispersed for almost 24h, the further away from the threshold concentration, the faster the coalescence. The additional amount of cation introduces more screening resulting in greater Debye lengths over the concentration series. The critical cation concentration for the onset of coacervation is independent of the pH value (adjusted with HCl) resulting in a constant ratio of AA/M^{2+}. Therefore, the calculated AA^-/M^{2+} decreases with a decrease in pH, indicating that less transition metal cations are complexed at lower pH values, which is directly visible in **Figure VI-5b**.

6.4.3 Mineralization of the Coacervates

Depending on the time Na_2CO_3/Na_2S is added, different structures will be created, as implied in **Figure VI-3b**. Although previous results by Kaempfe et al. [12] showed an increase in particle size with larger coacervate droplets, no direct correlation between particle size and

coacervate droplet size could be established due to the rather fast coalescence of the droplets over time. Controlling particle size via coacervate size was therefore not investigated further here.

Interestingly, this differs from previous reports, which have suggested a relationship between droplet and particle size [12]. This discrepancy may be due to the faster precipitation kinetics of the transition-metal compounds investigated here [35–38]. In these systems, nucleation and growth potentially occur on a similar timescale to coacervate coalescence, or even faster [39,40]. This would decouple particle formation and coalescence. The chemical reactivity of the confined cations is then more important than the geometrical size of the template [41].

Instead, the mineralization was done immediately after the formation of the coacervates or, as different approach, only in the separated coacervate phase. Due to the insolubility and the highly viscous state of the separated coacervate phase, it is assumed that structures only formed by leaking cations into the supernatant and were not mediated by the coacervate phase itself. Some formed structures are shown in SI compared to structures derived from uncontrolled precipitation (cf. **Figure SVI-5**). The similarity of the found structures validates the unmediated growth of the particles in the supernatant. Synthesis of particles below ($AA/M^{2+} > 2.6$) and beyond ($AA/M^{2+} < 2.6$), the threshold concentration results in different structures, as visible in **Figure VI-6** for CoS and in **Figure SVI-6 f**or $CoCO_3$.

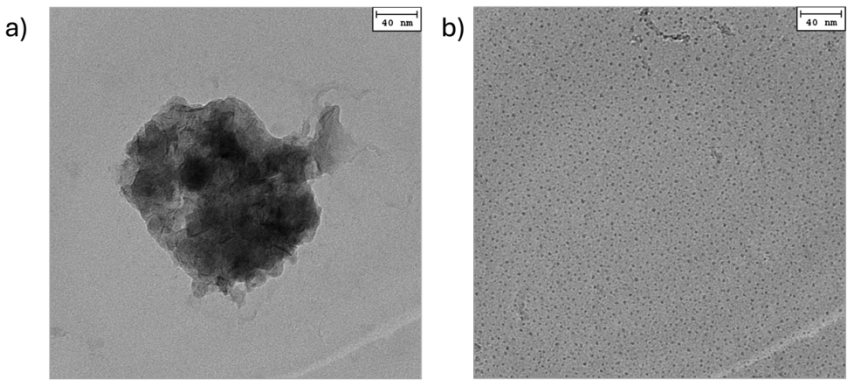


Figure VI-6. TEM micrograph of CoS particles derived from PAA^-/Co^{2+} mixtures at different ratios. (a) AA/Co^{2+} ratio of 2.65, just below the threshold concentration. (b) AA/Co^{2+} ratio of 1.33, above the threshold concentration.

For concentrations below the threshold, big clusters of smaller particles that have grown together form (**Figure VI-6a**), whereas at higher concentrations, small particles, of a few nanometers in size, surround aggregates of bigger particles (**Figure VI-6b**). Even those aggregated particles are smaller than particles seen for particles derived from below the

threshold concentration and still are distinguishable (**Figure VI-6b**, **Figure SVI-7-Figure SVI-9**). This immense size reduction of particles comes from the reduced chemical potential of the bound Co^{2+} cations and therefore the greatly reduced reactivity. Further, the coacervate phase could act as a confining reaction environment [23]. The locally high polymer concentration results in high viscosity, which directly reduces ion mobility and mass transport during nucleation [42–44]. In addition, PAA could potentially further stabilize the surfaces of the resulting nuclei against pronounced aggregation, Ostwald ripening, and growth beyond the nanoscale [45–48].

Even though the formation of the smallest particles is enhanced in the synthesis farther away from the threshold concentration, due to the higher amount of bound cations, synthesis above but still near the threshold results in an easier process and more reproducible particle sizes due to the slower coalescence of the coacervate droplets and therefore more homogeneous distribution of cation prior to synthesis. Also, higher pH values were preferred for the synthesis, first, to prevent excessive gas development from the added carbonate/sulfide, and second, to use the smallest possible coacervate droplets and reduce coalescence as much as possible. The amount of bound cations in the coacervates also is higher at higher pH values due to more ion bridging, as shown in **Figure VI-5b**. The mineralization immediately after the addition of the MCl_2 solution then results in a mixture of two or sometimes three distinguishable particle distributions (cf. **Table SVI-1**). The different structures formed are shown in **Figure SVI-7 t**o **Figure SVI-9 f**or the different cations, Co^{2+}, Mn^{2+}, and Ni^{2+}. Visible in all samples, regardless of the cation or the anion, relatively big almost circular/spherical structures occur. These are direct remains of the synthesis and just represent the coacervate droplets (c.f. **Figure SVI-10**). The measurable size correlates to the hydrodynamic radii derived from DLS measurements evaluated using the Cumulants method (c.f. **Table SVI-1**). These particles also seem to be substructured and their poor contrast on the carbon film indicates that they consist mainly of similar electron-dense material as the background and be therefore just coacervate droplets. There are also two other structures visible. First small particles, only a few nanometers in size (5-15 nm), and second bigger particles in the range of 20-60 nm. The bigger particles occur also in other samples such as the particles derived from unaided precipitation (c.f. **Figure SVI-5c**,d) and in the synthesis below the threshold concentration (c.f. **Figure VI-6a**) and reduce in number the further above the threshold concentration. Nevertheless, the most interesting particles are the smallest ones about 5 nm in size. These are visible in almost all samples but in different quantities (cf. **Figure VI-7** for CoS and **Figure SVI-11** for $CoCO_3$).

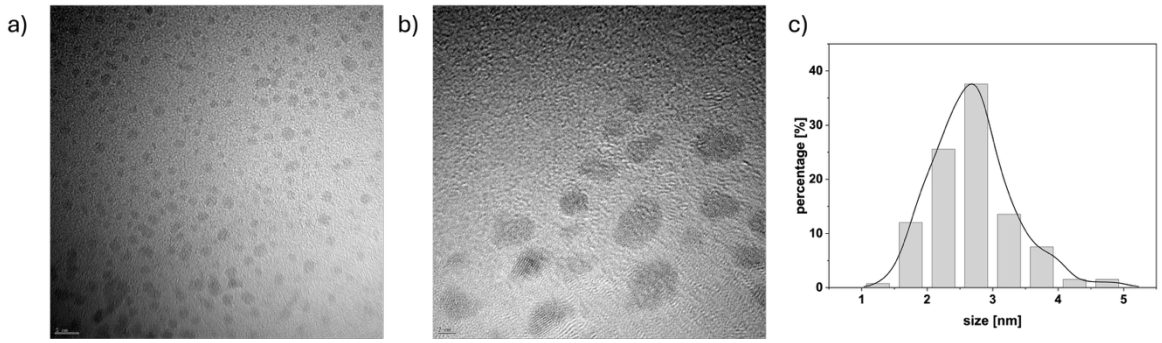


Figure VI-7. High resolution TEM micrograph of particles synthesized at AA/M^{2+} of around 1.3. (a) and (b) CoS with scale bars of 5 and 2 nm in length, respecitvely. (c) Histogramm derived from particles measured in HRTEM micrographs as shown in (a) and (b). The particles show an average diameter of 2.7 +- 0.60 nm (n = 133), corresponding to a coefficient of variation of 0.22, indicating moderate polydispersity.

Generally, they appear more often the lower the AA/M^{2+} ratio is, until the saturation of cations in the coacervates, then the number of big particles increases again. The evaluation of the DLS data with the CONTIN algorithm fits the measured sizes very well (cf. **Table SVI-1**). Filtration using a 200 nm syringe filter or centrifugation (< 700 g) can further decrease the polydispersity leading only to two distinct structures, small particles of a few nanometers and their aggregates (c.f. **Table SVI-1** and ref [12]). Measurements of the small particles results in a particle fraction with moderately narrow size distributions. (cf. **Figure VI-7c** for CoS and **Figure SVI-11c** for $CoCO_3$)

The size difference between the sulfide and carbonate can directly be backtracked to the difference in the solubility product (K_{sp}) and the resulting critical radius for germination/the critical nucleation barrier. As the value for CoS is less than half that of $CoCO_3$, the nucleation is much faster for CoS resulting in more and smaller germs and then in turn smaller/less grown particles than for $CoCO_3$ [49,50].

For generalization and comparison, the critical nucleation barrier (ΔG*) can be calculated [51,52], even though the classical nucleation theory (CNT) was originally developed for homogeneous nucleation in bulk solutions [51,52]. Nevertheless, it can be used for these systems as a useful framework for comparing relative nucleation tendencies [53]. The calculated ΔG^* values should therefore be regarded not as absolute values but as qualitative indicators of the ease of nucleation. The calculated lower nucleation barriers (cf. **Table SVI-2**) for the sulfides are consistent with the experimentally observed tendency for smaller particles to form, following this size trend:

$$CuCO_3 \approx NiCO3 > MnCO3 > CoCO3 > MnS > CoS > NiS > CuS$$

This trend could partly be seen from evaluation of the DLS measurements and the TEM micrographs. (cf. **Table SVI-1**) Also, sulfides were observed to always precipitate more rapidly due to significantly lower $\Delta G^* / k_B T$, wich is only one-tenth of the value for the carbonates. (cf. **Table SVI-2**)

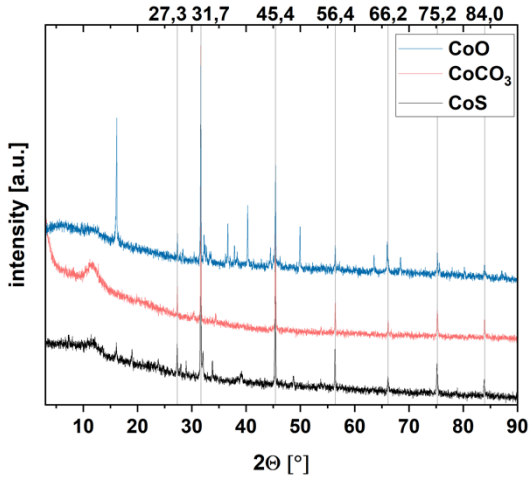


Figure VI-8. XRD measurement of Co-particles derived from PAA/Co^{2+} coacervates at pH 5.45 with different anions, CoS (black), $CoCO_3$ (red), and CoO (blue). The reflexes visible and the reference lines correspond to the NaCl lattice derived from NaCl residues.

XRD measurements, shown in **Figure VI-8** indicate crystalline NaCl residues from the synthesis. Even though the concentration of the respective cobalt species is higher than for the residues, almost no clear reflexes can be detected except for CoO. Instead, a broad reflex at small angle is visible, hinting at amorphous crystal structures. Amorphous crystal structures were expected, as this was shown already before for ACC particles [12]. The formation of amorphous structures is consistent with the rapid precipitation conditions and the presence of strongly interacting polymers [54,55]. The interaction of PAA with the surface can hinder the reorganization of atoms into thermodynamically stable crystalline structures and stabilize kinetically amorphous structures [56,57]. Such metastable phases are frequently observed in biomineralization processes [58].

In the high-resolution TEM images, some of the particles, which are only a few nanometers in size, appear to have a crystal structure that cannot be resolved, neither in XRD nor in SAED, due to their small size (c.f. **Figure VI-7b** and **Figure SVI-11b**). The calcination of the carbonates to the oxides does not show the amorphous reflex anymore, but instead shows,

depending on the calcination temperature, the respective crystal structure of the formed oxide. This indicates the rearranging of the atoms in the lattice resulting in a defined crystal structure, while maintaining the small size. This can also be seen for the other cations, Mn^{2+} and Ni^{2+}(c.f. **Figure SVI-12**). The amount of formed particles for Cu^{2+} is lower, compared to the other cations due to the necessity of lower pH values for the coacervate formation and therefore less bound cations in the coacervates. This is also visible in the XRD spectra of the Cu-containing particles (cf. **Figure SVI-12**), as the amorphous structures are less expressed, and the evaluation of the DLS data results in only a small percentage of the smallest particles if even possible (cf. **Table SVI-1**).

6.5 Conclusion

The current chapter shows that simple PAA/transition-metal coacervates offer a versatile and robust platform for the synthesis of transition-metal carbonate, sulfide, and oxide nanoparticles. Coacervation occurred over a wide pH range and with various divalent cations. The underlying mechanism is driven by the interaction between metal-ion bridging of deprotonated carboxylate groups and hydrogen bonding among partially protonated PAA chains.

Independently of the used transition metal, coacervate formation required a threshold cation concentration. Only when this concentration was exceeded, liquid-liquid phase separation occured. A significant portion of both the polymer and the cation became concentrated in the coacervate phase. Higher cation concentrations increased coalescence and phase separation. At the same time, higher pH values increased ion binding because more deprotonated carboxylate groups were available.

Mineralization of freshly formed coacervates led to nanoparticles of just a few nanometers. The formation of these ultrafine particles happens because metal ions are confined within the coacervate phase. This confinement reduces the chemical potential of the complexed ions, lowering their reactivity and changing the nucleation and growth processes compared to regular bulk precipitation. As a result, particle sizes were much smaller than those from unsupported precipitation experiments.

Even with variations in hydroxide solubility, complexation strength, and accessible pH range, the overall synthesis concept applied to Co^{2+}, Mn^{2+}, Ni^{2+}, and Cu^{2+} systems. For Cu^{2+}, coacervation tended to happen only at lower pH values due to the formation of competing hydroxides, which led to lower incorporation efficiencies and reduced nanoparticle yields. Still, the general coacervate-assisted synthesis method remained valid.

When comparing carbonate and sulfide systems, it became clear that the final particle size is greatly affected by the nucleation barrier related to the solubility product. Sulfides generally showed lower calculated nucleation barriers and produced smaller particles than carbonates, aligning with classical nucleation theory and the size distributions observed in experiments.

X-ray diffraction and electron microscopy suggested that the initially formed particles were mostly amorphous or only weakly crystalline. These amorphous nanostructures are particularly interesting because they often have a high density of structural defects and unsaturated surface sites. Calcining the carbonate particles transformed them into their crystalline oxide counterparts while mostly maintaining the nanoscale size of the original particles.

Overall, this approach offers simplicity and broad usability. It does not need surfactants, complex ligands, hydrothermal conditions, or intricate reactor designs. The combination of nanoscale particle sizes, high expected surface area, and partially amorphous structure makes these materials strong candidates for further studies in catalysis, electrocatalysis, and energy-related applications. Future research should aim to clarify the detailed nucleation process within the coacervate phase, measure the local ion concentrations and transport properties, and establish direct structure-property relationships for catalytic performance.

6.6 References

[1] Rödig B, Denk P, Schürmann U, Kellermeier M, Kunz W. Nanoparticle formation utilizing simple polyacrylic acid-cation coacervates as template. RSC Adv 2026;16:8633–40. https://doi.org/10.1039/D6RA00330C.

[2] Astruc D. Introduction: Nanoparticles in Catalysis. Chem Rev 2020;120:461–3. https://doi.org/10.1021/acs.chemrev.8b00696.

[3] Payal, Pandey P. Role of Nanotechnology in Electronics: A Review of Recent Developments and Patents. Recent Pat Nanotechnol 2021;16:45–66. https://doi.org/10.2174/1872210515666210120114504.

[4] Pomerantseva E, Bonaccorso F, Feng X, Cui Y, Gogotsi Y. Energy storage: The future enabled by nanomaterials. Science (1979) 2019;366. https://doi.org/10.1126/science.aan8285.

[5] Sabela M, Balme S, Bechelany M, Janot JM, Bisetty K. A Review of Gold and Silver Nanoparticle-Based Colorimetric Sensing Assays. Adv Eng Mater 2017;19:1–24. https://doi.org/10.1002/adem.201700270.

[6] Jiang C cong, Cao Y ke, Xiao G yong, Zhu R fu, Lu Y peng. A review on the application of inorganic nanoparticles in chemical surface coatings on metallic substrates. RSC Adv 2017;7:7531–9. https://doi.org/10.1039/c6ra25841g.

[7] Kumar S, Ye F, Dobretsov S, Dutta J. Nanocoating Is a New Way for Biofouling Prevention. Frontiers in Nanotechnology 2021;3:1–16. https://doi.org/10.3389/fnano.2021.771098.

[8] Parashar M, Shukla VK, Singh R. Metal oxides nanoparticles via sol–gel method: a review on synthesis, characterization and applications. Journal of Materials Science: Materials in Electronics 2020;31:3729–49. https://doi.org/10.1007/s10854-020-02994-8.

[9] Hayashi H, Hakuta Y. Hydrothermal Synthesis of metal oxide nanoparticles in supercritical water. Materials 2010;3:3794–817. https://doi.org/10.3390/ma3073794.

[10] Jaji ND, Othman MBH, Lee HL, Hussin MH, Hui D. One-pot solvothermal synthesis and characterization of highly stable nickel nanoparticles. Nanotechnol Rev 2021;10:318–29. https://doi.org/10.1515/ntrev-2021-0019.

[11] Tsuzuki T. Mechanochemical synthesis of metal oxide nanoparticles. Commun Chem 2021;4. https://doi.org/10.1038/s42004-021-00582-3.

[12] Kaempfe P, Lauth VR, Halfer T, Treccani L, Maas M, Rezwan K. Micromolding of calcium carbonate using a bio-inspired, coacervation-mediated process. Journal of the American Ceramic Society 2013;96:736–42. https://doi.org/10.1111/jace.12194.

[13] Bungenberg De Jong HG, Kruyt HR. Coacervation (partial miscibility in colloid systems). Proc K Ned Akad Wet 1929;32:849–856.

[14] Booij HL, Bungenberg de Jong HG. Colloid Systems. Biocolloids and their Interactions, Vienna: Springer Vienna; 1956, p. 8–14. https://doi.org/10.1007/978-3-7091-5456-4_2.

[15] Moulik SP, Rakshit AK, Pan A, Naskar B. An Overview of Coacervates: The Special Disperse State of Amphiphilic and Polymeric Materials in Solution. Colloids and Interfaces 2022;6. https://doi.org/10.3390/colloids6030045.

[16] Ou Z, Muthukumar M. Entropy and enthalpy of polyelectrolyte complexation: Langevin dynamics simulations. Journal of Chemical Physics 2006;124. https://doi.org/10.1063/1.2178803.

[17] Veis A. A review of the early development of the thermodynamics of the complex coacervation phase separation. Adv Colloid Interface Sci 2011;167:2–11. https://doi.org/10.1016/j.cis.2011.01.007.

[18] Arnold R. The titration of polymeric acids. J Colloid Sci 1957;12:549–56. https://doi.org/10.1016/0095-8522(57)90060-0.

[19] Swift T, Swanson L, Geoghegan M, Rimmer S. The pH-responsive behavior of poly(acrylic acid) in aqueous solution is dependent on molar mass. Soft Matter 2016;12:2542–9. https://doi.org/10.1039/c5sm02693h.

[20] Overbeek JTG, Voorn MJ. Phase separation in polyelectrolyte solutions. Theory of complex coacervation. J Cell Comp Physiol 1957;49:7–26. https://doi.org/10.1002/jcp.1030490404.

[21] Chollakup R, Smitthipong W, Eisenbach CD, Tirrell M. Phase behavior and coacervation of aqueous poly(acrylic acid)-poly(allylamine) solutions. Macromolecules 2010;43:2518–28. https://doi.org/10.1021/ma902144k.

[22] Zhang P, Wang ZG. Interfacial Structure and Tension of Polyelectrolyte Complex Coacervates. Macromolecules 2021;54:10994–1007. https://doi.org/10.1021/acs.macromol.1c01809.

[23] Kleber D. Complex Coacervates as Confined Microenvironments for Controlled Inorganic Crystallization 2019:59.

[24] Fan Y, Wang Y. Applications of small-angle X-ray scattering/small-angle neutron scattering and cryogenic transmission electron microscopy to understand self-assembly of surfactants. Curr Opin Colloid Interface Sci 2019;42:1–16. https://doi.org/10.1016/j.cocis.2019.02.011.

[25] Lauth V, Maas M, Rezwan K. Coacervate-directed synthesis of CaCO3 microcarriers for pH-responsive delivery of biomolecules. J Mater Chem B 2014;2:7725–31. https://doi.org/10.1039/c4tb01213e.

[26] Koppel DE. Analysis of macromolecular polydispersity in intensity correlation spectroscopy: The method of cumulants. J Chem Phys 1972;57:4814–20. https://doi.org/10.1063/1.1678153.

[27] Frisken BJ. Revisiting the method of cumulants for the analysis of dynamic light-scattering data. Appl Opt 2001;40:4087. https://doi.org/10.1364/AO.40.004087.

[28] Provencher SW. Contin: A general purpose constrainded regularization program for inverting noisy linear algebraic and integral equations. Comput Phys Commun 1984;35:C-818-C–819. https://doi.org/10.1016/S0010-4655(84)82935-5.

[29] Provencher SW. A constrained regularization method for inverting data represented by linear algebraic or integral equations. Comput Phys Commun 1982;27:213–27. https://doi.org/10.1016/0010-4655(82)90173-4.

[30] Hollemann AF, Wiberg E. Lehrbuch der Anorganischen Chemie. 103rd ed. New York, NY: Walter de Gruyter & Co.; 2017.

[31] Ali S, Bleuel M, Prabhu VM. Lower Critical Solution Temperature in Polyelectrolyte Complex Coacervates. ACS Macro Lett 2019;8:289–93. https://doi.org/10.1021/acsmacrolett.8b00952.

[32] Kayitmazer AB, Koksal AF, Kilic Iyilik E. Complex coacervation of hyaluronic acid and chitosan: Effects of pH, ionic strength, charge density, chain length and the charge ratio. Soft Matter 2015;11:8605–12. https://doi.org/10.1039/c5sm01829c.

[33] Kayitmazer AB, Bohidar HB, Mattison KW, Bose A, Sarkar J, Hashidzume A, et al. Mesophase separation and probe dynamics in protein-polyelectrolyte coacervates. Soft Matter 2007;3:1064–76. https://doi.org/10.1039/b701334e.

[34] Irving H, Williams RJP. 637. The stability of transition-metal complexes. Journal of the Chemical Society (Resumed) 1953;3245:3192. https://doi.org/10.1039/jr9530003192.

[35] Kolthoff IM. The solubilities and solubility products of metallic sulfides in water. Journal of Physical Chemistry 1931;35:2711–21. https://doi.org/10.1021/j150327a019.

[36] Estay H, Barros L, Troncoso E. Metal sulfide precipitation: Recent breakthroughs and future outlooks. Minerals 2021;11. https://doi.org/10.3390/min11121385.

[37] Pokrovsky OS, Schott J. Surface chemistry and dissolution kinetics of divalent metal carbonates. Environ Sci Technol 2002;36:426–32. https://doi.org/10.1021/es010925u.

[38] Spanos N, Koutsoukos PG. Kinetics of Precipitation of Calcium Carbonate in Alkaline pH at Constant Supersaturation. Spontaneous and Seeded Growth. J Phys Chem B 1998;102:6679–84. https://doi.org/10.1021/jp981171h.

[39] Blocher McTigue WC, Voke E, Chang LW, Perry SL. The benefit of poor mixing: Kinetics of coacervation. Physical Chemistry Chemical Physics 2020;22:20643–57. https://doi.org/10.1039/d0cp03224g.

[40] Gupta A, Bohidar HB. Kinetics of phase separation in systems exhibiting simple coacervation. Phys Rev E Stat Nonlin Soft Matter Phys 2005;72. https://doi.org/10.1103/PhysRevE.72.011507.

[41] Koehler JM, Visaveliya N, Knauer A. Controlling formation and assembling of nanoparticles by control of electrical charging, polarization, and electrochemical potential. Nanotechnol Rev 2014;3:553–68. https://doi.org/10.1515/ntrev-2014-0006.

[42] Vekilov PG. Nucleation 2010;10:5007–19. https://doi.org/10.1021/cg1011633.

[43] Jun YS, Zhu Y, Wang Y, Ghim D, Wu X, Kim D, et al. Classical and Nonclassical Nucleation and Growth Mechanisms for Nanoparticle Formation. Annu Rev Phys Chem 2022;73:453–77. https://doi.org/10.1146/annurev-physchem-082720-100947.

[44] Rempel JY, Bawendi MG, Jensen KF. Insights into the Kinetics of Semiconductor Nanocrystal Nucleation and Growth 2009;69:4479–89.

[45] Dahirel V, Jardat M. Effective interactions between charged nanoparticles in water: What is left from the DLVO theory? Curr Opin Colloid Interface Sci 2010;15:2–7. https://doi.org/10.1016/j.cocis.2009.05.006.

[46] Kim CR, Uemura T, Kitagawa S. Inorganic nanoparticles in porous coordination polymers. Chem Soc Rev 2016;45:3828–45. https://doi.org/10.1039/c5cs00940e.

[47] Franconetti A, Carnerero JM, Prado-Gotor R, Cabrera-Escribano F, Jaime C. Chitosan as a capping agent: Insights on the stabilization of gold nanoparticles. Carbohydr Polym 2019;207:806–14. https://doi.org/10.1016/j.carbpol.2018.12.046.

[48] Dobrynin A V., Rubinstein M. Theory of polyelectrolytes in solutions and at surfaces. Progress in Polymer Science (Oxford) 2005;30:1049–118. https://doi.org/10.1016/j.progpolymsci.2005.07.006.

[49] Fan C, Chen J, Chen Y, Ji J, Teng HH. Relationship between solubility and solubility product: The roles of crystal sizes and crystallographic directions. Geochim Cosmochim Acta 2006;70:3820–9. https://doi.org/10.1016/j.gca.2006.06.011.

[50] LaMer VK, Dinegar RH. Theory, Production and Mechanism of Formation of Monodispersed Hydrosols. J Am Chem Soc 1950;72:4847–54. https://doi.org/10.1021/ja01167a001.

[51] Becker R, Döring W. Kinetische Behandlung der Keimbildung in übersättigten Dämpfen. Ann Phys 1935;416:719–52. https://doi.org/10.1002/andp.19354160806.

[52] Gibbs JW. The collected works of J. Willard Gibbs. 2nd ed. New York: Longmans, Green and Co.; 1928.

[53] Gebauer D, Raiteri P, Gale JD, Cölfen H. On classical and non-classical views on nucleation. Am J Sci 2018;318:969–88. https://doi.org/10.2475/09.2018.05.

[54] Lei Z, Sun S, Wu P. Ultrafast, Scale-Up Synthesis of Pure and Stable Amorphous Carbonate Mineral Nanoparticles. ACS Sustain Chem Eng 2017;5:4499–504. https://doi.org/10.1021/acssuschemeng.7b00313.

[55] Sun Y, Zhu L, Wu T, Cai T, Gunn EM, Yu L. Stability of amorphous pharmaceutical solids: Crystal growth mechanisms and effect of polymer additives. AAPS Journal 2012;14:380–8. https://doi.org/10.1208/s12248-012-9345-6.

[56] M. Aguilar N, Perez-Aguilar JM, González-Coronel VJ, Soriano Moro JG, Sanchez-Gaytan BL. Polymers as Versatile Players in the Stabilization, Capping, and Design of Inorganic Nanostructures. ACS Omega 2021;6:35196–203. https://doi.org/10.1021/acsomega.1c05420.

[57] Madkour M, Bumajdad A, Al-Sagheer F. To what extent do polymeric stabilizers affect nanoparticles characteristics? Adv Colloid Interface Sci 2019;270:38–53. https://doi.org/10.1016/j.cis.2019.05.004.

[58] Gorna K, Muñoz-Espí R, Gröhn F, Wegner G. Bioinspired mineralization of inorganics from aqueous media controlled by synthetic polymers. Macromol Biosci 2007;7:163–73. https://doi.org/10.1002/mabi.200600209.

[59] Lide DR. CRC Handbook of Chemistry and Physics. Boca Raton, FL, USA: 2005.

6.7 Supporting Information

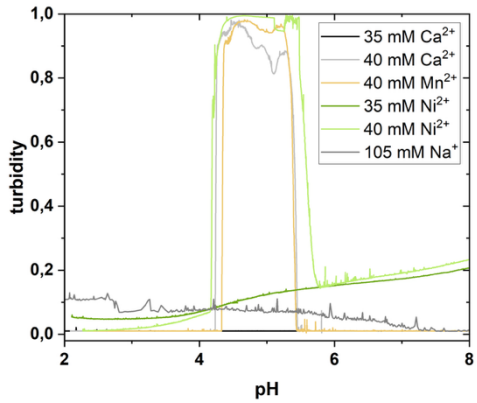


Figure SVI-1. Titration of a solution of 1w% 100k PAA / 40mM MCl_2 with 1M NaOH with continuous measurements of pH and turbidity at $\lambda = 660$ nm. The concentration of PAA and MCl_2 was held constant by titrating a solution of 2w% 100k PAA / 80mM MCl_2 in the same volumetric amounts as the NaOH. Note that the increase in "turbidity" for Ni^{2+} comes due to absorption of the AA/Ni^{2+} complex at $\lambda = 660$ nm.

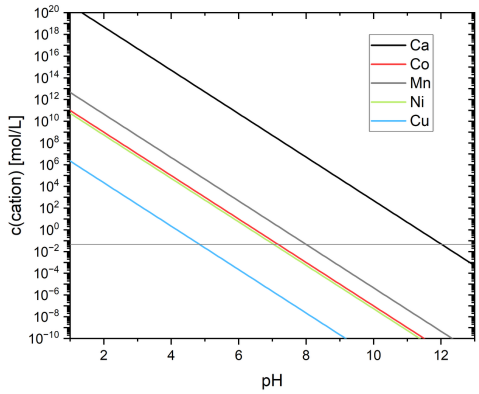


Figure SVI-2. Solubility products of the tested cation (Ca^{2+}, Co^{2+}, Mn^{2+}, Ni^{2+}, Cu^{2+}) hydroxides against the pH. The reference line indicates the threshold concentration of the cation for coacervate formation. Note that the threshold concentration for PAA/Cu^{2+} coacervates is lower than for the others, and the reference line represents only the other cations. Extracted pH values are: pH(Ca^{2+}) = 12, pH(Co^{2+}) = 7.2, pH(Mn^{2+}) = 8, pH(Ni^{2+}) = 7, pH(Cu^{2+}) = 4.8.

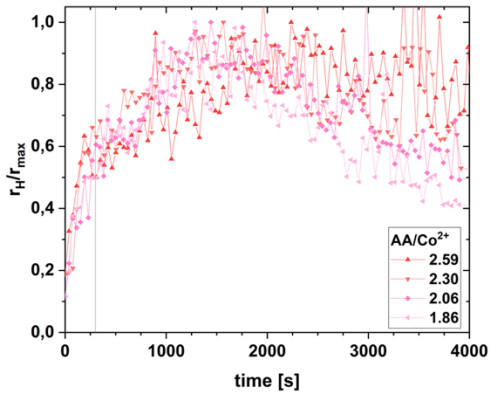


Figure SVI-3. Aggregation and coalescence/precipitation kinetic of freshly prepared Co-coacervates as shown in Figure 4c. Typical DLS-measurements were measured in the first 300s. Note that no coacervate sizes are given in this figure but a r_H/r_{max} ratio to show the coalescence rates independend of actual size. Hydrodynamic radii (r_H) were determined using Cumulants analysis on DLS measurements of coacervate droplet suspensions at different AA/Co^{2+} ratios every 30s for at least 1h. r_{max} represents the maximum value for hydrodynamic radius observed in this timeframe. The increase in droplet size does not stagnate after 1000s but the sedimentation of the coalesced droplets removes the largest droplets from measurable solution, seemingly decreasing the droplet size again.

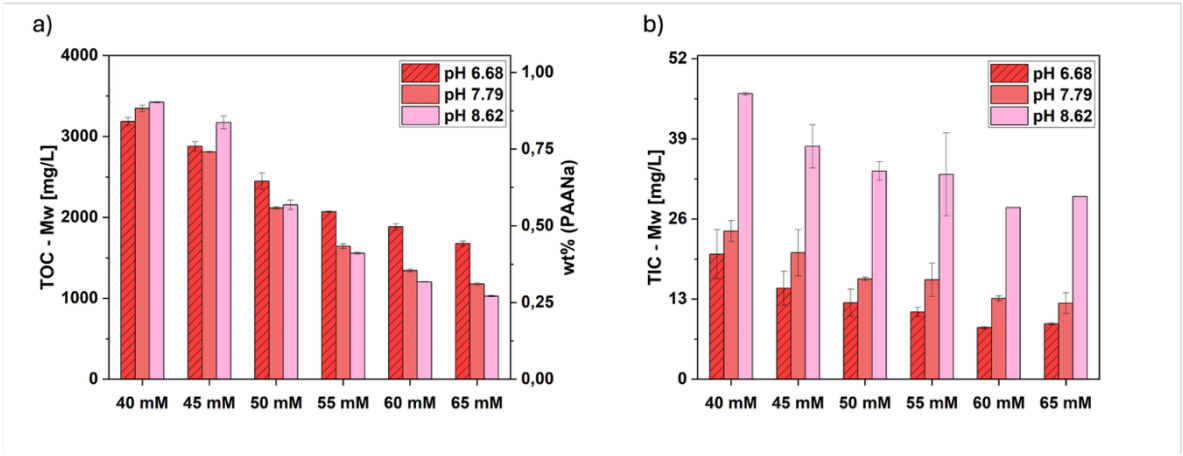


Figure SVI-4. Total organic carbon (a) and total inorganic carbon (b) of the supernatants shown in **Figure VI-5a**. Also visible in a is the calculated wt% of remaining PAA in the supernatant.

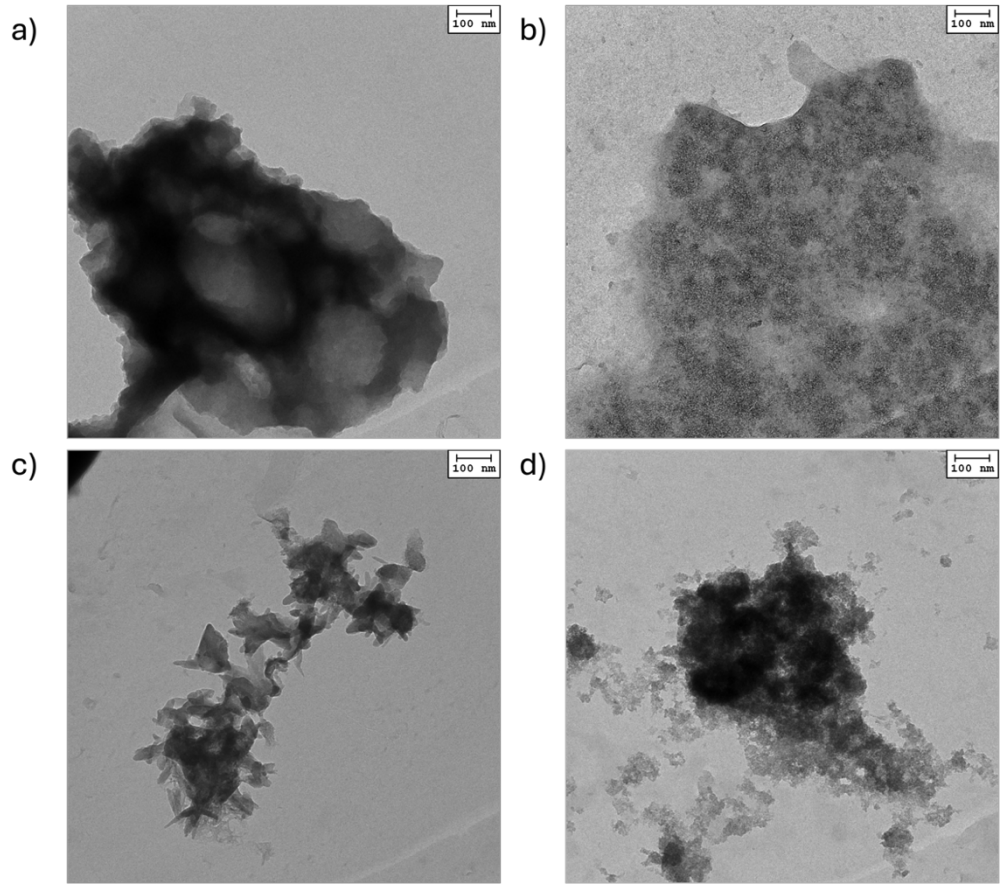


Figure SVI-5. TEM micrographs, at a magnification of 1:13000, of particles derived from PAA^{-}/Co^{2+} coacervates at pH 5.45 (a) $MnCO_3$. b) CoS) and TEM micrographs of particles derived from unsupported precipitation of c) $CoCO_3$ and d) CoS.

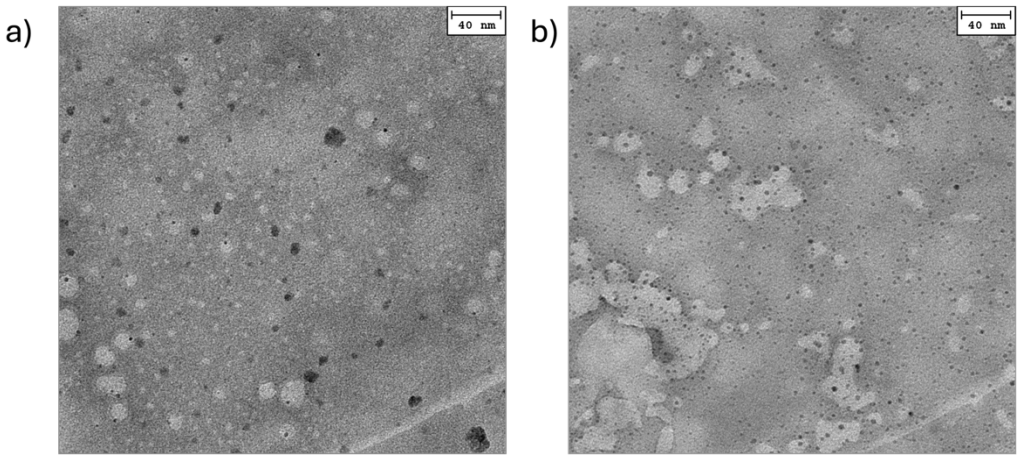


Figure SVI-6. TEM micrograph of $CoCO_3$ particles derived from PAA^{-}/Co^{2+} mixtures at different ratios. a) AA/Co^{2+} ratio of 2.65, just below the treshold concentration. B) AA/Co^{2+} ratio of 1.33, way above the treshold concentration.

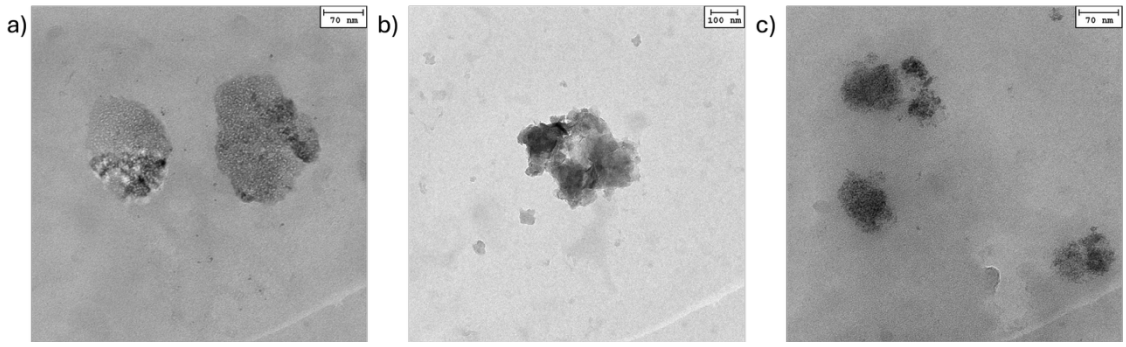


Figure SVI-7. TEM micrograph of particles derived from PAA^{-}/Co^{2+} coacervates at pH 5.45. a) $CoCO_3$, 1:28000. b) CoO derived from $CoCO_3$ after calcination at 650°C, 1:13000. c) CoS, 1:28000.

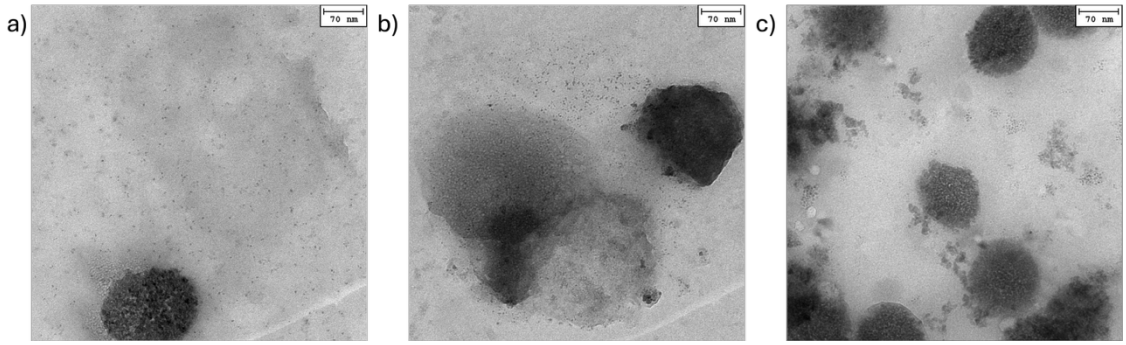


Figure SVI-8. TEM micrograph of particles derived from PAA^{-}/Mn^{2+} coacervates at pH 5.45. a) $MnCO_3$. b) MnO derived from $MnCO_3$ after calcination at 650°C. c) MnS. Magnification of 1:28000.

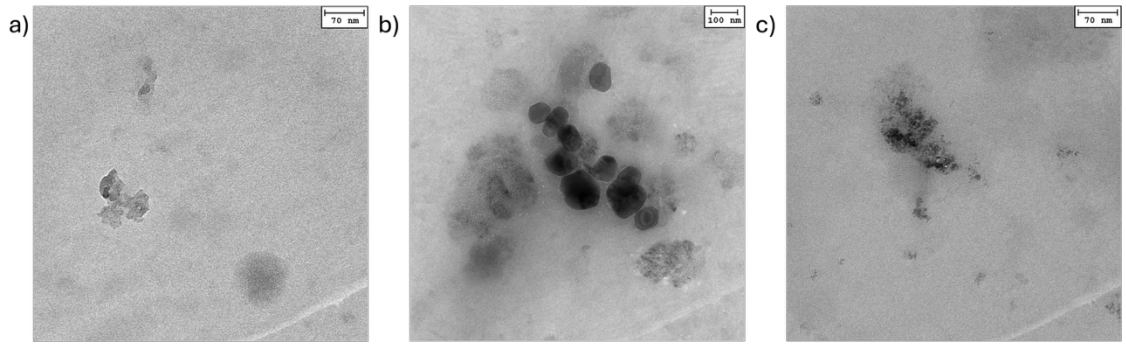


Figure SVI-9. TEM micrograph of particles derived from PAA^{-}/Ni^{2+} coacervates at pH 5.45. a) $NiCO_3$, 1:28000. b) NiO derived from $NiCO_3$ after calcination at 650°C, 1:13000. c) NiS, 1:28000.

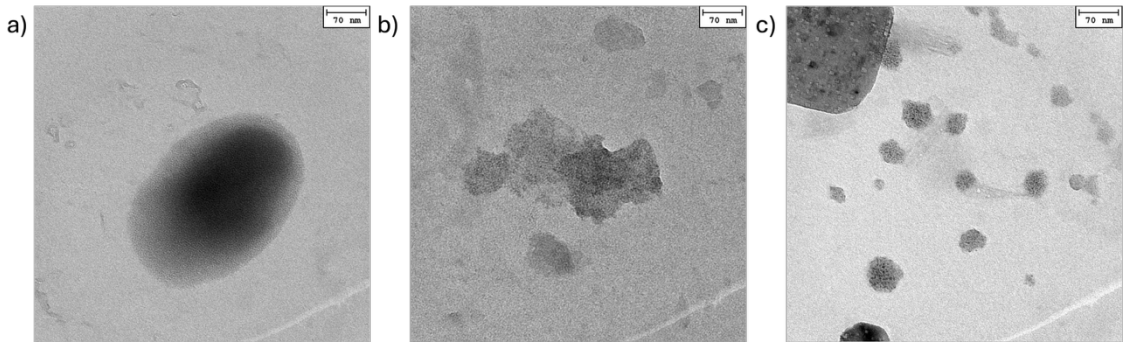


Figure SVI-10. TEM micrograph of different PAA^{-}/M^{2+} coacervates at a magnification of 1:28000. a) M = Ca. b) M = Co. c) M = Cu, note that the cubic structure in the top left corner is NaCl residue left from synthesis.

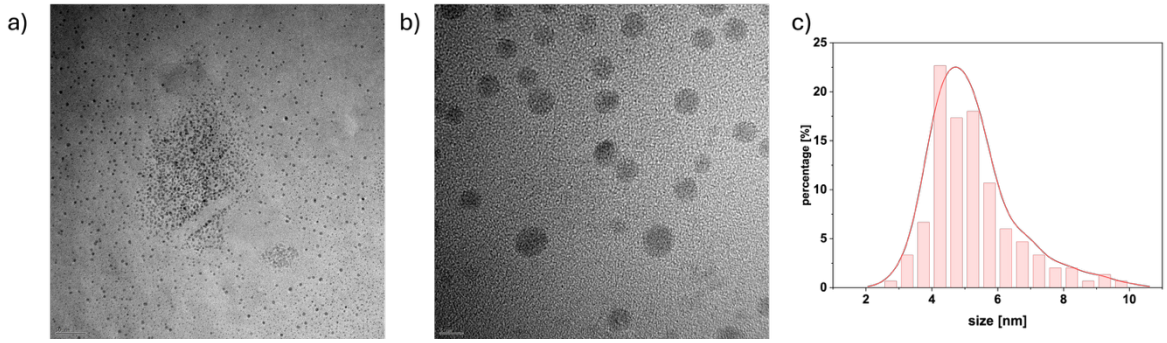


Figure SVI-11. High resolution TEM micrograph of particles synthesized at AA/M^{2+} of around 1.3. (a) and (b) $CoCO_3$ with scale bars of 50 and 2 nm in length, respecitvely. (c) Histogramm derived from particles measured in HRTEM micrographs as shown in (a) and (b). The particles show an average diameter of 5.27 +- 1.41 nm (n = 152), corresponding to a coefficient of variation of 0.27, indicating moderate polydispersity.

Table SVI-1. Mean radius (r) determined from TEM micrographs like those shown in **Figure SVI-7**, **Figure SVI-8**, and **Figure SVI-9 f**or nanoparticles of different metal cations with different anions. Carbonate and sulfide samples were obtained via from coacervate-forming solutions at pH 7 for Mn^{2+} and Co^{2+}, at pH 8 for Ni^{2+}, and pH 4 for Cu^{2+}. Oxide particles were formed upon calcination of their carbonate counterparts. For each system, a statistically relevant number (n>50) of nanoparticles was analyzed, giving a reliable mean radius with corresponding standard deviations. Because of different morphologies, these particles can be separated by different sizes. Also shown, are the particle and aggregate sizes determined by dynamic light scattering. Average diameters were derived from the DLS data using the cumulants method [26] and the CONTIN algorithm [28,29], which gives apparent sizes for both the primary particles and their aggregates. The values (r_H < 2 nm) derived from CONTIN correspond to remains of the used PAA in the synthesis. Note that for the cumulants analysis, the first value depicts the suspension as it is, whereas the second value is created after filtration using a 200 nm CA membrane.

Particle	**r [nm] / TEM**	**r_H [nm] / DLS(Cumulants)**	**r_H [nm] / DLS(CONTIN)**
$CoCO_3$	5.27 ± 1.41 31.99 ± 9.69 171.85 ± 48.79	118.97 ± 79.53 (PD.I. 0.447) 32.61 ± 23.57 (PD.I. 0.522)	0.927 (0.7%) 3.63 (11.2%) 32.6 (45.1%) 388 (40%)

CoO	12.09 ±4.24 35.62 ± 11.47 351.08 ± 35.75	1379.21 ± 829.8 (PD.I. 0.362) 60.75 ± 28.68 (PD.I. 0.223)	3.75 (0.4%) 54.1 (71.6%) 427 (22.2%)
CoS	2.70 ± 0.60 63.19 ± 18.81 126.36 ± 21.99	214.25 ± 72.63 (PD.I. 0.115) 69.09 ± 41.24 (PD.I. 0.356)	4 (1.3%) 61.5 (66.6%) 414 (30.2%)
$MnCO_3$	3.95 ± 0.97 38.58 ± 15.02 143 ± 17.93	143.08 ± 89.65 (PD.I. 0.393) 100.01 ± 64.96 (PD.I. 0.422)	1.93 (0.7%) 67.6 (48%) 427 (47.7%)
MnO	5.58 ± 2.73 188.81 ± 55.35	519 ± 361.21 (PD.I. 0.483) 2003.06 ± 1177.4 (PD.I. 0.346)	16.2 (16.4%) 441 (83.6%)
MnS	7.36 ± 4.31 19.65 ± 4.03 129.81 ± 17.22	130.32 ± 88.72 (PD.I. 0.463) 57.99 ± 27.89 (PD.I. 0.231)	0.843 (0.03%) 29.6 (19%) 95.5 (76.7%)
$NiCO_3$	39.29 ± 10.78 247.62 ±124.78	99.47 ± 69.22 (PD.I. 0.484) 42.4 ± 30.03 (PD.I. 0.502)	1.09 (0.9%) 6.24 (8.8%) 55.9 (58.7%) 364 (28.5%)
NiO	73.81 ± 15.93 139.09 ± 44.41	222 ± 134.26 (PD.I. 0.366) 77.88 ± 30.18 (PD.I. 0.15)	79.2 (84.3%) 414 (11.7%)
NiS	9.17 ± 5.08 98.87 ± 12.23	139.9 ± 36.02 (PD.I. 0.0663) 41.87 ± 19.74 (PD.I. 0.222)	0.957 (0.3%) 4.69 (0.4%) 54.1 (94.1%) 353 (1.1%)
$CuCO_3$		5723.56 ± 3475.32 (PD.I. 0.369) 35.68 ± 27.06 (PD.I. 0.575)	1.23 (10.1%) 7.31 (19.9%) 441 (73.6%)
CuO		419.24 ± 165.74 (PD.I. 0.156) 6145.34 ± 3666.75 (PD.I. 0.356)	/
CuS		220.1 ± 137.03 (PD.I. 0.388) 234.44 ± 150.99 (PD.I. 0.415)	/

Table SVI-2. Calculation of the critical nucleation barrier ΔG^* and the used parameters for the different particles. K_{sp} and ρ values were taken from [30,35,59]. The concentration used for calculation represents a AA/Co^{2+} ratio of 1.33. In general, the concetration and the critical nucleation barrier ΔG^* are linked by $\Delta G^* \sim \frac{1}{(2lnc - lnK_{SP})^2}$.

Particle	K_{sp} [mol^2/L^2]	ln(S)	v_M / N_A [10^{-29} m^3]	r^* [nm]	ΔG^* [10^{-20} J]	ΔG^* / k_BT
CoS	$4.00*10^{-21}$	41.65	2.78	0.06	0.35	0.86
$CoCO_3$	$1.40*10^{-13}$	24.28	4.80	0.19	3.10	7.53
MnS	$3.00*10^{-14}$	25.82	3.63	0.14	1.57	3.82
$MnCO_3$	$1.80*10^{-11}$	19.42	5.18	0.26	5.63	13.69
NiS	$3.00*10^{-19}$	37.33	2.58	0.07	0.38	0.92
$NiCO_3$	$6.60*10^{-9}$	13.52	4.51	0.32	8.80	21.41
CuS	$6.00*10^{-37}$	78.09	3.35	0.04	0.15	0.35
$CuCO_3$	$1.40*10^{-10}$	17.37	5.15	0.29	6.96	16.92

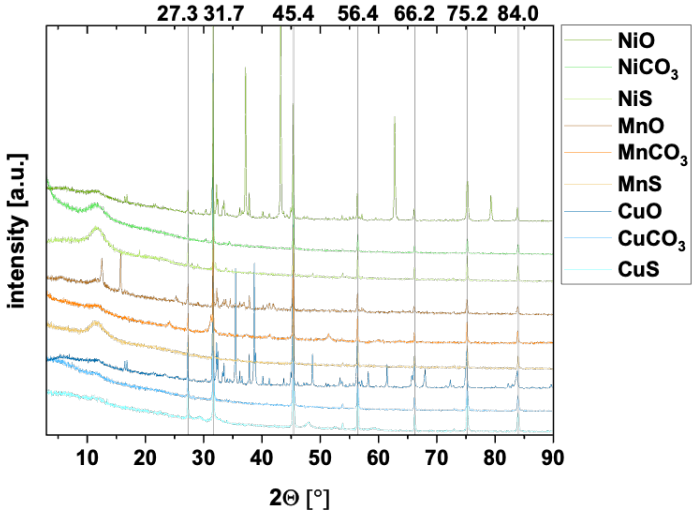


Figure SVI-12. XRD spectra of sulfide/carbonate/oxide particles derived from PAA/M^{2+} coacervates for different cations. The visible reference lines and the reflexes visible in all spectra correspond to the crystal structure of NaCl residues. Also, visible the broad reflex expressing the presence of amorphous substance for $MnCO_3$, MnS, $NiCO_3$, and NiS. It is also slightly visible for $CuCO_3$ and CuS, but due to the synthesis at lower pH and therefore less produced particles, it is less expressed. For the calcinated carbonates reflexes appear and the intensity of the amorphous reflex decreases indicating the formation of ordered crystal structures.

General Conclusion and Outlook

Across the systems investigated in this thesis, namely, surfactant-free ternary mixtures for silica synthesis, coupled precipitation of transition metal carbonates and sulfides within silica matrices, ligand-controlled coprecipitation of semiconductor sulfides, and polyelectrolyte–metal coacervates as templates for transition metal sulfides and carbonates, nanoparticle formation was consistently governed by a limited set of kinetic parameters rather than by the complexity of the synthetic protocol. In all cases, particle size, composition, and functional performance were determined by the rate and spatial availability of reactive species for nucleation and growth. Exploiting this kinetic bottleneck enables precise particle control using straightforward, water-based chemistry under ambient conditions.

Interfacial and diffusive mass transport emerged as a key parameter in the investigation of surfactant-free microemulsions (SFMEs) for Stöber-type silica synthesis (**Chapter II**). The ternary H_2O / EtOH / TEOS system remained molecularly dispersed rather than forming SFME aggregates, resulting in particle formation that followed conventional Stöber kinetics. However, employing high water content and low ammonia concentration produced highly monodisperse silica particles in the low-nanometer range, with regrowth steps enabling straightforward size control under significantly greener conditions than classical Stöber synthesis. In contrast, genuine SFME systems containing more hydrophobic oils, such as toluene or 1-octanol, exhibited pronounced mesoscale structuring in the pre-Ouzo and bicontinuous regions. In these systems, diffusion of hydrolyzed silica species across the SFME interphase was identified as the rate-determining step, resulting in an induction period followed by three-stage growth (nucleation burst, rapid growth, and slow subsequent growth) and particle sizes ranging from a few to several hundred nanometers, depending on the oil and microstructure. This establishes interphasial transport, rather than templating, as the operative control parameter in these compartmentalized environments.

A related yet chemically distinct kinetic coupling governs the spontaneous, one-pot coprecipitation of transition-metal carbonates and sulfides within silica matrices (**Chapter III**). In this process, particle growth is self-limiting: the formation of metal carbonate or sulfide nuclei locally decreases the pH, which in turn drives the condensation of dissolved silicate species into an encapsulating amorphous silica shell. As this process is regulated by pH, silicate speciation, and condensation kinetics rather than equilibrium alone, the thickness and permeability of the resulting shell—and thus the accessibility of the encapsulated core—can be directly tuned through reaction conditions. The synthesis demonstrated robustness against

various external influences, including the addition of different compounds. Even when transitioning to diffusion-dominated transport regimes using microfluidic reactors, only minor changes in particle properties were observed.

The practical significance of controlling particle properties was demonstrated using iron oxide/silica particles as heterogeneous Fenton-like catalysts at circumneutral pH (**Chapter IV**). Catalytic performance depended on a balance between colloidal stabilization and iron-site accessibility determined by the silica shell. Performance was influenced more by the used iron precursor and site accessibility than by surface area alone. Further tuning was achieved through partial shell removal or modification of silica condensation conditions. With iron leaching remaining below 0.5% under most conditions, these catalysts achieved performance comparable to, or exceeding, that of considerably more elaborate multistep systems. These findings demonstrate that kinetically controlled, one-pot aqueous synthesis can match or surpass the benchmarks established by more complex synthetic routes.

Precursor complex stability and ligand-mediated surface passivation constituted a third, chemically distinct approach to kinetic control, as applied to the synthesis of transition metal sulfide nanoparticles via coupled coprecipitation (**Chapter V**). Complex stability primarily regulated the concentration of free metal ions and, consequently, nucleation, while ligand-mediated surface passivation governed subsequent growth and the coupling of the resulting quantum dots to silica condensation. Cysteine exhibited the strongest effect, stabilizing particle growth within the quantum dot size range due to its high affinity for both metal ions and sulfide surfaces. However, this strong passivation limited coupling to silica. The combination of cysteine with a second amino acid ligand partially mitigated this limitation and improved coprecipitation efficiency without significantly altering the size or optical properties of the resulting particles. Alloying with zinc enabled further bandgap tuning, producing the expected blue shift, while ligand chemistry continued to dominate nucleation and growth. Collectively, these results indicate that precursor speciation and surface chemistry, rather than nominal synthesis parameters alone, are the primary levers for rational control in this class of systems.

Confinement within a soft, non-templating matrix represented a fourth kinetic parameter, achieved through liquid–liquid phase separation of polyacrylic acid (PAA) and transition-metal cations into coacervates (**Chapter VI**). Coacervation, driven by metal-ion bridging of deprotonated carboxylate groups and hydrogen bonding among partially protonated PAA chains, occurred above a threshold cation concentration across a broad pH range and was applicable to calcium, Co^{2+}, Mn^{2+}, Ni^{2+}, and Cu^{2+}. However, Cu^{2+} was more restricted by competing hydroxide formation at higher pH. Confinement of metal ions within the coacervate

phase reduced their effective chemical potential. Mineralization of the coacervates produced carbonate, sulfide, and oxide nanoparticles of only a few nanometers, consistently smaller than those obtained by unsupported precipitation. The observed size difference between sulfides and carbonates could be directly explained by classical nucleation theory (CNT).

Collectively, these four studies demonstrate that the diverse chemistries examined in this thesis are best interpreted as manifestations of a common underlying principle. Once the rate-limiting step of a nanoparticle-forming reaction, such as interfacial diffusion, pH-coupled condensation, complex dissociation, or confinement-induced changes in chemical potential, is accurately identified, it can serve as a deliberate and quantitative parameter for particle control, even in simple aqueous, ambient-temperature systems. This perspective reframes nanoparticle synthesis, at least for the systems studied here, from a predominantly empirical process of optimizing individual protocol parameters to a more predictive approach grounded in reaction kinetics.

These conclusions should be considered in light of certain limitations. The focus on mild, water-based synthesis necessarily entails some loss of fine-grained size and shape control compared to more elaborate high-temperature or organic-phase methods. Several materials produced in this work still require system-specific optimization before they can be deemed application-ready. Functional testing has thus far been restricted to model reactions and laboratory-scale conditions, most notably phenol degradation as a probe for Fenton-like activity. The performance of these materials in more complex, application-relevant matrices remains to be determined. Nevertheless, the results for the Fenton catalyst indicate that this trade-off is not inevitable. A kinetically well-understood, simple synthesis was able to match or surpass materials produced by considerably more complex methods.

The kinetic framework developed in this thesis suggests several avenues for future research. Most immediately, the proposed mechanistic models would benefit from more direct, time-resolved validation. Time-resolved dynamic light scattering (DLS) has already provided valuable insights into the induction and growth regimes of the SFME-structured Stöber system. Extending in situ or time-resolved techniques, such as small- and wide-angle X-ray scattering (SWAXS) or in situ DLS/SWAXS measurements, to the coupled coprecipitation and coacervate systems would enable direct testing of the proposed nucleation and growth mechanisms, rather than relying solely on ex situ or endpoint characterization.

A second direction involves systematically expanding the parameter space within each system. For SFME-based synthesis, comparing multiple genuinely SFME-forming ternary systems at equivalent R and S values would clarify the generality of the oil-dependent size and shape

control observed for toluene and 1-octanol. In the ligand-controlled synthesis, broadening the range of mixed-ligand combinations and independently varying absolute ligand concentration, rather than composition alone, may enable independent tuning of nucleation and surface passivation, as suggested but not fully achieved by the present results. For the coacervate system, direct measurement of local ion concentration and transport within the coacervate phase would provide a more precise understanding of the nucleation process than the largely indirect evidence currently available.

A third direction involves integrating these mechanistic insights with predictive models of precursor speciation and reaction kinetics, thereby moving beyond the case-by-case rationalization achieved in this work toward the development of quantitative, transferable design rules. For example, employing solubility products and complex stability constants to predict achievable particle sizes a priori would build upon the observed agreement between sulfide/carbonate size trends and classical nucleation theory (CNT).

Finally, advancing these materials toward practical application will require testing beyond the model systems employed in this study. For the Fenton-like catalysts specifically, evaluating performance in more complex, application-relevant water matrices and under continuous-flow operation, including the effects of competing inorganic and organic constituents, will be essential for assessing real-world viability. Given the amorphous structure and small size of several materials produced in this thesis, extending functional testing beyond Fenton chemistry to other catalytic, electrocatalytic, and energy-related applications constitutes a logical and promising next step.

Collectively, these future directions share a common objective: transitioning from empirical, system-specific optimization that has historically characterized nanoparticle synthesis toward a kinetically based, transferable framework for the design of simple, sustainable, and precisely tunable nanomaterials.

Appendix

List of Figures

Figure I-1. Scale of NPs with some examples for size comparison. Reprinted with permission from ref [12]. 1

Figure I-2. (a) Change in Gibbs free energy $\boldsymbol{\Delta G}$ for nucleation as a function of radius ($\boldsymbol{r}$) for homogeneous nucleation (blue line) and heterogeneous nucleation (red line) according to CNT. The curves show a maximum free energy ($\boldsymbol{\Delta G}$) at the critical radius $\boldsymbol{rc}$. (b) Schematic representation of the diffusion layer on the surface of forming nuclei. The plot represents the concentration as a function of distance from the surface. After a distance of r + δ the concentration of the bulk phase is reached [36]. 4

Figure I-3. (a) Schematic DLVO plot of potential energy against the distance of two particles, showing the attractive van der Waals forces (green), the repulsive double layer forces (red), and the resulting total interaction at differing ionic strengths (blue). (b) Dependence of the Debye screening length $\boldsymbol{\kappa - 1}$ on the ionic strength $\boldsymbol{I}$. 6

Figure I-4. Schematic representation of the ion association around charged particles in electrolyte solution. Visualization of the moving particle with its corona and differentiation between surface charge and zeta potential. 7

Figure I-5. Osmotic pressure and elastic repulsive forces caused by polymer coatings. 8

Figure I-6. The principle of NP nucleation due to LaMer's mechanism based on CNT. The curve describes the monomer concentration as function of time. 9

Figure I-7. (a) Surface-to-volume ratio for small particles with an estimated surface layer thickness of 0.5 nm. (b) Quantum confinement model for particles smaller than the materials Bohr exciton radius. ... 12

Figure II-1. Graphical Abstract: The oil-rich domains of the SFME act as precursor reservoirs, while the transport into water-rich domains across the ethanol-rich interphase regulates silicate monomer availability and thereby nanoparticle nucleation and growth. 23

Figure II-2. (a) Ball and stick model, showing the tetrahedral coordination of silicon (grey) with oxygen (red), (b) space-filling model based on packed spheres for the silica tetrahedron, (c) solid tetrahedron model, (d) two-dimensional representation of Si$\boldsymbol{O44-}$ tetrahedra packing for crystalline silica, (e) and for amorphous/random packing, (f) two-dimensional representation of fully hydroxylated silica colloid. For amorphous silica, the bond angles may vary, but the Si-O distances are constant, and oxygen is linked to no more than two silicon atoms. Reproduced with permission of refs [4,6]. 26

Figure II-3. Mechanism of base (BI) catalyzed hydrolysis (II-2) and condensation (II-5) of tetraalkylorthosilicates (TAOS). 27

Figure II-4. Particle growth diagram during multistage growth by TEOS in water, EtOH, and ammonia medium. Adapted with permission from ref [29]. 30

Figure II-5. Schematic ternary phase diagram for a solution containing water/hydrotrope/oil. The grey domain represents the two-phasic region. Above, one phasic structured phase can be found, like water-rich pre-Ouzo (direct micellar) (blue shade), bicontinuous (green shade), and oil-rich inverse micellar

(orange shade). Further away from the phase boundary, the solution loses self-structuring, resulting in a molecularly dispersed solution. MD simulations show the distribution of pseudo-phases across the different structured regions in the H_2O/EtOH/1-Octanol system, reprinted with permission from ref [43]. 31

Figure II-6. Phase diagrams of the ternary mixture of H_2O / EtOH / TEOS expressed in molar fractions x. The positions in the ternary space of relevant publications on Stöber syntheses were plotted. (a) The highlighted areas correspond to screenings conducted by [1,66–68]. The single points were chosen as all references investigated rather different concentration ranges. [12,14,15,17] (b) The shown references only conducted experiments on a few points within the ternary phase diagram [13,16,19–21,23,24,28,30,31,66,69–76] Note that a majority of the conducted experiments are at reduced water concentrations ($x(H_2O) < 0.5$). This figure can be found in high resolution in the online repository. 33

Figure II-7. Phase diagrams of the ternary mixture of H_2O / EtOH / TEOS expressed in weight percent wt% (a) and molar fraction x (b). The exact fractions of the various points visible in (a) and (b) are given in Table SII-1. 39

Figure II-8. Correlation functions of DLS measurements of the respective points A1, B, B‘, C, and D directly after preparation (a) and after 4 d without stirring (b). The exact compositions of the various points shown in (a) and (b) are given in Table SII-1 and the sizes of the formed particles in Table SII-2. 40

Figure II-9. Phase diagrams of the ternary mixture of H_2O / EtOH / Oil + TEOS expressed in weight percent wt% (a) and molar fraction x (b). The red phase boundary represents 10 vol% TEOS in Toluene and the green phase boundary represents 10 vol% TEOS in 1-Octanol. The exact fractions of the points f, j, g, f‘, j’, and g‘ visible in (a) and (b) are shown in Table SII-3. 42

Figure II-10. (a) Correlation function of DLS measurements of the points f, g, and j and their respective alternated points after a theoretical complete TEOS hydrolysis f‘, g’, and j‘. The points F, G, and J represent the same points without the addition of TEOS. Samples were prepared immediately before the measurement. (b) SWAXS-spectra of the points f, F, g, G, j, and J. The increase at $q < 0.2\ nm^{-1}$ results from the X-ray beam (no beamstop). 43

Figure II-11. Correlation function of multiple DLS measurements during the formation of particles in the ternary mixture H_2O / EtOH / TEOS at point C with the addition of NH_3 as catalyst (a) and a regrowth step after 24h (b). The gradient from yellow (t_0) to purple (t_{end}) visualizes the change of the samples over time. The hydrolysis ratio is R = 92.5 and the solvent ratio is S = 1.7. 44

Figure II-12. Correlation function of multiple DLS measurements during the formation of particles after the addition of NH_3 to (a) f, (b) g, and (c) j. The gradient from yellow (t_0) to purple (t_{end}) visualizes the change of the samples over time. $[TEOS]/[NH_3] = 8.9$. 45

Figure II-13. (a) TEM micrograph of silica particles derived from point C in the H_2O / EtOH / TEOS system at a magnification of 40000x. The scale bar corresponds to 200 nm. (b) TEM micrograph of silica particles derived from point f in the H_2O / EtOH / toluene + TEOS system at a magnification of 6000x. The scale bar corresponds to 1000 nm. (c) TEM micrograph of silica particles derived from point j in the H_2O / EtOH / octanol + TEOS system at a magnification of 40000x. The scale bar corresponds to 200 nm (d) TEM micrograph of silica particles derived from point g in the H_2O / EtOH / octanol + TEOS system at a magnification of 6000x. The scale bar corresponds to 1000 nm. 47

Figure II-14. Proposed mechanism of Stöber particle formation in SFME. The pseudo-oil phase acts as a reservoir for TEOS, which diffuses across the interphase. Hydrolysis and condensation occur in the pseudo-water phase. 49

Figure SII-1. Correlation functions of DLS-measurements of the respective points E, E‘, E’’, and E’’’ directly after preparation. The exact fractions of the various are shown in Table SII-1..... 61

Figure SII-2. (a) SWAXS spectra of a) point B and C in the H_2O/EtOH/TEOS system. The increase at $q < 0.2\ nm^{-1}$ results from the X-ray beam. (b) Visualization of the contrast (ΔSLD^2) in the SWAXS measurements relative to the distribution of the hydrotrope ethanol in the pseudo-phases. The molar fraction x(EtOH) indicates the amount of ethanol in the aqueous pseudo-phase. In this simplified assumption no oil is solubilized in the aqueous pseudo-phase and no water in the oil pseudo-phase. The dashed line at $\Delta SLD^2 = 0.5$ shows the threshold below which the resolution of the SWAXS measurements is questionable. For J/j a value of literature was found to be x(EtOH) = 0.6 [96]..... 62

Figure SII-3. Correlation function of multiple DLS measurements during the formation of particles in the ternary mixture H_2O / EtOH / TEOS at point C (a) without the addition of a catalyst and (b) with arginine as catalyst (b). The gradient from yellow (t_0) to purple (t_{end}) visualizes the change of the samples over time. The hydrolysis ratio R = 92.5 and the solvent ratio S = 1.7. 63

Figure SII-4. Correlation function of multiple DLS measurements during the formation of particles in the ternary mixtures (a) H_2O / EtOH / TEOS at point C, (c) H_2O / EtOH / 1-octanol + TEOS at point g and (d) H_2O / EtOH / toluene + TEOS at point f with the addition of arginine as catalyst. The gradient from yellow (t_0) to purple (t_{end}) visualizes the change of the samples over time. The respective change in hydrodynamic radius over time is shown in (b), (d), and (f). 64

Figure SII-5. Hydrodynamic radius (r_H) derived from time dependent DLS measurements of the point C in the H_2O / EtOH / TEOS ternary mixture with (a) no catalyst and (b) arginine as catalyst. The corresponding correlation functions can be found in Figure SII-3a and Figure SII-3b, respectively..... 65

Figure SII-6. Hydrodynamic radius (r_H) derived from time dependent DLS measurements of the point C in the H_2O / EtOH / TEOS ternary mixture with (a) NH_3 as catalyst ([TEOS]/[NH_3] = 8.9) and (b) further addition of TEOS after reaching equilibria (~24h) in (a). The corresponding correlation functions can be found in Figure II-11a and Figure II-11b, respectively. 65

Figure SII-7. Hydrodynamic radius (r_H) derived from time dependent DLS measurements of the points (a) f in the H_2O / EtOH / toluene+TEOS ternary mixture, (b) g in the H_2O / EtOH / octanol+TEOS pseudo-ternary mixture, and (c) f in the H_2O / EtOH / octanol+TEOS pseudo-ternary mixture with NH_3 as catalyst ([TEOS]/[NH_3] = 8.9). The corresponding correlation functions can be found in **Figure II-12.** The dashed (DLS) and the dotted (calculated) lines correspond to the values shown in Table SII-5. As the exact distribution of ethanol changes as the reaction progresses, only the boundaries of the range, within which the x(EtOH) is most likely, were plotted. 66

Figure SII-8. (a) FFT of the micrograph shown in Figure II-13a. The white circle corresponds to the distance between individual particles giving an estimate for their size between 5.51 nm and 12.81 nm after radial integration. (b) FFT of the micrograph shown in Figure II-13c. The white circle corresponds to the distance between individual particles giving an estimate for their size between 3.53 nm and 7.43 nm after radial integration..... 66

Figure SII-9. Histograms of measured particles from TEM micrographs. (a) 415 particles were measured for g and (b) 1026 particles were measured for f. Corresponding TEM micrographs can be found in Figure II-13b and Figure II-13d. 67

Figure SII-10. Viscosities of various binary mixtures of ethanol and the used solvents in the SFME systems as functions of the molar fraction of ethanol (x(EtOH)). While the value of the water ethanol mixture was measured, the others were taken from literature [97–100]. 67

Figure III-1. Graphical Abstract: The combination of two aqueous solutions results in spontaneous coprecipitation of transition metal sulfides/carbonates and silica resulting in core-shell like aggregates. The precipitate can be centrifuged and lyophilized to obtain nanoparticle powder. 69

Figure III-2. Spontaneous coating of metal carbonate particles (red circles) with shells of amorphous silica (blue rims) as a consequence of local pH gradients (green halos) in alkaline solutions, caused by bicarbonate dissociation and triggering polycondensation of dissolved silicate species (blue shreds) in the immediate vicinity of growing particles. Redrawn according to the concept introduced in ref [27]. 72

Figure III-3. Photographs of samples obtained by mixing equal volumes of 10 mM solutions of $CoCl_2$ and $(NH_4)_2CO_3$, with the latter containing different amounts of dissolved sodium silicate (from left to right): 0, 0.83, 4.99, 11.65, 16.64, 24.97, and 33.29 mM SiO_2. The pH was adjusted to (a) 9.0 and (b) 11.0 after mixing by addition of HCl and NaOH. 82

Figure III-4. TEM micrographs of typical reaction products obtained from mixtures containing 10 mM each of $CoCl_2$, Na_2CO_3 and SiO_2 at native pH. (a) Colloidal aggregates formed by cation-induced condensation of silicate species. (b) Structures of diffuse silica matrix with multiple embedded nanodots. (c) Numerous $CoCO_3$ nanodots (dark spots), partially embedded in diffuse silica matrices (areas of lower contrast), typically found in the near vicinity of the structure shown in (b), indicated by the red arrows. Scale bars: 70 nm and 100 nm, respectively. 83

Figure III-5. ADF-STEM micrographs of nanostructures obtained by mixing equal volumes of 10 mM solutions of $CoCl_2$ and Na_2CO_3, with the latter containing 5 mM SiO_2 at native pH of 10.35. Scale bars: 50 nm. 84

Figure III-6. TEM micrographs of silica-coated nanoparticles of a) $CdCO_3$, b) $CoCO_3$, c) $CuCO_3$, d) $MnCO_3$, e) $NiCO_3$, and f) $ZnCO_3$, obtained by spontaneous coprecipitation from solutions containing 10 mM each of metal chloride, Na_2CO_3, and sodium silicate, at the respective native pH of around 10.5. Scale bars: 50 nm. 85

Figure III-7. TEM micrographs of oxide nanoparticles obtained by calcination of silica-coated precursors of a) $CdCO_3$, b) $CoCO_3$, c) $CuCO_3$, d) $MnCO_3$, e) $NiCO_3$, and f) $ZnCO_3$, as shown in Figure III-6. Note that numerous individual nanodots can be observed across the entire fields of view in (e) and (f). Scale bars: 50 nm. 87

Figure III-8. TEM micrographs of silica-coated nanoparticles of a) CdS, b) CoS, c) CuS, d) MnS, e) NiS, and f) ZnS, obtained by spontaneous coprecipitation from solutions containing 10 mM each of metal chloride, Na_2S, and sodium silicate, at the respective native pH. Scale bars: 50 nm. 88

Figure III-9. (a) Hydrodynamic radius and concentration for $ZnSxSiO_2$ particles derived from mixtures with [Si]/[Zn] = 1, but differing in silica source and synthesis pH. Shown values are averages of multiple measurements to highlight trends. The more detailed NTA derived size distributions can be found in Figure SIII-11a. (b) QD radius derived from calculation using the Brus equation and DE determined by fitting the emission tail of the transformed emission spectra (cf. Figure SIII-11b). 89

Figure III-10. QD radius derived from calculation using the Brus equation and DE determined by fitting the emission tail of the transformed emission spectra (cf. Figure SIII-12b). 90

Figure III-11. Hydrodynamic radius and concentration for (a) $ZnSxSiO_2$ and (b) $CdSxSiO_2$ particles derived from mixtures at differing pH values and increasing silica concentrations. Shown values are averages of multiple measurements to highlight trends. The more detailed NTA derived size distributions can be found in Figure SIII-14a and Figure SIII-14b respectively. 92

Figure III-12. (a) Emission and excitation peak of fitted fluorescence spectra (cf. Figure SIII-16a). (b) QD radius derived from calculation using the Brus equation and DE determined by fitting the emission tail of the transformed emission spectra (cf. Figure SIII-16b). 93

Figure III-13. Hydrodynamic radius and PDI for $ZnSxSiO_2$ particles derived from mixtures with [Si]/[M] = 2, at differing pH values and [SHMP]/[Si] = 2. Shown values are averages of multiple measurements to highlight trends. The more detailed CONTIN [37,38] derived size distributions and the respective correlation functions can be found in Figure SIII-25. The structural formula of SHMP is shown in the top left corner. . 97

Figure III-14. (a) Emission and excitation peak of fitted fluorescence spectra (cf. Figure SIII-26a). (b) QD radius derived from calculation using the Brus equation and DE determined by fitting the emission tail of the transformed emission spectra (cf.Figure SIII-26b). 98

Figure III-15. (a) Hydrodynamic radius and (b) polydispersity index (PDI) for $ZnSxSiO_2$ particles derived from mixtures with differing [Si]/[Zn] ratios, at differing pH values and added SHMP in differing [SHMP]/[Si] ratios. Shown values are averages of multiple measurements to highlight trends. Correlation functions and the more detailed size distributions derived from CONTIN analysis can be found in Figure SIII-30. The structural formula of SHMP is shown in the bottom right corner of (b). 99

Figure III-16. (a) Emission and excitation peak of fitted fluorescence spectra for samples derived from syntheses at pH 11(cf. Figure SIII-28a). (b) QD radius derived from calculation using the Brus equation and DE determined by fitting the emission tail of the transformed emission spectra (cf. Figure SIII-28c). 100

Figure SIII-1. Bjerrum-plot of the HS^-/S^{2-} system (yellow), the HCO_3^-/CO_3^{2-} system (red), and the $H_4SiO_4/H_3SiO_4^-/H_2SiO_4^{2-}$ system (blue). Suitable for coprecipitation is thepH range where the overlap between the HS^-/HCO_3^- and the $H_3SiO_4^-$ is the greatest. 115

Figure SIII-2. TEM micrographs of particles derived from a synthesis containing 10 mM of each Na_2S, $CoCl_2$, and sodium silicate. a) Cloud-like appearance of the formed particle around bigger aggregates. Scale bar: 50 nm. b) Scale bar: 100 nm. 115

Figure SIII-3. Elemental mapping of nanostructures as shown by Figure III-5b in the main text: (a) HAADF-STEM micrograph, (b) elemental map, (c) carbon, (d) oxygen, (e) cobalt and (f) silicon. Scale bars: 250 nm. 117

Figure SIII-4. TEM (left) and HAADF-STEM (middle) micrographs of nanostructures formed upon calcination of silica-stabilized cobalt carbonate precursors as shown in Figure III-6b of the main text and obtained by mixing equal volumes of 10 mM solutions of $CoCl_2$ and Na_2CO_3, with the latter containing 10 mM SiO_2. Elemental maps (right) confirm the presence of Co, Si and O, consistent with silica-coated cobalt oxide nanocrystals. 117

Figure SIII-5. Electron diffraction (ED) pattern (left) and the corresponding diffractogram obtained by radial integration (right) from the nanostructures shown in Figure SIII-4. The observed reflections suggest a spinel structure, probably Co_3O_4. 117

Figure SIII-6. UV/Vis spectra of CdS (black) and CuS (red) particles formed from aqueous solutions containing 10 mM each of transition metal chloride, sodium sulfide, and sodium silicate. Using the Brus equation with an onset of absorption of 312 nm for CdS and 304 nm for CuS, diameters of 2.51 nm and 2.56 nm can be calculated, respectively. 118

Figure SIII-7. DLS measurements of particles derived by mixing equal volumes of 10 mM solutions of metal chloride and Na_2CO_3, with the latter containing 5 mM SiO_2, at native pH of 10.41 (Mn), 10.35 (Co), 10.40 (Ni), 10.22 (Cu), 10.10 (Zn), and 10.51 (Cd). (a) DLS correlation function of particles derived from various transition metal cations. b) Size distributions derived from correlation functions shown in a). 118

Figure SIII-8. DLS measurements of particles derived by calcination of the carbonates obtained by mixing equal volumes of 10 mM solutions of metal chloride and Na_2CO_3, with the latter containing 5 mM SiO_2, at native pH of 10.41 (Mn), 10.35 (Co), 10.40 (Ni), 10.22 (Cu), 10.10 (Zn), and 10.51 (Cd). (a) DLS correlation function of particles derived from various transition metal cations. (b) Size distributions derived from correlation functions shown in (a). 119

Figure SIII-9. DLS measurements of particles derived by mixing equal volumes of 10 mM solutions of metal chloride and Na_2S, with the latter containing 5 mM SiO_2, at native pH of 10.82 (Mn), 11.14 (Co), 11.21 (Ni), 10.87 (Cu), 10.92 (Zn), and 11.15 (Cd). a) DLS correlation function of particles derived from various transition metal cations. b) Size distributions derived from correlation functions shown in a). 119

Figure SIII-10. NTA measurements of particles derived by mixing equal volumes of 10 mM solutions of metal chloride and Na_2S/Na_2CO_3, with the latter containing 5 mM SiO_2. a) Size distributions of carbonate samples at dilutions of 1:500. b) Size distributions of carbonate samples at dilutions of 1:100. c) Size distributions of calcinated carbonate samples at dilutions of 1:100. d) Size distributions of sulfide samples at dilutions of 1:1000. 120

Figure SIII-11. (a) NTA measurements of $ZnSxSiO_2$ particles derived from mixtures with [Si]/[M] = 1, but differing in silica source and synthesis pH. (b) Fluorescence measurements (λ_{exc} = 300 nm, λ_{em} = 430 nm) and corresponding fit functions. 120

Figure SIII-12. (a) Fluorescence measurements (λ_{exc} = 300 nm, λ_{em} = 430 nm) of $ZnSxSiO_2$ particles derived from mixtures with [Si]/[M] = 1, TEOS as silica source, a pH of 11, but differing hydrolysis times. (b) Respective transformed emission spectra and corresponding fit functions. 121

Figure SIII-13. DLS measurements of $FeSxSiO_2$ samples derived from a synthesis at a pH of 11 and [Si]/[Fe]-ratio. (a) [Si]/[Fe] = 0.5, (c) [Si]/[Fe] = 1, and (e) [Si]/[Fe] = 2. (b), (d), and (f) unweighted size distribution derived from the respective DLS measurements shown in (a), (c), and (e) using the CONTIN algorithm [38]. 122

Figure SIII-14. NTA measurements of (a) $ZnSxSiO_2$ and (b) $CdSxSiO_2$ particles derived from mixtures with differing [Si]/[M] ratio at differing pH values. 123

Figure SIII-15. (a) Fluorescence spectra (λ_{exc} = 390 nm, λ_{em} = 532 nm) for $CdSxSiO_2$ particles derived from mixtures with differing [Si]/[M] ratio at differing pH values. (b) Visual appearance of the synthesized samples dispersed in their native solution. 123

Figure SIII-16. (a) Fluorescence spectra (λ_{exc} = 300 nm, λ_{em} = 430 nm) for $ZnSxSiO_2$ particles derived from mixtures with differing [Si]/[M] ratio at differing pH values. (b) Respective transformed emission spectra and fit functions. 123

Figure SIII-17. (a) NTA measurements for $ZnSxSiO_2$ particles derived from solutions with [Si]/[Zn] = 1, at differing pH values in buffered and unbuffered solutions. (b) Evaluated hydrodynamic radii and concentrations derived from the NTA measurements. (c) Fluorescence (λ_{exc} = 300 nm, λ_{em} = 440 nm) measurement with corresponding fits and (d) evaluation of peak emission/excitation wavelengths. (d) Transformed emission spectra and corresponding fits. (e) QD size calculated using the Brus equation and DE determined by fitting the tail of the transformed emission spectra. 124

Figure SIII-18. Measurements for $Zn_{0.8}Cd_{0.2}SxSiO2$ particles derived from solutions with [Si]/[Zn] = 1, a pH value of 11 at differing synthesis temperatures. (a) Unweighted size distributions derived from DLS measurements using the CONTIN algorithm. (b) Hydrodynamic radius and PDI derived from DLS measurements. Shown values are averages of multiple measurements to highlight trends. (c) Fluorescence (λ_{exc} = 360 nm, λ_{em} = 500 nm) measurements and corresponding fits. (d) DE determined by fitting the emission tail of the transformed emission spectra. (e) UV/vis measurement. (f) QD size determined using the Brus equation and relative quantum yield..... 125

Figure SIII-19. SEM and Tem micrographs for $ZnCdSxSiO_2$ particles derived from solutions with [Si]/[Zn] = 2, a pH value of 11 at (a), (b), (c) 10°C and (d), (e), (f) 85°C. The scale bars correspond to (a) and (d) 20 µm, (b) and (e) 1 µm, and (c) and (f) 100 nm, respectively. 126

Figure SIII-20. (a) NTA measurements for $ZnSxSiO_2$ particles derived from solutions with [Si]/[Zn] = 2, a pH value of 11 and differing added ions from differing positions in the Hofmeister series. (b) Evaluated hydrodynamic radii and concentrations derived from the NTA measurements. (c) Fluorescence (λ_{exc} = 300 nm, λ_{em} = 440 nm) measurement and corresponding fits and (d) evaluation of peak emission/excitation wavelengths. (e) Transformed emission spectra and corresponding fits. (f) QD size calculated using the Brus equation and DE determined by fitting the tail of the transformed emission spectra. 127

Figure SIII-21. (a) NTA measurements for $Zn_{0.8}Cd_{0.2}SxSiO_2$ particles derived from a modified synthesis using a microfluidic system (Q_S = 0.05 mL/min, Q_M = 0.1 mL/min) at a pH value of 11 with a final ratio of [Si]/[M] = 2. Schematic depictions of the used microfluidic device (flow from left to right) from top to bottom: tesla valve, serpentine. (b) Fluorescence (λ_{exc} = 360 nm, λ_{em} = 500 nm) measurement and corresponding fits. (c-f) TEM micrographs of the particles derived from (c), (d) tesla valve and (e), (f) serpentine. The scale bars correspond to 100 nm for (c) and (e) and 70 nm for (d) and (f), corresponding to a magnification of 13000x and 28000x respectively..... 128

Figure SIII-22. (a) NTA measurements for $Zn_{0.8}Cd_{0.2}SxSiO_2$ particles derived from solutions with [Si]/[M] = 2 at a pH value of 11 before and after sequential centrifugation at increasing rotational speeds. (b) Fluorescence (λ_{exc} = 360 nm, λ_{em} = 500 nm) measurement and corresponding fits. (c-f) TEM micrographs of particles derived from centrifugation steps at (c), (d) 5000g and (e), (f) 20000g. The scale bars correspond to 100 nm for (c) and (e) and 70 nm for (d) and (f), corresponding to a magnification of 13000x and 28000x respectively. 129

Figure SIII-23. NTA measurements for $ZnSxSiO_2$ particles derived from solutions with [Si]/[M] = 2 at a pH value of 11 before and after lyophilization. Differing amounts of lyoprotective agent (LA) (a) trehalose, (b) glycerol were added before the lyophilization. The structural formulas of the used LA are shown in (a) and (b). (c) Relative redispersed amount of particles after lyophilization at differing [LA]/[Si] ratios..... 129

Figure SIII-24. (a) DLS measurements of $Zn_{0.8}Cd_{0.2}SxSiO_2$ particles derived from mixtures with [Si]/[Zn] = 2 at a pH value of 11 before and after dialysis/filtration. (b) Fluorescence (λ_{exc} = 360 nm, λ_{em} = 500 nm) measurement and corresponding fits. (c-e) TEM micrographs of dialyzed particles at a MWCO of (c) 3kDa,

(d) 1000kDa and of filtrated particles (e) using a 30kDa ultracentrifuge filter. Scale bars correspond to 70 nm and a magnification of 28000x. 130

Figure SIII-25. DLS measurements of $ZnSxSiO_2$ samples derived from a synthesis with a [Si]/[Zn] = 2 at (a) pH 10, (b) pH 11, and (c) pH 12. Unweighted size distribution derived from the respective DLS measurements shown in (a), (b), and (c) using the CONTIN algorithm [38]. 131

Figure SIII-26. Fluorescence spectra (λ_{exc} = 300 nm, λ_{em} = 430 nm) for $ZnSxSiO_2$ particles derived from mixtures with [Si]/[M] = 2 and [SHMP]/[Si] = 2 with differing SHMP positions at differing pH values. (b) Respective transformed emission spectra and fit functions. 132

Figure SIII-27. TEM micrographs for $ZnSxSiO_2$ particles derived from mixtures with [Si]/[M] = 2 and [SHMP]/[Si] = 2 with differing SHMP positions. (a) and (e) reference, (b) and (f) SHMP in silica containing solution, (c) and (g) SHMP in metal containing solution, and (d) and (h) 50/50 in both, silica and metal containing solution. The scale bar corresponds to 100 nm for (a), (c), (d), and (h) with a magnification of 13000x, and to 70 nm for (b), (e), (f), and (g) with a magnification of 28000x. 132

Figure SIII-28. Fluorescence spectra (λ_{exc} = 300 nm, λ_{em} = 430 nm) for $ZnSxSiO_2$ particles derived from mixtures with differing [Si]/[M] ratio and differing [SHMP]/[Si] ratios at (a) pH 11 and (b) pH 12. (c) and (d) Respective transformed emission spectra and fit functions. 133

Figure SIII-29. Emission and excitation peak of fitted fluorescence spectra for samples derived from syntheses at pH 12 (cf. Figure SIII-28b). (b) QD radius derived from calculation using the Brus equation and DE determined by fitting the emission tail of the transformed emission spectra (cf. Figure SIII-28d). 133

Figure SIII-30. DLS measurements of $ZnSxSiO_2$ samples derived from a synthesis with varying pH and [SHMP]/[Si]-ratio. (a) [Si]/[Zn] = 1, (b) [Si]/[Zn] = 2, and (c) [Si]/[Zn] = 3. Unweighted size distribution derived from the respective DLS measurements shown in (a), (b), and (c) using the CONTIN algorithm [38]. 134

Figure SIII-31. DLS measurements of $FeSxSiO_2$ samples derived from a synthesis with varying pH and [SHMP]/[Si]-ratio. (a) particles derived from Fe(II), (c) particles derived from Fe(III). Unweighted size distribution derived from the respective DLS measurements shown in (b), and (d) using the CONTIN algorithm [38]. 135

Figure IV-1. Graphical Abstract: Visualization of surface Fenton reaction on a silica coated iron oxide surface at circumneutral pH values. The hydroxyl radicals are generated on the iron oxides surface and the oxidants are stabilized afterwards by the silica matrix. They can then be used to oxidize organic pollutants such as phenol. Inspired by ref [1]. 137

Figure IV-2. (a) TEM micrograph of particles derived from Fe(II) at 5 mM TEOS and a pH value of 11. The scale bar corresponds to 100 nm. (b) XRD spectra of FeS derived from Fe(II) and Fe(III), respectively. The vertical lines indicate the crystal structure of the synthesis residue NaCl. 149

Figure IV-3. Relative amount of phenol degraded after 8 h reaction time for particles derived from modified syntheses. The white squares represent the reference hematite. In (a) particles derived from FeS and in (b) particles derived from $FeCO_3$ are shown. The green triangles represent particles derived from a synthesis from Fe(III) at a pH value of 11. 151

Figure IV-4. a) Normalized degradation of phenol over the reaction time of 8 h for different particles derived from Fe(II) or Fe(III) and the reference, hematite. First-order linear fit to determine reaction rates. b) Normalized degradation of H_2O_2 over the reaction time of 8 h for different particles derived from Fe(II) or

Fe(III) and the reference, hematite, including first-order linear fits. pH values (cf. Figure SIV-5a) and reaction rates (cf. Figure SIV-5b) can be found in the SI. 153

Figure IV-5. (a) Concentration of Fe(II) in solution after 8 h of reaction time for different particles derived from Fe(II) or Fe(III). Note that only a small portion of approximately 0.5% is leached out in relation of the total amount of Fe. (b) Normalized degradation of phenol respective to the normalized degradation of H_2O_2 for different particles derived from Fe(II) or Fe(III) at different [Si]/[Fe] ratios and the reference, hematite. 154

Figure IV-6. Normalized degradation of phenol respective to the normalized degradation of H_2O_2 for different particles derived from (a) Fe(II) and (b) Fe(III) with different [Si]/[Fe] ratios and differing TEOS hydrolysis times before particle synthesis. pH values (cf. Figure SIV-7) and reaction rates (cf. Figure SIV-8) can be found in the supporting information. Note that negative values result from a very slight H_2O_2 degradation over the time period with a magnitude similar to the measurement accuracy. 155

Figure IV-7. Normalized degradation of phenol respective to the normalized degradation of H_2O_2 for different particles derived from Fe(II) with different [Si]/[Fe] ratios and subsequent silica removal by HF addition. The sample names correspond to the etched percentage of silica. (a) Particles derived from FeS at pH 10 and [Si]/[Fe] = 1. (b) Particles derived from FeS at pH 10 and [Si]/[Fe] = 2. The corresponding pH values (cf. Figure SIV-12) and reaction rates (cf. Figure SIV-13) can be found in the supporting information. 157

Figure IV-8. Normalized degradation of phenol respective to the normalized degradation of H_2O_2 for different particles derived from (a) Fe(II) and (b) Fe(III) with different [Si]/[Fe] ratios and differing [SHMP]/[Si] ratios. pH values (cf. Figure SIV-15) and reaction rates (cf. Figure SIV-16) can be found in the supporting information. 159

Figure SIV-1. TEM micrographs of various iron oxides (a-c) Fe(II) and (d-f) Fe(III) with increasing [Si]/[Fe] ratio from left to right (a&d) 0.5, (b&e) 1, and (c&f) 2. The scale bar corresponds to 70 nm. 170

Figure SIV-2. XRD spectra of iron carbonate derived from Fe(II) and Fe(III), respectively. The vertical lines indicate the crystal structure of the synthesis residue NaCl. 171

Figure SIV-3. TEM micrograph of FeCO3 and FeO 2p5 und 5 und 5 Fe(III) 171

Figure SIV-4. SEM micrographs of various iron oxides (a-c) Fe(II) and (d-f) Fe(III) with increasing [Si]/[Fe] ratio from left to right (a&d) 0.5, (b&e) 1, and (c&f) 2. The scale bar corresponds to (a) 8 µm and (b-f) 10 µm, respectively. 172

Figure SIV-5. (a) pH values of the reaction solutions in the 8 h time period. (b) First order reaction rates of both, H_2O_2 and phenol degradation, determined from linear fits in Figure IV-4. 172

Figure SIV-6. Hydrodynamic radius (r_H) of particles derived from (a) Fe(II) and (b) Fe(III) with varying [Si]/[Fe] ratios and increasing TEOS hydrolysis time before the synthesis. 173

Figure SIV-7. pH values over 8 h reaction time for samples derived from (a) Fe(II) and (b) Fe(III) with varying [Si]/[Fe] ratios and increasing TEOS hydrolysis time before the synthesis. The degradation of phenol/H_2O_2 is shown in Figure IV-6. 174

Figure SIV-8. First order reaction rates of both, H_2O_2 and phenol degradation, determined by linear fits of the normalized reaction profile for (a) Fe(II) and (b) Fe(III) derived materials. Samples deviated from linear behavior (cf. Figure SIV-10), were only fitted in the linear region (< 4h). 174

Figure SIV-9. (a) Leached iron concetration after 8 h of reaction time for samples derived from Fe(II) and Fe(III) with varying [Si]/[Fe] ratios and increasing TEOS hydrolysis time before the synthesis. (b) Visualization of the dissolution over the 8 h reaction for selected samples. 175

Figure SIV-10. (a) Normalized phenol degradation over normalized H_2O_2 degradation for selected samples. (b) pH over 8 h reaction time for selected samples. 175

Figure SIV-11. (a) Hydrodynamic radius (r_H) of particles derived from FeS at pH 10 with differing [Si]/[Fe] ratios of 0.5, 1, and 2. The etched particles show significant size increase, which can be directly backtracked to the increased aggregation of these samples. (b) Cyclic voltammograms of particles derived from FeS at pH 10 with [Si]/[Fe] = 1. The same points are shown, which are used in Figure IV-7a. 175

Figure SIV-12. pH values over 8 h of reaction time for the samples with etched silica shell. The degradation of phenol/H_2O_2 is shown in Figure IV-7. Samples derived from syntheses with (a) [Si]/[Fe] = 1 and (b) [Si]/[Fe] = 2 before subsequent etching with HF. 176

Figure SIV-13. First order reaction rates of both, H_2O_2 and phenol degradation, determined by linear fits of the normalized reaction profiles. 176

Figure SIV-14. Hydrodynamic radius (r_H) of particles derived from Fe(II) and Fe(III) with varying [SHMP]/[Si] ratios. (a) Fe(II) and (b) Fe(III). 177

Figure SIV-15. pH values over 8 h reaction time for particles derived from (a) Fe(II) and (b) Fe(III) with varying [SHMP]/[Si] ratios. The degradation of phenol/H_2O_2 is shown in Figure IV-8. 177

Figure SIV-16. First order reaction rates of both, H_2O_2 and phenol degradation, determined by linear fits of the normalized reaction profile for (a) Fe(II) and (b) Fe(III) derived materials. 177

Figure SIV-17. Cyclic voltamogramms for particles derived from (a, c) Fe(II) and (b, d) Fe(III) with varying [SHMP]/[Si] ratios. 178

Figure V-1. Graphical Abstract: The combination of two aqueous solutions results in spontaneous coprecipitation of transition metal sulfides (red) in a silica matrix (blue) as shown in Chapter III. The formation of transition metal complexes prior to combination alters the precipitation process. With increasing complex stability, the number of nuclei (red), and with decreasing ligand exchange rate, the amount of growth prior to capture can be controlled. Ultimately, ligands with high surface affinity can hinder the silica condensation on the nucleus surface (black rim). 179

Figure V-2. Visualization of used complexes from top to bottom: valence structural formula of the ligands (neutral charge), Natta projection of formed octahedral complex with ligand charges corresponding to a pH value of 11, and the three-dimensional shape as balls and stick model. For polyacrylic acid (PAA), one complex center is shown exemplary even though multiple centers may occur along one chain. For Cysteine (f) both bidentate complexation modes with the sidechain and the carboxylate/the amino group are shown (S,O and S,N). Note that the metal center/complex is shown without charges. For the typically used charge in the experiments (2+) the charged complexes from left to right are: $[M(EDTA)(H_2O)_2]^{2-}$, $[M(NTA)(H_2O)_2]^{-}$, $[M(TETA)(H_2O)_2]^{2+}$, $[M(AA)_4(H_2O)_2]^{2-}$, $[M(His)_2(H_2O)]^{0}$, $[M(Cys)_2(H_2O)_2]^{2-}$. 184

Figure V-3. Hydrodynamic radius and polydispersity index (PDI) for (a) copper, zinc, and cadmium sulfides and (b) cobalt, iron, and nickel sulfides, derived from various complexes, as shown in Figure V-2. Shown values are averages of multiple measurements to highlight trends. The more detailed size distributions derived from CONTN analysis can be found in Figure SV-1. Missing values indicate highly aggregating samples that cannot be measured reproducibly (Cd–PAA, Ni–Cys, Ni–EDTA, Ni–NTA). 191

Figure V-4. HRTEM micrographs of CuS derived from (a) cysteine complex, (b) histidine complex, and CoS derived from (d) cysteine complex, and (e) histidine complex. The scale bar corresponds to 50 nm for (a), (b), and (e) and to 100 nm for (d), equivalent to a magnification of 20000x and 10000x, respectively. The size distributions for (c) CuS and (f) CoS are derived from size measurements in the TEM micrographs (n > 50). Further SEM/TEM micrographs can be found in Figure SV-3 and Figure SV-4 for CuS and in Figure SV-6 and Figure SV-7 for CoS. Diffraction patterns and the respective radial averages can be found in Figure SV-5 for CuS and in Figure SV-8 for CoS. 194

Figure V-5. HRTEM micrographs of CdS derived from (a) cysteine complex, (b) histidine complex, and ZnS derived from (d) cysteine complex, and (e) histidine complex. The scale bar corresponds to 50 nm for (a), (b), and (d) and to 100 nm for (e), equivalent to a magnification of 20000x and 10000x, respectively. The size distributions for (c) CdS and (f) ZnS are derived from size measurements in the TEM micrographs (n > 50). Further SEM/TEM micrographs can be found in Figure SV-9 and Figure SV-10 for CdS, Figure SV-12 and Figure SV-6 for ZnS, and Figure SV-14 for CdS/ZnS from a reference synthesis [5,7] without silica. Diffraction patterns and the respective radial averages can be found in Figure SV-11 for CdS, in Figure SV-13 for ZnS, and in Figure SV-15 for the reference samples. 195

Figure V-6. Fluorescence spectra of CdS samples derived from different complexes synthesized at pH values of 11 and 12. Samples in (a) derived from EDTA and NTA complexes are directly compared to a reference (see Chapter III) (λ_{exc} = 387 nm, λ_{em} = 530 nm). Samples in (b) are derived from TETA, cysteine, and histidine complexes (λ_{exc} = 407 nm, 418 nm, and 420 nm, λ_{em} = 530 nm, 545 nm, and 570 nm). 196

Figure V-7. (a) Emission and excitation peak of fitted fluorescence spectra (cf. Figure V-6b) and relative area of the emission for samples derived from complexes with TETA, cysteine, or histidine at pH of 11 or 12. (b) QD radius derived from calculation using the Brus equation and DE determined by fitting the emission tail of the transformed emission spectra (cf. Figure SV-17) for samples derived from complexes with TETA, cysteine, or histidine at pH of 11 or 12. 197

Figure V-8. Hydrodynamic radius and polydispersity index (PDI) for CdS derived from cysteine complex at different silica and sulfide concentrations. Shown values are averages of multiple measurements to highlight trends. Correlation functions and the more detailed size distributions derived from CONTN analysis can be found in Figure SV-18. 199

Figure V-9. (a) Emission and excitation peak of fitted fluorescence spectra (cf. Figure SV-19a) and relative area of the emission for samples derived from complexes with cysteine at a pH value of 11 and varying silica content and increasing sulfide concentration during synthesis. (b) QD radius derived from calculation using the Brus equation and DE determined by fitting the emission tail of the transformed emission spectra (cf. Figure SV-19b) for samples derived from complexes with cysteine at a pH value of 11 and varying silica content and increasing sulfide concentration during synthesis. 200

Figure V-10. Hydrodynamic radius and polydispersity index (PDI) for CdS derived from cadmium complexes containing mixed ligands of cysteine and other amino acids. Shown values are averages of multiple measurements to highlight trends. Correlation functions and the more detailed size distributions derived from CONTIN analysis can be found in **Figure SV-20. Structural** formulas of the amino acids used, from left to right: L-alanine, L-arginine, glycine, L-lysine, L-tyrosine, and L-histidine. 202

Figure V-11. (a) Emission and excitation peak of fitted fluorescence spectra (cf. Figure SV-21a) and relative area of the emission for samples derived from mixed ligand complexes with cysteine and other amino acids in a 1 to 2 ratio. (b) QD radius derived from calculation using the Brus equation and DE determined by fitting the emission tail of the transformed emission spectra (cf. Figure SV-21b) for samples derived from mixed ligand complexes with cysteine and other amino acids in a 1 to 2 ratio. 203

Figure V-12. (a) Emission and excitation peak of fitted fluorescence spectra (cf. Figure SV-23) and relative area of the emission for samples derived from mixed ligand complexes with cysteine and histidine in varying [Cys]/[His] ratios. (b) QD radius derived from calculation using the Brus equation and DE determined by fitting the emission tail of the transformed emission spectra (cf. Figure SV-24) for samples derived from mixed ligand complexes with cysteine and histidine in varying [Cys]/[His] ratios. 206

Figure V-13. (a) Emission and excitation peak of fitted fluorescence spectra (cf. Figure SV-26a) for samples derived from cysteine complexes with subsequent size exclusion by filtration with 30k and 10k MWCO ultracentrifuge filters. (b) QD radius derived from calculation using the Brus equation and DE determined by fitting the emission tail of the transformed emission spectra (cf. Figure SV-26b). 208

Figure V-14. HRTEM micrographs of (a), (b) ZnCdS (x = 0.8) derived from reference synthesis without complexation and (d), (e) ZnCdS (x = 0.8) derived from a cadmium cysteine complex and a zinc histidine complex. The scale bar corresponds to 100 nm for (a), to 50 nm for (d), and to 20 nm for (b) and (e), equivalent to a magnification of 10000x, 20000x and 60000x, respectively. (c) The size distributions for (a) and (d) are derived from size measurements in the TEM micrographs (n > 50). Diffraction patterns and the respective radial averages can be found in Figure SV-29..... 209

Figure V-15. (a) Emission and excitation peak of fitted fluorescence spectra (cf. Figure SV-28a, c, and e) for samples derived mixtures of zinc and cadmium His/Cys complexes in varying concentrations (b) QD radius derived from calculation using the Brus equation and DE determined by fitting the emission tail of the transformed emission spectra (cf. Figure SV-28b, d, and f). 210

Figure SV-1. Unweighted size distributions derived from DLS measurements of samples of (a) CuS, (b) ZnS, (c) CdS, (d) CoS, (e) FeS, and (f) NiS. derived from attempted coupled coprecipitation from various complexes as shown in Figure V-2, using the CONTIN algorithm [50]. 225

Figure SV-2. Pictures of synthesis mixtures of CdS from cysteine complexes at [Si]/[Cd] = 2 at pH 11 after differing reaction times. (a) 1h, (b) 6h, and (c) 12h. 226

Figure SV-3. SEM micrographs of CuS derived from complexes of (a) and (b) cysteine and (c) and (d) histidine. The scale bars correspond to (a) 8 µm, (b) 2 µm, and (c) and (d) 5 µm. 226

Figure SV-4. HRTEM micrographs of CuS derived from (a), (c) cysteine complex, (b), (d) histidine complex. The scale bar corresponds to 50 nm for (a), (b), and to 20 nm for (c), (d), equivalent to a magnification of 20000x and 60000x, respectively. Size distribution can be found in Figure V-4c. 227

Figure SV-5. HRTEM diffraction pattern and radial average derived from HRTEM micrographs of CuS derived from (a) cysteine complex and (b) histidine complex. The SAED pattern was indexed according to the hexagonal chovellite structure of CuS (space group P63/mmc, COD ID: 1010920). The observed deviations from the reference d-spacings are attributed to the partially amorphous character of the sample..... 227

Figure SV-6. SEM micrographs of CoS derived from (a), (b) cysteine complex, (c), (d) histidine complex, (e), (f) EDTA complex, (g), (h) NTA complex, and (i), (j) PAA complex. The scale bars correspond to 30 µm for (e) and (i), 20 µm for (c) and (g), 10µm for (f) and (j), 8 µm for (a), 3 µm for (d) and (h), and 2 µm for (b)..... 228

Figure SV-7. HRTEM micrographs of CoS derived from (a), (c) cysteine complex, (b), (d) histidine complex. The scale bar corresponds to 100 nm for (a), 50 nm for (b), and to 20 nm for (c), (d), equivalent to a magnification of 10000x, 20000x, and 60000x, respectively. Size distribution can be found in Figure V-4f. 228

Figure SV-8. HRTEM diffraction pattern and radial average derived from HRTEM micrographs of CoS derived from (a) cysteine complex and (b) histidine complex. The SAED pattern was indexed according to the hexagonal NiAs structure of CoS (space group P63/mmc, ICSD No. 624857). The observed deviations from the reference d-spacings are attributed to the partially amorphous character of the sample..... 229

Figure SV-9. SEM micrographs of CoS derived from (a), (b) cysteine complex, (c), (d) histidine complex, (e), (f) EDTA complex, and (g), (h) NTA complex. The scale bars correspond to 20 µm for (c) and (g), 10µm for (a), (e) and (h), 5 µm for (b), and 2 µm for (d) and (f). 229

Figure SV-10. HRTEM micrographs of CdS derived from (a), (c) cysteine complex, (b), (d) histidine complex. The scale bar corresponds to 50 nm for (a), (b), and to 20 nm for (c), (d), equivalent to a magnification of 20000x and 60000x, respectively. Size distribution can be **found in Figure V-5c.**..... 230

Figure SV-11. HRTEM diffraction pattern and radial average derived from HRTEM micrographs of CdS derived from (a) cysteine complex and (b) histidine complex. The SAED pattern was indexed according to the cubic zinc-blende structure of CdS (space group F43m, ICSD No. 31075). The observed deviations from the reference d-spacings are attributed to the amorphous SiO_2 matrix and the partially amorphous character of the sample. 230

Figure SV-12. HRTEM micrographs of ZnS derived histidine complex. The scale bar corresponds to 100 nm for (a), 50 nm for (c), and to 20 nm for (c), equivalent to a magnification of 10000x, 20000x and 60000x, respectively. Size distribution can be found in Figure V-5f..... 231

Figure SV-13. HRTEM diffraction pattern and radial average derived from HRTEM micrographs of ZnS derived from histidine complex. The SAED pattern was indexed according to the cubic zinc-blende structure of ZnS (space group F43m, ICSD No. 162754). The observed deviations from the reference d-spacings are attributed to the amorphous SiO_2 matrix and the partially amorphous character of the sample. 231

Figure SV-14. HRTEM micrographs of (a), (c) CdS derived from cysteine complex, and (b), (d) ZnS derived from histidine complex (precipitation without silica). The scale bar corresponds to 50 nm for (a), (b), and to 20 nm for (c), (d), equivalent to a magnification of 20000x and 60000x, respectively. Size distribution can be found in Figure V-5c and Figure V-5f, respectively. 231

Figure SV-15. HRTEM diffraction pattern and radial average derived from HRTEM micrographs of (a) CdS derived from cysteine complex and (b) ZnS derived from histidine complex in a reference synthesis[5,7]. The SAED pattern was indexed according to the cubic zinc-blende structure of CdS (space group F43m, ICSD No. 31075) and of ZnS (space group F43m, ICSD No. 162754), respectively. The observed deviations from the reference d-spacings are attributed to the amorphous SiO_2 matrix and the partially amorphous character of the sample. 232

Figure SV-16. SEM micrographs of NiS derived from (a), (b) cysteine complex, (c), (d) histidine complex, (e), (f) EDTA complex, (g), (h) NTA complex, and (i), (j) PAA complex. The scale bars correspond to 200 µm for (g), 30 µm for (i), 20 µm for (e), 10µm for (a), (c) and (h), 8 µm for (f), 5 µm for (b), and 3 µm for (d) and (j). 232

Figure SV-17. Transformed emission spectra and fits for samples derived from TETA, cysteine, and histidine complexes at pH values of 11 and 12. The measured spectra can be found in Figure V-6b. 233

Figure SV-18. (a) DLS measurements for CdS derived from cysteine complex at different silica and sulfide concentrations. (b) Unweighted size distribution derived from DLS measurements shown in (a) using the CONTIN algorithm [50]..... 233

Figure SV-19. (a) Fluorescence spectra of CdS for samples derived from complexes with cysteine at a pH value of 11 and varying silica content and increasing sulfide concentration during synthesis. For the excitation spectra the emission wavelength was set to 545 nm, 610 nm, and 660 nm and for the emission spectra the excitation wavelength of 420 nm, 430 nm, and 440 nm was used, respectively. (increasing with increasing sulfide concentration) (b) Respective transformed emission spectra and fits. Note that for both, (a) and (b) a second y-axis is used to visualize the spectra of samples with [S]/[Cd] > 1 together with the samples with [S]/[Cd] = 1. 233

Figure SV-20. (a) DLS measurements for CdS samples derived from mixed ligand complexes with cysteine and other amino acids in a 1 to 1 ratio. (b) Unweighted size distribution derived from DLS measurements shown in (a) using the CONTIN algorithm [50]. 234

Figure SV-21. (a) Fluorescence (λ_{exc} = 420 nm, λ_{em} = 550 nm) spectra for CdS samples derived from mixed ligand complexes with cysteine and other amino acids in a 1 to 1 ratio. (b) Respective transformed emission spectra and fits. 234

Figure SV-22. Unweighted size distribution derived from DLS measurements for samples derived from mixed ligand complexes with cysteine and histidine in varying [Cys]/[His] ratios, using the CONTIN algorithm [50]. (a) [Si]/[Cd] = 2, (b) [Si]/[Cd] = 6..... 235

Figure SV-23. Fluorescence spectra for samples derived from mixed ligand complexes with cysteine and histidine in varying [Cys]/[His] ratios. (a) [Si]/[Cd] = 2, (b) [Si]/[Cd] = 6. For the excitation spectra the emission wavelength was set to 550 nm ([Cys]/[His] > 0.5), 540 nm, 535 nm, 520 nm, and 545 nm and for the emission spectra the excitation wavelength of 420 nm ([Cys]/[His] > 0.5), 418 nm, 410 nm, 402 nm, and 415 nm was used. (ordered in decreasing [Cys]/[His] ratio). Also, references are shown in (a) comparable to Figure V-6b. 235

Figure SV-24. Transformed emission spectra and fits for samples derived from mixed ligand complexes with cysteine and histidine in varying [Cys]/[His] ratios. (a) [Si]/[Cd] = 2, (b) [Si]/[Cd] = 6. 236

Figure SV-25. (a) DLS measurements for samples derived from cysteine complexes with subsequent size exclusion by filtration with 30k and 10k MWCO ultracentrifuge filters. (b) Unweighted size distribution derived from DLS measurements shown in (a) using the CONTIN algorithm [50]. 236

Figure SV-26. (a) Fluorescence (λ_{exc} = 420 nm, λ_{em} = 550 nm) spectra for samples derived from cysteine complexes with subsequent size exclusion by filtration with 30k and 10k MWCO ultracentrifuge filters. (b) Respective transformed emission spectra and fits. 236

Figure SV-27. DLS measurements for samples derived from (a) cysteine, (b) histidine, and (c) mixed ligand complexes with differing molar fractions of Zn. Respective unweighted size distribution derived from DLS measurements shown in (d), (e), and (f) using the CONTIN algorithm [50]..... 237

Figure SV-28. Fluorescence spectra for samples derived from (a) cysteine, (b) histidine, and (c) mixed ligand complexes with differing molar fractions of Zn. For the excitation spectra the emission wavelength was set

to 550 nm and for the emission spectra the excitation wavelength of 420 nm was used. (d), (e), and (f) Respective transformed emission spectra and fits. The used wavelengths and the respective fit parameters are available in the online repository. 238

Figure SV-29. HRTEM diffraction pattern and radial average derived from HRTEM micrographs of $Zn_{0.8}Cd_{0.2}S$ derived from (a) cysteine complex and (b) reference reaction without complex precursor. The SAED pattern for (a) was indexed according to the hexagonal wurtzite structure of ZnCdS (space group P63mc, ICSD No. 620387). The SAED pattern ob (b) could not be indexed to a defined crystal structure. The observed deviations from the reference d-spacings are attributed to the partially amorphous character of the sample. 239

Figure VI-1. Graphical Abstract: Increasing the concentration of divalent cations in a PAA containing solution in the right pH regime results in a liquid-liquid phase separation, called coacervation. The solution separates into a polymer rich (condensed phase) and polymer depleted (dilute phase) phase. Adding sulfide/carbonate anions results in the formation of nanoparticles. The coacervates dissolve, slowly releasing cations, and the polymers stabilize the nanoparticles surfaces. 241

Figure VI-2. a) The two main attractive interactions to form simple PAA/M^{2+} coacervates. Divalent cation (M^{2+}) is complexed by deprotonated carboxylic groups and can bridge between two PAA chains (highlighted gray). Protonated carboxylic groups can form hydrogen bonds between different PAA chains (highlighted green). b) Fractional charge of PAA molecule calculated from Eqn VI-1 [19]. Reference lines correspond to the highest (6.63) and lowest (4.09) pH values at which coacervation was observed in this work. 244

Figure VI-3. Scheme of the simple coacervating system: (a) PAA^-/Co^{2+} coacervate droplets form at concentrations greater than a certain threshold ratio and coalesce over time. (b) Mineralization with Na_2CO_3/Na_2S results in different structures before and after phase separation. (inspired by ref [12]) 249

Figure VI-4. (a) DLS correlation function of PAA^-/Co^{2+} coacervates formed at different pH values measured at 25°C. Debye length with decreasing pH: 0.488 nm, 0.522 nm, 0.664 nm, 0.739 nm. (b) Unweighted size distribution of PAA^-/Co^{2+} coacervates at different pH values, derived from DLS using the CONTIN [28,29] algorithm. Further information on coalescence rates can be found in Figure SVI-3. 251

Figure VI-5. (a) Picture of PAA/Co^{2+} solutions with different AA/Co^{2+} ratios after an equilibration time of 24h containing PAA/Co^{2+} coacervates after coalescence. (b) Share of the Co^{2+} concentration in the coacervates of the total concentration at the different AA/Co^{2+} ratios derived from UV/vis measurements of the supernatants after coalescence (equilibration time 24h). (c) DLS correlation functions of PAA/Co^{2+} solutions at the different AA/Co^{2+} ratios (3.4-1.9), measured immediately after coacervate formation, when the coacervates were still finely dispersed as droplets (cf. Figure SVI-3). 253

Figure VI-6. TEM micrograph of CoS particles derived from PAA^-/Co^{2+} mixtures at different ratios. (a) AA/Co^{2+} ratio of 2.65, just below the threshold concentration. (b) AA/Co^{2+} ratio of 1.33, above the threshold concentration. 254

Figure VI-7. High resolution TEM micrograph of particles synthesized at AA/M^{2+} of around 1.3. (a) and (b) CoS with scale bars of 5 and 2 nm in length, respecitvely. (c) Histogramm derived from particles measured in HRTEM micrographs as shown in (a) and (b). The particles show an average diameter of 2.7 +- 0.60 nm (n = 133), corresponding to a coefficient of variation of 0.22, indicating moderate polydispersity. 256

Figure VI-8. XRD measurement of Co-particles derived from PAA/Co^{2+} coacervates at pH 5.45 with different anions, CoS (black), $CoCO_3$ (red), and CoO (blue). The reflexes visible and the reference lines correspond to the NaCl lattice derived from NaCl residues. 257

Figure SVI-1. Titration of a solution of 1w% 100k PAA / 40mM MCl_2 with 1M NaOH with continuous measurements of pH and turbidity at λ = 660 nm. The concentration of PAA and MCl_2 was held constant by titrating a solution of 2w% 100k PAA / 80mM MCl_2 in the same volumetric amounts as the NaOH. Note that the increase in "turbidity" for Ni^{2+} comes due to absorption of the AA/Ni^{2+} complex at λ = 660 nm. 266

Figure SVI-2. Solubility products of the tested cation (Ca^{2+}, Co^{2+}, Mn^{2+}, Ni^{2+}, Cu^{2+}) hydroxides against the pH. The reference line indicates the threshold concentration of the cation for coacervate formation. Note that the threshold concentration for PAA/Cu^{2+} coacervates is lower than for the others, and the reference line represents only the other cations. Extracted pH values are: pH(Ca^{2+}) = 12, pH(Co^{2+}) = 7.2, pH(Mn^{2+}) = 8, pH(Ni^{2+}) = 7, pH(Cu^{2+}) = 4.8..... 266

Figure SVI-3. Aggregation and coalescence/precipitation kinetic of freshly prepared Co-coacervates as shown in **Figure 4c.** Typical DLS-measurements were measured in the first 300s. Note that no coacervate sizes are given in this figure but a r_H/r_{max} ratio to show the coalescence rates independend of actual size. Hydrodynamic radii (r_H) were determined using Cumulants analysis on DLS measurements of coacervate droplet suspensions at different AA/Co^{2+} ratios every 30s for at least 1h. r_{max} represents the maximum value for hydrodynamic radius observed in this timeframe. The increase in droplet size does not stagnate after 1000s but the sedimentation of the coalesced droplets removes the largest droplets from measurable solution, seemingly decreasing the droplet size again. 267

Figure SVI-4. Total organic carbon (a) and total inorganic carbon (b) of the supernatants shown in Figure VI-5a. Also visible in a is the calculated wt% of remaining PAA in the supernatant. 267

Figure SVI-5. TEM micrographs, at a magnification of 1:13000, of particles derived from PAA^-/Co^{2+} coacervates at pH 5.45 (a) $MnCO_3$. b) CoS) and TEM micrographs of particles derived from unsupported precipitation of c) $CoCO_3$ and d) CoS. 268

Figure SVI-6. TEM micrograph of $CoCO_3$ particles derived from PAA^-/Co^{2+} mixtures at different ratios. a) AA/Co^{2+} ratio of 2.65, just below the treshold concentration. B) AA/Co^{2+} ratio of 1.33, way above the treshold concentration..... 268

Figure SVI-7. TEM micrograph of particles derived from PAA^-/Co^{2+} coacervates at pH 5.45. a) $CoCO_3$, 1:28000. b) CoO derived from $CoCO_3$ after calcination at 650°C, 1:13000. c) CoS, 1:28000. 269

Figure SVI-8. TEM micrograph of particles derived from PAA^-/Mn^{2+} coacervates at pH 5.45. a) $MnCO_3$. b) MnO derived from $MnCO_3$ after calcination at 650°C. c) MnS. Magnification of 1:28000..... 269

Figure SVI-9. TEM micrograph of particles derived from PAA^-/Ni^{2+} coacervates at pH 5.45. a) $NiCO_3$, 1:28000. b) NiO derived from $NiCO_3$ after calcination at 650°C, 1:13000. c) NiS, 1:28000. 269

Figure SVI-10. TEM micrograph of different PAA^-/M^{2+} coacervates at a magnification of 1:28000. a) M = Ca. b) M = Co. c) M = Cu, note that the cubic structure in the top left corner is NaCl residue left from synthesis. 270

Figure SVI-11. High resolution TEM micrograph of particles synthesized at AA/M^{2+} of around 1.3. (a) and (b) $CoCO_3$ with scale bars of 50 and 2 nm in length, respecitvely. (c) Histogramm derived from particles measured in HRTEM micrographs as shown in (a) and (b). The particles show an average diameter of 5.27 +- 1.41 nm (n = 152), corresponding to a coefficient of variation of 0.27, indicating moderate polydispersity. 270

Figure SVI-12. XRD spectra of sulfide/carbonate/oxide particles derived from PAA/M^{2+} coacervates for different cations. The visible reference lines and the reflexes visible in all spectra correspond to the crystal structure of NaCl residues. Also, visible the broad reflex expressing the presence of amorphous substance for $MnCO_3$, MnS, $NiCO_3$, and NiS. It is also slightly visible for $CuCO_3$ and CuS, but due to the synthesis at lower pH and therefore less produced particles, it is less expressed. For the calcinated carbonates reflexes appear and the intensity of the amorphous reflex decreases indicating the formation of ordered crystal structures. 272

List of Tables

Table SII-1. Weight percentage and molar fraction of various points of the ternary mixture H_2O / EtOH / TEOS as shown in Figure II-7a, Figure II-8, and Figure SII-1. 61

Table SII-2. Hydrodynamic radius (r_H) derived from the DLS measurements shown in Figure II-8b. These sizes correspond to particles/aggregates formed after 4d in the respective solutions without catalyst/stirring. For evaluation the viscosity and refractive index of the corresponding water/ethanol mixture (x(EtOH) = 0.477; 0.281; 0.302; 0.370; 0.610) was used. As the composition D formed no clear correlation function, fitting was not possible. 62

Table SII-3. Weight percentage and molar fraction of various points of the ternary mixture H_2O / EtOH / Oil + TEOS. The point f represents the mixture containing toluene and f' the total hydrolyzed state of the same point. For the points g and j the same is true in the mixtures containing 1-octanol [96]. 63

Table SII-4. Estimated x(EtOH) for the points f, g, and j from SWAXS-measurements and their respective hydrodynamic radius evaluated from the DLS measurements. The value for j was taken from literature [96] whereas the values for f and g were estimated to be around 0.4 due to their contrast (Figure SII-2b) and their position near the critical point. 63

Table SII-5. Hydrodynamic radii of particles synthesized in the different systems. Values derived from DLS measurements and calculated from distribution fits of the histograms or are derived from the FFTs of the respective micrographs (cf. Figure SII-8 and Figure SII-9). x(EtOH) was estimated to be around 0.6 for all samples except C. For C the composition of a fully hydrolyzed solution was used with x(EtOH) = 0.37. ... 67

Table III-1. Mean diameters (d) determined from TEM micrographs like those shown in Figure III-6, Figure III-7, and Figure III-8 for silica-stabilized nanoparticles of different metal cations with different anions. Carbonate and sulfide samples were obtained via spontaneous coprecipitation from solutions containing 10 mM each of metal chloride, sodium silicate, and sodium carbonate or sodium sulfide. Oxide particles were formed upon calcination of their carbonate counterparts. For each system, a statistically relevant number (n) of nanoparticles was analyzed, giving reliable mean diameters with corresponding standard deviations. Note that calcination leads to a decrease in the average size, with relative changes ranging from 12 (Cu^{2+}) to 47 % (Zn^{2+}). 85

Table SIII-1. Apparent particle and aggregate sizes determined by dynamic light scattering for $CoCO_3$ dispersions obtained by mixing equal volumes of 10 mM $CoCl_2$ and $(NH_4)_2CO_3$ solutions in the presence of different amounts of silicate at varying final pH. Average diameters were derived from the DLS data using the cumulants method and the CONTIN algorithm, which gives apparent sizes for both the primary particles and their aggregates. Note that corresponding analyses of samples containing 2.5 or 5.8 mM SiO_2 did not yield meaningful results due to the formation of large particles, which subsequently aggregated and sedimented (as shown in Figure III-3 of the main text). (The oddity of the selected values comes from the conversion from ppm to mM.) 115

Table SIV-1. Hydrodynamic radii (r_H) derived from DLS measurements of iron oxide particles derived from Fe(II) and Fe(III), respectively at different [Si]/[Fe] ratios. The pH value for synthesis was 11..... 169

Table IV-1. Specific surface area per gram of nanoparticles measured with BET. Particles derived from an FeS synthesis at different silicate concentrations. 151

Table SIV-2. Theoretical [Si]/[Fe] ratio and calculated mean values [Si]/[Fe] derived from EDX measurements from multiple SEM pictures as shown in Figure SIV-4. 172

Table SIV-3. Calculation of the critical nucleation barrier $\Delta \boldsymbol{G}*$ and the used parameters for the different particles. K_{sp} and ρ values were taken from [54–56]. The concentration used for calculation was 5 mM. 172

Table SVI-1. Mean radius (r) determined from TEM micrographs like those shown in Figure SVI-7, Figure SVI-8, and Figure SVI-9 for nanoparticles of different metal cations with different anions. Carbonate and sulfide samples were obtained via from coacervate-forming solutions at pH 7 for Mn^{2+} and Co^{2+}, at pH 8 for Ni^{2+}, and pH 4 for Cu^{2+}. Oxide particles were formed upon calcination of their carbonate counterparts. For each system, a statistically relevant number (n>50) of nanoparticles was analyzed, giving a reliable mean radius with corresponding standard deviations. Because of different morphologies, these particles can be separated by different sizes. Also shown, are the particle and aggregate sizes determined by dynamic light scattering. Average diameters were derived from the DLS data using the cumulants method [26] and the CONTIN algorithm [28,29], which gives apparent sizes for both the primary particles and their aggregates. The values (r_H < 2 nm) derived from CONTIN correspond to remains of the used PAA in the synthesis. Note that for the cumulants analysis, the first value depicts the suspension as it is, whereas the second value is created after filtration using a 200 nm CA membrane. 270

Table SVI-2. Calculation of the critical nucleation barrier $\Delta \boldsymbol{G}*$ and the used parameters for the different particles. K_{sp} and ρ values were taken from [30,35,59]. The concentration used for calculation represents a AA/Co^{2+} ratio of 1.33. In general, the concetration and the critical nucleation barrier ΔG^* are linked by $\boldsymbol{\Delta G} * \sim \boldsymbol{12lnc - lnKSP2}$ 272

Scientific Contributions

Conference contributions:

04/2023 18th Zsigmondy Colloquium of the German Colloid Society, Berlin, Germany, *Core/Shell Nanoparticle Formation by Coprecipitation* (poster presentation)

10/2024 24th Biennial Assembly of the German Colloid Society, Dresden, Germany, *Nanoparticle Formation Utilizing Simple PAA-Cation Coacervates as Template* (poster presentation)

Publications:

(1) **Rödig, B.**; Funkner, D; Frank, T; Schürmann, U; Rieder, J; Kienle, L; Kunz, W; Kellermeier, M. Nanodots of Transition Metal Sulfides, Carbonates, and Oxides Obtained Through Spontaneous Co-Precipitation with Silica. *Nanomaterials* **2024**.

(2) Denk, P; Reigl, S; **Rödig, B**; Sztucki, M, Prevost, S; Zemb, T; Kunz, W. Biliquid oil-in-water nanofoams and spontaneous emulsification obtained with a surfactant resistant to curvature changes. *Journal of Colloid and Interface Science* **2025**.

(3) **Rödig, B**; Denk, P; Schürmann, U; Kellermeier, M; Kunz, W. Nanoparticle Formation utilizing simple Polyacrylic Acid-Cation Coacervates as Template. *RSC Advances* **2026**.

(4) **Rödig, B**; Nagin, D.; Müller, R.; Kunz, W. Heterogeneous Fenton Reaction at Circumneutral pH Values Catalyzed by Novel One-Pot Synthesized Iron Oxide/Silica Core Shell Nanoparticles. *ACS Omega* ***2026***.

(5) **Rödig, B.**; Schmauser, L.; Denk, P.; Kunz, W. Surfactant-free Microemulsions as Template for Stöber Silica Nanoparticle Synthesis. *ACS Omega* ***2026***.

Eidesstattliche Erklärung

(1) Ich erkläre hiermit an Eides statt, dass ich die vorliegende Arbeit ohne unzulässige Hilfe Dritter und ohne Benutzung anderer als der angegebenen Hilfsmittel angefertigt habe; die aus anderen Quellen direkt oder indirekt übernommenen Daten und Konzepte sind unter Angabe des Literaturzitats gekennzeichnet.

(2) Die zu Beginn eines Kapitels aufgeführten Personen haben meine Arbeit in der beschriebenen Weise unentgeltlich unterstützt.

(3) Weitere Personen waren an der inhaltlich-materiellen Herstellung der vorliegenden Arbeit nicht beteiligt. Insbesondere habe ich hierfür nicht die entgeltliche Hilfe eines Promotionsberaters oder anderer Personen in Anspruch genommen. Niemand hat von mir weder unmittelbar noch mittelbar geldwerte Leistungen für Arbeiten erhalten, die im Zusammenhang mit dem Inhalt der vorgelegten Dissertation stehen.

(4) Die Arbeit wurde bisher weder im In- noch im Ausland in gleicher oder ähnlicher Form einer anderen Prüfungsbehörde vorgelegt.

_____ _____

Ort, Datum Bastian Rödig